TESIS DE LA UNIVERSIDAD
DE ZARAGOZA

2022 197

Alberto Montolio Marco

Computational methods for new clinical applications using imaging techniques

Director/es

Pérez Del Palomar Aldea, María Amaya
Cegoñino Banzo, José

ISSN 2254-7606

Prensas de la Universidad
Universidad Zaragoza

Servicio de Publicaciones

ISSN 2254-7606

Tesis Doctoral

COMPUTATIONAL METHODS FOR NEW CLINICAL APPLICATIONS USING IMAGING TECHNIQUES

Autor

Alberto Montolio Marco

Director/es

Pérez Del Palomar Aldea, María Amaya
Cegoñino Banzo, José

UNIVERSIDAD DE ZARAGOZA
Escuela de Doctorado

Programa de Doctorado en Ingeniería Mecánica

2022

Computational methods for new clinical applications using imaging techniques

PhD thesis by

Alberto Montolío Marco

Doctoral advisors

Amaya Pérez del Palomar Aldea

José Cegoñino Banzo

Doctoral Degree in

Mechanical Engineering

Universidad Zaragoza
1542

Computational methods for new clinical applications using imaging techniques

PhD thesis by

Alberto Montolío Marco

Doctoral advisors

Amaya Pérez del Palomar Aldea

José Cegoñino Banzo

Doctoral Degree in

Mechanical Engineering

Universidad
Zaragoza
1542

D. José Cegoñino Banzo y Dña. Amaya Pérez del Palomar Aldea, Profesores Titulares del Departamento de Ingeniería Mecánica de la Universidad de Zaragoza, y directores de la Tesis Doctoral titulada: "Computational methods for new clinical applications using imaging techniques", realizada por el aspirante a título de doctor, D. Alberto Montolío Marco,

DISPONEN,

Que la memoria de Tesis Doctoral ha sido realizada bajo su supervisión en el programa de doctorado en Ingeniería Mecánica de la Universidad de Zaragoza.

Que la memoria de Tesis Doctoral cumple con los requisitos para su presentación en modalidad de Tesis por compendio de publicaciones, recogidos en el art. 20 del Reglamento sobre Tesis Doctorales de la Universidad de Zaragoza y en el art. 12.4 del Procedimiento de depósito, autorización y defensa de tesis de la Universidad de Zaragoza.

Que el proyecto de Tesis Doctoral reúne los requisitos para optar a la mención de "Doctor Internacional", establecidos por el art. 18 del Reglamento sobre Tesis Doctorales de la Universidad de Zaragoza y el art. 12.2 del Procedimiento de depósito, autorización y defensa de tesis de la Universidad de Zaragoza.

Fdo.: D. José Cegoñino Banzo

Fdo.: Dña. Amaya Pérez del Palomar Aldea

De acuerdo con el art. 15 de Real Decreto 99/2011, modificado por el Real Decreto 195/2016, esta Tesis Doctoral reúne los requisitos para incluir la mención internacional en el título de doctor, ya que la memoria cumple con lo establecido y el doctorando ha realizado una estancia de investigación de tres meses en una institución de enseñanza superior fuera de España, concretamente en *Experimental and Clinical Research Center (ECRC)* perteneciente a *Charité – Universitätsmedizin Berlin* en Alemania del 1 de abril de 2021 al 30 de junio de 2021, bajo la supervisión del Profesor Dr. Friedemann Paul.

Asimismo, en virtud del art. 15 del Real Decreto 99/2011, modificado por el Real Decreto 195/2016, la presente memoria ha sido revisada por dos expertos doctores pertenecientes a instituciones de educación superior o institutos de investigación no españoles. Concretamente, esta memoria ha sido revisada favorablemente por Alberto Dominguez Vicent, *Assistant Professor, Division of Eye and Vision, Department of Clinical Neuroscience, Karolinska Institutet (Stockholm, Sweden)*; y por Alexander Ulrich Brandt, *Adjunct Associate Professor, Multiple Sclerosis Center, Department of Neurology, University of California (Irvine, USA).*

Adicionalmente, de acuerdo con el art. 20 del Reglamento sobre Tesis Doctorales de la Universidad de Zaragoza, esta Tesis Doctoral reúne los requisitos para ser presentada bajo la modalidad de tesis por compendio de publicaciones, al cumplir los requisitos establecidos por la Comisión Académica del programa de doctorado en Ingeniería Mecánica, y tener un mínimo de cuatro artículos con unidad temática, de los que al menos tres están publicados en revistas del "Journal Citation Reports", como se detalla a continuación:

- **Manuscrito 1:** A mathematical model to predict the evolution of retinal nerve fiber layer thinning in multiple sclerosis patients
  Autores: Alberto Montolío, José Cegoñino, Elvira Orduna, Berta Sebastian, Elena Garcia-Martin, Amaya Pérez del Palomar
  Estado: Publicado, 2019. Computers in Biology and Medicine 111, 103357
  https://doi.org/10.1016/j.compbiomed.2019.103357
  Revista: Computers in Biology and Medicine
  Factor de impacto de la revista (JCR): 3.434, Q1 (2019)
  Categorías temáticas de Web of Sciences: Engineering, Biomedical; Computer Sciences, Interdisciplinary Applications; Mathematical & Computational Biology; Biology

- **Manuscrito 2:** Swept source optical coherence tomography to early detect

multiple sclerosis disease. The use of machine learning techniques
Autores: Amaya Pérez del Palomar, José Cegoñino, Alberto Montolío, Elvira Orduna, Elisa Vilades, Berta Sebastian, Luis E. Pablo, Elena Garcia-Martin
Estado: Publicado, 2019. PLos ONE 14(5), e0216410
https://doi.org/10.1371/journal.pone.0216410
Revista: PLoS ONE
Factor de impacto de la revista (JCR): 2.740, Q2 (2019)
Categorías temáticas de Web of Sciences: Multidisciplinary Sciences

- **Manuscrito 3:** Machine learning in diagnosis and disability prediction of multiple sclerosis using optical coherence tomography
  Autores: Alberto Montolío, Alejandro Martín-Gallego, José Cegoñino, Elvira Orduna, Elisa Vilades, Elena Garcia-Martin, Amaya Pérez del Palomar
  Estado: Publicado, 2021. Computers in Biology and Medicine 133, 104416
  https://doi.org/10.1016/j.compbiomed.2021.104416
  Revista: Computers in Biology and Medicine
  Factor de impacto de la revista (JCR): 4.589, Q1 (2020)
  Categorías temáticas de Web of Sciences: Engineering, Biomedical; Computer Sciences, Interdisciplinary Applications; Mathematical & Computational Biology; Biology

- **Manuscrito 4:** Comparison of machine learning methods using Spectralis OCT for diagnosis and disability progression prognosis in multiple sclerosis
  Autores: Alberto Montolío, José Cegoñino, Elena Garcia-Martin, Amaya Pérez del Palomar
  Estado: Publicado, 2022. Annals of Biomedical Engineering, s10439-022-02930-3
  https://doi.org/10.1007/s10439-022-02930-3
  Revista: Annals of Biomedical Engineering
  Factor de impacto de la revista (JCR): 3.934, Q2 (2020)
  Categorías temáticas de Web of Sciences: Engineering, Biomedical

Además de los 4 artículos anteriores incluidos en esta Tesis Doctotal por compendio de publicaciones, en el capítulo 2 de esta memoria se incluyen 2 manuscritos también publicados en revistas indexadas en el "Journal Citation Reports" que no forman parte del compendio de publicaciones a evaluar.

A mis padres y mis hermanos.
A Pilar.

Acknowledgments

This thesis marks the end of a stage in my life and I would like to thank all the people who have accompanied me throughout this time.

First of all, to my thesis supervisors, Amaya Pérez del Palomar and José Cegoñino, for trusting me more than five years ago, guiding me during this journey and contributing to my personal growth. I cannot forget Elena García and María Jesús Rodrigo, without your work and effort this thesis would not have been possible. I would also like to mention here the people who made my research stay in Berlin possible, especially Alenxander Brandt and Amir Motamedi, for giving me the opportunity to live this experience that I will never forget.

In these years I have been able to meet wonderful people who have become true friends, especially Silvia, Belén, Jara, Diego and Nicolás. You made the work have moments of laughter with which to gather strength for the rest. I know you will go far in life and hopefully our paths will meet again at some point. To those of us who already knew each other, thank you for being by my side. Special mention to Alejandro, who was there at the beginning of all this. And, of course, my lifelong friends, those from the village. No matter how many years go by, the people I have grown up with will always be special.

I want to dedicate all my efforts to my family, especially my parents and my brothers who have always taken care of me. I remember my grandparents who left before I embarked on this adventure, I know you will be proud of the person I am today thanks to the values you instilled in me. I would also like to mention my niece África who has become the joy of the house.

And my fundamental support, Pilar. My life partner, thank you for loving me every day. I cannot forget her family, which is now mine too.

To all of you, thank you from the bottom of my heart.

Agradecimientos

Con esta tesis pongo el punto final a una etapa de mi vida y por eso me gustaría dar las gracias a todas las personas que me han acompañado durante todo este tiempo.

En primer lugar, a mis directores de tesis, Amaya Pérez del Palomar y José Cegoñino, por confiar en mí hace ya más de cinco años, guiarme durante esta andadura y contribuir en mi crecimiento personal. No puedo olvidarme de Elena García y María Jesús Rodrigo, sin vuestro trabajo y esfuerzo esta tesis no hubiera sido posible. También quiero mencionar aquí a las personas que hiceron posible mi estancia de investigación en Berlín, especialmente a Alenxander Brandt y Amir Motamedi, por brindarme la oportunidad de vivir esa experiencia que nunca olvidaré.

En estos años he podido conocer a personas maravillosas que se han convertido en verdaderos amigos, destacando a Silvia, Belén, Jara, Diego y Nicolás. Hicisteis que el trabajo tuviera momentos de risa con los que coger fuerzas para el resto. Sé que llegaréis lejos en la vida y ojalá nuestros caminos se vuelvan a encontrar en algún momento. A los que ya nos conocíamos, gracias por seguir a mi lado. Mención especial a Alejandro, quien estuvo en el principio de todo esto. Y, cómo no, a mis amigos de toda la vida, los del pueblo. Por muchos años que pasen, la gente con la que he crecido siempre será especial.

Quiero dedicar todo mi esfuerzo a mi familia, en especial a mis padres y mis hermanos que siempre han cuidado de mí. Me acuerdo de mis abuelos que se marcharon antes de que yo me embarcara en esta aventura, sé que estaréis orgullosos de la persona que soy hoy en día gracias a los valores que me inculcasteis. También quiero mencionar a mi sobrina África que se ha convertido en la alegría de la casa.

Y mi apoyo fundamental, Pilar. Mi compañera de vida, gracias por quererme cada día. No me puedo olvidar de su familia, que ahora tambien es la mía.

A todos, gracias de corazón.

Abstract

This thesis aims to develop different computational methods with clinical application in various diseases. In this way, the research presented here aims to increase knowledge on how the analysis and study of data from imaging techniques can be of great clinical value to medical professionals. Therefore, these methods can be incorporated into clinical practice, which is of benefit to the patient.

On the one hand, the improvement of different imaging devices increases the range of possibilities for data analysis and presentation. Some imaging techniques directly yield numerical data that were traditionally only used for disease monitoring. However, these data can be used as biomarkers for both diagnosis and disease prediction using artificial intelligence. Today, artificial intelligence is used in many fields as everything that provides data can be addressed by these new technologies. There seems to be no limit and new applications are being developed that only a few decades ago seemed impossible.

On the other hand, imaging techniques allow us to analyse different parts of the human body in the respective patients and compare them with healthy controls. In the same way, imaging can be used to monitor the treatments applied to these patients and, thus, verify their efficacy. Moreover, these technologies, which provide high-resolution images, are easy to use, cost-effective and objective.

To summarise, this thesis has focused on developing several clinical applications, based on the described numerical methods, which could be a powerful tool to provide further information to help clinicians in decision making.

Resumen

Esta tesis tiene por objetivo desarrollar diferentes métodos computacionales con aplicación clínica en varias enfermedades. De este modo, la investigación aquí presentada pretende aumentar el conocimiento sobre cómo el análisis y el estudio de los datos procedentes de técnicas de imagen pueden convertirse en un gran valor clínico para los profesionales de la medicina. Por lo tanto, dichos métodos pueden ser incorporados en la práctica clínica, lo que supone un beneficio para el paciente.

Por un lado, la mejora de los diferentes dispositivos de imagen aumenta el abanico de posibilidades de análisis y presentación de los datos. Algunas técnicas de imagen arrojan directamente datos numéricos que tradicionalmente sólo se usaban para la monitorización de enfermedades. Sin embargo, dichos datos pueden ser empleados como biomarcadores tanto para el diagnóstico como para la predicción de enfermedades mediante la inteligencia artificial. Hoy en día, la inteligencia artificial se utiliza en muchos campos ya que todo lo que proporciona datos es abordable por estas nuevas tecnologías. Parece que no hay límite y se están desarrollando nuevas aplicaciones que hace sólo unas décadas parecían imposibles.

Por otro lado, las técnicas de imagen nos permiten analizar diferentes partes del cuerpo humano en los respectivos pacientes y compararlas con controles sanos. Del mismo modo, con las imágenes se puede realizar el seguimiento de los tratamientos aplicados en dichos pacientes y, así, verificar su eficacia. Además, estas tecnologías, que proporcionan imágenes de alta resolución, son fáciles de usar, rentables y objetivas.

Para resumir, esta tesis se ha centrado en desarrollar varias aplicaciones clínicas, basadas en los métodos numéricos descritos, que podrían ser una poderosa herramienta para aportar mayor información que ayude a los clínicos en la toma de decisiones.

Contents

List of Figures

List of Tables

List of Abbreviations

A-scans	One-dimensional scan
AI	Artificial intelligence
ANN	Artificial neural network
APS	Anatomic positioning system
B-scan	Two-dimensional scan
BM	Bruch's membrane
BRI/LAP	Brimonidine–Laponite
CC	Choriocapillaris
CF	Central fovea
CIS	Clinically isolated syndrome
CNN	Convolutional neural network
CNS	Central nervous system
CSF	Cerebrospinal fluid
DRI	Deep range imaging
DT	Decision tree
EC	Ensemble classifier
EDSS	Expanded disability status scale
ELM	External limiting membrane
EP	Evoked potential

ETDRS	Early treatment diabetic retinophaty study
EVV	Enhanced vitreous visualization
GCIPL	Ganglion cell-inner plexiform layer
GCL	Ganglion cell layer
HEYEX	Heidelber eye explorer
I	Inferior
IF	Intravitreal formulation
II	Inner inferior
ILM	Internal limiting membrane
IN	Inner nasal
INL	Inner nuclear layer
IOP	Intraocular pressure
IPL	Inner plexiform layer
IS	Inner superior
IT	Inner temporal
k-NN	k-nearest neighbours
LGN	Lateral geniculate nucleus
LR	Logistic regression
mGCIPL	Macular ganglion cell-inner plexiform layer
MRI	Magnetic resonance imaging
mRNFL	Macular retinal nerve fiber layer
MS	Multiple sclerosis
N	Nasal
NB	Naïve Bayes

NI	Inferonasal
NS	Superonasal
NTG	Normal-tension glaucoma
OCT	Optical coherence tomography
ODE	Ordinary differential equation
OI	Outer inferior
ON	Outer nasal
ONL	Outer nuclear layer
OPL	Outer plexiform layer
OS	Outer superior
OT	Outer temporal
PLGA	Poly (lactic-co-glycolic) acid
PMB	Papillomacular bundle
PPMS	Primary-progressive multiple sclerosis
PR	Photoreceptor layer
PRMS	Progressive-relapsing multiple sclerosis
pRNFL	Peripapillary retinal nerve fiber layer
RF	Random forest
RGC	Retinal ganglion cell
RNFL	Retinal nerve fiber layer
RNN	Recurrent neural network
RPE	Retinal pigment epithelium
RRMS	Repalsing-remitting multiple sclerosis
S	Superior

SD-OCT	Spectral-domain optical coherence tomography
SLO	Scanning laser ophthalmoscopy
SPMS	Secondary-progressive multiple sclerosis
SS-OCT	Swept-source optical coherence tomography
SVM	Support vector machine
T	Temporal
TABS	Topcon advanced boundary software
TI	Inferotemporal
TS	Superotemporal
VIT/RPE	Vitreous/retinal pigment epithelium

Chapter 1

Introduction

This chapter presents a brief description of the anatomy of the eye, with special attention to the retina. The retina can be monitored using ocular imaging technologies such as optical coherence tomography (OCT), which allow a non-invasive, rapid, objective and reproducible evaluation. Then, two of the most devastating neurodegenerative diseases are summarized and some clinical applications of OCT to treat these diseases are detailed. A broad overview of the clinical, animal and computational studies conducted on this topic is provided. Finally, the motivation, main objectives and outline of this thesis are presented at the end of this chapter.

1.1 Eye anatomy

This section describes the anatomy of the human eye, paying special attention to the retina. The function of the eye is to capture the images of our environment and send them to the brain for processing. The cornea is the transparent part that acts as a protective covering and allows light to pass through. The iris, the part that gives color to the eye, contracts and expands so that the pupil allows the right amount of light to pass through, which is focused on the retina thanks to the crystalline lens (see Figure 1).

The sense of sight is a complex process in which the retina, as part of the central nervous system (CNS), is responsible for receiving light rays and transforming their electromagnetic energy into nerve impulses [98]. These nerve stimuli are transported by the axons of the nerve fiber layer through the optic nerve from the retinal ganglion cells (RGCs) to the lateral geniculate nucleus (LGN) [155]. Visual perception takes

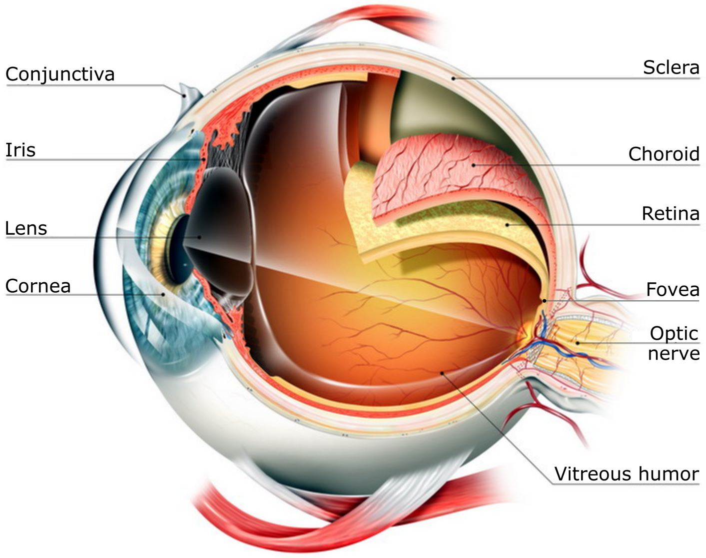

Figure 1: Eye anatomy

place in the brain, thanks to which we are able to perceive the shape of objects, identify distances, detect colors and appreciate movement. As shown in Figure 2, when the nerve fibers reach the chiasm, the temporal fibers of the optic nerve remain on the same side, while the nasal fibers of each eye cross to the opposite side of the brain. As a consequence of this distribution and crossing, the so-called optic tracts are formed, which terminate in LGN. This multilayered structure is a relay center in the thalamus and plays an essential role in the visual pathway [157]. Thus, the right optic tract carries information to the left visual field, while the left optic tract carries it to the right visual field.

The retina is located at the back of the eyeball and is divided into several layers, as shown below and can be seen in Figure 3:

- **Internal limiting membrane (ILM)** is the basal lamina of the inner retina and acts as boundary between vitreous humor and retina. It is formed by astrocytes and the footplates of Müller cells and is composed of collagen fibers, glycosaminoglycans, laminin and fibronectin [51].

- **Retinal nerve fiber layer (RNFL)** lies between ILM and somas of RGCs. RNFL is composed of the unmyelinated axons of the RGCs, astrocytes, retinal vessels, and Müller cells processes that form ILM as the basal lamina covering the surface of RNFL [63]. As can be seen in Figure 4, RGC axons are myelinated in the optic nerve, but remain unmyelinated in the RNFL [167].

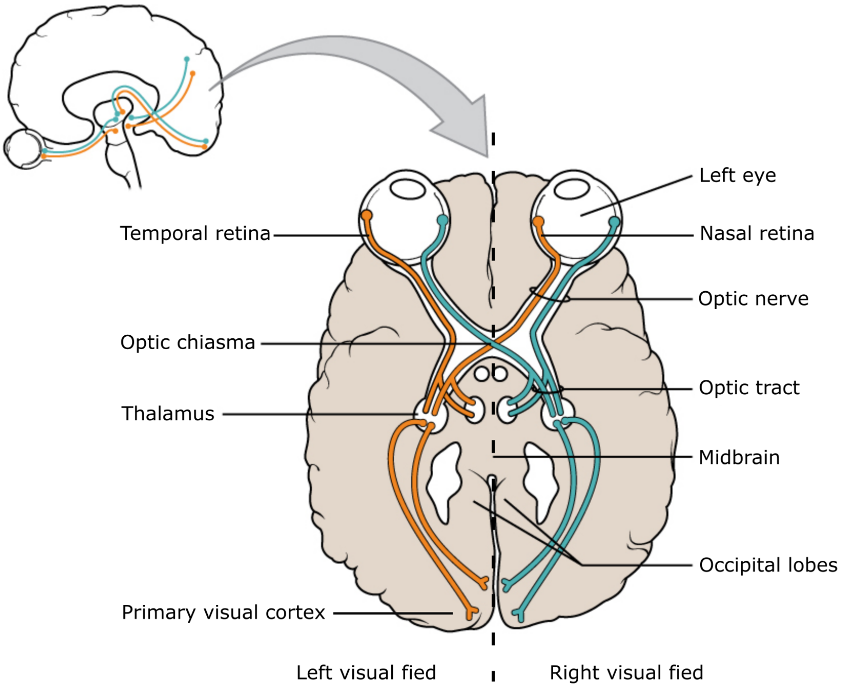

Figure 2: Visual nervous system

- **Ganglion cell layer (GCL)** is composed of RGCs, which receive information from photoreceptors via interneurons, and displaced amacrine cells. GCL is generally a single cell thick. Although the cells lie side by side, RGCs are separated from each other by glial processes of the Müller cells [121].

- **Inner plexiform layer (IPL)** is formed by the synaptic connections between bipolar cell axons and ganglion cell dendrites. There are also synapses between amacrine processes and bipolar axons; amacrine processes and ganglion cell bodies and dendrites; amacrine cells; and amacrine cells and interplexiform neurons [73]. In this layer begins the processing of motion detection and brightness changes, as well as contrast and hue recognition [80]. In some OCT devices, GCL and IPL are measured together as ganglion cell-inner plexiform layer (GCIPL).

- **Inner nuclear layer (INL)** consists of three classes of neuronal cells (horizontal, bipolar and amacrine cells) and one class of glia (Müller cells). The nuclei of the horizontal cells are located next to the outer plexiform layer. The nuclei of the amacrine cells are located next to IPL. Bipolar cells have their dendrite in the outer plexiform layer and their axon in the IPL [99]. There are also interplexiform neurons whose function is to receive input from IPL and project it to the outer plexiform layer [73].

- **Outer nuclear layer (ONL)** contains the nuclei of the cone and rod photoreceptors [58]. The cell body and nucleus of cones are larger than those of rods. The outer fibers of the cones are very short so that the cone nuclei are close to the external limiting membrane. The rod cell bodies are arranged in several rows inside the cone cell bodies.
- **Outer plexiform layer (OPL)** is composed of the synapses between retinal photoreceptors, horizontal cells and bipolar cells. Cone pedicles and rod spherules synapse with various bipolar and horizontal cells processes [72].

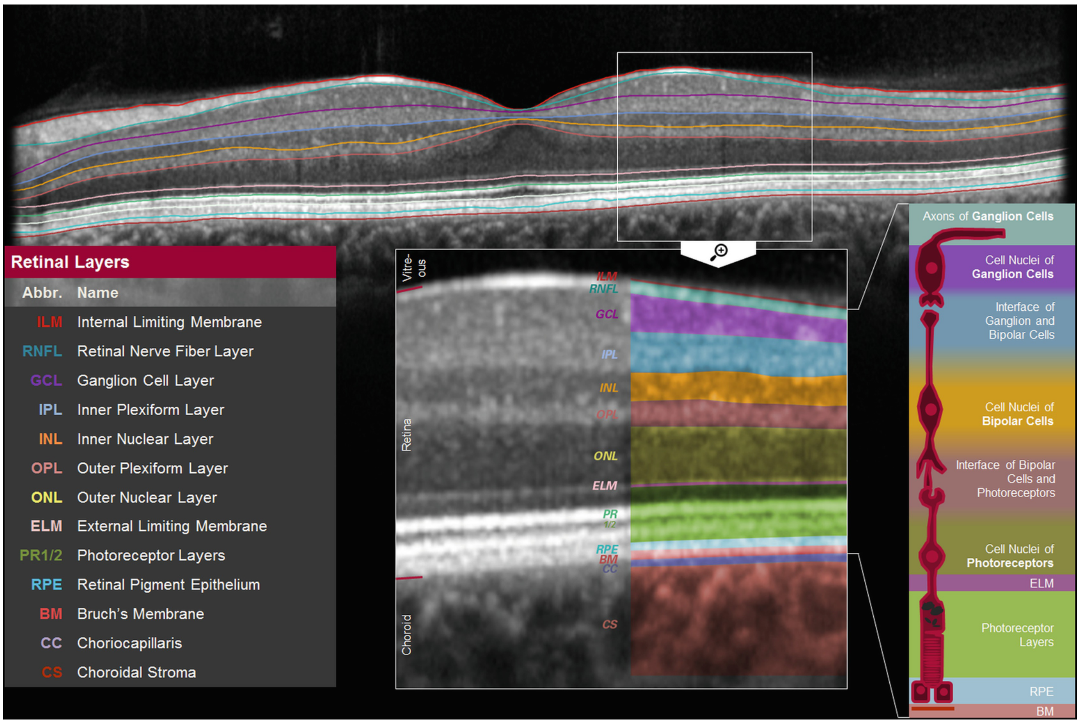

Figure 3: Anatomy of the retina showing the distribution of retinal layers and cells involved in vision. Multilayer segmentation of a retinal OCT scan with the naming convention [3].

- **External limiting membrane (ELM)** is a structure that separates the inner segments from the ONL and is composed of junctions between photoreceptors cells and Müller cells. This membrane has the potential to act as a metabolic barrier against some large molecules [23].
- **Photoreceptor layer 1/2 (PR)** contains the outer and inner segments of rods and cones. The apex of Müller cells is found in this player, while the basal aspect is located on the inner surface of the retina [80].
- **Retinal pigment epithelium (RPE)** is formed from a single layer of pigmented cells arranged at the outermost layer of the retina. The outer face of

the EPR is connected to Bruch's membrane and the choroid, and the inner face is connected to the outer segment of the photoreceptor cells [166].

It is important that light has few obstacles on its way to the outer segments of the photoreceptors. The blood-retinal barrier does not allow blood plasma components to enter the retinal tissue as these components can impede the passage of light. This barrier is composed of RPE, Bruch's membrane (BM) and choriocapillaris (CC). RPE and CC interact with each other and collaborate to form BM. This membrane is a multi-layered structure that joins RPE on its inner surface and CC on its outer surface [40]. Finally, the choroid, a dense network of blood vessels and pigmented stroma between the retina and sclera, supplies nutrition to the outer retina, and maintains the temperature and volume of the eye.

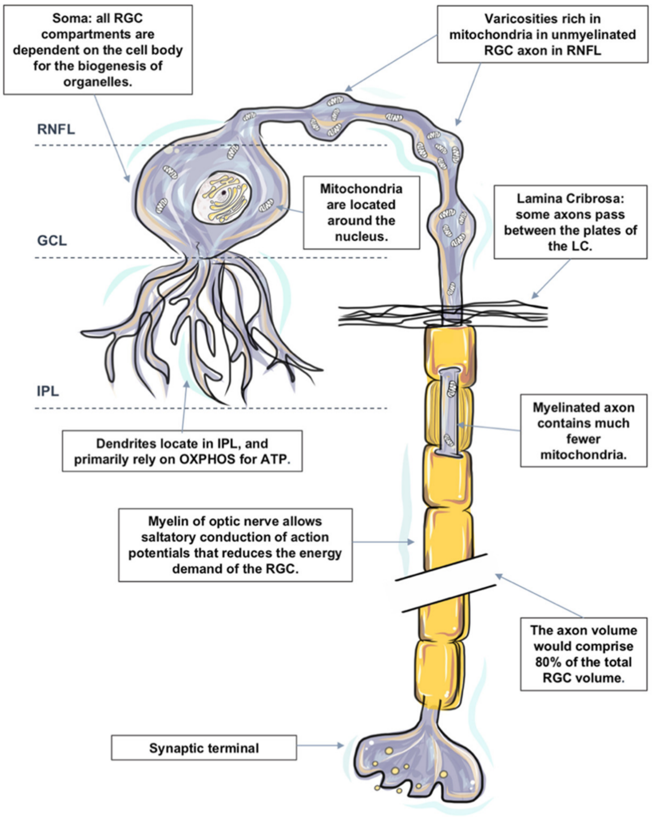

Figure 4: Scheme of RGC characteristics. RGC dendrites are located in IPL and axons of these cells form RNFL. Axons are unmyelinated in the retina and are myelinated beyond the lamina cribrosa [94].

One of the most important parts of this research focused on GCL and RNFL, where RNFL is formed by the unmyelinated axons of the RGCs. The parts that compose a RGC are detailed in order to better understand its functioning. All cells have the basic functions of receiving signals with information, integrating these signals to decide whether the information received should be transmitted and sending them to other cells, muscles or glands. Cells possess a cell body called soma, which contains abundant cytoplasm and cell organelles. Soma receives information from the dendrites and send action potentials through the axon. It is the fundamental part to keep the cell alive and support the dendrites and axon. RGC bodies are located in GCL.

Dendrites are specialized branches that extend from the cell body and acts as a receptor receiving messages from other neurons. It produces voltage changes in response to stimuli and assists in the formation of the nerve impulse. RGC dendrites receive inputs from bipolar cells and branch in IPL. Clearly differentiated from the rest of the soma extensions is the axon, an extension longer than the dendrites. The axon or nerve fiber carries information from the soma to the synaptic terminals of other cells, muscles or glands. It is very small in diameter but can be very long. Each cell has only one. If an axon breaks, the distal part degenerates due to a disruption of the cytoplasm extending from the soma. RGC axons are coated with myelin, a substance that surrounds and protects these axons, whose main function is to increase the speed of nerve impulse transmission. In the part of the axons located in the retina, these axons lack myelin [94, 63] (see Figure 4). Axon terminals are the bulbous endings of the many branches that extend from the end of the axon. These synaptic terminals serve as the secretory component that releases neurotransmitters in response to nerve impulses.

1.2 Optical coherence tomography

OCT is an easy-to-use, cost-effective and objective technology that provides high-resolution images. This tool is widely used in clinical practice and research to analyse neuroretinal structure. With the proliferation of different OCT devices, the range of possibilities for data analysis and presentation increases. In the following sections of the chapter we will discuss the scanning protocols of the devices available for this work at Miguel Servet University Hospital (Zaragoza, Spain). Special emphasis will be placed on spectral-domain OCT (SD-OCT) and swept-source OCT (SS-OCT) devices, addressing the differential characteristics and the main image acquisition and analysis protocols of the most common devices. Current SD-OCT and SS-OCT devices use lasers of different wavelengths to acquire OCT images in the same way [87]. For our studies, the SD-OCT devices available are Cirrus HD-OCT and Spectralis OCT, while OCT Triton employs SS-OCT technology.

1.2.1 Cirrus HD-OCT

Cirrus HD-OCT (model 4000; Carl Zeiss Meditec, Dublin, CA, USA) is a digital retinal imaging technology used to monitor axonal loss. SD-OCT devices scan a square of macular and peripapillary area (6 x 6 mm), obtaining a data cube for thickness and volume analysis. They provide a wide flexibility, since they allow to choose between different scanning protocols. The number of lines and scans per line can be modified to increase the resolution or to decrease the acquisition time [69, 130].

The macular cube protocol allows analysis of macular volume and thickness, and generates a statistical significance map of thicknesses compared to a normative baseline, as well as contour maps of ILM, RPE and ILM-RPE. In the Cirrus HD-OCT segmentation algorithm, the inner retinal boundary is identified at the vitreoretinal interface and is detected by the increase in reflectivity between a non-reflective (vitreous) and a hyper-reflective (ILM) area. The outer limit of the retina is located in the hyperreflective band generated by the RPE-CC, located after a double line of reflectivity, which corresponds to the junction of the inner and outer segments of the photoreceptors.

The use of the macular cube protocol provides an scanning laser ophthalmoscopy (SLO) image for localization of the analysed lines and zones. Over these zones can be superimposed the color-scale ILM-RPE measurement or the fovea location established by early treatment diabetic retinophaty study (ETDRS). These protocol generates a numerical report of macular thickness in a central circular subfield divided into the nine sectors defined in the ETDRS. It consists of three concentric circles with diameters of 1, 3 and 6 mm. Except for the central circle, they are divided into superior, nasal, inferior and temporal quadrants. The device reports the mean value of macular thickness in each of these sectors. There are two types of optic macular cube protocol:

- **Optic macular cube 512 x 128:** scans an area of 6 x 6 mm. The image is obtained from 128 two-dimensional scans (B-scans) each composed of 512 one-dimensional scans (A-scan), except for the central scans which have 1024 A-scans each.
- **Optic macular cube 200 x 200:** scans an area of 6 x 6 mm with 200 B-scans of 200 A-scans each, except for the central lines which consist of 1000 A-scans each.

Comparing these two protocols (see Figure 5), macular cube 512 x 128 has higher resolution from left to right (512 A-scans vs. 200 A-scans) but lower vertical resolution (128 B-scans vs. 200 B-scans).

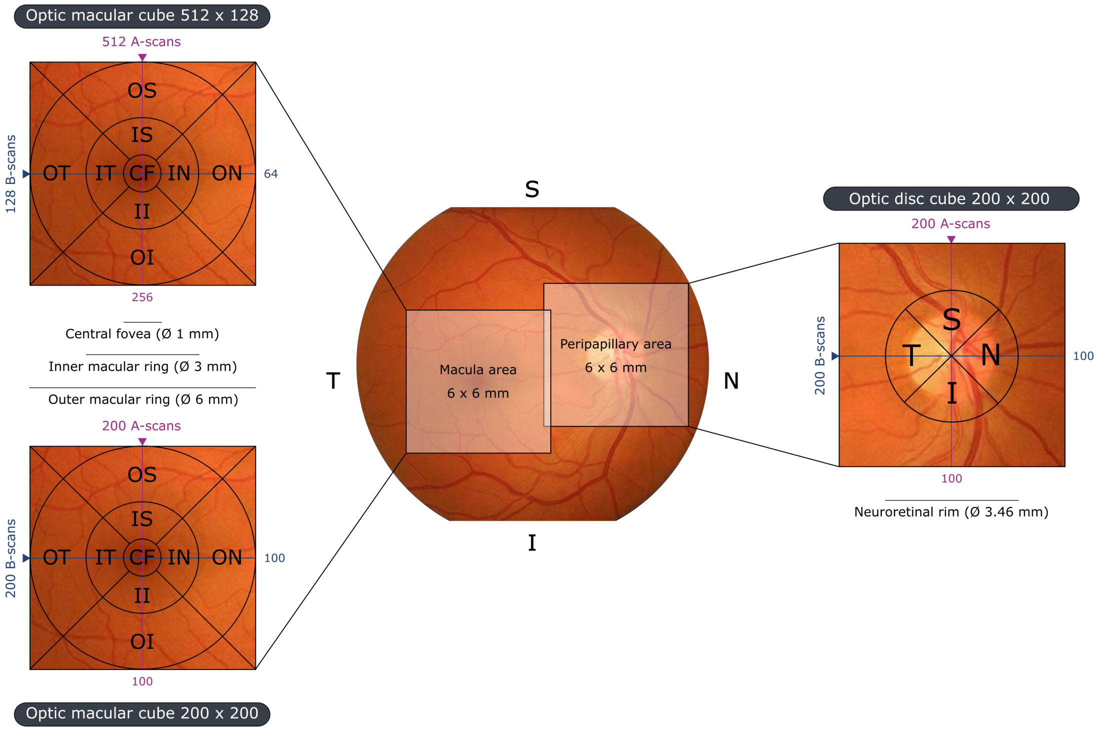

Figure 5: Schematic representation of Cirrus HD-OCT acquisition protocols on a right eye retina. Optic macular cube 512 x 128 and optic macular cube 200 x 200 measure total volume and macular thickness in nine sectors (CF: central fovea; IN: inner nasal; ON: outer nasal; IS: inner superior; OS: outer superior; IT: inner temporal; OT: outer temporal; II: inner inferior; OI: outer inferior). Optic disc cube 200 x 200 measures peripapillary area and the quadrants into which it is divided (S: superior; N: nasal; I: inferior; T: temporal).

As will be detailed in later chapters, the measurement of RNFL thickness is extremely useful in different pathologies of the optic nerve [131, 92]. The protocol for the study of both RNFL and papilla with Cirrus HD-OCT is:

- **Optic disc cube 200 x 200:** scans a 6 x 6 mm area, capturing a data cube of 200 B-scans x 200 A-scans (40,000 points) in 1.5 seconds (27,000 A-scans/sec). As can be seen in Figure 5, this protocol automatically identifies the center of the papilla and creates a circle-shaped sweep 3.46 mm in diameter. Mean thickness values are given for the complete circle as well as by quadrants (superior, nasal, inferior and temporal).

To achieve this correct alignment, the device identifies the hyperreflectivity band boundary corresponding to RPE. The next step consists of RNFL segmentation, the inner boundary is located at the vitreoretinal interface and the outer boundary is located in the innermost low-reflectivity area corresponding to GCL. In this way, a three-dimensional map of the RNFL thickness is constructed, providing visualization within the 6 x 6 mm of the peripapillary area.

The following factors must be taken into account for the acquired image to be reliable: absence of off-center scans, signal strength greater than 6, absence of motion artifacts and good centering around papilla.

1.2.2 Spectralis OCT

Spectralis OCT (Heidelberg Engineering, Heidelberg, Germany) is an instrument consisting of a combination of a confocal laser ophthalmoscope and an SD-OCT with a laser eye fixation system. One of its main features is the TruTrack eye-tracking system to accurately scan the same areas throughout different scans. In this way, the system retains the alignment over successive patient visits, so that the change in the different measurements at the same point on the retina can be accurately quantified [84]. The scans obtained are processed to remove noise from the images and improve their resolution using the Heidelberg Noise Reduction system.

This device combines the patented Anatomic Positioning System (APS) with scan protocols to assess the optic nerve head, RNFL and GCL. These APS-based scan patterns automatically adjust to the unique anatomical landmarks of each eye. APS identifies two fixed landmarks to place the scans in the correct anatomical location: the fovea and the center of the BM opening. This technology increases the precision and accuracy of results by ensuring that all scans are anatomically aligned with the reference database taking into account the configuration of axons in each eye. The customized anatomical alignment provided by APS allows for reliable diagnostic imagines and data.

The minimum distance between ILM and BM opening around the optic nerve head is identified to provide the true anatomic disc margin and accurate measurement of the neuroretinal rim [123]. This parameter is an objective, sensitive and specific diagnostic tool for both the detection and management of optic neuropathies.

Heidelberg Eye Explorer (HEYEX) segments GCL independently of IPL and RNFL. In this way, the loss of each anatomical component of RGCs (axons, somas and dendrites) can be reliably identified. HEYEX is a multilayer automatic segmentation algorithm. The ability to discern each layer provides an accurate method for early detection of damage. Spectralis OCT provides direct visualization of segmentation and the ability to make adjustments when metrics may be confounded by pathological factors such as epiretinal membranes or blood vessels.

To measure the macular thickness of the retina, a volume scan composed of 61 B-scans is taken across the macula and segmented into individual retinal layers. The report includes a thickness map, thickness deviation map and classification chart. The thickness deviation maps of the total retina, RNFL, GCL and IPL reveal regions that have significantly thinner or thicker measurement values compared to eyes included in the reference database and highlight areas that are not within normal limits [55].

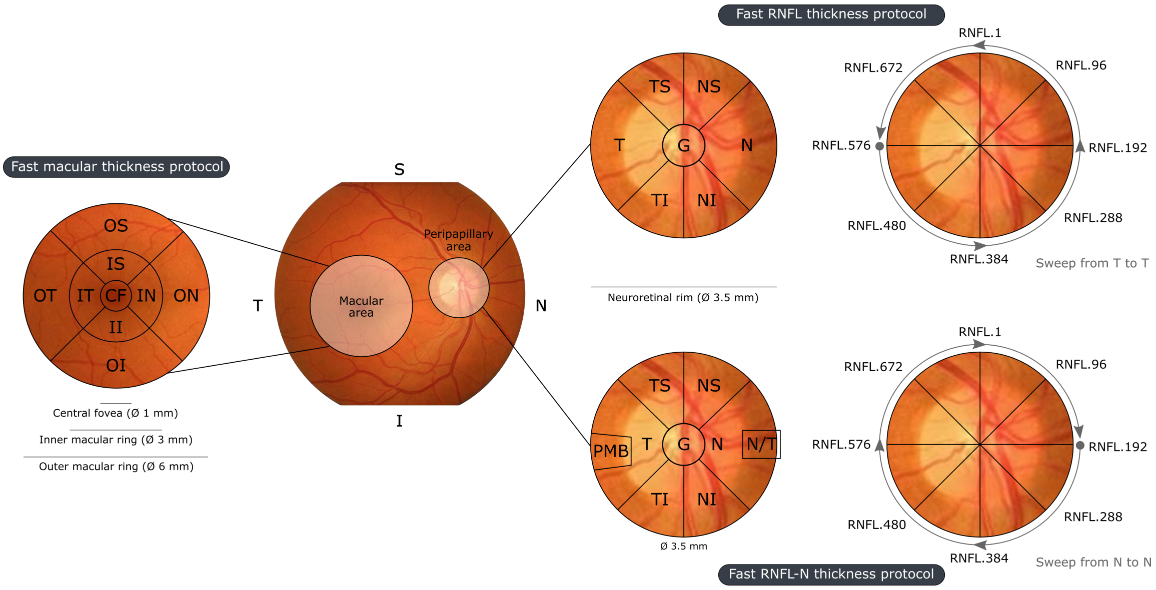

Figure 6: Schematic representation of Spectralis OCT acquisition protocols on a right eye retina. Fast macular thickness protocol measures total volume and macular thickness in nine sectors (CF: central fovea; IN: inner nasal; ON: outer nasal; IS: inner superior; OS: outer superior; IT: inner temporal; OT: outer temporal; II: inner inferior; OI: outer inferior). Fast RNFL thickness protocol measures mean pRNFL thickness (G) and pRNFL thickness in six sectors (NS: superonasal; N: nasal; NI: inferonasal; TI: inferotemporal; T: temporal; TS: superotemporal). Fast RNFL-N thickness protocol adds two parameters: nasal/temporal sector ratio (N/T) and papillomacular bundle (PMB).

- **Fast macular thickness protocol:** consists of a map around the fovea that reports the total macular volume and the macular thickness in nine sectors established by ETDRS.

Software for RNFL analysis in the peripapillary area is also included. This system performs circular tracking for peripapillary RNFL (pRNFL) thickness using an alignment system to avoid variability in measurements due to changes in head position, eye position or eye rotation [163]. As can be seen in Figure 6, a 3.5 mm diameter pRNFL scan is used.

- **Fast RNFL thickness protocol:** diagram with six sectors, in which the superior and inferior quadrants are divided into superonasal, superotemporal, inferonasal and inferotemporal, keeping the nasal and temporal sectors of the four-quadrant diagram. The mean pRNFL thickness is shown in the center of the diagram with the symbol G. In addition, this protocol also generates 768 pRNFL thickness measurements during the circular peripapillary scan. The image sweep is performed from temporal to temporal.

- **Fast RNFL-N thickness protocol:** allows to focus the analysis on the temporal sector. To the six-sector pRNFL diagram, two parameters are added: nasal/temporal sector ratio (N/T) and papillomacular bundle (PMB) corresponding to the temporal quadrant section between -22° and +8°. In this protocol, the sweep of the 768 pRNFL thickness measurements is done from nasal to nasal.

1.2.3 DRI OCT Triton

The deep range imaging (DRI) OCT Triton (Topcon, Tokyo, Japan) combines SS-OCT technology with multimodal fundus imaging. This device has a scanning speed of 100 kHz and a wavelength of 1,050 nm resulting in clear and detailed images. Automated functions, such as single-scan captures and SMART Track, are designed to optimise workflow by simplifying data capture, analysis and follow-up. The 100,000 A-scans/sec scanning speed provides clear B-scans and the invisible 1,050 nm wavelength light helps patients to focus on the fixation target during the scan, reducing unintended eye movement artifacts [71].

Dynamic Focus enables images with near uniform focus and image quality throughout the depth of the image, helping to enhance the typically weaker signal of the vitreous. In addition, Enhanced Vitreous Visualization (EVV) helps clinicians assess abnormalities of the vitreous and vitreoretinal interface. EVV allows to quickly adjust the contrast, depending on the area of interest.

The retinal layers are automatically segmented by Topcon Advanced Boundary Software (TABS), allowing to measure the thickness of the retina and its layers [164, 1]. This software performs a 7-boundary segmentation and provides the following thickness maps: retina (between ILM and RPE boundaries), RNFL (between ILM and GCL boundaries), GCL+ (between RNFL and INL boundaries), GCL++ (between ILM and INL boundaries) and choroid (between BM and choroidal-scleral interface).

SS-OCT incorporates multimodal fundus imaging so that DRI OCT Triton can acquire the OCT and fundus image in a single capture. PinPoint registration positions the location of the B-scan on the fundus image. DRI OCT Triton also offers true color and non-mydriatic fundus images. Follow-up function allows retrieving and re-analyzing the same location, allowing the comparison of images at different times.

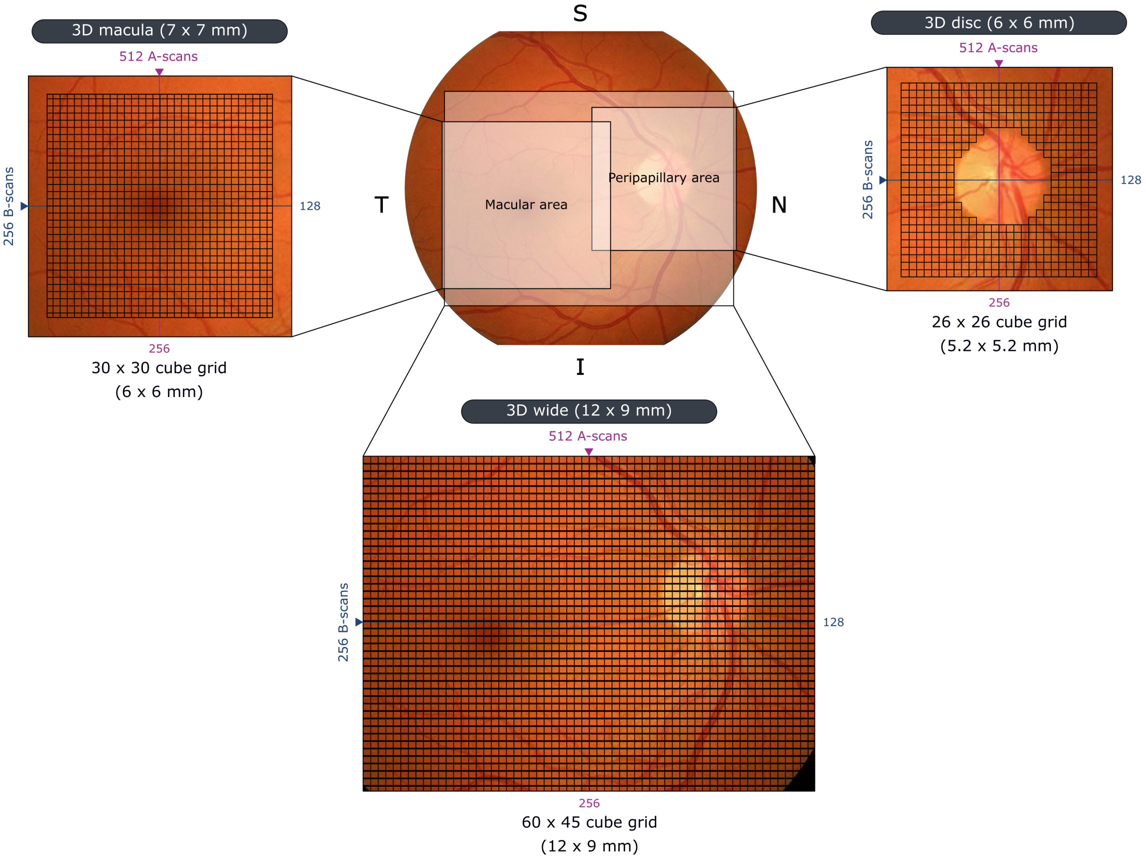

Figure 7: Schematic representation of DRI OCT Triton acquisition protocols on a right eye retina. 3D wide protocol measures an area that includes macular and peripapillary areas using a 60 x 45 cube grid. 3D macular protocol measures macular thickness with a grid composed of 30 x 30 cubes. 3D disc protocol is centered on the optic nerve and uses a 26 x 26 cube grid. For all 3D scans, each grid cube measures 200 x 200 µm.

The 512 x 256 OCT scan pattern captures twice as much OCT data as conventional 512 x 128 scan patterns, significantly increasing the available data. PixelSmart is an image processing algorithm that reduces speckle noise to improve contrast, producing better quality images. PixelSmart can be used in all Triton 3D scans:

- **3D wide:** this protocol covers an area of 12 x 9 mm, including the macula and optic nerve, and the thickness map uses a grid of 60 x 45 cubes. The dimensions of each grid cube are 200 x 200 µm.
- **3D macula:** scans an area of 7 x 7 mm. The grid of the macular protocol is composed of 30 x 30 cubes centered on the fovea. As each cube of the grid measures 200 x 200 µm, the macular thickness is reported in an area of 6 x 6 mm (see Figure 7).
- **3D disc:** scans a 6 x 6 mm area with the 26 x 26 grid centered on the optic disc. In this case, the peripapillary thickness is measured in an area of 5.2 x 5.2 mm. The central area is not shown because the OCT thickness is always zero.

1.3 Neurodegenerative diseases

Neurodegenerative diseases are a broad group of brain diseases with diverse neuropathological and clinical manifestations. These can affect movement, language, memory, reasoning, and many other capacities, leading to a progressive loss of autonomy. All neurodegenerative diseases are characterized by a progressive process of degeneration and neuronal death in the brain and/or other parts of the central or peripheral nervous system. What distinguishes them from each other are the different neuronal groups or brain areas affected in each disease, producing different symptoms and evolution. However, some neurodegenerative diseases share characteristics, both in terms of clinical symptomatology and neuropathological alterations, which make diagnosis difficult. In addition, there are currently no diagnostic tools capable of accurately identifying most neurodegenerative diseases that can cause different combinations of cognitive and motor problems. For these reasons, it is not uncommon for a patient to receive a first diagnosis and, as the disease progresses, the diagnosis is redefined.

It is estimated that there are a few hundred neurodegenerative diseases, with a frequent overlap of clinical and neuropathological features among many of them, which leads to a relevant difficulty in accurate classification and diagnosis. Two of these diseases are multiple sclerosis and glaucoma. The main characteristics of these diseases are presented in this section.

1.3.1 Multiple sclerosis

Multiple sclerosis (MS) is a neurodegenerative disease that affects the CNS, specially the brain, spinal cord and optic nerve [56]. 2.5 million people worldwide suffer from this disease. All MS symptoms are the results of the modification of some CNS function. This pathology presents a great clinical variability since not all patients experience the same symptoms or the same severity, so that each clinical case is unique. Due to the disease progression and the absence of curative treatment, patients are forced to adapt to the deterioration of the disease. The most affected functions are: motor function (causing paresis and spasticity if the pyramidal pathway is affected or imbalance and poor coordination if the damage occurs in the cerebellum), sensory function (causing the appearance of hypoesthesia, paresthesia or dysesthesia) and the visual function. Some of these symptoms are obvious and can be recognized quickly, while others are more difficult for the patient to describe and difficult to recognize.

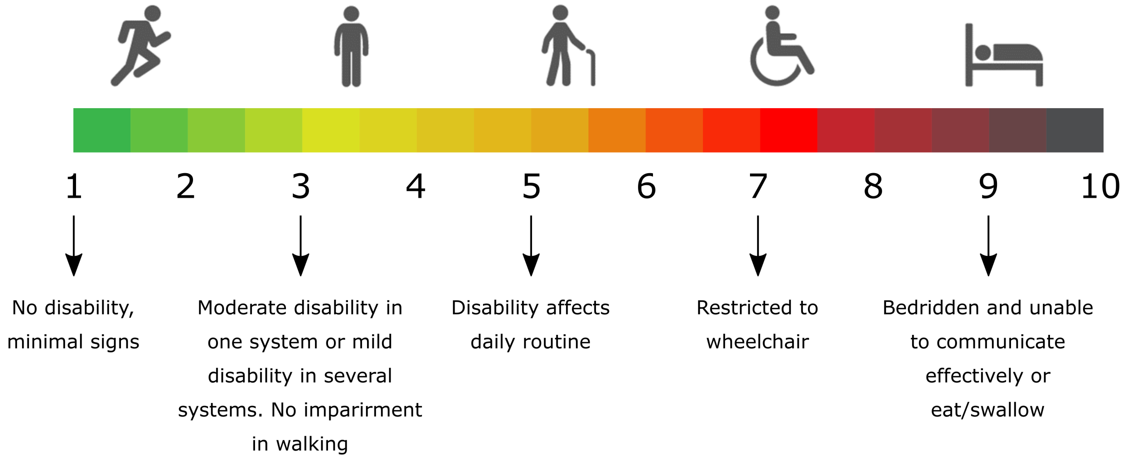

Figure 8: Schematic representation of EDSS.

Assessing the status of MS patients is complex because the disease affects several CNS functions. The expanded disability status scale (EDSS) is one of the most widely used methods to evaluate the progression of this disease [102]. This scale, performed by a neurologist, assigns scores from 0 to 10, with increments of 0.5 as the level of disability increases (see Figure 8). EDSS values between 1 and 4.5 correspond to patients who can walk without problems, while scores ranging from 5 to 7.5 refer to patients who need help to walk. In the worst cases, from values greater than 8, MS patient is totally dependent.

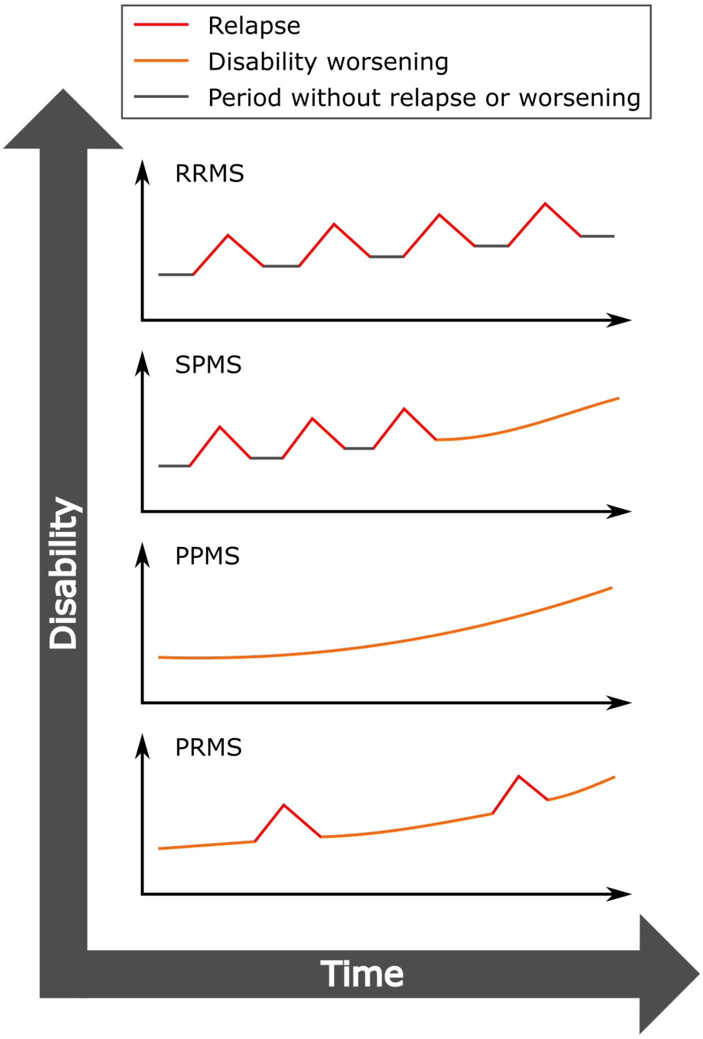

Figure 9: Progression of MS subtypes. RRMS: unpredictable outbreaks that may or may not result in permanent disability, followed by periods of remission. SPMS: initial RRMS that suddenly begins to decline without periods of remission. PPMS: steady disability worsening without relapses. PRMS: worsening from the onset of the disease with outbreaks.

There is no standard progression of the disease, as each person experiences a different pattern. However, the following types of progression can be distinguished [11]:

- **Repalsing-remitting MS (RRMS):** is the most common type of MS, affecting more than 80% of patients. Although symptoms may not appear in the early stages of the disease, damage to the CNS is already occurring. In this type of evolution, the outbreaks are unpredictable, last a few days or weeks and disappear. Between outbreaks the disease does not seem to worsen, but there may be sequelae that cause increasing disability.

- **Secondary-progressive MS (SPMS):** initially has several relapses and thereafter has a progressive course without outbreaks during the course of the disease. Between 30 and 50% of patients who experience a RRMS phase subsequently develop SPMS. This type of evolution is the one that causes the greatest degree of disability.
- **Primary-progressive MS (PPMS):** has as main characteristic the absence of outbreaks, at the beginning the evolution is slow but the symptoms appear progressively (see Figure 9). This type occurs in 10-15% of patients, mainly affecting motor function.
- **Progressive-relapsing MS (PRMS):** causes disability progression from the onset of the pathology with the presence of acute outbreaks. In the period between outbreaks, the disease progresses progressively. It is the least common as it affects only 5% of patients.

Related to the MS disease courses, it is also important to define clinically isolated syndrome (CIS) . This term refers to a first episode of neurological symptoms that lasts at least 24 hours and is caused by inflammation or demyelination in the CNS. Patients who suffer from CIS may or may not develop MS.

About 50% of MS patients have some type of visual impairment. Vision can be affected at two different times: during the relapse, with vision disturbances that partially or completely cease after that, or after the relapse, when the changes make it difficult to perform daily tasks. Some of the most common direct visual disturbances during an outbreak are optic neuritis, double vision and ocular dysmetria. While indirect visual disturbances are usually accommodation and convergence abnormalities, blurred vision, pupil dysfunction and oculomotor disturbances.

This pathology is an axonal degeneration disease since the immune system attacks the myelin that covers the nerve fibers, interrupting the transmission of information [56].The demyelination process interrupts or slows axonal conduction as the destruction of myelin results in plaques of hardened tissue that hinder the passage of nerve impulses. On the other hand, the barrier that isolates the brain from the immune system deteriorates, allowing the passage of immune cells into the brain that can damage the axons. For these reasons, loss of vision and balance, numbness or locomotor system failures occur [153, 37].

The diagnosis of MS is based on the concurrence of dissemination in space (at least two lesions of different location in the CNS) and in time (at least two episodes of neurological dysfunction separated in time). Currently, MS diagnosis requires several tests, such as magnetic resonance imaging (MRI) to detect lesions in brain, cerebrospinal fluid (CSF) analysis, and multiple evoked potential (EP) tests to detect possible decreases in the rate of neurotransmission in the CNS [148]. Therefore, the diagnostic process is complex and lengthy, and can even be challenging for the most experienced neurologist.

Several studies have shown that MS results in RNFL thinning as it causes optic nerve damage leading to axonal degeneration. In addition, GCL and GCIPL thinning has been reported to be a biomarker of neuroaxonal injury [122, 2]. OCT technology allows to obtain in vivo tomographic images of optically accessible biological tissues. In this way, advances in the field of neurology allow OCT to be used to measure the thickness of the different retinal layers in order to understand the MS evolution [112, 138].

1.3.2 Glaucoma

Glaucoma is one of the leading causes of irreversible blindness and will affect 111.8 million people by 2040 [120, 147]. This disease is a group of eye conditions that damage the optic nerve due to an increase in intraocular pressure (IOP), caused by a lack of drainage of the aqueous humor whose function is to nourish and oxygenate the structures of the eyeball. The optic nerve transmits images from the eye to the brain and the increase in IOP slowly and progressively affects its nerve fibers, producing a lesion that is irreversible. The loss of vision depends on the degree of destruction of the optic nerve [62].

The mechanisms that cause glaucomatous neurodegeneration are not fully understood. However, it has been shown that RGC degeneration persists after IOP returns to a normal level. Chen et al. demostrated that neurodegeneration in glaucoma is mediated in part by T cells [22, 97]. RGC pathologies lead to both anterograde and retrograde degeneration of these cells, as well as anterograde trans-synaptic degeneration. In addition, some studies have reported brain changes in glaucoma patients outside the retino-geniculo-cortical patyway [89]. Lee et al. and Schmidt et al. concluded that LGN volumes were significantly smaller than those of healthy controls in glaucoma patients. Moreover, LGN volume correlated with GCIPL and RNFL thicknesses [90, 133]. Therefore, evaluation of the central and peripheral nervous systems by MRI confirmed that patients with glaucoma had smaller optic nerve dimensions and LGN height compared to the control group [43].

Certain parameters increase the likelihood of glaucoma, such as family history, diabetes, smoking, myopia and hyperopia, prolonged treatment with corticosteroids or age. Aging is one of the most important risk factors. With age, the depth and volume of the anterior chamber decreases, predisposing to pupillary block and thus increasing the prevalence of angular closure glaucoma. In addition, the cells of the trabeculum, which is the area through which the aqueous humor drains, change with age, making drainage of the aqueous humor more difficult. If the drainage angle does not work properly, the fluid accumulates, the IOP increases and this damages the optic nerve. In this regard, glaucoma is most often associated with elevated IOP. However, it can also appear when IOP is at normal levels [101].

There are several types of glaucoma, but the most common are:

- **Open-angle glaucoma:** is the most common form of glaucoma, accounting for at least 90% of glaucoma cases. The drainage angle formed by the cornea and iris remains open, but the trabecular meshwork is partially blocked. This causes the pressure in the eye to gradually increase and, as a consequence, the optic nerve is damaged. It happens so slowly that vision can be lost before symptoms and damage are noticed. Open-angle glaucoma is also called primary or chronic glaucoma.

- **Angle-closure glaucoma:** pathology produced by a significant increase in IOP. It is caused by a closure of the angle, which is the structure through which the aqueous humor is eliminated. The production of aqueous humor is continuous, and due to the inability to eliminate it, it accumulates and elevates the tension of the eye. It causes redness and pain in the eye, as well as headaches, and sometimes nausea and vomiting. Early treatment is essential to reduce the pressure in the eye as the consequences can be serious, even leading to blindness. Angle-closure glaucoma may occur suddenly (acute angle-closure glaucoma) or gradually (chronic angle-closure glaucoma) [86].

- **Normal-tension glaucoma (NTG):** is a type of glaucoma that occurs when the IOP is at normal levels, but even so, the optic nerve fibers show damage and visual field loss occurs. The causes of this type of disease are unknown. It may be hereditary factors, vascular problems or sporadic closures of the aqueous humor drainage angle. As with most common glaucomas, it is essential that this disease be diagnosed as early as possible to avoid serious or irreversible damage.

- **Congenital glaucoma:** this type of glaucoma occurs in infants when there is incorrect or incomplete development of the drainage canals of the eye during the prenatal period. It is a rare disease that may be hereditary. When there are no complications, microsurgery usually corrects the structural defects. More severe cases are treated with medication and surgery.

Early diagnosis of glaucoma can prevent significant visual impairment. People suffering from glaucoma should undergo regular check-ups, as glaucoma can worsen without the patient noticing it. For the diagnosis of this disease, numerous tests must be carried out. With tonometry, the IOP can be measured using a warm blast of air. The normal pressure range is 12 to 22 mm HG, in most cases glaucoma is diagnosed when it exceeds 20 mmHG. Pachymetry measures corneal thickness and can aid in diagnosis as there is a possibility that corneal thickness may influence IOP readings. Ophthalmoscopy helps the physician examine the optic nerve for damage. If IOP is not within the normal range or the optic nerve looks unusual, two other complementary tests may be performed: perimetry and gonioscopy. Perimetry is a visual field test that generates a visual field map, with which the ophthalmologist can identify whether glaucoma has affected vision. And gonioscopy determines whether the angle where the iris meets the cornea is open and wide or narrow and closed.

Treatment of this disease may include surgery, laser or medication, depending on the progression and severity of the glaucoma. Initially, eye drops are usually used along with medications to reduce IOP. It is up to the specialist to decide which medications are most appropriate based on the type of glaucoma, medical history and current medication regimen. On the other hand, glaucoma can be the trigger for ocular thrombosis, which affects the retinal veins, producing a sudden loss of central vision.

In cases where topical treatment (and eventually laser) fails to control disease progression, surgical treatment is indicated. Glaucoma surgery consists of performing a fistula that connects the interior of the eyeball with the subconjunctival space, allowing the IOP to be relieved by draining the aqueous humor. Surgeries of this type can be performed under topical and/or subtenonian anesthesia, but the most common is to perform an injection of anesthetic behind the eyeball that anesthetizes both the eyeball and its muscles. The surgery begins by detaching the conjunctiva from the eyeball, after which a small lamina of the sclera is carved to reach the trabeculae.

1.4 State of the art for OCT clinical applications

The latest OCT devices allow specific analysis of the thickness of the different retinal layers [144, 26]. In addition, improved OCT devices are capable of analysing the vitreous in normal and inflamed states, and studying its changes after treatment [156, 68, 142]. In this section, a brief review of the clinical and computational studies performed to date is presented, detailing the different OCT clinical applications discussed in this dissertation.

1.4.1 RNFL evolution in MS patients

MS is characterized by inflammation and demyelination of nerve fibers and axonal degeneration. As a consequence, the ability of the cells to transmit nerve impulses is partially or totally impaired [56]. RNFL thickness evolution is affected by aging, however, several studies have shown that RNFL thickness in MS patients is thinner than in healthy controls [139, 49]. Since RNFL is composed of the unmyelinated axons of RGCs, this thinning may be linked to axonal inflammation and degeneration [111].

The most widely used technique to measure RNFL thickness is OCT. In this way, OCT allows diagnosing and monitoring diseases that affect the retina and the optic nerve [149, 111]. One of the first studies showing RNFL thickness thinning in MS patients was performed by Parisi et al. using the older third-generation time-domain OCT [109]. Since then, the evolution of OCT technology has incorporated more accurate segmentation processes to quantify retinal layers [82]. Sepulcre et al. [137] found that the decrease in this thickness in MS patients exceeds that associated with ageing. Talman et al. [145] described a decrease of 2 µm/year in RNFL thickness in MS patients, whereas in healthy controls this thinning was 0.49 µm over 3 years.

Currently, predicting the MS course is challenging because the interaction and evolution of inflammatory and degenerative processes are poorly understood. On the one hand, some authors consider that the changes produced in this disease are the consequence of simultaneous inflammatory and degenerative processes [95]. On the other hand, other studies propose that the MS progression occurs in discrete phases [91]. However, it is well known that axonal damage in MS is caused by autoimmune inflammatory processes and by axonal degeneration. In early stages of the disease, the causes of axonal damage are demyelination and axonal transection, whereas, as MS progresses, inflammation and axonal degeneration predominate [79].

Kotelnikova et al. proposed the hypothesis that MS course is conditioned by an autoimmune response leading to inflammation, axonal degeneration and myelin loss or regeneration. Their mathematical model of brain damage and disease progression fits experimental data of brain volume quantified by MRI in a longitudinal study of 66 MS patients [75]. This mathematical model is based on ordinary differential equations (ODEs) and represents the evolution of the fraction of brain volume occupied by myelinated axons, A_m, and demyelinated axons, A_d. Myelination capacity, M, and axonal degeneration, D, are also defined. M decreases by the demyelination process and is restored by the production of myelin by oligodendrocytes which can extend along demyelinated axons [168, 141]. δ represents the growth rate of myelinization capacity and q is the cooperativity coefficient of myelin production by oligodendrocytes. The remyelination process is defined by k_m rate. k_{md} is the myelinated-axonal loss rate due to inflammatory infiltrates and k_d is the demyelinated-axonal loss rate due to degenerative processes. These authors assume that all axons are initially healthy ($A_m = 1$) and, therefore, there are no demyelinated axons or axonal degeneration ($A_d = 0$, $D = 0$). Moreover, the myelination capacity corresponds to the healthy control state ($M = 1$).

$$\frac{dA_m}{dt} = k_m A_d M - \lambda(t) A_m - k_{md} A_m \tag{1}$$

$$\frac{dA_d}{dt} = -k_m A_d M + \lambda(t) A_m - k_d A_d \tag{2}$$

$$\frac{dM}{dt} = -k_m A_d M + \delta A_d M^q \tag{3}$$

$$\frac{dD}{dt} = k_d A_d + k_{md} A_m \tag{4}$$

In this model, the autoimmune attack, represented by the time-dependent parameter $\lambda(t)$, is modeled in terms of time to capture the dynamics of the damage. They used the distribution of ΔEDSS as a source of $\lambda(t)$. This distribution of ΔEDSS was defined using the time between clinical relapses.

In contrast to the model developed by Kotelnikova et al. [75], the model of RNFL evolution should not take into account myelin-related processes since RNFL nerve fibers are not myelinated. In this way, this dissertation will propose a mathematical model, based on ODEs, that relates the processes involved in the evolution of RNFL

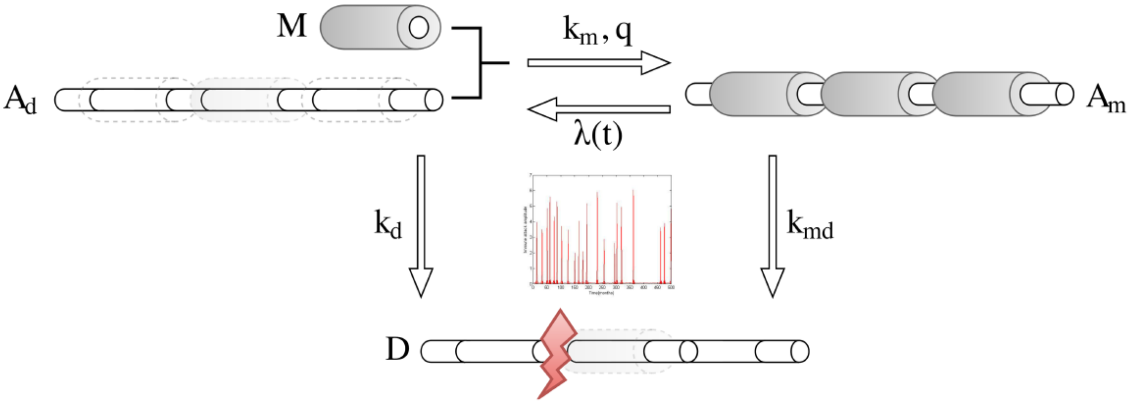

Figure 10: The ODE model of brain damage in MS patients proposed by Kotelnikova et al. [75]. The healthy brain is composed of myelinated axons (A_m), while the MS brain comprises the combination of A_m, demyelinated axons (A_d), remyelination capacity (M) and axonal degeneration (D).

thinning in MS patients such as autoimmune inflammation and axonal degeneration and regeneration. The autoimmune attack occurs in all types of MS, but its contribution and time profile varies from patient to patient [41]. The axonal degeneration is not regulated by autoimmune dynamics, but rather damage accumulates due to the poor regenerative capacity of the CNS [29, 53]. Therefore, this dissertation is a valuable scientific reference that analytically demonstrates the applicability of OCT data to distinguish the different biological processes that contribute to RNFL thinning and predict its evolution.

1.4.2 MS diagnosis and prognosis by OCT and AI

MS diagnosis is a slow and complex process because it focuses on the exclusion of other diseases by performing several tests that are lengthy, expensive and invasive [116]. It is well known that axonal damage is the main cause of disability in MS patients [4], however, detecting it is not an easy task. The McDonald criteria [148] for the diagnosis of MS include MRI to detect inflammation and lesions in the brain, but it is not sensitive enough to reveal the extent of axonal loss [42]. CSF analysis increases diagnostic sensitivity, but decreases specificity and accuracy. In addition, this test is extremely invasive due to the lumbar puncture required to extract the samples. EP, which is time-consuming, measures CNS activity in response to light, sound and touch.

The visual pathway is one of the most affected systems in this disease because axonal damage in MS patients also occurs in the neuroretina [5, 34]. For this reason, the neuroretina has recently emerged as a faster alternative method for the diagnosis and monitoring of MS [28, 117]. OCT devices can specifically measure the thickness of the different retinal layers, paying special attention to RNFL and GCL since thinning of these layers is a direct measure of axonal damage [14, 129, 45]. Studies in MS patients have demonstrated significant thinning of both RNFL and GCL compared to healthy controls [82, 61].

As seen previously, retinal neurodegeneration and MS disability can be related by OCT measurements [4, 146]. Thus, some studies tested the use of artificial intelligence (AI) as an early diagnostic tool. It is very common to confuse the terminology and field of application of AI, machine learning and deep Learning. For this reason, it is important to understand that deep learning is part of machine learning, just as machine learning is part of AI (see Figure 11).

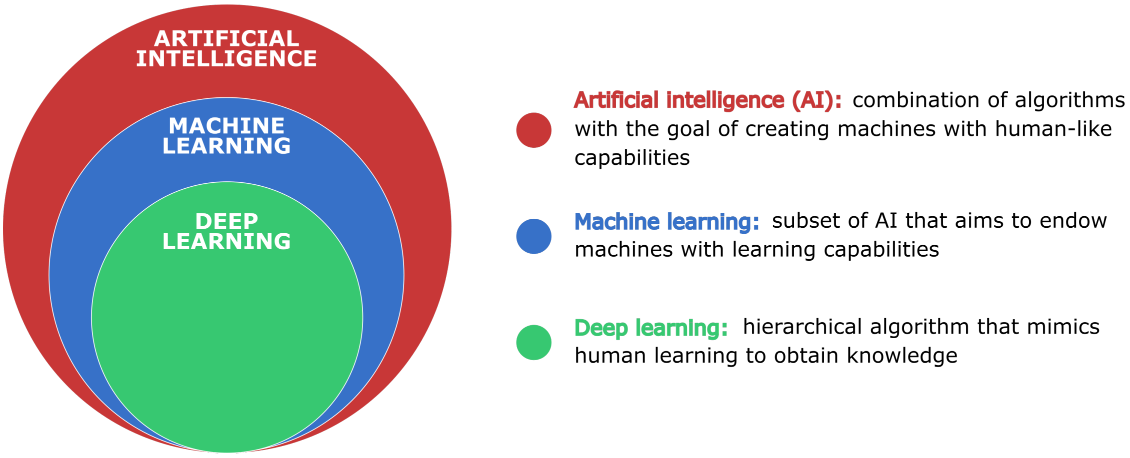

● **Artificial Intelligence (AI):** combination of algorithms with the goal of creating machines with human-like capabilities

● **Machine learning:** subset of AI that aims to endow machines with learning capabilities

● **Deep learning:** hierarchical algorithm that mimics human learning to obtain knowledge

Figure 11: Hierarchical explanation of artificial intelligence.

Garcia-Martin et al. applied artificial neural networks (ANNs) with pRNFL thickness data measured by Spectralis OCT to diagnose this disease [48, 46]. Unlike traditional statistical analyses, which fit data to a set of model variables, ANNs non-linearly adapt the classification decision based on the data. ANNs look for patterns in the training dataset to learn them and classify new samples correctly [9, 38, 13]. Cavaliere et al. developed a diagnostic method based on support vector machine (SVM) with macular RNFL (mRNFL) and pRNFL measurements performed by DRI OCT Triton [18]. In a binary classification problem, SVM searches for the hyperplane that separates the two classes with maximum margins. If the problem data are not linearly separable, a nonlinear transformation to a higher dimensional space is performed using a kernel function, which increases the separability between the classes [57, 100]. The above-mentioned database was also used by Garcia-Martin et al. comparing SVM and ANNs to detect MS using RNFL, GCL, retinal and choroid thickness [47].

After demonstrating the usefulness of retinal thicknesses in diagnosing MS, the next step is to evaluate the potential of retinal layers to predict disease progression, which would be of great help to clinicians in selecting patient-specific treatment [50]. To analyse the progression of disability state, there are several approaches such as analysing whether SPMS development occurs in RRMS patients [96]. Another widely used approach is based on the variation in disability state as measured by EDSS. The progression of disability depends on the variation of EDSS over time with respect to the initial measurement, so that this variation represents a relevant neurological worsening [64]. There are several criteria but the most commonly used standard criteria for disability progression were defined as follows: an increase in EDSS by 1.5 points if the baseline EDSS was 0, an increase in EDSS by 1 point if the baseline EDSS was between 1 and 5.5, and an increase in EDSS by 0.5 points if the baseline EDSS was greater than 5.5 (see Table 1).

Baseline EDSS	Standard criteria
0	ΔEDSS ≥ 1.5
1 - 5.5	ΔEDSS ≥ 1
≥ 6	ΔEDSS ≥ 0.5

Table 1: Standard criteria for disability progression in MS patients based on ΔEDSS.

To date, most studies using retinal thickness to predict disease progression have focused their prognosis on correlations and traditional statistical analyses. For example, the study conducted by Rothman et al. demonstrated how a lower baseline macular volume was associated with a higher EDSS score after 10 years, with a mean ΔEDSS of 0.75 per 1 mm^3 of total macular volume loss [127]. Lambe et al. showed that a baseline GCIPL thickness <70 µm was associated with a 4-fold increased likelihood of significant worsening of EDSS [81]. Along the same lines, another study established that a baseline macular GCIPL (mGCIPL) thickness <77 µm was associated with a higher disability progression. In addition, an annual thickness loss of mGCIPL $\geqslant$1 µm identified patients with disability progression with high accuracy [15]. Schurz et al. reached the same conclusion, establishing that mGCIPL thinning $\geq$1.0 µm/year and pRNFL >1.5 µm/year represent an increased risk of worsening disability in MS patients [134]. This annual pRNFL thinning rate was associated with a 15-fold increased risk of disability progression and was also used by Bsteh et al. to distinguish between stable and progressing RRMS [17]. In addition, these authors concluded that a baseline pRNFL thickness <88 µm results in a 3-fold increased risk of progression of disability state [16].

After using traditional statistical analyses, the authors evaluated AI methods to predict disease progression in MS patients, which would help clinicians in decision making [50, 136]. Tousignant et al. developed an automatic deep learning framework for the prediction of patients' disability progression after one year from baseline based on MRI data [152]. Zhao et al. tested SVM, logistic regression (LR) and different ensemble classifiers (ECs) to predict progression of MS-associated disability at 5-year follow-up using brain MRI data acquired during the first 24 months [173]. EC consists of combining several algorithms in such a way that the new classifier performs better than any of its component classifiers [77]. The study conducted by Law et al. [88] evaluated LR, SVM, EC and decision tree (DT) for MS prognosis after two years from baseline using also MRI data. DT is composed of a root node, several internal nodes and several leaf nodes. This tree is traversed from root to leaf until the criteria are met.

As detailed before, MRI is the most common test for diagnosis and prognosis in MS patients using AI. Zurita et al. used SVM to classify RRMS patients and healthy controls based on functional and diffusion MRI data [174]. Another study presented a deep learning approach on MRI for the classification of multiple sclerosis and its mimics, and compared the performance with that of expert neuroradiologists. These authors concluded that neural networks performed better than expert raters in terms of accuracy in classifying white matter disorders [124]. The work of Saccà et al. evaluated SVM, random forest (RF), Naïve Bayes (NB), k-nearest neighbours (k-NN) and ANN to distinguish MS patients from control subjects using resting-state functional-MRI [128]. RF or random decision forest is an ensemble learning method consisting of a multitude of DTs [57]. NB applies density estimation to the data according to Bayesian theory, assuming that the predictors are conditionally independent in a way that increases the simplicity of the model [21]. K-NN is one of the most widely used algorithms in machine learning [27, 60], which classifies samples according to the class of their nearest neighbours.

Another machine learning approach based on MRI data is used to predict the conversion from CIS to MS. Yoo et al. used convolutional neural networks (CNNs) to extract latent MS lesion patterns associated with MS conversion [169]. CNN is a type of ANN used in image recognition and processing, specifically designed to process pixel data. In the same vein, study conducted by Zhang et al. [171] evaluated RF using MRI data from 3-year follow-up of 84 CIS patients. In addition, MRI scans were also used to identity MS subtypes using an unsupervised machine learning method [33].

In addition to MRI, other tests included in the McDonald criteria, such as EP or CSF analysis, have also been analysed using different AI approaches [31]. Yperman et al. evaluated RF and LR to predict disability progression after 2 years using PE data [170]. Data obtained by MRI, CSF analysis and EP were used by Pinto et al. [113] to predict the disability progression, comparing linear regression, SVM, DT and k-NN. Seccia et al. predicted the progression from RRMS to SPMS by applying RF, SVM, k-NN and EC to MRI and liquor analysis data from the last available visit and recurrent neural network (RNN) to the complete clinical history data [135]. RNN is a type of ANN that works with sequential data and maintains knowledge about the past. Furthermore, other authors [67] examined a machine learning framework for identifying MS through spatio-temporal and kinetic gait characteristics obtained during self-paced walking on a treadmill.

As can be seen, most of the aforementioned studies predicted disability progression based on data obtained using the tests included in the McDonald criteria. None of them focus the AI approach on OCT data for MS prognosis. However, in this thesis, AI approaches are proposed to predict long-term disability state using OCT data. First, we will diagnose MS using RNFL and GCL thickness measured by DRI OCT Triton. Second, we will use Cirrus HD-OCT to meausure RNFL thickness in order to diagnose and predict this disease. And, third, we will perform a comparison of machine learning methods using Spectralis OCT for diagnosis and prognosis in MS patients.

1.4.3 Glaucoma monitoring with vitreous imaging

Glaucoma is a pathology linked to aging caused by the progressive death of RGCs, leading to an irreversible deterioration of the visual field [62, 86]. An increase in IOP is the modifiable risk factor most associated with the onset and progression of this disease. The campimetric alteration is detected when around 30% of the RGCs have died, which leads to a late diagnosis. This demonstrates the need to study new techniques and biomarkers to achieve an early diagnosis. For these reasons, numerous studies have developed different models of ocular hypertension in animals using genetic engineering [132, 20], injection of neurotoxic substances [105], increased IOP using pre- and posttrabecular mechanisms [32, 103].

Part of the neurodegeneration of this disease does not depend on IOP, but is related to the immune response [8, 154, 22]. It has been shown that slow and damaging inflammation triggered by innate immune elements is also implicated in processes considered purely degenerative, such as age-related macular degeneration, diabetic retinopathy and glaucoma [52, 107]. Several studies have specified signs of inflammation in glaucoma, such as a more acidic pH with increased immune proteins in the aqueous humor and vitreous, or activation of astrocytes and microglia and deposits of immunocomplexes and immunoglobulins in the retina [54, 162, 151]. Microglia are innate immune cells located in the CNS and retina, where they perform immune surveillance functions. This cell type presents different morphologies depending on its activation state. Kozlowski et al. [76] demonstrated that soma size can be used as a biomarker of microglial activation in the neocortex. Thus, microglial activation could be the earliest detectable change in the retina [12].

The vitreous body consists mainly of water, collagen fibers, hyaluronic acid and hyalocytes. Hyalocytes are hematopoietic cells located at the periphery of the vitreous cavity, mainly at the anterior base of the vitreous and in the vicinity of the optic nerve head. These cells are involved in immune regulation of vitreous cavity-associated immune deviation and modulation of intraocular inflammation, so that their changes serve as early indicators of ocular diseases [158]. Therefore, analysis of changes in the vitreous under parainflammatory conditions would increase knowledge about the pathophysiology of glaucoma.

To date, almost all glaucoma research has focused on neuroretinal analysis, either by histological or imaging techniques. On the one hand, histology is very time-consuming and it is very complicated to create large databases. On the other hand, OCT is an objective and fast technique available in practically all hospitals. OCT devices allow the acquisition of high resolution images in vivo. In this way, it is possible to analyse the vitreous in a non-invasive way [68, 142]. The use of OCT to analyse vitreous opacities can provide a rapid way to measure vitreous and intraretinal ocular inflammation [74].

The activation and/or increased number of hyperreflective vitreous opacities can be analysed more easily than intraretinal opacities due to the optical transparency of the vitreous. The hypothesis is that these opacities, detected in the vitreous images obtained by OCT, correspond to immune cells. OCT has a greater clinical application as this tool does not require modification of the animal's genetics or injection of contrast to express fluorescence. This dissertation analyses the vitreous signal intensity in rat eyes in two models of chronic glaucoma induced by ocular hypertension, and compares the results with healthy controls. The first model (MEPI) is the Morrison model generated with sclerosing injections of the episcleral veins of the right eye of Long-Evans rats [104]. The second model (Ms) is generated by injecting a 2 microliter (10% w) suspension of 20/10 biodegradable poly (lactic-co-glycolic) acid (PLGA) microspheres into the anterior chamber of the right eye of the rat [44]. As can be seen in Figure 12, vitreous intensity is quantified using vitreous/retinal pigment epithelium (VIT/RPE) relative intensity as an indirect measure of the immune response [68]. We will also analyse the hyperreflective vitreous opacities and their evolution by quantifying their number, size, intensity, eccentricity and orientation.

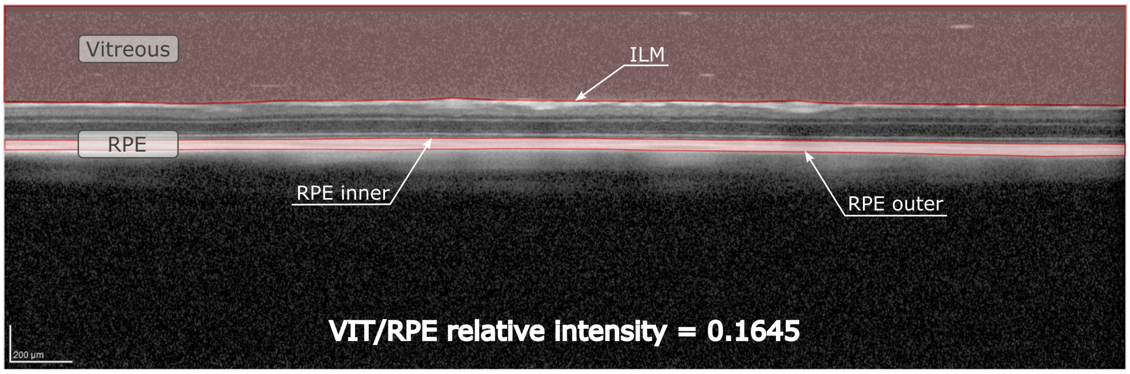

Figure 12: Quantitative assessment of VIT/RPE relative intensity from an OCT image (1536 x 496 pixels) of a right eye of a rat with induced glaucoma.

Intravitreal injection is the most commonly used treatment for posterior segment pathologies such as age-related macular degeneration, diabetic retinopathy or vascular occlusions. This technique has long been used in ophthalmic practice as it maintains therapeutic drug levels close to the neuroretina and eliminates ocular barriers [10, 59]. But repeated ocular injections lead to complications such as elevated IOP, intraocular inflammation, cataract formation or retinal detachment [110, 78]. However, sustained drug delivery systems maintain the therapeutic concentration for prolonged periods, improving the half-life and bioavailability of the drug. Therefore, drug delivery avoids the need for re-injections and their side effects [83].

In clinical practice, no intravitreal treatment for glaucoma that lowers IOP and prevents neuroretinal damage is used. In this thesis, a glaucoma treatment consisting of a hypotensive and neuroprotective intravitreal formulation (IF) of brimonidine–Laponite (BRI/LAP) will be analysed. As Rodrigo et al. demostrated [125], the sustained-release BRI/LAP IF, administered as a single intravitreal injection, exerts an ocular hypotensive and neuroprotective effect lasting at least 6 months in an animal model of glaucoma.

Brimonidine is one of the most widely used ocular hypotensive drugs in clinical practice. This drug has also shown a neuroprotective effect on RGCs, photoreceptors and other retinal cells [106]. This neuroprotective effect was produced in both animals and humans, using both topical and intravitreal administration [140, 70]. The short half-life of brimonidine makes periodic administration, recommended twice daily, necessary to achieve therapeutic efficacy. The peak occurs after 2-3 hours and lasts up to 10-14 hours [160]. Therefore, to reduce IOP to optimal therapeutic levels, administration should be twice daily. But, as previously mentioned, repeated injections cause sight-threatening side effect. This fact highlights the need to develop a sustained drug delivery method for brimonidine administration.

Laponite® $Na^{+0.7}[(Si_8Mg_{5.5}Li_{0.3})O_{20}(OH)_4]^{-0.7}$ is a biocompatible and biodegradable synthetic clay used in biomedical and biomaterials applications, especially in nanomedicine, regenerative medicine and tissue engineering [150]. Laponite® consists of two-dimensional disk-shaped crystal (0.92 nm height, 25 nm diameter, 2650 g/cm density) comprising an octahedral magnesia sheet sandwiched between two tetrahedral silica sheets. When dispersed in an aqueous medium, it forms a transparent gel with a three-dimensional house-of-cards structure. This transparent gel has thixotropic and viscoelastic characteristics, facilitating administration by injection [85]. Laponite® can interact with other molecules, so that it is possible to put into solution compounds that are insoluble in water [143]. Therefore, it can carry drugs and release them in a controlled manner depending on environmental conditions such as pH or temperature [161, 165]. Prieto et al. demonstrated the safety of Laponite® in animal studies, analysing the pharmacokinetics and pharmacodynamics up to 24 weeks of injection of the dexamethasone-Laponite IF in rabbit eyes [118, 119].

Currently, the loss of therapeutic efficacy of IF is assessed in terms of changes in neuroretinal structure or decreases in subjective visual acuity measurements, which indicate increased disease activity. Therefore, it is necessary to find an objective vitreous monitoring marker with which to quantify the IF degradation. In this way, the loss of therapeutic effect could be anticipated before structural changes in the retina are detected. The use of OCT could be useful for this purpose compared to other more expensive and invasive techniques, such as positron emission tomography or MRI [93, 39].

In the study by Rodrigo et al., the BRI/LAP IF was visualized by OCT in the vitreous cavity as hyperreflective aggregates [125]. In this thesis, OCT will also be used to analyse the changes in the BRI/LAP IF hyperreflectivity signal in the vitreous humor in rat eyes over a 24-week period. Therefore, this technique will serve to relate the vitreous signal to the level of drug maintenance.

1.5 Motivation

The main motivation for this research is based on the high social and economic impact of neurodegenerative diseases such as MS or glaucoma. MS is the most common inflammatory neurological disease in young adults. In addition, epidemiological studies indicate that 2-5% of people with MS are diagnosed before the age of eighteen [25]. In 2016, there were 2.2 million prevalent cases of MS worldwide, correspondeding to a 10.4% increase in age-standardized prevalence since 1990. Although MS is present in all regions of the world, its prevalence varies greatly (see Figure 13) [35]. According to the Global Burden of Diseases, Injuries, and Risk Factors Study, the highest age-standardised MS prevalence estimates per 100,000 population were in North America, western Europe and Australasia, while the lowest were in eastern sub-Saharan Africa, central sub-Saharan African and Oceania [159].

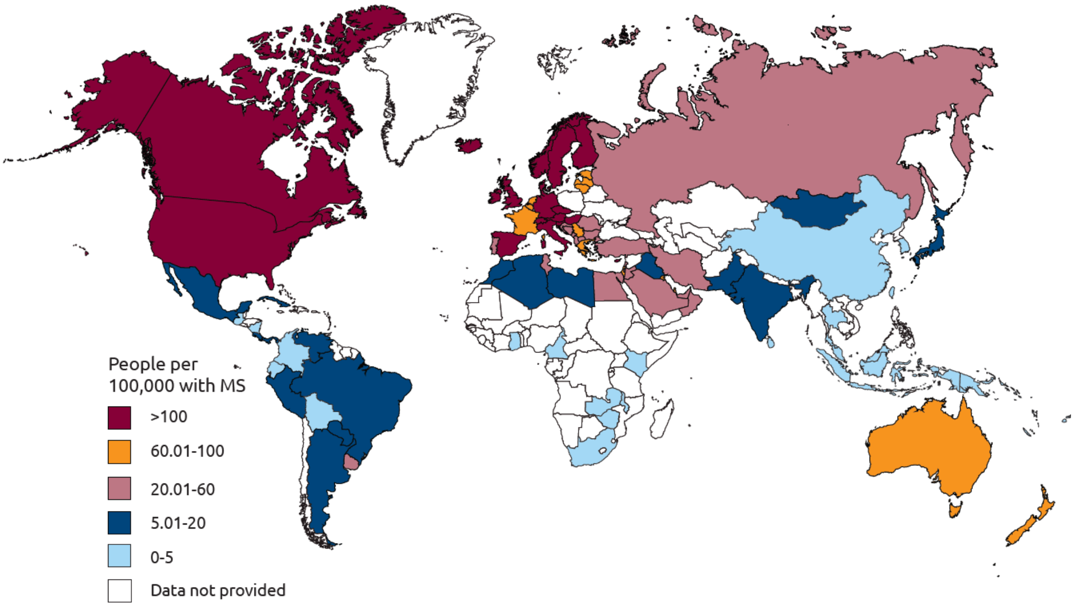

Figure 13: MS prevalence per 100,000 people by country.

The McDonald criteria make use of MRI techniques for earlier diagnosis, offering the possibility of earlier treatment and support [115]. Although the availability of MRI machines has improved since 2008 in almost all countries, they are still not accessible to all people. Therefore, the use of older diagnostic criteria was higher in low- and middle-income countries.

It is well known that MS has no cure. In general, MS treatments focus on speeding recovery after attacks, slowing the disability progression and treating symptoms. Availability of drugs to treat MS were partially or fully funded by the government in most countries. The platform therapies for MS are interferon β1a, interferon β1b and glatiramer acetate. These therapies were available in 96% of the countries in the high-income group, but in only 45% of the countries in the middle-income group and in none of the countries in the low-income group. Access to new therapies such as natalizumab and fingolimod is widespread only in high-income group countries and limited in middle-income group countries.

On the other hand, glaucoma is the leading cause of irreversible blindness and represents a major public health problem. The current prevalence is 80 million people with glaucoma of whom 11.2 million are blind. The global prevalence of glaucoma is 3.54% of the world's population, with the highest prevalence in Africa [120]. The global prevalence of open-angle glaucoma is 3.05% (see Figure 14) and that of angle-closure glaucoma is 0.50%, which in number of affected in 2020 was 52.7 million cases of open-angle glaucoma and 23.4 million cases of angle-closure glaucoma [65, 30]. According to race, the highest prevalence of open-angle glaucoma is in Africans, while angle-closure glaucoma is in Asians [19, 24]. The prevalence is higher in males in age-adjusted, and the same is true for all races.

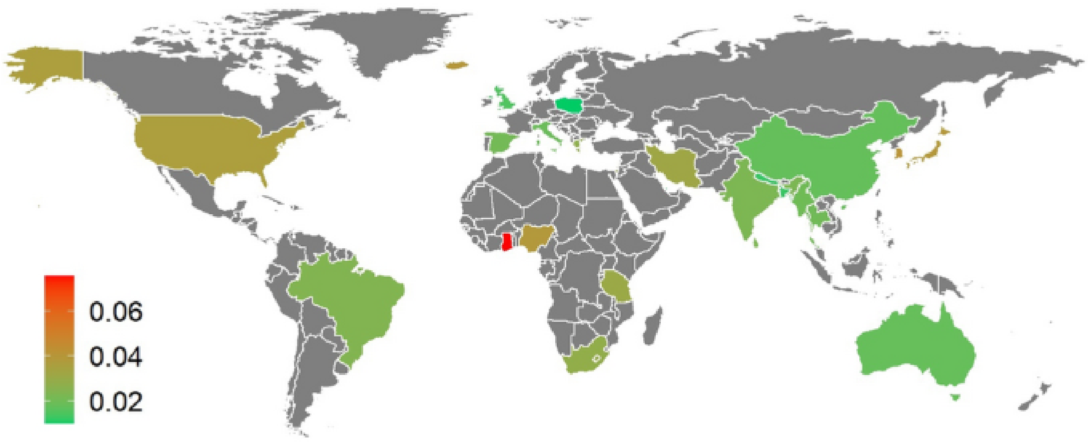

Figure 14: Global prevalence of open-angle glaucoma by country [172].

Glaucoma is diagnosed when significant signs of optic nerve damage appear and other causes are ruled out. Therefore, it is very important to identify risk factors in order to develop early detection and prevention strategies. The damage caused by glaucoma is irreversible, but treatment can help delay or prevent vision loss, especially if the disease is detected in its early stages. This disease is treated by lowering IOP through eye drops, oral medications, laser treatment, surgery or a combination of any of these [7, 66, 36]. Most drops are to be used 2 or 3 times a day throughout life. Sometimes, after some time, they are not well tolerated and the patient must be treated with a laser or undergo surgery. Laser trabeculoplasty is performed in a few minutes, but it is only useful in older patients and, in many cases, its effect disappears after a while. Diode laser cyclophotocoagulation is only useful in very advanced glaucomas. The most widely used surgical technique is trabeculectomy, which consists of seeking a new outflow of aqueous humor from the eye to the outside. However, to date no surgery has shown clear advantages over the others.

Thus, this thesis is motivated by the need to understand the underlying problems of these pathologies and to improve the quality of life of the patients who suffer from them.

1.6 Objectives

Considering the above motivation, the main objective of this dissertation is to analyse and explain the use of OCT for the diagnosis and treatment of neurodegenerative diseases using computational models. Therefore, this dissertation focuses on answering two questions. First, is there a significant relationship between the back of the eyeball and the progression of these neurodegenerative diseases? And, secondly, how could OCT help in the diagnosis, prediction and/or treatment of these diseases?

Although some researchers have attempted to address these questions, very few studies relate and answer both questions simultaneously. To answer the first question, several clinical studies linked neuroretina to the course of MS [114, 108] and glaucoma [126, 123]. The neuroretina is a functional unit of the CNS that converts a light signal into a nerve impulse. Thanks to current imaging methods, it is possible to increase the knowledge of the anatomical and functional characteristics of neuroretina, which are still imperfectly described [6]. OCT is a non-invasive, relatively cost-effective, rapid and reproducible imaging technique that obtains images of the retina and optic nerve head, which can be used to assess the loss of CNS axons and neurons. Therefore, it is a potential tool to establish the neuroretina as an objective and measurable biomarker for the progression and follow-up of patients with neurodegenerative diseases.

Regarding the second question, Kotelnikova et al. [75] used MRI to analyse the evolution of brain volume in MS patients but there is no mathematical model of the retina, measured by OCT, to reproduce the dynamics of CNS damage caused by MS. Another point is that there are previous cross-sectional studies that use OCT data, in combination with machine learning techniques, to diagnose MS [48, 46]. However, the highest accuracies were obtained with too small or imbalanced datasets [18]. In addition, there are also longitudinal studies that used OCT data to obtain information on how the disease will progress, but these studies approached prediction from traditional statistical analysis [127, 15]. Most of the works predicting disability progression in MS patients with AI limited data to those included in the McDonald criteria (MRI, CSF analysis and EP) and performed short-term predictions. Then, it is necessary to analyse the use of RNFL thickness, measured by OCT, to predict long-term disability progression using machine learning techniques.

Finally, while intravitreal injection is the gold standard treatment for posterior segment pathologies [10], an alternative long-lasting release is necessary to avoid reinjections. Currently, there is neither an effective intravitreal treatment for glaucoma nor a non-invasive method to control drug levels in the vitreous. These facts demonstrate the need to employ OCT to monitor glaucoma and different sustained release formulations administered in a single intravitreal injection.

Therefore, to achieve the main objective of this dissertation it is necessary to complete the following partial objectives for each OCT clinical application.

- RNFL evolution in MS patients
    - To verify the use of RNFL thickness as a biomarker of MS, comparing the thinning of this layer between patients and controls.
    - To develop, implement and evaluate a mathematical model to predict the temporal evolution of the RNFL thickness in MS patients, taking into account each of the biological processes involved in thinning.
- MS diagnosis and prognosis by OCT and AI
    - To establish, through the use of AI, OCT technology as a technique for early diagnosis of MS and long-term prediction of disability progression.
    - To analyse which OCT device (DRI OCT Triton, Cirrus HD-OCT or Spectralis OCT) and which acquisition protocol works best for the above two purposes.

  - To compare machine learning methods (LR, SVM, DT, k-NN, NB, EC or ANN) for MS diagnosis and prognosis.

- Glaucoma monitoring with vitreous imaging
  - To monitor vitreous parainflammation and analyse in vivo hyperreflective vitreous opacities by OCT in two animal models of chronic glaucoma, comparing both models to healthy controls.
  - To propose OCT as a more cost-effective, simple and non-invasive method for in vivo monitoring of IFs such as BRI/LAP.

To summarize, this thesis aims to improve the understanding of how the neuroretina, monitored by OCT, can be used as a biomarker for neurodegenerative diseases, in order to make early diagnoses and adapt treatments.

1.7 Thesis outline

This dissertation is presented under the modality of a thesis by a compendium of publications according to the requirements established by art. 20 of the Doctoral Thesis Regulations, approved by agreement of 25/06/2020 of the Governing Council of the University of Zaragoza. In accordance with this requirements, this thesis is mainly composed of the introduction presenting the objectives, a copy of the published papers and the discussion of the contributed papers and the final conclusions.

Chapter 1, *Introduction*, is the current chapter where the objectives of this thesis and the works carried out are presented, justifying their thematic unity. A literature review of the previous knowledge on which the published papers are based is also detailed. This chapter presents a detailed description of the retina as well as the OCT technology that allows it to be monitored non-invasively, rapidly and cost-effectively. Next, the characteristics of two neurodegenerative diseases such as multiple sclerosis and glaucoma are explained. And the state of the art of various clinical applications of OCT to treat these diseases is detailed, analysing the clinical and computational studies performed on this topic to date. Finally, the motivation and main objectives of this dissertation are described.

In **chapter 2**, *Manuscripts*, the published manuscripts that constitute the main body of this thesis are compiled.

Manuscript 1 describes the proposed biological damage model for the evolution of RNFL thickness in patients with MS. This mathematical model, based on ODEs, includes the processes involved in the evolution of RNFL thinning in MS patients: autoimmune inflammation, axonal degeneration and axonal regeneration. Clinical data were obtained from a 10-year follow-up study of 114 patients with MS. This methodology would allow the use of OCT data to predict the evolution of RNFL thinning and, therefore, disease progression, facilitating the selection of patient-specific therapies.

Manuscript 2 discusses the use of RNFL and GCIPL thickness measured by DRI OCT Triton to diagnose MS using machine learning techniques. All Triton 3D scans are compared: 3D wide, 3D macula and 3D disc. The performance of DT, ANN and SVM is evaluated.

In manuscript 3, machine learning techniques are applied for both diagnosis and prediction of MS disability progression. These predictive models use clinical data and RNFL thickness measured by Cirrus HD-OCT. Optic macular cube 200 x 200 and optic disc cube 200 x 200 acquisition protocols were used in 104 healthy controls and 108 MS patients. Of these MS patients, 82 were included in a 10-year follow-up.

Manuscript 4 performs a comparison of machine learning methods (SVM, DT, k-NN, NB, EC and RNN) using Spectralis OCT for diagnosis and prognosis of disability progression in MS. Fast macular, fast RNFL and fast RNFL-N thickness protocols were used to meausure RNFL thickness. This work confirms RNFL thickness as a biomarker for early diagnosis and prediction of the disability progression in MS patients.

Manuscript 5 monitors immune response in two animal model of chronic glaucoma induced by ocular hypertension over 6 months using vitreous-OCT imaging. This work analyses changes in vitreous signal in rat eyes, and characterizes hyperreflective opacities and their dynamics by changes in number, size, intensity, eccentricity and orientation.

And, in manuscript 6, a glaucoma treatment combining a hypotensive and neuroprotective IF of BRI/LAP is shown. The BRI/LAP IF is monitored non-invasively using vitreoretinal interface imaging captured by OCT over 24 weeks of follow-up in rat eyes.

Chapter 3, *Conclusions and contributions*, summarizes the main conclusions of this work and lists the original contributions published in scientific journals and presented at international congresses as a result of this thesis.

Finally, the *Bibliography* section shows the references of this dissertation and the *Appendix* details the data of the works that compose this thesis by compendium of publications.

Chapter 2

Manuscripts

2.1 RNFL evolution in MS patients

Manuscript 1: A mathematical model to predict the evolution of retinal nerve fiber layer thinning in multiple sclerosis patients

Alberto Montolío, José Cegoñino, Elvira Orduna, Berta Sebastian, Elena Garcia-Martin, Amaya Pérez del Palomar

Abstract

Multiple sclerosis (MS) is a neurodegenerative disease of the central nervous system (CNS). Many studies of MS patients have described axonal loss in the optic nerve of the retina, and specifically progressive thinning of the retinal nerve fiber layer (RNFL). We hypothesize that RNFL thinning involves the participation of 2 processes that cause CNS damage: autoimmune inflammation and axonal degeneration. To test this hypothesis, we developed a mathematical model based on ordinary differential equations to relate the evolution of RNFL thickness (measured by optical coherence tomography [OCT]) with that of the Expanded Disability Status Scale (EDSS) score in MS patients. Data were obtained from a longitudinal study of 114 MS patients who were followed-up for 10 years. After adjusting the parameters using a genetic algorithm, the model's prediction of the evolution of RNFL thickness accurately reflected the progression revealed by the 10-year clinical data. Our findings suggest that differences in the relative contributions of autoimmune inflammation and axonal degeneration can account for the complex dynamics of MS, which vary from one patient to the next. Moreover, our results show that CNS damage occurs

cumulatively from the onset of MS and that most RNFL thinning occurs before the appearance of significant disability. RNFL thickness could therefore serve as a reliable biomarker of MS disease course. Our proposed methodology would enable the use of OCT data from new MS patients to predict the evolution of RNFL thinning and hence the progression of MS in individual patients, and to facilitate the selection of patient-specific therapies.

Computers in Biology and Medicine 111 (2019) 103357

Contents lists available at ScienceDirect

Computers in Biology and Medicine

journal homepage: www.elsevier.com/locate/compbiomed

A mathematical model to predict the evolution of retinal nerve fiber layer thinning in multiple sclerosis patients

Alberto Montolío[a,b], José Cegoñino[a,b], Elvira Orduna[c,d], Berta Sebastian[e], Elena Garcia-Martin[c,d], Amaya Pérez del Palomar[a,b,*]

[a] Group of Biomaterials, Aragon Institute of Engineering Research (I3A), University of Zaragoza, Zaragoza, Spain
[b] Department of Mechanical Engineering, University of Zaragoza, Zaragoza, Spain
[c] Ophthalmology Department, Miguel Servet University Hospital, Zaragoza, Spain
[d] GIMSO Research and Innovative Group, Aragon Institute for Health Research (IIS Aragón), Zaragoza, Spain
[e] Neurology Department, Miguel Servet University Hospital, Zaragoza, Spain

ARTICLE INFO

Keywords:
Multiple sclerosis
Retinal nerve fiber layer
Optical coherence tomography
Optic nerve
Longitudinal study
Genetic algorithm

ABSTRACT

Multiple sclerosis (MS) is a neurodegenerative disease of the central nervous system (CNS). Many studies of MS patients have described axonal loss in the optic nerve of the retina, and specifically progressive thinning of the retinal nerve fiber layer (RNFL). We hypothesize that RNFL thinning involves the participation of 2 processes that cause CNS damage: autoimmune inflammation and axonal degeneration. To test this hypothesis, we developed a mathematical model based on ordinary differential equations to relate the evolution of RNFL thickness (measured by optical coherence tomography [OCT]) with that of the Expanded Disability Status Scale (EDSS) score in MS patients. Data were obtained from a longitudinal study of 114 MS patients who were followed-up for 10 years. After adjusting the parameters using a genetic algorithm, the model's prediction of the evolution of RNFL thickness accurately reflected the progression revealed by the 10-year clinical data. Our findings suggest that differences in the relative contributions of autoimmune inflammation and axonal degeneration can account for the complex dynamics of MS, which vary from one patient to the next. Moreover, our results show that CNS damage occurs cumulatively from the onset of MS and that most RNFL thinning occurs before the appearance of significant disability. RNFL thickness could therefore serve as a reliable biomarker of MS disease course. Our proposed methodology would enable the use of OCT data from new MS patients to predict the evolution of RNFL thinning and hence the progression of MS in individual patients, and to facilitate the selection of patient-specific therapies.

1. Introduction

Multiple sclerosis (MS) is a degenerative disease that affects the central nervous system (CNS) and is characterized by nerve fiber inflammation and demyelination and by axonal degeneration. As a result of these phenomena, neurons partially or completely lose their ability to conduct nerve impulses, giving rise to the various symptoms of this pathology [1].

Several studies [2–4] have demonstrated increased thinning of the retinal nerve fiber layer (RNFL) in MS patients versus healthy controls. The mechanism by which this thinning occurs in MS patients that have not experienced an episode of optic neuritis remains unclear. Because the RNFL is composed of the unmyelinated axons of the retinal ganglion cells (RGCs) that form the optic nerve, thinning of this layer may be linked to the aforementioned phenomena of inflammation and axonal degeneration [5].

Several longitudinal studies have shown that the decrease in RNFL thickness in MS patients exceeds that associated with ageing [6–8]. A follow-up study of 61 patients [7] found that the progressive decrease in RNFL thickness was more pronounced in MS patients than in aging healthy controls. Similarly, Talman et al. [8] described a decrease in RNFL thickness of 2 μm/year in MS patients, as compared with 0.49 μm over 3 years in controls.

There are numerous non-invasive imaging techniques currently available that allow measurement of the thickness of the different retinal layers. The most widespread technique is optical coherence tomography (OCT) [9], which is used to diagnose and monitor multiple diseases of the retina and optic nerve [5].

---

[*] Corresponding author. C/Maria de Luna s/n, 50018, Zaragoza, Spain.
E-mail address: amaya@unizar.es (A. Pérez del Palomar).

https://doi.org/10.1016/j.compbiomed.2019.103357
Received 11 April 2019; Received in revised form 12 July 2019; Accepted 13 July 2019
0010-4825/

A key use of OCT in monitoring MS progression is to determine whether variations in RNFL thickness are linked to irreversible damage caused by the disease or, conversely, are the result of acute episodes of the disease. It has been shown that a single episode of optic neuritis does not imply a greater risk of a progressive decrease in RNFL thickness [10].

In this study, we focus on the mechanisms that cause thinning of the unmyelinated fibers that comprise the RNFL. Because the interaction and evolution of the inflammatory and degenerative processes caused by MS are poorly understood, is particularly difficult to predict the course of MS [11]. Several hypotheses have been proposed to explain the dynamics of MS: some consider the underlying pathological changes to be the result of simultaneous inflammatory and degenerative processes, while others propose that the disease course consists of a series of discrete phases [12,13]. Regardless, it is clear that CNS damage in MS is caused by acute inflammatory processes initiated by the immune system and by axonal degeneration caused by demyelination [14,15].

Recently, Kotelnikova et al. [16] hypothesized that the evolution of MS is driven by an autoimmune response against the CNS itself that causes inflammation, axonal degeneration, and loss or regeneration of myelin. They concluded that the manner in which each process occurs varies between different clinical subgroups. They designed a mathematical model to explain experimental data derived from brain magnetic resonance images (MRI) [17] obtained from a longitudinal study of 66 MS patients. Other studies have attempted to establish whether there is any relationship between RNFL thickness and patient disability, as measured using the Expanded Disability Status Scale (EDSS) in transversal studies, but failed to produce sufficiently robust data [18,19].

In the present study, we propose a mathematical model that relates axonal degeneration to disease progression in MS patients. This model is consistent with clinical data obtained in a longitudinal study of 114 MS patients over 10 years, and distinguishes between the relative contributions of different biological processes (inflammation, axonal degeneration, and axonal regeneration) in different patient groups. Two novel aspects of this study underscore its importance in furthering our understanding of MS. First, we have exploited the accessibility of the retina, which provides a window into the brain, in order to develop the first mathematical model to analyze CNS damage (RNFL thinning) in MS patients, [20,21]. Second, we have used OCT data to distinguish between the different biological processes that contribute to RNFL thinning.

The ultimate goal of this research is to obtain a validated numerical model that can predict the evolution of RNFL thinning in new MS patients using only OCT data and EDSS scores obtained at their first visit. RNFL thinning is known to be linked to the progression of MS-associated disease disability [18]. Sufficient control of disease activity in MS patients is crucial to prevent unfavorable outcomes. Therefore, our model could be highly useful to clinicians, helping them to establish patient-specific treatments and deciding between first- and second-line therapies.

2. Materials and methods

2.1. Longitudinal study

The longitudinal study followed a cohort ("discovery cohort") of 114 MS patients from the Miguel Servet University Hospital (Zaragoza, Spain). All patients underwent complete ophthalmologic evaluations during the course of the 10 year follow-up period (baseline, 2.5 years, 5 years, and 10 years). This examination includes assessment of best-corrected visual acuity (BCVA) using the Snellen scale, colour vision, a visual field examination, and an OCT examination. Simultaneously, the same protocol was applied to a cohort of 60 healthy control patients in order to distinguish between age-associated RNFL thinning and that caused by disease progression. Finally, 5-year follow-up data obtained from a third cohort of 70 MS patients (validation cohort) were used to validate the proposed mathematical model. From these 3 cohorts of patients of white European origin, one eye from each subject was randomly selected for analysis (excluding eyes for which previous episodes of optic neuritis were recorded) [22]; in total 244 eyes were included in the longitudinal study. The main clinical features of these 3 cohorts are summarized in Table 1.

The required inclusion criteria were as follows: BCVA of 20/40 or higher; refractive error within ± 5.00 diopters equivalent sphere and ± 2.00 diopters astigmatism; and transparent ocular media (nuclear colour/opalescence, cortical or posterior subcapsular lens opacity < 1), according to the Lens Opacities Classification System III system [23]. Exclusion criteria included previous intraocular surgery, diabetes or other diseases affecting the visual field or nervous system, any optic neuritis episode in the 6 months preceding inclusion in the study, and ongoing use of medications that could affect visual function.

All subjects gave prior consent to participate in this study, which was conducted in accordance with the Declaration of Helsinki, and the protocol was approved by the Ethics Committee for Clinical Research of Aragon (CEICA) for the protection of human subjects. After the baseline visit, patients were evaluated 2.5, 5, and 10 years later in order to assess changes in RNFL thickness and EDSS score. The ophthalmologic evaluation was performed by an ophthalmologist expert in MS and the EDSS score was determined by a neurologist.

The objective of this study was to characterize the relationship between RNFL thinning and MS disease progression, and thereby assess

Table 1

Clinical parameters, multiple sclerosis (MS) data, and retinal nerve fiber layer (RNFL) measurements determined using optical coherence tomography (OCT) for the baseline visit of healthy controls and the discovery and validation cohorts. Data for MS patients (discovery and validation cohorts) also include disease duration, MS subtypes (RR, relapsing-remitting; SP, secondary-progressive; PP, primary-progressive) and EDSS scores.

Baseline evaluation	Healthy controls (n = 60)	Discovery cohort (n = 114)	Validation cohort (n = 70)
General parameters			
Age [years]	43.0 ± 13.3	41.3 ± 10.5	43.1 ± 10.3
Sex (M - F)	10–50	32–82	28–42
BCVA [Snellen]	0.972 ± 0.219	0.846 ± 0.205	0.837 ± 0.335
MS parameters			
Disease duration [years]	–	10.5 ± 7.9	9.2 ± 9.2
Subtypes (RR - SP - PP)	–	104 - 8 - 2	65 - 4 - 1
EDSS	–	2.5 ± 2.1	2.7 ± 2.1
OCT parameters – RNFL thickness			
Mean thickness [µm]	100.93 ± 10.30	89.99 ± 18.84	89.72 ± 12.82
Superior thickness [µm]	123.36 ± 18.34	110.11 ± 23.91	114.16 ± 19.82
Nasal thickness [µm]	79.53 ± 15.62	74.75 ± 21.50	72.55 ± 13.90
Inferior thickness [µm]	131.55 ± 17.58	115.96 ± 27.99	114.34 ± 18.63
Temporal thickness [µm]	71.13 ± 19.09	60.08 ± 20.17	57.16 ± 16.76

the utility of RNFL thickness as biological marker of disease progression. RNFL thickness was measured using Cirrus HD-OCT technology (model 4000; Carl Zeiss Meditec, Dublin, CA). Specifically, we used the Optic Disc Cube 200 × 200 study protocol, which scans an area of 6 × 6 mm centered on the papilla, capturing a data cube of 200 × 200 sweeps for a total of 40,000 data points in 1.5 s. The image quality is based on the signal strength measurement, which combines the signal-to-noise ratio with the uniformity of the signal within a scan. The quality score ranges from 0 (poor) to 10 (excellent). Only images with a quality score of ≥7 were included in our analysis. The OCT system automatically identifies the center of the papilla and creates a circle-shaped sweep of 3.46 mm in diameter. This protocol calculates mean RNFL thickness by first determining the values corresponding to each of 4 quadrants into which the peripapillary area is divided (Fig. 1).

2.2. Clustering of patients

To reduce the high level of clinical heterogeneity among patients, clustering of the patients in the discovery cohort was performed using the k-means clustering algorithm, which assigns patients to k sub-groups based on proximity to the mean value of a given sub-group. The k-means clustering algorithm is one of the most commonly used techniques for this purpose, owing to its ability to quickly and efficiently segment large samples, including outliers. Since this method is highly sensitive to the initial number of groups assigned, the algorithm was executed several times using k-values (i.e. number of clusters) ranging from 2 to 10. The Silhouette method was used to validate the number of groups that best classified the data set. This method measures how close each data point is to its own cluster and its closest neighbors in order to determine the optimum k-value. Silhouette analysis is widely used in the evaluation of k-means clustering since it is faster and more cost-effective than other available methods (e.g. cost function analysis) [24].

The proposed methodology was developed to predict the evolution of RNFL thickness in new MS patients after their first visit. Baseline parameters were used to classify patients. We applied a 3D classification procedure using the following variables: EDSS score (patient's disability is related to axonal damage [2]); BCVA (50% of patients present some form of visual impairment); and disease duration ratio (time since disease onset relative to patient's age), which represents the proportion of patient's life spent with MS.

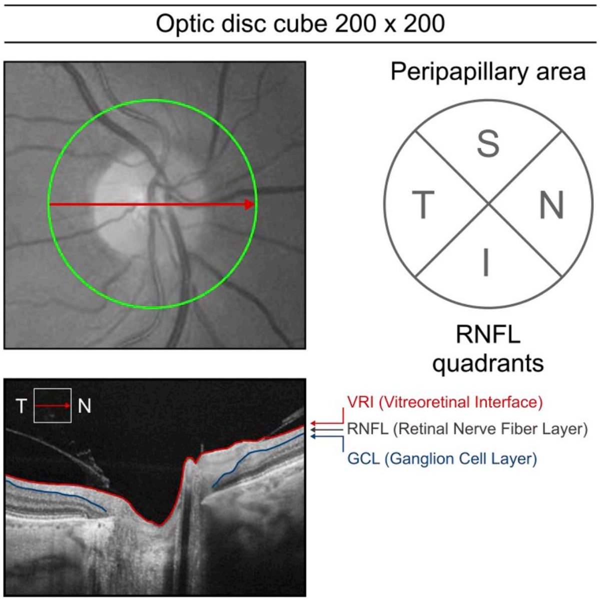

Fig. 1. Optic disc cube 200 × 200 scan protocol (right eye). This peripapillary scanning protocol centers on the optic nerve and determines the thickness of the retinal nerve fiber layer (RNFL) in each of 4 quadrants (S, superior; N, nasal; I, inferior; T, temporal) into which the peripapillary area is divided, based on which the total mean RNFL thickness is calculated. The RNFL is delimited by the vitreoretinal interface (VRI, red line) and the ganglion cell layer (GCL, blue line).

2.3. Mathematical model

In this section we describe the development of a mathematical model to characterize the evolution of RNFL thickness in MS patients.

2.4. Biological considerations

At disease onset, the predominant pathological consequences of MS are demyelination and axonal transection (i.e. complete and transversal section of the nerve fiber). However, as the pathology progresses, CNS inflammation and axonal degeneration predominate [25]. Unlike the study performed by Kotelnikova et al. [16], which modeled inflammatory attack, demyelination, remyelination, and nerve fiber loss, our model does not account for myelin-related processes, since RNFL nerve fibers are unmyelinated.

The proposed mathematical model, based on ordinary differential equations (ODEs), comprises 3 processes thought to be implicated in the evolution of the RNFL thinning in MS patients: autoimmune inflammation; axonal degeneration; and axonal regeneration. While autoimmune inflammation occurs in all forms of MS, its overall contribution relative to axonal degeneration and regeneration, as well as its temporal profile, can vary from one patient to the next [26]. By contrast, axonal degeneration does not follow autoimmune dynamics: damage accumulates as a consequence of the poor regenerative capacity of the CNS [15]. As is well documented, both inflammation and axonal degeneration cause numerous types of disabilities [26]. Finally, while axonal regeneration and functional recovery can occur in the peripheral nervous system (PNS), the regenerative capacity of the CNS after injury is very limited [27].

We distinguish between healthy axons, which have not yet been affected by the disease, and damaged axons, which decrease in thickness as a consequence of the inflammatory process (see Fig. 2). A and A_d represent the proportion of the total RNFL thickness corresponding to healthy and damaged axons, respectively. The temporal evolution of these parameters is described by the following equations:

$$\frac{dA}{dt} = -k_{inf}AR(t)A + k_{reg}A_d - k_{degA}A \tag{1}$$

$$\frac{dA_d}{dt} = k_{inf}AR(t)A - k_{reg}A_d - k_{degA_d}A_d \tag{2}$$

where the constant k_{inf} and the time-dependent parameter autoimmune response $AR(t)$ represent the inflammation process. Thus, healthy axons that are affected by an inflammatory outbreak or by progressive inflammation become damaged axons, with subsequent loss of volume and even total transection of the nerve fiber. The constants k_{degA} (healthy axons) and k_{degAd} (damaged axons) model axonal loss by volume reduction or axonal transection. Finally, the poor regeneration of damaged axons, which can partially recover from an inflammatory episode, is represented by constant k_{reg}.

Axonal degeneration D is defined as the process by which axons decrease in size, ultimately atrophying and degenerating:

$$\frac{dD}{dt} = k_{degA}A + k_{degA_d}A_d \tag{3}$$

Note that both axonal degeneration and transection cause problems in the CNS by impairing the transmission of nerve impulses.

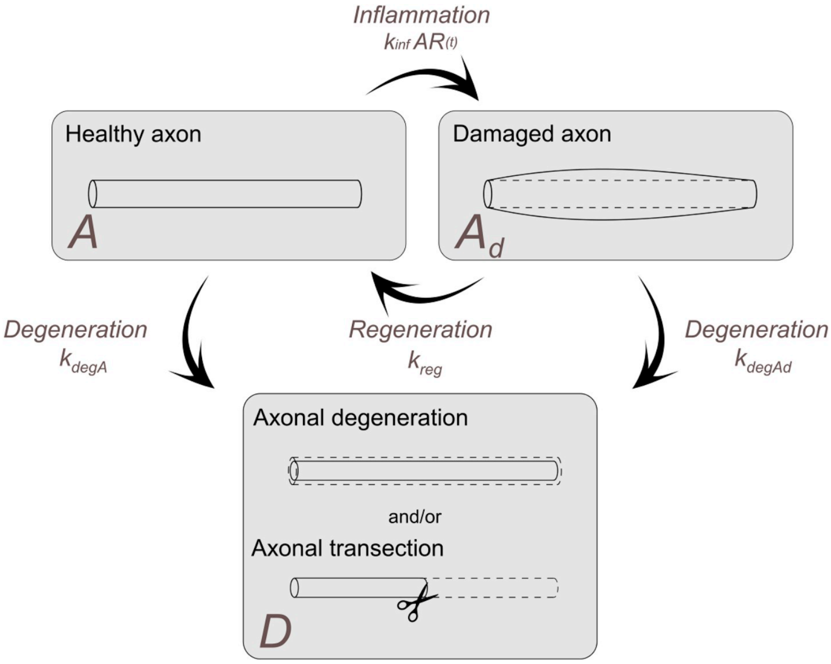

Fig. 2. Graphical representation of the proposed mathematical model. The model represents the evolution in MS patients of the thickness of the RNFL, which is composed of healthy axons (A) and by axons affected by autoimmune inflammation (A_d). The inflammatory process is modeled by the autoimmune response *AR(t)* and constant k_{inf}. Both healthy and damaged axons can decrease in volume as a result of axonal degeneration or transection (D), according to constants k_{degA} and k_{degAd}, respectively. A small proportion of damaged axons can regenerate, recovering their initial volume: constant k_{reg} represents this weak regenerative capacity.

2.5. Representation of autoimmune inflammation

Autoimmune inflammation is represented by EDSS scores obtained during the 10-year follow-up of the discovery cohort, since progression of this score correlates with a significant change in neurological status [28]. Hence, incremental changes in disability (ΔEDSS) were considered when EDSS score increased by ≥ 1 between visits (selection of larger increments would exclude patients with slower progressing disability). Autoimmune inflammation is modeled considering the time between changes in EDSS score. Time intervals (ΔT) between ΔEDSS were computed. Mean ΔT values were calculated for each patient in the discovery cohort. These data were grouped by clustering and then the probability distribution that best fit these experimental values was determined. By adjusting *AR(t)* to these probability distributions, we can represent the autoimmune inflammation that corresponds to an increase in disability and consequently, in EDSS score. Thus, in our proposed model patients with more slowly progressing disability experience autoimmune inflammation later than patients with faster progressing disability.

2.6. Adaptation of the model to clinical outcomes

In order to adjust the constants of the model to the clinical data it is necessary to set boundary conditions, taking into account both biological considerations and conservation laws.

The variable measured by OCT corresponds to RNFL thickness. In our numerical model, this thickness is the sum of the thickness of both healthy and damaged axons:

$$A_t(t) = A(t) + A_d(t) \tag{4}$$

In all simulations, we assume that all axons are healthy at the start of the follow-up period and therefore that damaged axons and degeneration are absent at baseline. The thickness measurement at baseline is thus considered the reference and the starting point:

$$A_t(0) = A(0) = baseline\ visit\ ;\ A_d(0) = D(0) = 0 \tag{5}$$

Conservation law states that the sum of healthy axons, damaged axons and degenerated axonal thickness must remain constant in time:

$$A(t) + A_d(t) + D(t) = A_t(t) + D(t) = constant \tag{6}$$

Based on data from literature, a range of values and a hierarchy between constants was defined in order to satisfy the different biological processes. Because the rate of CNS regeneration is very low [27], this parameter will have the smallest value (range, 0–0.0001). For axonal loss, the parameters represent the percentage of healthy or damaged axons involved in each process, and therefore the corresponding values can range from 0 (no axonal loss) to 1 (entire volume of the axon is affected) [1]. Finally, autoimmune inflammation is represented by the constant k_{inf} (range, 0–10) and the autoimmune response *AR(t)* [16]. The units of all constants are 1/day since thickness is measured in μm and its evolution is expressed in μm/day.

2.7. Optimization of model parameters

An optimization algorithm was used to determine the optimal parameters for the proposed model, minimizing the root mean square error (RMSE) between the values predicted by our mathematical model and the clinical data. RMSE quantifies the difference between analytical and experimental values in units of thickness. Specifically, Matlab (version R2017b, Mathworks Inc., Natick, MA) was used to implement a genetic algorithm based on natural selection and genetics, and designed to drive evolution of an initial population towards optimal fitness. This use of this type of algorithm for a similar purpose has been previously described [29].

For the purposes of our analysis, the chromosome is composed of our 4 constants (k_{inf}, k_{reg}, k_{degA} and k_{degAd}). Each individual is represented by 56 bits, which corresponds to the binary coding of these 4 constants. The selection method used was fit-fit, whereby the most competitive individuals cross with the best and the least competitive with the worst. For the creation of new individuals, the 2-point crossover operator was used for binary coding, where children contain entire variables of both parents [30]. To avoid the loss of diversity that crossing processes can cause and to prevent blocking of the algorithm, a mutation probability of 20% was established. Mutation was applied to new descendants, introducing a random modification in one or several genes.

An optimization cycle was simulated for each group of patients and for each zone of the peripapillary area, with 100 iterations and a population size of 1000 individuals, since in this problem the initial population had a greater influence on the results than the number of iterations.

3. Results

3.1. Longitudinal study

Differences in the evolution of RNFL thickness between the discovery cohort and healthy controls were compared using the Wilcoxon test (p-values < 0.05 were considered significant). The mean and standard deviation were computed for each cohort and for different peripapillary areas. As described in the Supplementary Material (Fig. S1), thinning of the RNFL in both MS patients and controls was observed between the baseline and 10-year follow-up visits, confirming that natural aging is an important component of this phenomenon. However, as also described previously [31], this thinning was of a greater magnitude in MS patients, confirming that RNFL thinning is also caused by MS progression. Specifically, at baseline mean RNFL thickness was 10.89% lower in MS patients than in respect to healthy controls. The reduction in RNFL thickness was even more pronounced at the 10-year follow up visit (7.80% and 14.12% decreases relative to corresponding baseline values in controls and MS patients, respectively).

Comparison of 10-year follow-up data for the control and MS groups revealed the following p-values: mean RNFL, 0.00029; superior RNFL, 0.0069, nasal RNFL, 0.5653; inferior RNFL, 0.0047; temporal quadrant RNFL, 0.00023. Therefore, significant differences in RNFL thinning were observed between MS patients and controls in all areas, except in the nasal quadrant.

3.2. Clustering of patients

After performing group selection using Silhouette analysis in the k-means clustering algorithm, an optimal number of 3 groups was established, with a Silhouette value of 0.8349. As shown in Fig. 3, group 1 corresponds to patients who began follow-up with a higher EDSS score while group 3 corresponds to those with the least advanced disability. While subjects were classified using other variables and different combinations thereof, the resulting Silhouette values were always lower than 0.8349.

Table 2
Decrease in retinal nerve fiber layer (RNFL) thickness in the entire peripapillary area and in the 4 quadrants into which it is divided. Values represent the median thinning in μm during the 10-year duration of the longitudinal study. The decrease observed over the 10-year follow-up period is represented as a percentage of baseline RNFL thickness.

RNFL thinning [μm]	Group 1	Group 2	Group 3
Peripapillary area	7.67 (9.1%)	13.20 (14.9%)	17.07 (17.0%)
Superior quadrant	7.50 (7.1%)	14.50 (13.6%)	24.00 (19.8%)
Nasal quadrant	6.50 (9.1%)	9.50 (13.3%)	14.50 (17.3%)
Inferior quadrant	6.50 (5.7%)	11.00 (9.6%)	20.00 (16.0%)
Temporal quadrant	9.50 (17.3%)	8.00 (14.3%)	15.00 (21.4%)

Once patients in the discovery cohort were grouped into different clusters, the evolution of RNFL thickness over the 10-year follow-up period could be analyzed. Fig. S2 shows the temporal evolution (baseline and 2.5, 5, and 10 years) of RNFL thickness for each group and for each quadrant of the peripapillary area. These values always decrease over time. To provide a comprehensive overview of RNFL thinning in MS patients, these data are summarized in Table 2, which shows the percentage decrease over the 10-year follow-up period. Group 1 shows a smaller decrease in RNFL thickness in 4 of the 5 areas analyzed with respect to group 2, and in all 5 areas with respect to group 3. RNFL thinning in the peripapillary area in group 1 was 1.64 times lower than that observed in group 2, which in turn was 1.14 times lower than that observed in group 3. Taken together these data reveal a lower magnitude of RNFL thinning in patients who began the follow-up period with greater disability (group 1). Therefore, most of this thinning occurs during the initial stages of disability (groups 2 and 3). However, the differences in RNFL thinning between the 3 patient groups were not significant ($p > 0.05$).

Furthermore, Fig. 2S shows that in all 3 groups the evolution of RNFL thickness follows a linear trend during follow-up. The negative slope of this trend decreases as the initial EDSS score increases.

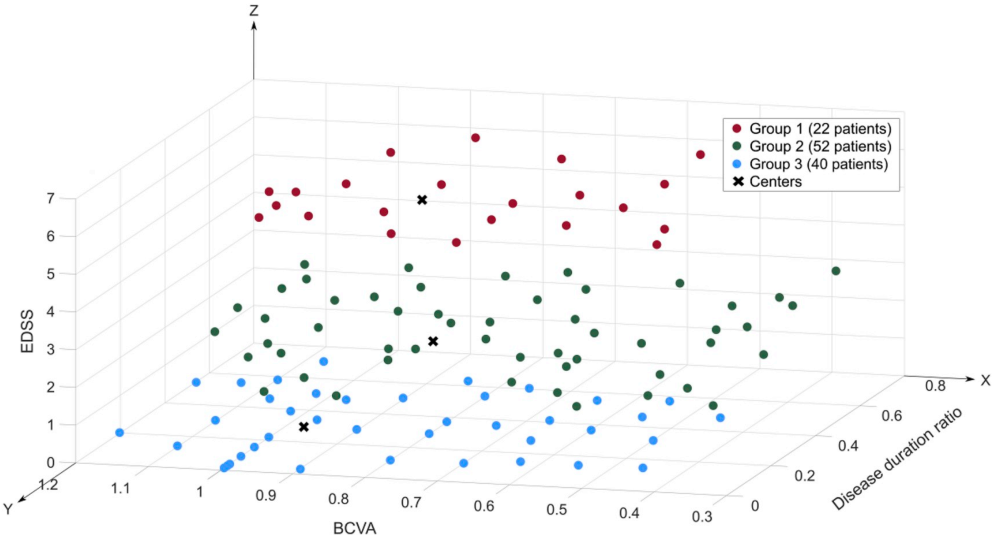

Fig. 3. Clustering of patients into the optimal number of groups according to Silhouette criterion. 3D classification was performed using the following variables: BCVA (X axis), disease duration ratio (Y axis), and EDSS score (Z axis). Patient clustering was as follows: group 1, 22 patients (age, 45.7 ± 11.9; disease duration, 14.7 ± 10.6; EDSS, 6.1 ± 0.3); group 2, 52 patients (age, 41.7 ± 9.2; disease duration, 11.1 ± 7.6; EDSS, 2.6 ± 0.6); group 3, 40 patients (age, 38.3 ± 11; disease duration, 7.2 ± 5; EDSS, 0.5 ± 0.5).

3.3. Mathematical model

The autoimmune response *AR(t)* is assumed to be defined by the probability distribution that best fits the clinical data. For group 1, the distribution is an extreme value distribution, with the following probability density function:

$$AR(t)_1 = \sigma^{-1} e^{\frac{t-\mu}{\sigma}} e^{-e^{\frac{t-\mu}{\sigma}}} = 677.\ 7^{-1} e^{\frac{t-2711.8}{677.7}} e^{-e^{\frac{t-2711.8}{677.7}}} \tag{7}$$

For groups 2 and 3, the optimal fits are Weibull and Rayleigh distributions, respectively:

$$AR(t)_2 = \frac{b}{a}\left(\frac{t}{a}\right)^{b-1} e^{-\left(\frac{t}{a}\right)^b} = \frac{3.2}{1947.2}\left(\frac{t}{1947.2}\right)^{3.2-1} e^{-\left(\frac{t}{1947.2}\right)^{3.2}} \tag{8}$$

$$AR(t)_3 = \frac{t}{\sigma^2} e^{\frac{-t^2}{2\sigma^2}} = \frac{t}{818.\ 7^2} e^{\frac{-t^2}{2\cdot 818.7^2}} \tag{9}$$

Fig. 4 shows clinical data for each group of the discovery cohort and the optimal distribution for these data. Each bar represents the probability density of the number of days between changes in EDSS score. These distributions reflect the rate of EDSS increase. Thus, group 3 has the highest probability of a 1-point increase in EDSS score (818.7 days) while group 1 has the lowest (2711.8 days). Therefore, the progression

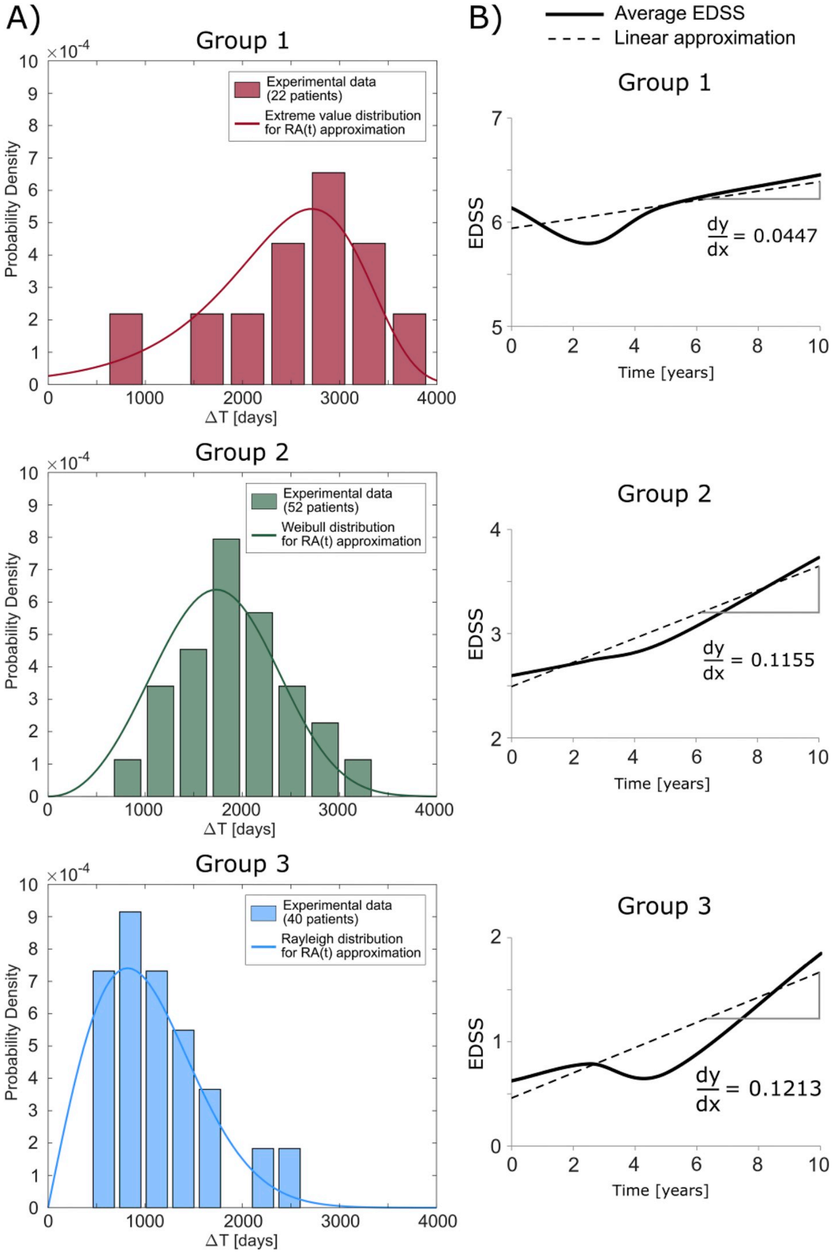

Fig. 4. A) Distribution of ΔT values for increments ≥1 point on the Expanded Disability Status (EDSS) scale for each group in the discovery cohort. The following probability density functions best fit each group: group 1, extreme value distribution; group 2, Weibull distribution; group 3, Rayleigh distribution. B) Evolution of mean EDSS score for each group for the 10-year follow-up period. Dashed line represents the linear approximation of EDSS score evolution.

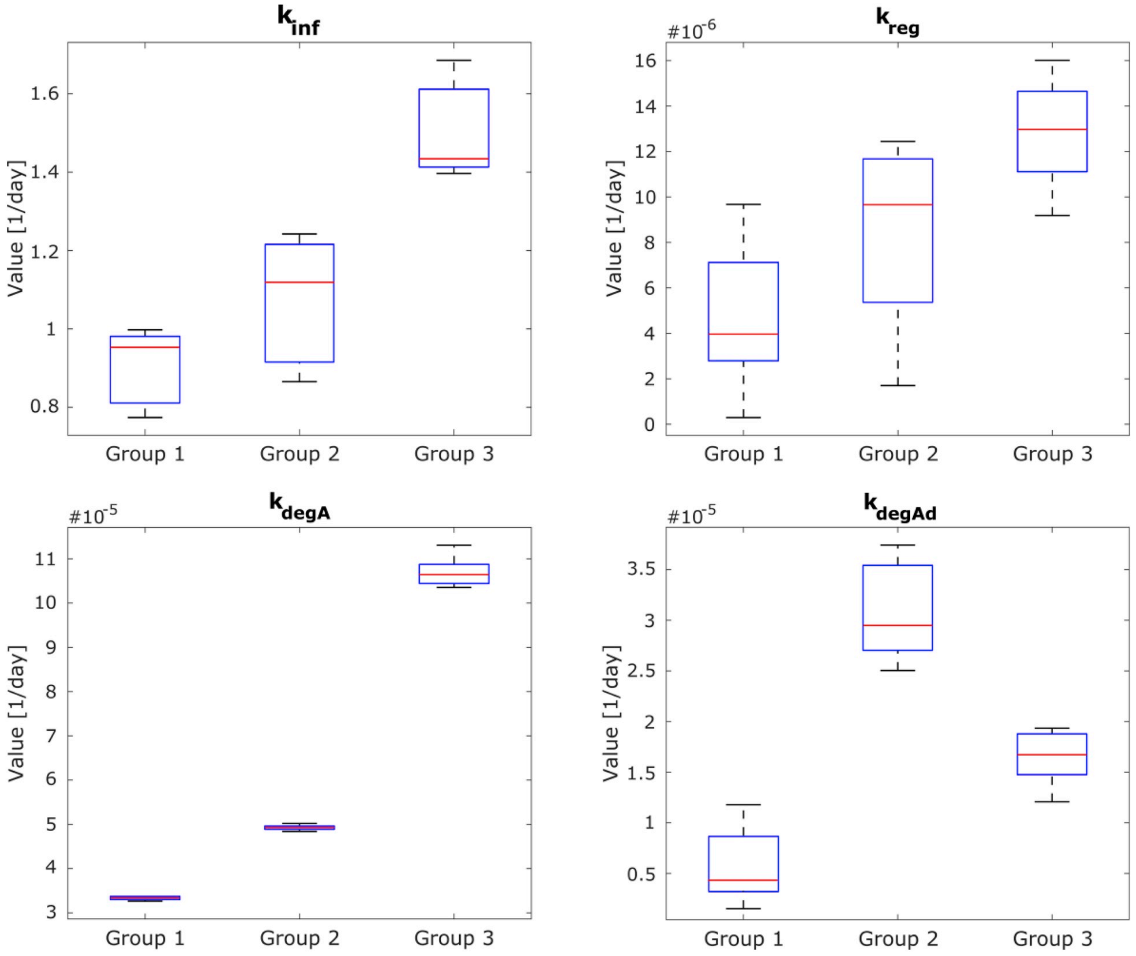

Fig. 5. Parameter distribution for the 3 groups of patients in the discovery cohort. This box-diagram was generated using the 10 best combinations of parameters (values are shown in Table 1S). Autoimmune inflammation is represented by k_{inf}, constants k_{degA} and k_{degAd} relate to axonal degeneration, and k_{reg} is the regeneration ratio.

of disability in patients in the initial stages of the disease is faster than that observed in patients with higher EDSS scores. This observation is also reflected in the slope of the linear approximation for EDSS score evolution; this slope decreases as the disability state increases.

After defining the autoimmune response, it is necessary to determine the constants for the model by adjusting it to the clinical data from the discovery cohort. These parameters were optimized using our genetic algorithm. The best adjustment for these 4 constants (k_{inf}, k_{reg}, k_{degA} and k_{degAd}) is shown in the Supplementary Material (Table 1S). In all cases the RMSE value obtained to fit the mathematical model to the clinical data was very low. The maximum RMSE value was 2.30 μm for the superior quadrant of group 1 and the minimum value was 0.12 μm for the peripapillary area of group 2. The values obtained for these constants are also shown in Fig. 5. To identify the biological processes that most influence the dynamics of each group, we compared the parameters corresponding to each of the different processes between groups. We found that patients with greater disability experienced less autoimmune inflammation ($\mathrm{k_{inf}}$(group1) < $\mathrm{k_{inf}}$(group2) < $\mathrm{k_{inf}}$(group3)), and that consequently the number of damaged axons slowly increased in group 1 ($\mathrm{k_{degAd}}$(group1) < $\mathrm{k_{degAd}}$(group2, group3)). A similar trend was observed for the degeneration of healthy axons ($\mathrm{k_{degA}}$(group1) < $\mathrm{k_{degA}}$(group2) < $\mathrm{k_{degA}}$(group3)), revealing that axonal degeneration in MS patients is greater during early disease stages. However, the degeneration of damaged axons did not follow this same trend: in this case, the degeneration of damaged axons was greater in group 2 than group 3 ($\mathrm{k_{degAd}}$(group2) > $\mathrm{k_{degAd}}$(group3)).

Finally, we observed that the regeneration process was consistent with the degree of disability: patients with lower EDSS scores had a greater regenerative capacity than patients with higher EDSS scores ($\mathrm{k_{reg}}$(group1) < $\mathrm{k_{reg}}$(group2) < $\mathrm{k_{reg}}$(group3)).

The evolution of each axon type (healthy or damaged) included in our model is depicted in Fig. 6. This mathematical model allows determination of the evolution of healthy and damaged axons. Therefore, the sum of the thicknesses of each of these axon types should correspond to the experimental RNFL thickness measured by OCT. As shown in Fig. 6 (right panel), the evolution of RNFL thickness as determined numerically fit precisely with the OCT clinical data. Our model can be adjusted to the RNFL thickness data for all patient groups with minimum error, verifying the model's ability to reproduce the different dynamics that occur during MS progression.

The evolution of total thickness A_t, healthy axon thickness A, damaged axon thickness A_d, and cumulative damage D are shown for each group of the discovery cohort in Fig. 6 (left panel). Based on our assumption that all axons are healthy at the start of follow-up, patients

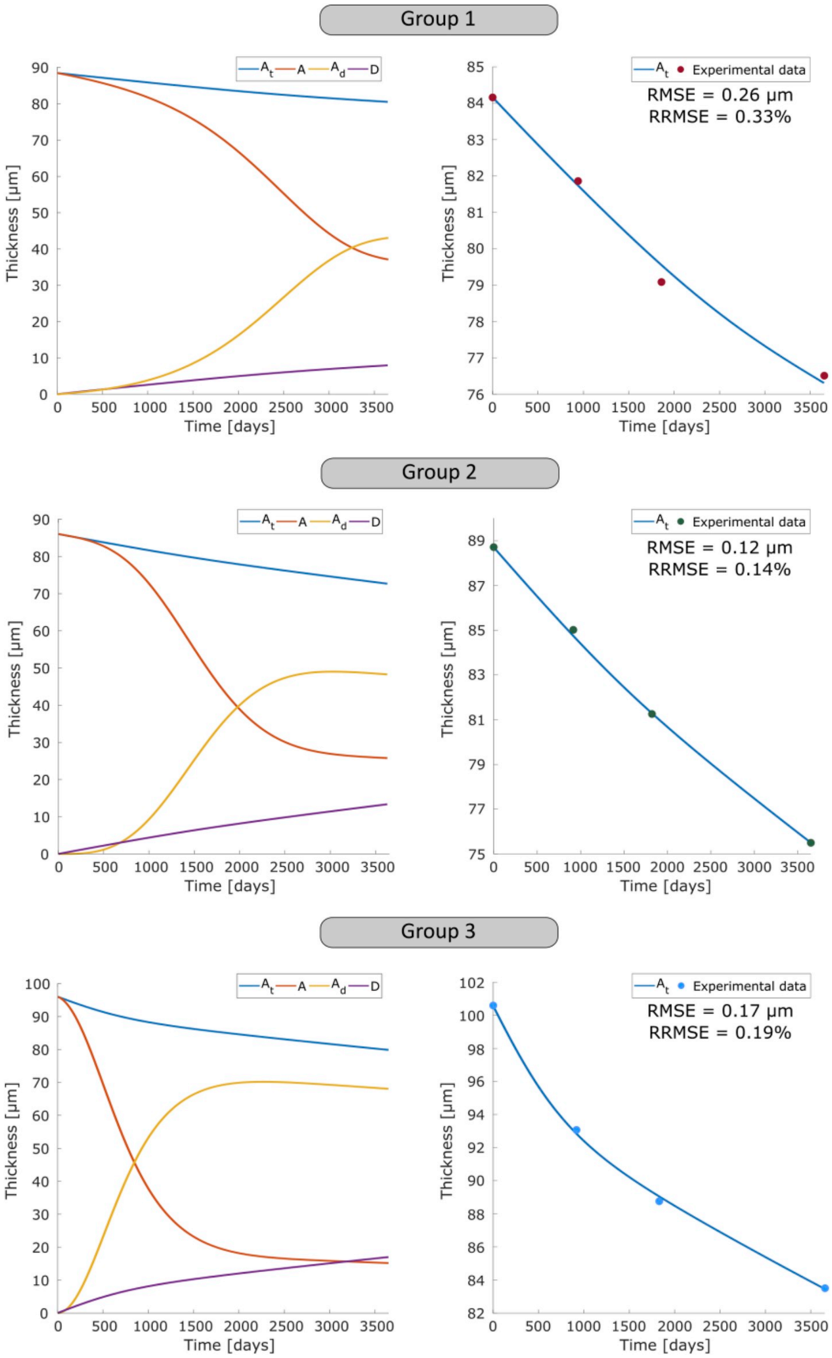

Fig. 6. Theoretical-experimental comparison of the evolution of retinal nerve fiber layer (RNFL) thickness for each group. Left: temporal evolution of healthy axons A, damaged axons A_d, and degeneration D. Right: adjustment of RNFL thicknesses obtained with the numerical model to the clinical data.

with the greatest disability (group 1) experience less autoimmune inflammation caused by MS, and therefore only a small proportion of healthy axons transform into damaged axons. However, in MS patients with less disability (groups 2 and 3), the number of damaged axons increases markedly. This behavior is conditioned both by the autoimmune response $AR(t)$ and constant k_{inf}. The results obtained for groups 2 and 3 show how damaged axons, which have undergone autoimmune inflammation, are degenerated, since most of the axons affected by MS degenerate in the initial stages of the disease. After peaking, the curve representing the evolution of damaged axons in groups 2 and 3 acquires a negative slope because the rate of degeneration is greater than at the beginning. Finally, due to the aforementioned effect degeneration D is greater in patients with less disability (D(group1) $<$ D(group2) $<$ D(group3)).

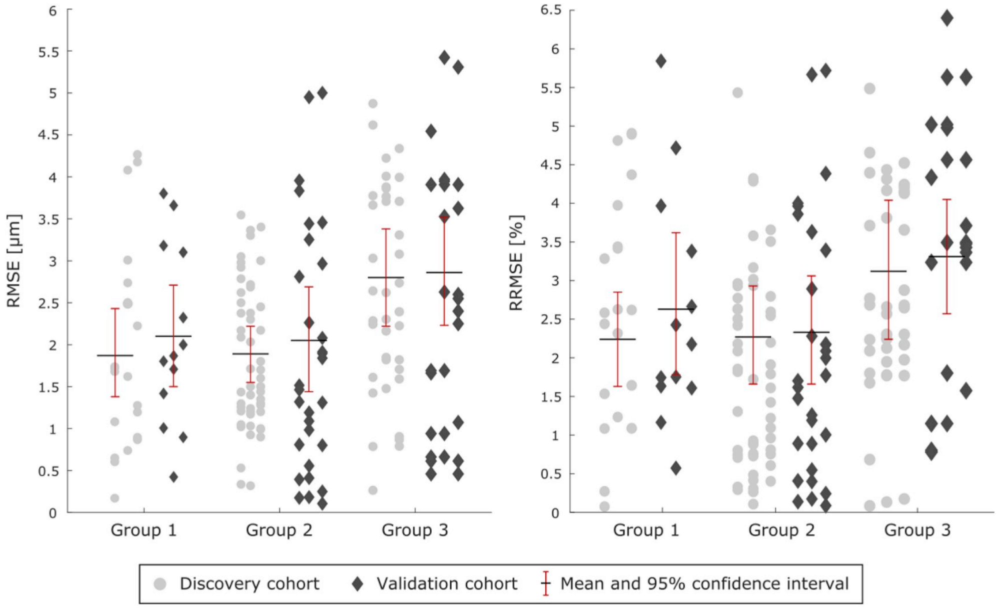

Fig. 7. Root mean square error (RMSE) and relative RMSE (RRMSE) values for individual patients in the discovery and validation cohorts. Mean values and 95% confidence intervals were obtained after performing a bootstrap method with random replacement of the original sample 10,000 times.

3.4. Mathematical model validation

Finally, to validate the model generated using mean data from each group in the discovery cohort over the 10 years of the longitudinal study, we investigated whether the model could correctly determine the evolution of RNFL thickness in individual patients. We calculated RMSE and relative RMSE (RRMSE) for each patient in the discovery cohort and used a bootstrap procedure to determine mean RMSE and the corresponding 95% confidence interval (CI) for each group. This bootstrap method was applied randomly, replacing the original sample 10,000 times. Using the 10-year follow-up data, the following values (shown in Fig. 7) were obtained for RMSE (group 1, 2.45 μm [95% CI, 1.87–3.06]; group 2, 3.20 μm [95% CI, 2.74–3.66]; group 3, 4.01 μm [95% CI, 3.32–5.59]) and RRMSE (group 1, 3.05% [95% CI, 2.34–3.79]; group 2, 4.20% [95% CI, 3.52–4.88]; group 3, 4.48% [95% CI, 3.63–5.25]).

We also validated our proposed model using data from a new cohort of patients (validation cohort) followed-up for 5 years. First, we assigned each patient in the validation cohort to one of the 3 groups previously defined for the discovery cohort, using data recorded on their first visit. Next, for each group we computed the evolution of RNFL thickness over 5 years using our mathematical model. Finally, following the same procedure described for the discovery cohort, we compared the theoretical values obtained for the validation cohort with the corresponding clinical data. As shown in Fig. 7, the mean RMSE and RRMSE values for the validation cohort were sufficiently low and very similar to those obtained for the discovery cohort. Therefore, this validation exercise revealed that our proposed model can predict RNFL thinning in new MS patients with a high level of accuracy.

In summary, we demonstrate that the different disease dynamics in MS patients can be represented by a combination of the 3 biological processes studied here: autoimmune inflammation, degeneration, and axonal regeneration. After clustering patients, our results indicate that RNFL thinning occurs cumulatively from the onset of MS and that most of this thinning occurs before the appearance of significant disability. In new MS patients, the proposed model allows prediction of the evolution of RNFL thickness, which in turn serves as a biomarker of MS evolution.

4. Discussion

Using OCT to measure RNFL thickness allows direct visualization of a part of CNS. Because the RNFL is composed of unmyelinated axons, this parameter can serve as a measure of axonal loss in MS patients [32]. The use of OCT as a biomarker of MS progression has been previously demonstrated [18]. Long-term OCT studies could provide a useful means of evaluating axonal degeneration and MS progression, and objectively assessing treatment response in MS patients.

The many commercially available OCT devices include OCT Triton, Optovue RTVue OCT, Spectralis OCT, and Cirrus HD-OCT. Our selection of Cirrus HD-OCT was based on the results of a study [33] that compared these 4 OCT devices, analyzing several parameters, and found that Cirrus HD-OCT performed best.

We used OCT data to relate RNFL thinning with disease progression in MS patients. It is well known that RNFL thinning occurs as part of normal aging. A longitudinal study of 187 eyes of healthy patients performed by Parikh et al. [34] found that mean RNFL thickness decreased by 0.16 μm/year. In our study, healthy controls showed a mean decrease of 7.86 μm over 10 years, as compared with a decrease of 12.59 μm in MS patients. These results show that pathophysiological mechanisms associated with MS cause axonal damage. Similar conclusions were reached in previous studies in which RNFL thickness in MS patients was measured by OCT [4,5]. However, to date no studies have attempted to characterize differences in the underlying pathological processes among MS patients or the corresponding implications in terms of the degree of disability.

In contrast the study of Kotelnikova and coworkers, who used MRI to analyze the evolution of brain volume in MS patients [16], we developed a mathematical model using RNFL thickness data, obtained by OCT, in order to reproduce the dynamics of CNS damage caused by MS. Our model is based on the hypothesis that MS is a dynamically heterogeneous disease, and proposes that differences in the relative contributions of 3 key mechanisms underlying RNFL thinning (autoimmune inflammation, axonal degeneration, and axonal regeneration) could account for the different disease dynamics observed among MS patients, and hence the differences between each of the 3 subgroups into which the MS patients are divided in this longitudinal study.

Before adjusting the parameters of the model using our clinical data, we sought to reduce the heterogeneity of the data by creating subgroups within the discovery cohort based on 3 parameters: the patients' degree of disability, visual function, and the length of time that they had been living with MS. Using the k-means algorithm, 3 subgroups were created. We opted not to classify patients using the 3 classic designations (relapsing-remitting MS [RRMS], secondary progressive MS [SPMS], and primary progressive MS [15]): because 91.22% of our patients had RRMS, classification using these categories would not reduce data heterogeneity.

Our model has been optimized to fit the clinical data corresponding to each of the 3 subgroups of the discovery cohort. Different optimization algorithms using stochastic search techniques, such as genetic algorithms and particle swarm optimization [35], can be used to minimize RMSE. Although genetic algorithms have a high computational cost, we chose this approach to avoid the main disadvantage of particle swarm optimization, which tends to get stuck in local minima [36,37]. Our results show that CNS damage occurs cumulatively, beginning at disease onset, and that most RNFL thinning occurs before the onset of significant disability (i.e. while EDSS scores are low). This conclusion is in line with the findings of a review by Petzold and coworkers [5] of several cross-sectional studies, but this is the first time it has been confirmed in a longitudinal study. Therefore, following prior corroboration of the validity of RNFL thickness as a diagnostic biomarker of MS [3], we demonstrate that this parameter can also be used to predict the evolution of MS-associated disability.

Our findings provide robust evidence demonstrating that RNFL thickness differs significantly between MS patients and healthy controls, and can be used to distinguish one group from the other, as previously suggested in several studies [6–8]. However, because RNFL thickness does not differ significantly among MS patients, it cannot be used to distinguish between them. By contrast, our classification based on EDSS score allows differentiation between 3 subgroups of MS patients categorized according to the relative contributions of the different biological processes that contribute to RNFL thinning.

Our model allowed us to quantify the degree to which each different biological process (autoimmune inflammation, axonal degeneration, and axonal regeneration) contributes to the evolution of RNFL thickness in the 3 subgroups of MS patients. As the degree of disability worsens, both autoimmune inflammation and axonal degeneration attenuate, and the regenerative capacity of the CNS decreases. Therefore, patients with the highest degree of disability have the lowest regeneration ratio. Our study is the first to analyze the influence of these biological processes on RNFL thinning in MS patients.

Some limitations of our study should be noted. Given the paucity of quantitative biological data on the biological processes described, we adjusted the parameters of the model to fit the clinical data, and then subsequently verified that the parameters were within the established range. The autoimmune response was supposed to follow the probability distribution of time intervals between incremental changes in the disability score. Thus, the inflammatory response was defined in terms of timing in order to capture the dynamics of the damage. Therefore, this assumption allows to relate the attack response to the increase of disability. Our results should therefore be considered as trends that help us better understand the evolution of RNFL thinning and the disease course of MS. Another limitation is that we cannot experimentally measure the separate proportions of healthy and damaged axons that comprise the RNFL; OCT only allows measurement of the thickness of the entire RNFL. It should also be noted that we did not model all biological processes that can cause CNS damage, instead focusing on those known to contribute to axonal damage of retinal nerve fibers in MS. Although EDSS scores and disease duration varied considerably between patients at the beginning of follow-up, our clustering method classified patients according to disease status at baseline (including EDSS score and disease duration ratio). Therefore, differences in disease status between patients should not affect our results, and, consequently, RNFL evolution was calculated using parameters specific to each sub-group. Moreover, the same initial boundary conditions were applied to all groups, since no data on the percentage of damaged axons at the beginning of follow-up were available. Further research will be required to identify the specific regions of the RNFL in which damage occurs. Finally, parameters such as age, disease duration, and degree of disability of the validation cohort were similar to those of the discovery cohort, which may have influenced our validation process.

Future studies analyzing larger amounts of quantitative data on the biological processes underlying CNS damage in MS will facilitate the development of more specific predictive models that could be of benefit to clinicians. The use of OCT techniques in combination with our mathematical model allows prediction of the evolution of RNFL thinning. OCT is an objective, reproducible, cost-effective and noninvasive technique that can be conducted by any clinician in a few minutes, without causing the patient any discomfort. Therefore, clinicians can rapidly predict the evolution of RNFL thinning and, consequently, the course of MS-related disability. The next step will be to incorporate this mathematical model into OCT equipment in order to directly obtain a prediction of the course of RNFL thinning. This would be of significant benefit to patients, hastening the process and obviating the need for a separate data analysis process after OCT examination. Our model will also need to be validated in other populations in order to demonstrate its utility and to confirm the validity of RNFL thickness as a reliable biomarker of MS disease course that could be used to facilitate the selection of therapies specific to a given patient.

5. Conclusion

In summary, our proposed model, generated using 10-year follow-up data collected from MS patients, demonstrates that differences in the contributions of the specific biological processes analyzed here can give rise to varying dynamics of MS progression. This may help explain the high degree of clinical heterogeneity observed among MS patients. Furthermore, our results indicate that the contribution of each of these biological processes varies at different disease stages. MS should be considered as a progressive disease, the course of which follows the dynamics of CNS damage, and therapeutic strategies should seek to reduce this damage beginning in early disease stages. Our results confirm that RNFL thinning occurs cumulatively from the moment of disease onset. Our proposed mathematical model allows prediction in new MS patients of the progression of RNFL thinning, which in turn may serve as a biomarker of MS disease progression.

Conflicts of interest

The authors state that there are no conflicts of interest.

Acknowledgements

This work was supported by the Spanish Ministry of Economy and Competitiveness through project DPI 2016-79302-R, by the Spanish Ministry of Science, Innovation and Universities (grant BES-2017-080384) and by PI17/01726 (Instituto de Salud Carlos III).

Appendix A. Supplementary data

Supplementary data to this article can be found online at https://doi.org/10.1016/j.compbiomed.2019.103357.

References

[1] J.D. Haines, M. Inglese, P. Casaccia, Axonal damage in multiple sclerosis, Mt. Sinai J. Med. A J. Transl. Pers. Med. 78 (2011) 231–243, https://doi.org/10.1002/msj.20246.
[2] T.A.M. Siepman, M.W. Bettink-Remeijer, R.Q. Hintzen, Retinal nerve fiber layer

thickness in subgroups of multiple sclerosis, measured by optical coherence tomography and scanning laser polarimetry, J. Neurol. 257 (2010) 1654–1660, https://doi.org/10.1007/s00415-010-5589-1.

[3] A. Pérez del Palomar, J. Cegoñino, A. Montolío, E. Orduna, E. Vilades, B. Sebastián, L.E. Pablo, E. Garcia-Martin, Swept source optical coherence tomography to early detect multiple sclerosis disease. The use of machine learning techniques, PLoS One 14 (2019) e0216410, , https://doi.org/10.1371/journal.pone.0216410.

[4] E. Garcia-Martin, V. Polo, J.M. Larrosa, M.L. Marques, R. Herrero, J. Martin, J.R. Ara, J. Fernandez, L.E. Pablo, Retinal layer segmentation in patients with multiple sclerosis using spectral domain optical coherence tomography, Ophthalmology 121 (2014) 573–579, https://doi.org/10.1016/j.ophtha.2013.09.035.

[5] A. Petzold, L.J. Balcer, P.A. Calabresi, F. Costello, T.C. Frohman, E.M. Frohman, E.H. Martinez-Lapiscina, A.J. Green, R. Kardon, O. Outteryck, F. Paul, S. Schippling, P. Vermersch, P. Villoslada, L.J. Balk, ERN-EYE IMSVISUAL, Retinal layer segmentation in multiple sclerosis: a systematic review and meta-analysis, Lancet Neurol. 16 (2017) 797–812, https://doi.org/10.1016/S1474-4422(17)30278-8.

[6] F. Costello, W. Hodge, Y.I. Pan, L. Metz, R.H. Kardon, Retinal nerve fiber layer and future risk of multiple sclerosis, Can. J. Neurol. Sci. 35 (2008) 482–487, https://doi.org/10.1017/S031716710000915X.

[7] J. Sepulcre, M. Murie-Fernandez, A. Salinas-Alaman, A. García-Layana, B. Bejarano, P. Villoslada, Diagnostic accuracy of retinal abnormalities in predicting disease activity in MS, Neurology 68 (2007) 1488–1494, https://doi.org/10.1212/01.wnl.0000260612.51849.

[8] L.S. Talman, E.R. Bisker, D.J. Sackel, D.A. Long, K.M. Galetta, J.N. Ratchford, D.J. Lile, S.K. Farrell, M.J. Loguidice, G. Remington, A. Conger, T.C. Frohman, D.A. Jacobs, C.E. Markowitz, G.R. Cutter, G.S. Ying, Y. Dai, M.G. Maguire, S.L. Galetta, E.M. Frohman, P.A. Calabresi, L.J. Balcer, Longitudinal study of vision and retinal nerve fiber layer thickness in multiple sclerosis, Ann. Neurol. 67 (2010) 749–760, https://doi.org/10.1002/ana.22005.

[9] S. Niu, Q. Chen, L. de Sisternes, D.L. Rubin, W. Zhang, Q. Liu, Automated retinal layers segmentation in SD-OCT images using dual-gradient and spatial correlation smoothness constraint, Comput. Biol. Med. 54 (2015) 116–128, https://doi.org/10.1016/j.compbiomed.2014.08.028.

[10] E. Garcia-Martin, V. Pueyo, J.R. Ara, C. Almarcegui, J. Martin, L. Pablo, I. Dolz, E. Sancho, F.J. Fernandez, Effect of optic neuritis on progressive axonal damage in multiple sclerosis patients, Mult. Scler. J. 17 (2011) 830–837, https://doi.org/10.1177/1352458510397414.

[11] A.J. Thompson, B.L. Banwell, F. Barkhof, W.M. Carroll, T. Coetzee, G. Comi, J. Correale, F. Fazekas, M. Filippi, M.S. Freedman, K. Fujihara, S.L. Galetta, H.P. Hartung, L. Kappos, F.D. Lublin, R.A. Marrie, A.E. Miller, D.H. Miller, X. Montalban, E.M. Mowry, P.S. Sorensen, M. Tintoré, A.L. Traboulsee, M. Trojano, B.M.J. Uitdehaag, S. Vukusic, E. Waubant, B.G. Weinshenker, S.C. Reingold, J.A. Cohen, Diagnosis of multiple sclerosis: 2017 revisions of the McDonald criteria, Lancet Neurol. 17 (2018) 162–173, https://doi.org/10.1016/S1474-4422(17)30470-2.

[12] C. Louapre, C. Lubetzki, Neurodegeneration in multiple sclerosis is a process separate from inflammation: Yes, Mult. Scler. J. 21 (2015) 1626–1628, https://doi.org/10.1177/1352458515587598.

[13] E. Leray, J. Yaouanq, E. Le Page, M. Coustans, D. Laplaud, J. Oger, G. Edan, Evidence for a two-stage disability progression in multiple sclerosis, Brain 133 (2010) 1900–1913, https://doi.org/10.1093/brain/awq076.

[14] A. Bar-Or, J.P. Antel, Central nervous system inflammation across the age span, Curr. Opin. Neurol. 29 (2016) 381–387, https://doi.org/10.1097/WCO.0000000000000331.

[15] G. Giovannoni, G. Cutter, M. Pia-Sormani, S. Belachew, R. Hyde, H. Koendgen, V. Knappertz, D. Tomic, D. Leppert, R. Herndon, C.A.M. Wheeler-Kingshott, O. Ciccarelli, D. Selwood, E.V. di Cantogno, A.F. Ben-Amor, P. Matthews, D. Carassiti, D. Baker, K. Schmierer, Is multiple sclerosis a length-dependent central axonopathy? The case for therapeutic lag and the asynchronous progressive MS hypotheses, Mult. Scler. Relat. Disord. 12 (2017) 70–78, https://doi.org/10.1016/j.msard.2017.01.007.

[16] E. Kotelnikova, N.A. Kiani, E. Abad, E.H. Martinez-Lapiscina, M. Andorra, I. Zubizarreta, I. Pulido-Valdeolivas, I. Pertsovskaya, L.G. Alexopoulos, T. Olsson, R. Martin, F. Paul, J. Tegnér, J. Garcia-Ojalvo, P. Villoslada, Dynamics and heterogeneity of brain damage in multiple sclerosis, PLoS Comput. Biol. 13 (2017) e1005757, , https://doi.org/10.1371/journal.pcbi.1005757.

[17] M. Filippi, M.A. Rocca, O. Ciccarelli, N. De Stefano, N. Evangelou, L. Kappos, A. Rovira, J. Sastre-Garriga, M. Tintorè, J.L. Frederiksen, C. Gasperini, J. Palace, D.S. Reich, B. Banwell, X. Montalban, F. Barkhof, MRI criteria for the diagnosis of multiple sclerosis: MAGNIMS consensus guidelines, Lancet Neurol. 15 (2016) 292–303, https://doi.org/10.1016/S1474-4422(15)00393-2.

[18] E.H. Martinez-Lapiscina, S. Arnow, J.A. Wilson, S. Saidha, J.L. Preiningerova, T. Oberwahrenbrock, A.U. Brandt, L.E. Pablo, S. Guerrieri, I. Gonzalez, O. Outteryck, A.-K. Mueller, P. Albrecht, W. Chan, S. Lukas, L.J. Balk, C. Fraser, J.L. Frederiksen, J. Resto, T. Frohman, C. Cordano, I. Zubizarreta, M. Andorra, B. Sanchez-Dalmau, A. Saiz, R. Bermel, A. Klistorner, A. Petzold, S. Schippling, F. Costello, O. Aktas, P. Vermersch, C. Oreja-Guevara, G. Comi, L. Leocani, E. Garcia-Martin, F. Paul, E. Havrdova, E. Frohman, L.J. Balcer, A.J. Green, P.A. Calabresi, P. Villoslada, Retinal thickness measured with optical coherence tomography and risk of disability worsening in multiple sclerosis: a cohort study, Lancet Neurol. 15 (2016) 574–584, https://doi.org/10.1016/S1474-4422(16)00068-5.

[19] E. Garcia-Martin, D. Rodriguez-Mena, R. Herrero, C. Almarcegui, I. Dolz, J. Martin, J.R. Ara, J.M. Larrosa, V. Polo, J. Fernández, L.E. Pablo, Neuro-ophthalmologic evaluation, quality of life, and functional disability in patients with MS, Neurology 81 (2013) 76–83, https://doi.org/10.1212/WNL.0b013e318299ccd9.

[20] T.M. Jenkins, A.T. Toosy, Optic neuritis: the eye as a window to the brain, Curr. Opin. Neurol. 30 (2017) 61–66, https://doi.org/10.1097/WCO.0000000000000414.

[21] F. London, H. Zéphir, E. Drumez, J. Labreuche, N. Hadhoum, J. Lannoy, J. Hodel, P. Vermersch, J.-P. Pruvo, X. Leclerc, O. Outteryck, Optical coherence tomography: a window to the optic nerve in clinically isolated syndrome, Brain 142 (2019) 903–915, https://doi.org/10.1093/brain/awz038.

[22] R.A. Armstrong, Statistical guidelines for the analysis of data obtained from one or both eyes, Ophthalmic Physiol. Opt. 33 (2013) 7–14, https://doi.org/10.1111/opo.12009.

[23] L.T. Chylack, J.K. Wolfe, D.M. Singer, M.C. Leske, M.A. Bullimore, I.L. Bailey, J. Friend, D. McCarthy, S.Y. Wu, The lens Opacities classification system III. The longitudinal study of cataract study group, Arch. Ophthalmol. (Chicago, Ill. 1960) 111 (1993) 831–836, https://doi.org/10.1001/archopht.1993.01090060119035.

[24] F. Wang, H.-H. Franco-Penya, J.D. Kelleher, J. Pugh, R. Ross, P. Perner (Ed.), An Analysis of the Application of Simplified Silhouette to the Evaluation of K-Means Clustering Validity, Springer International Publishing, Cham, 2017, pp. 291–305, , https://doi.org/10.1007/978-3-319-62416-7_21.

[25] A. Kutzelnigg, H. Lassmann, Pathology of multiple sclerosis and related inflammatory demyelinating diseases, Handb. Clin. Neurol, first ed., Elsevier B.V., 2014, pp. 15–58, , https://doi.org/10.1016/B978-0-444-52001-2.00002-9.

[26] J.M. Frischer, S.D. Weigand, Y. Guo, N. Kale, J.E. Parisi, I. Pirko, J. Mandrekar, S. Bramow, I. Metz, W. Brück, H. Lassmann, C.F. Lucchinetti, Clinical and pathological insights into the dynamic nature of the white matter multiple sclerosis plaque, Ann. Neurol. 78 (2015) 710–721, https://doi.org/10.1002/ana.24497.

[27] M. Curcio, F. Bradke, Axon regeneration in the central nervous system: facing the challenges from the inside, Annu. Rev. Cell Dev. Biol. 34 (2018) 495–521, https://doi.org/10.1146/annurev-cellbio-100617-062508.

[28] F.D. Lublin, S.C. Reingold, J. a Cohen, G.R. Cutter, P.S. Sorensen, A.J. Thompson, J.S. Wolinsky, L.J. Balcer, B. Banwell, F. Barkhof, B. Bebo, P.A. Calabresi, M. Clanet, G. Comi, R.J. Fox, M.S. Freedman, A.D. Goodman, M. Inglese, L. Kappos, B.C. Kieseier, J.A. Lincoln, C. Lubetzki, A.E. Miller, X. Montalban, P.W. O'Connor, J. Petkau, C. Pozzilli, R.A. Rudick, M.P. Sormani, O. Stuve, E. Waubant, C.H. Polman, Defining the clinical course of multiple sclerosis: the 2013 revisions, Neurology 83 (2014) 278–286, https://doi.org/10.1212/WNL.0000000000000560.

[29] C. Stamile, G. Kocevar, F. Cotton, D. Sappey-Marinier, A genetic algorithm-based model for longitudinal changes detection in white matter fiber-bundles of patient with multiple sclerosis, Comput. Biol. Med. 84 (2017) 182–188, https://doi.org/10.1016/j.compbiomed.2017.03.028.

[30] P. Kora, P. Yadlapalli, Crossover operators in genetic algorithms: a review, Int. J. Comput. Appl. 162 (2017) 34–36, https://doi.org/10.5120/ijca2017913370.

[31] R. Alonso, D. Gonzalez-Moron, O. Garcea, Optical coherence tomography as a biomarker of neurodegeneration in multiple sclerosis: a review, Mult. Scler. Relat. Disord. 22 (2018) 77–82, https://doi.org/10.1016/j.msard.2018.03.007.

[32] J. Kucharczuk, Z. Maciejek, B.L. Sikorski, Optical coherence tomography in diagnosis and monitoring multiple sclerosis, Neurol. Neurochir. Pol. 52 (2018) 140–149, https://doi.org/10.1016/j.pjnns.2017.10.009.

[33] M.R. Munk, H. Giannakaki-Zimmermann, L. Berger, W. Huf, A. Ebneter, S. Wolf, M.S. Zinkernagel, OCT-angiography: a qualitative and quantitative comparison of 4 OCT-A devices, PLoS One 12 (2017) e0177059, , https://doi.org/10.1371/journal.pone.0177059.

[34] R.S. Parikh, S.R. Parikh, G.C. Sekhar, S. Prabakaran, J.G. Babu, R. Thomas, Normal age-related decay of retinal nerve fiber layer thickness, Ophthalmology 114 (2007) 921–926, https://doi.org/10.1016/j.ophtha.2007.01.023.

[35] H. Shokri-Ghaleh, A. Alfi, A comparison between optimization algorithms applied to synchronization of bilateral teleoperation systems against time delay and modeling uncertainties, Appl. Soft Comput. 24 (2014) 447–456, https://doi.org/10.1016/j.asoc.2014.07.020.

[36] R. Hassan, B. Cohanim, O. de Weck, G. Venter, A comparison of particle swarm optimization and the genetic algorithm, 46th AIAA/ASME/ASCE/AHS/ASC Struct. Struct. Dyn. Mater. Conf, American Institute of Aeronautics and Astronautics, Reston, Virigina, 2005, , https://doi.org/10.2514/6.2005-1897.

[37] M. Schmitt, R. Wanka, Particle swarm optimization almost surely finds local optima, Theor. Comput. Sci. 561 (2015) 57–72, https://doi.org/10.1016/j.tcs.2014.05.017.

2.2 MS diagnosis and prognosis by OCT and AI

2.2.1 MS diagnosis using DRI OCT Triton

Manuscript 2: Swept source optical coherence tomography to early detect multiple sclerosis disease. The use of machine learning techniques

Amaya Pérez del Palomar, José Cegoñino, Alberto Montolío, Elvira Orduna, Elisa Vilades, Berta Sebastian, Luis E. Pablo, Elena Garcia-Martin

Abstract

Objective

To compare axonal loss in ganglion cells detected with swept-source optical coherence tomography (SS-OCT) in eyes of patients with multiple sclerosis (MS) versus healthy controls using different machine learning techniques. To analyze the capability of machine learning techniques to improve the detection of retinal nerve fiber layer (RNFL) and the complex Ganglion Cell Layer–Inner plexiform layer (GCL+) damage in patients with multiple sclerosis and to use the SS-OCT as a biomarker to early predict this disease.

Methods

Patients with relapsing-remitting MS (n = 80) and age-matched healthy controls (n = 180) were enrolled. Different protocols from the DRI SS-OCT Triton system were used to obtain the RNFL and GCL+ thicknesses in both eyes. Macular and peripapilar areas were analyzed to detect the zones with higher thickness decrease. The performance of different machine learning techniques (decision trees, multilayer perceptron and support vector machine) for identifying RNFL and GCL+ thickness loss in patients with MS were evaluated. Receiveroperating characteristic (ROC) curves were used to display the ability of the different tests to discriminate between MS and healthy eyes in our population.

Results

Machine learning techniques provided an excellent tool to predict MS disease using SSOCT data. In particular, the decision trees obtained the best prediction (97.24%) using RNFL data in macular area and the area under the ROC curve was 0.995, while the wide protocol which covers an extended area between macula and papilla gave an accuracy of 95.3% with a ROC of 0.998. Moreover, it was obtained that the most significant area of the RNFL to predict MS is the macula just surrounding the

fovea. On the other hand, in our study, GCL+ did not contribute to predict MS and the different machine learning techniques performed worse in this layer than in RNFL.

Conclusions

Measurements of RNFL thickness obtained with SS-OCT have an excellent ability to differentiate between healthy controls and patients with MS. Thus, the use of machine learning techniques based on these measures can be a reliable tool to help in MS diagnosis.

PLOS ONE

RESEARCH ARTICLE

Swept source optical coherence tomography to early detect multiple sclerosis disease. The use of machine learning techniques

Amaya Pérez del Palomar[1,2]☯*, **José Cegoñino**[1,2]☯, **Alberto Montolío**[1,2], **Elvira Orduna**[3,4], **Elisa Vilades**[3,4], **Berta Sebastián**[5], **Luis E. Pablo**[3,4], **Elena Garcia-Martin**[3,4]

1 Group of Biomaterials, Aragon Institute of Engineering Research (I3A), University of Zaragoza, Zaragoza, Spain, **2** Department of Mechanical Engineering, University of Zaragoza, Zaragoza, Spain, **3** Department of Ophthalmology, Miguel Servet University Hospital, Zaragoza, Spain, **4** GIMSO Research and Innovative Group, Aragon Institute for Health Research (IIS Aragón), University of Zaragoza, Zaragoza, Spain, **5** Department of Neurology, Miguel Servet University Hospital, Zaragoza, Spain

☯ These authors contributed equally to this work.
* amaya@unizar.es

Citation: Pérez del Palomar A, Cegoñino J, Montolío A, Orduna E, Vilades E, Sebastián B, et al. (2019) Swept source optical coherence tomography to early detect multiple sclerosis disease. The use of machine learning techniques. PLoS ONE 14(5): e0216410. https://doi.org/10.1371/journal.pone.0216410

Editor: Sanjoy Bhattacharya, Bascom Palmer Eye Institute, UNITED STATES

Received: December 30, 2018

Accepted: April 21, 2019

Published: May 6, 2019

Data Availability Statement: All relevant data are within the manuscript and its Supporting Information files.

Funding: This work was supported by Ministerio de Ciencia, Innovación y Universidades, Spain to A. Perez del Palomar & J. Cegoñino, DPI2016-79302R, http://www.ciencia.gob.es/portal/site/MICINN/?lang_choosen=en; Ministerio de Educacion y Formación Profesional, Spain to A. Montolío, BES-2017-080384, http://www.

Abstract

Objective

To compare axonal loss in ganglion cells detected with swept-source optical coherence tomography (SS-OCT) in eyes of patients with multiple sclerosis (MS) versus healthy controls using different machine learning techniques. To analyze the capability of machine learning techniques to improve the detection of retinal nerve fiber layer (RNFL) and the complex Ganglion Cell Layer–Inner plexiform layer (GCL+) damage in patients with multiple sclerosis and to use the SS-OCT as a biomarker to early predict this disease.

Methods

Patients with relapsing-remitting MS (n = 80) and age-matched healthy controls (n = 180) were enrolled. Different protocols from the DRI SS-OCT Triton system were used to obtain the RNFL and GCL+ thicknesses in both eyes. Macular and peripapilar areas were analyzed to detect the zones with higher thickness decrease. The performance of different machine learning techniques (decision trees, multilayer perceptron and support vector machine) for identifying RNFL and GCL+ thickness loss in patients with MS were evaluated. Receiver-operating characteristic (ROC) curves were used to display the ability of the different tests to discriminate between MS and healthy eyes in our population.

Results

Machine learning techniques provided an excellent tool to predict MS disease using SS-OCT data. In particular, the decision trees obtained the best prediction (97.24%) using RNFL data in macular area and the area under the ROC curve was 0.995, while the wide protocol which covers an extended area between macula and papilla gave an accuracy of 95.3% with a ROC of 0.998. Moreover, it was obtained that the most significant area of the

educacionyfp.gob.es/portada.html; Instituto de Salud Carlos III to E. Orduna & E. Vilades & B. Sebastian & L.E. Pablo & E. Garcia-Martin, PI17/01726, http://www.isciii.es/; Ministerio de Ciencia, Innovación y Universidades, Spain to E. Orduna & E. Vilades & B. Sebastian & L.E. Pablo & E. Garcia-Martin, MAT2017-83858-C2-2, http://www.ciencia.gob.es/portal/site/MICINN/?lang_choosen=en.

Competing interests: The authors have declared that no competing interests exist.

RNFL to predict MS is the macula just surrounding the fovea. On the other hand, in our study, GCL+ did not contribute to predict MS and the different machine learning techniques performed worse in this layer than in RNFL.

Conclusions

Measurements of RNFL thickness obtained with SS-OCT have an excellent ability to differentiate between healthy controls and patients with MS. Thus, the use of machine learning techniques based on these measures can be a reliable tool to help in MS diagnosis.

Introduction

Multiple sclerosis (MS) is a neurodegenerative disease of the central nervous system that disrupts the flow of information within the brain, and between the brain and body. The cause of MS is still unknown and the progress, severity and specific symptoms of MS in any one person cannot yet be predicted. Most people with MS are diagnosed between the ages of 20 and 50, with at least two to three times more women than men being diagnosed with the disease. However, an early diagnosis is determinant to slow down the progression of the disease [1]. MS is diagnosed on the basis of clinical findings and supporting evidence, such as magnetic resonance imaging (MRI) of the brain and spinal cord and cerebrospinal fluid examination [2], but these tests are invasive and expensive, so they are performed when there are evidences of the disease but not in a routine way. However, in the last years, different studies suggest that retinal optical coherence tomography (OCT) should be used as a complement to MRI for the analysis of neurodegeneration process in MS [3][4].

Following this line, many studies [5] have reported a correlation between axonal loss in the optic nerve of the retina and MS. The retina can be considered as an extension of the central nervous system (CNS) [6]; it consists of retinal ganglion cells (RGCs) and their axons, known as retinal nerve fiber layer (RNFL), which are in fact CNS axons form the optic nerve. Thus, various eye-specific pathologies share characteristics of other CNS pathologies. Inflammatory disorders, such as multiple sclerosis (MS), and degenerative diseases, such as Alzheimer's disease (AD) and Parkinson's disease (PD), also show pronounced axonal pathology. In fact, it is recognized that significant RGCs and RNFL loss occurs in patients with CNS pathologies. It has been demonstrated that in patients suffering from CNS diseases, the thickness of the RNFL significantly decreases as the disease goes on [7].

Loss of retinal ganglion cells can be detected using ocular imaging technologies such as optical coherence tomography (OCT). Petzold et al. [8] showed that neuroaxonal injury can be detected with OCT measuring RNFL and GCL thickness decrements relative to normal control subjects. OCT provides a noninvasive, rapid, objective and reproducible method for evaluating the different layers of the retina [7]. Specifically, the layers that are part of the central nervous system are the retinal ganglion cell (GCL+) and the retinal nerve fiber layer (RNFL). OCT allows for cross-sectional imaging of the retina and the optic disc based on interference patterns produced by low coherence light reflected from retinal tissues [9][10]. The first description of reduced peripapilary retinal nerve fiber layer thickness in MS patients was made by Parisi et al. [11] using older third generation time domain OCT. Since then, the evolution of these platforms has provided accurate segmentation processes to quantify discrete retinal layers [4]. Actually, the technique really improved when Fourier-domain versions of OCT were introduced. Two main variations of Fourier-domain OCT have been developed over the last years: spectral-domain OCT (SD-OCT) and swept-source OCT (SS-OCT). The difference between them comes from the mechanism employed to measure interference corresponding to different frequencies. There are several different SD–OCT machines commercially available, such as RTVue (Optovue, Fremont, CA, USA), Spectralis OCT (Heidelberg Engineering, Dossenheim, Germany), and Cirrus SD–OCT (Carl Zeiss Meditec, Dublin, CA, USA). Here, SS-deep range imaging (DRI) OCT Triton (Topcon, Tokyo, Japan) was used and the main protocols of this device were analyzed to evaluate their ability to diagnose MS.

OCT studies performed in MS patients have proved a significant thinning of both RNFL and ganglion cell–inner plexiform layer (GCL+) [4]. However, some authors [12] have demonstrated that GCL+ thickness measures have better reliability and reproducibility than RNFL thickness measures. More recently, Martinez-Lapiscina et al. [5] studied a large cohort of 879 patients with clinically isolated syndrome (CIS) of MS with baseline OCT and clinical follow-up. This study found that baseline RNFL thickness give a measure of the risk of disability progression.

In this paper we explore the use of machine learning techniques to detect the disease using data from SS-OCT. To the best of our knowledge, this is the first study evaluating MS eyes using swept source OCT technology in combination with machine learning techniques. Some preliminary studies [13][14] have analyzed the role of these techniques using specific protocols and other OCT devices. Here, different protocols obtained by DRI OCT Triton were analyzed and compared in order to specify the success ratio of different machine learning techniques for determining MS disease.

The final goal of this research is to obtain a simple classification algorithm that could be implemented in the OCT device software using only data from baseline visit. Thus, the OCT technique could be an easy, non-invasive and costless test that could be used in routine explorations in order to help neurologists in early detect MS disease.

Material and methods

Subjects and measurement protocol

The experimental protocol was approved by the Ethics Committee of the Miguel Servet Hospital, and all participants provided written informed consent to participate in this research. This study adhered to the tenets of the Declaration of Helsinki.

Two independent samples of 180 healthy controls (114 female and 66 male) and 80 patients (54 female and 26 male) with relapsing-remitting (RR) MS were prospectively recruited in this observational cross-sectional study. The diagnosis of MS was based on standard clinical and neuroimaging criteria: objective demonstration of dissemination of lesions in both time and space and magnetic resonance imaging is integrated with clinical and other paraclinical diagnostic methods [15]. Related medical records were carefully reviewed for information regarding disease duration, the Expanded Disability Status Scale (EDSS), disease-modifying treatments, acute MS attacks, and the presence of prior episodes of optic neuritis as reported by the treating neurologist and patient. The diagnosis of prior episodes of optic neuritis (ON) was based on clinical findings, which included the presence of decreased visual acuity, a visual field defect, color vision loss, relative afferent pupil defect and a compatible fundus examination [16].

Required inclusion criteria were as follows: best-corrected visual acuity (BCVA) of 20/40 or better, refractive error within ±5.00 diopters equivalent sphere and ±3.00 diopters astigmatism, transparent ocular media (nuclear color/opalescence, cortical or posterior subcapsular lens opacity <1) according to the Lens Opacities Classification System III system [17]. Exclusion criteria included previous intraocular surgery, diabetes or other diseases affecting the visual field or neurological system, and current use of medications that could affect visual function. All participants underwent a full ophthalmologic examination: clinical history, visual acuity, biomicroscopy of the anterior segment using a slit lamp, Goldmann applanation tonometry and ophthalmoscopy of the posterior segment. One eye from each patient/healthy control was randomly selected (excluding eyes with previous episodes of ON) [18].

A total of 258 eyes of white European origin (179 from healthy individuals and 79 from patients with MS) were included in the analysis.

Structural measurements of the retina were acquired using the DRI Triton SS-OCT device (Topcon, Tokyo, Japan), which is a multi-modal swept source OCT with a non-mydriatic color fundus camera. This device utilizes a 1,050 nm wavelength and reaches a scanning speed of 100,000 A-scans per second, with 8 and 20 μm axial and transverse resolution in tissue, respectively. The scan provides separate thickness measurements of different retinal layers: retinal nerve fiber layer (RNFL) (between the inner limiting membrane (ILM) to the ganglion cell layer boundaries), ganglion cell layer (GCL) + (between RNFL to the inner nuclear layer boundaries), GCL++ (between ILM to the inner nuclear layer boundaries), and retinal thickness (from the ILM to the retinal pigment epithelium boundaries). Here, OCT scans were performed to obtain measurements of the macular, peripapilar and macular-peripapilar RNFL and GCL+ thicknesses (see Fig 1) using three of the main protocols of DRI OCT Triton device: Wide protocol 3D(H) + 5 LineCross 12x9mm Overlap 8; Macular protocol 3D Macula(H) 7x7mm; and Peripapilar protocol 3D Disc 6x6mm. All scans were performed by the same experienced operator, who was blinded for presence or not of MS in each subject.

Data analysis

All variables were registered in a database created with Excel 2010 (Microsoft Corporation). Statistical analysis was performed using commercial predictive analytics software (SPSS, version 20.0; SPSS, Inc., Chicago, IL). The normality of the samples distribution (MS patients and healthy controls) was confirmed using the Kolmogorov–Smirnov test ($p>0.05$). Comparison between data from healthy controls and MS patients was performed for each age group and for each layer using a t-Student analysis. The mean and standard deviation values of RNFL and GCL+ thicknesses were compared between subjects using wide, macular and peripapilar protocols. To obtain the p-value in each test, the Levene test statistic was previously computed. A significant difference between groups was considered for $p<0.05$.

Machine learning algorithms

We evaluated the performance of the machine learning algorithms for classifying RNFL and GCL+ thickness measurements obtained with the DRI OCT Triton as MS or healthy. Machine learning algorithms are data mining tools used fundamentally to look for patterns in training sets of data; these algorithms learn these patterns and develop the ability to accurately classify new patterns. In this study, WEKA [19] software was used and several supervised learning models were used. The same inputs and outputs were introduced in all cases. As inputs, it was considered that there is one class for sex (female-male), one attribute for the patient age and so many attributes as grid boxes (each box contains RNFL or GCL+ thickness) depending on the analyzed protocol (see Fig 1). Every attribute was normalized before entering in the data mining tool. As output, only one class for classifying the disease (YES-MS, NO-HEALTHY) was used.

First, a feed-forward neural network trained by a back-propagation algorithm multilayer perceptron (MLP) was tested [20]. The structure of MLP is based on different layers of nodes or neurons. There is always an input layer with so many neurons as inputs of the model and an

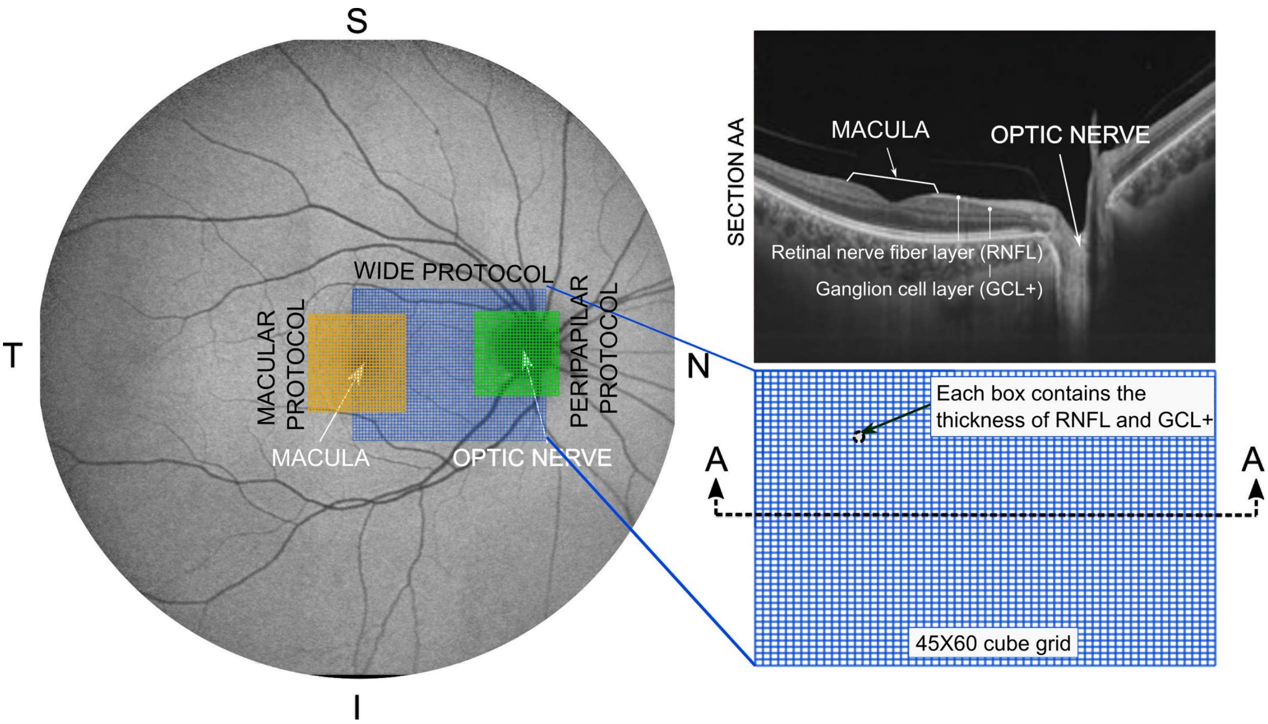

Fig 1. Schematic representation of the different analyzed protocols. The used protocols are shown on a retina image of a right eye (N: nasal; T: temporal; S: superior; I: inferior). The grid of the macular protocol is composed of 30x30 cubes centered in the fovea. The peripapilar protocol is centered in the optic nerve and it is composed of a 26x26 cube grid. A detail of the wide protocol which covers an area between macula and optic nerve using a 45x60 cube-grid is shown. The OCT software makes a scan of this area determining the thickness of the different retinal layers. In section AA, a cross section of the retina, where the retinal nerve fiber layer (RNFL) and the complex ganglion cell layer–inner plexiform layer (GCL+) are highlighted, is shown. For all cases, each box measures 200x200μm. As shown, each box contains the thickness of the different layers of the retina but in this work only data from RNFL and GCL+ were used.

https://doi.org/10.1371/journal.pone.0216410.g001

output layer with the same number of neurons as outputs. Furthermore, the hidden layer can be unique or several hidden layers can be defined. The structure of the MLP cannot be predefined and it highly depends on the problem to be solved. Here, the architecture of the MLP was different for each protocol, but the same rule was used to construct the hidden layer (only one hidden layer was considered). The number of neurons in the hidden layer was calculated using the following rule, number of neurons = (attributes + classes)/2.

The support vector machine (SVM) tools were also analyzed [21]. These tools are supervised learning models that analyze data used for classification and regression analysis. An SVM model is a representation of the different data as points in space, mapped so that the data of the separate categories (MS or healthy) are divided by a clear gap that is as wide as possible. Given a set of training examples, each marked as belonging to MS or healthy category, this machine learning algorithm develops a model that assigns new data to one category or the other. SVMs can efficiently perform a non-linear classification using what is called the kernel trick, implicitly mapping their inputs into high-dimensional feature spaces. In this research, different kernel functions were used: linear, polynomial, radial basis and sigmoid.

The ability of decision trees to accurately classify between healthy controls (HCs) and MS patients was investigated too. A decision tree is a flowchart-like structure in which each internal node represents a "test" on an attribute, each branch represents the outcome of the test, and each leaf node represents a class label (decision taken after computing all attributes). The paths from root to leaf represent classification rules. Here, C4.5 decision tree [22] and random forest [23] among others, were analyzed.

The above mentioned algorithms were also tested including an Attribute Classifier algorithm before. In order to find the importance of the attributes (or the inputs), feature selections algorithms are used. Thus, instead of processing all the attributes only relevant attributes are involved in the mining process. This kind of algorithms are designed to reduce the dimensionality, remove irrelevant and redundant data. Thus, in this case, only the most significant attributes fed the machine learning algorithm.

Finally, and taking into account that the data is very disperse among patients, the Adaptive Boosting (machine learning meta-algorithm) formulated by Freund and Schapire [24] was used in conjunction with the above mentioned learning algorithms to improve performance. Boosting is a general ensemble method that creates a strong classifier from a number of weak classifiers. In particular, AdaBoost is sensitive to noisy data and outliers. In some problems it can be less susceptible to the overfitting problem than other learning algorithms.

To compare among algorithms and combinations, a 10-fold cross validation resampling method was used. Cross validation is a technique to evaluate predictive models by partitioning the original sample into a training set to train de model and a test set to evaluate it. Here, all data were randomly divided into 10 subsets. Of the 10 subsets, a single subset is retained as the validation data for testing the model and the remaining 9 subsets are used as training data. The cross-validation is then repeated 10 times (the folds), with each of the 10 subsets used exactly once as the validation data. The 10 results from the folds are averaged to produce a single estimation. The prediction rate was analyzed as well as the receiver operating characteristic curve, i.e. ROC curve, a graph of a function that illustrates the diagnostic ability of a binary classifier system. The ROC curve is created by plotting the true positive rate (TPR) against the false positive rate (FPR) at various threshold settings. The true-positive rate is also known as sensitivity or probability of detection in machine learning.

Results

Subjects and measurement protocol

MS Seventy-nine eyes from relapsing-remitting (RR) MS patients with a mean age of 45.53 years (SD = 13), and 179 eyes from healthy individuals with a mean age of 49.02 years (SD = 15.34) were included in the study. Male/female ratio was 0.48 in the MS group and 0.57 in the control group. The intraocular pressure was 14.51±3.02 mm Hg in MS group and 14.77 ±2.87 mm Hg in healthy controls. Age, sex and intraocular pressure did not differ significantly between the groups (p = 0.222, 0.213, 0.520 respectively). Disease duration in the group of patients was 7.12 years (SD = 2.66). The median EDSS score was 2.52 (IQR = 0.53) and all patients suffered from relapsing-remitting MS subtype. All individuals in both cohorts were Caucasians.

Data analysis

The average thickness of the RNFL and GCL+ were computed for different age groups and for different protocols (see Fig 2 and Table 1). For an extended graphical information of the statistical analysis, refer to the Supplementary Material (S1 Fig).

Healthy persons and MS patients were distributed in four groups attending to their age. These groups were classified in the following form: G1: 20–34 years old; G2: 35–49 years old; G3: 50–64 years old and G4: 65–80 years old. Fig 2 shows the evolution of the average thickness for different age patients both for HCs and MS patients. It can be seen that the thickness for

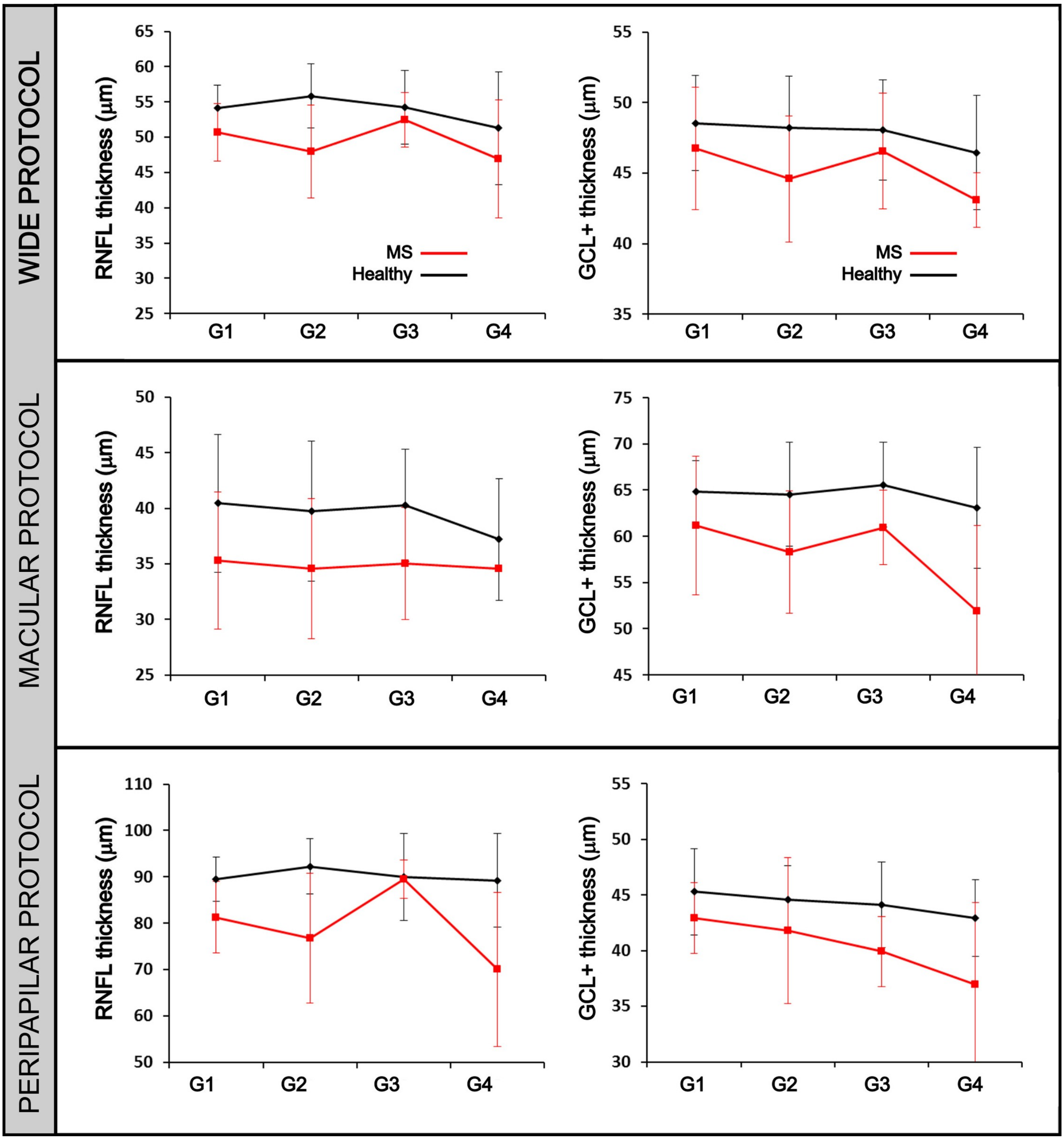

Fig 2. RNFL and GCL+ thickness data. Average retinal nerve fiber layer (RNFL) and complex ganglion cell layer–inner plexiform layer (GCL+) thicknesses for age group measured by different protocol.

https://doi.org/10.1371/journal.pone.0216410.g002

Table 1. Statistical analysis of the differences between healthy controls and MS patients in retinal layers thicknesses. P-value obtained by t-student test comparing the average thickness of RNFL and GCL+ of healthy controls (HC) and multiple sclerosis patients (MS) for each age group and different protocol. Mean and standard deviation thickness values shown in μm.

WIDE	**RNFL LAYER**							
PROTOCOL	G1		G2		G3		G4	
	HC	54.28±3.15	HC	55.61±4.46	HC	54.25±5.22	HC	51.19±8.10
	MS	50.70±4.05	MS	47.96±6.56	MS	52.44±3.88	MS	46.90±8.34
	p = 0.007		p = 0.0		p = 0.218		p = 0.194	
	GCL+ LAYER							
	G1		G2		G3		G4	
	HC	48.56±3.40	HC	48.06±3.67	HC	48.03±3.58	HC	46.39±4.10
	MS	46.75±4.34	MS	44.58±4.19	MS	46.55±3.99	MS	43.01±2.09
	p = 0.187		p = 0.001		p = 0.129		p = 0.059	
MACULAR	**RNFL LAYER**							
PROTOCOL	G1		G2		G3		G4	
	HC	40.59±3.95	HC	39.59±3.93	HC	40.31±4.32	HC	37.01±3.79
	MS	35.29±6.18	MS	34.57±6.30	MS	35.04±5.04	MS	34.60±5.46
	p = 0.035		p = 0.0		p = 0.005		p = 0.165	
	GCL+ LAYER							
	G1		G2		G3		G4	
	HC	64.85±3.39	HC	64.37±5.63	HC	65.60±4.60	HC	62.97±6.64
	MS	61.14±7.50	MS	58.30±6.61	MS	60.94±4.02	MS	51.88±9.29
	p = 0.182		p = 0.0		p = 0.003		p = 0.001	
PERIPAPILAR	**RNFL LAYER**							
PROTOCOL	G1		G2		G3		G4	
	HC	89.74±4.54	HC	91.89±5.68	HC	89.97±9.45	HC	89.09±10.29
	MS	81.26±7.71	MS	76.73±13.84	MS	89.46±4.10	MS	70.05±16.60
	p = 0.011		p = 0.0		p = 0.779		p = 0.004	
	GCL+ LAYER							
	G1		G2		G3		G4	
	HC	45.31±3.92	HC	44.55±3.10	HC	44.10±3.86	HC	42.93±3.50
	MS	42.93±3.17	MS	42.10±4.57	MS	39.93±3.15	MS	36.94±7.37
	p = 0.095		p = 0.01		p = 0.002		p = 0.018	

https://doi.org/10.1371/journal.pone.0216410.t001

both retinal layers was always smaller for MS patients than HCs for all ages. Moreover, while for HCs the same trend can be observed for both layers among age groups, MS patients showed an irregular behavior. The three analyzed protocols obtained similar results, a thinning of RNFL and GCL+ of MS patients for all age groups compared to the HCs.

Table 1 shows the results of the t-Student statistical analysis. P-values lesser than p = 0.05 are highlighted. It can be observed that more significant differences are obtained between HCs and MS patients for macular and peripapilar protocols than for wide protocol. Furthermore, both layers performed similarly. However, a more complex analysis should be performed to establish which measurement protocol and which layer would be the best to help in MS diagnosis.

Machine learning algorithms

Different machine learning algorithms were analyzed both for RNFL and GCL+. In this section, only the most relevant results are commented. For an extended information of the performance of other algorithms, refer to the Supplementary Material (S1 Table).

A schematic representation of the best performance of different algorithms for both layers is shown in Fig 3. In general, it can be seen that the best performance is obtained for the macular protocol using data of the RNFL. Wide protocol which covers a higher area between macula and papilla gives also a good prediction using RNFL data. However, the peripapilar area of the RNFL does not give valuable data for the machine learning algorithms to predict the disease. Although the accuracy is slightly better when using GCL+ data in this area, the value is not relevant (81%).

Analyzing in detail each protocol, the macular protocol (30x30 cube grid centered in the macula) using RNFL data resulted to be the best for predicting MS. Thus, the decision trees combined with an attribute classifier and Adaboost algorithm gave accuracies higher than 95%. In particular, the random forest obtained 97.24% precision. Conversely, ganglion cell layer would not be suitable to predict this disease in this area, since predictions were lower than 75%. Other machine learning algorithms (see supplementary material), as for example, support vector machines (SVM) give 91% accuracy. However, the accuracy of the decision trees was higher in all cases. Notwithstanding the fact that the random forest combined with other algorithms cannot be represented, a C4.5 decision tree has been included in the Supplementary material (S2 Fig) to show the classification process in a tree diagram.

With respect to the wide protocol, the same trend was obtained. Ganglion cell layer does not give enough information to construct powerful machine learning algorithms. However, decision trees present high accuracy to predict the disease using RNFL. The results are shown in Fig 3, and again the combination of attribute classifier, Adaboost algorithm and different decision trees gave accuracies higher than 92%. In detail, random forest had an accuracy of 93.38%.

Finally, as mentioned before, the peripapilar protocol resulted very weak in order to predict MS disease. Curiously, in this protocol obtained accuracies are better for GCL+ than RNFL, however they are still too low.

The confusion matrix was represented (Fig 4) for the best algorithm for each protocol (these are highlighted in Fig 3) in order to see the performance of the classification model. In our developments, there are two possible predicted classes: MS patient or HC. The confusion matrix represents the true positives (TP) and the false positives (FP), which means in how many cases the algorithm correctly or incorrectly classifies the MS patients. In the second row, the false negatives (FN) and true negatives (TN) are represented, which means how many times the class healthy is incorrectly/correctly classified. It can be seen that the ratio between FP and TP was lowest using the macular protocol for RNFL data.

Regarding to the receiving operating curve (ROC), again the best algorithms were selected and the ROC curve was plotted for each protocol (Fig 4). The ROC curve is created by plotting the true positive rate (TPR) against the false positive rate (FPR) at various thresholds settings. The ROC area was very high for wide (0.998) and for macular (0.995) protocols as can be seen on the right part of Fig 4. However, the ROC area was very low (0.775) for the peripapilar protocol.

On Table 2, different precision parameters are listed for the best algorithms highlighted on Fig 3. It can be seen that the best precision (when the algorithm predicts the disease, how often is correct) is achieved for the macular protocol and also the error rate is the lowest.

Finally, and attribute weighting algorithm was performed in order to stablish which areas of the retina are more significant to predict MS disease. Since only wide and macula protocols gave relevant results, this analysis has been performed only for these two protocols. The significance of each cube of the grid is reflected in Fig 5. It can be seen that the most significant part of the retina to detect the disease coincide with the macula in both protocols.

Discussion

Machine learning algorithms have a long history of development and successful application in many scientific fields, improving the ability of clinicians to predict patient outcome in different pathologies [25][26][27][28]. The goal of this work was to analyze the ability of these

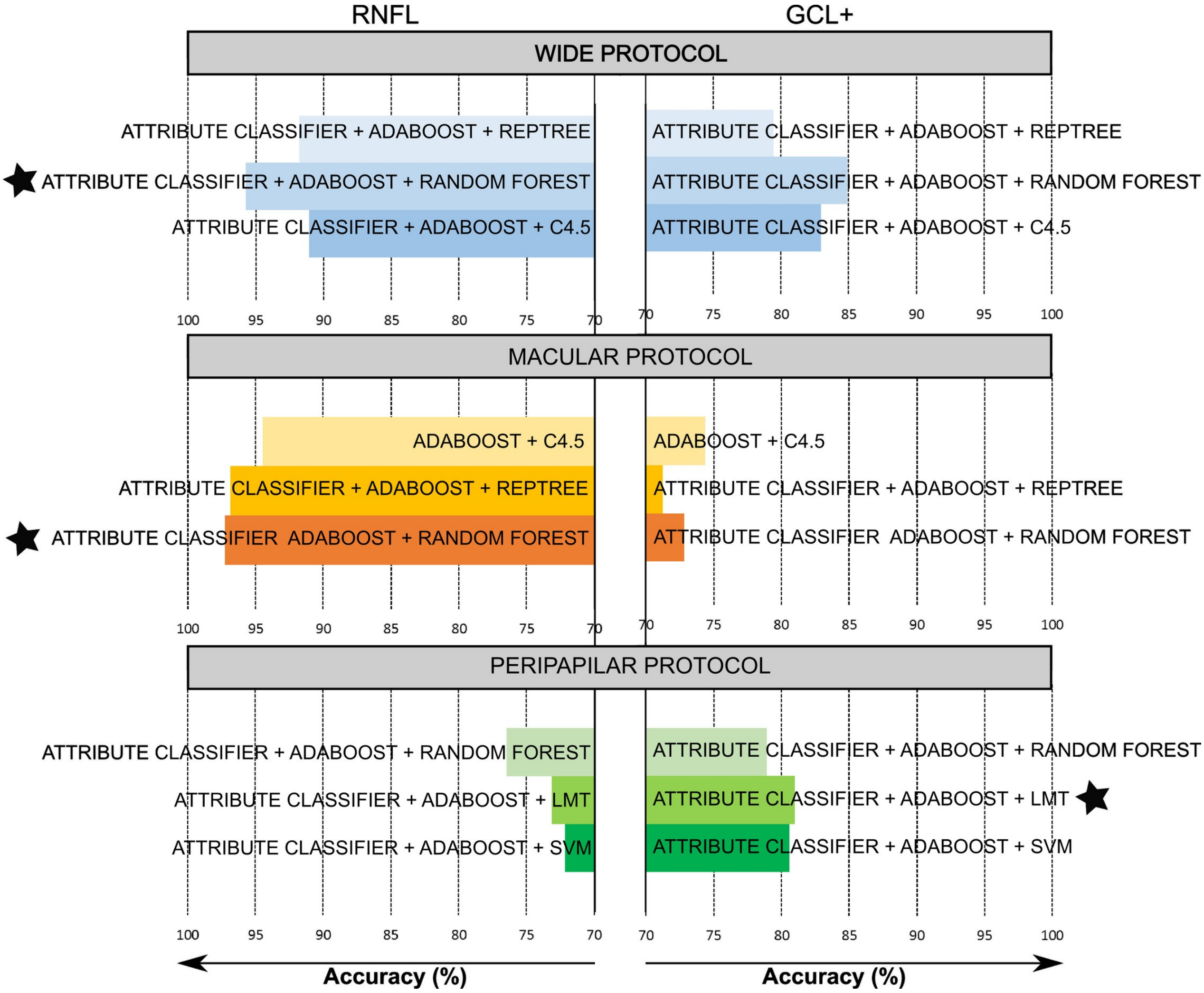

Fig 3. Accuracy of different machine learning algorithms to classify between healthy controls and multiple sclerosis patients. The accuracy of the different machine learning algorithms is shown for the different protocols and for each layer. On the left, results are presented for retinal nerve fiber layer (RNFL) and on the right for the complex ganglion cell layer–inner plexiform layer (GCL+). Only the best algorithms are shown for each analyzed protocol (wide protocol, macular protocol and peripapilar protocol). The results for different decision trees algorithms (RepTree: fast decision tree learner, Random Forest, C4.5 and LMT: logistic model tree) and support vector machine (SVM) are plotted. A star has been placed to highlight the best machine learning algorithm for each protocol.

https://doi.org/10.1371/journal.pone.0216410.g003

algorithms to classify between healthy controls and multiple sclerosis patients using SS-OCT data. For that, DRI OCT Triton was used and different protocols were studied to measure RNFL and GCL thicknesses.

Before data mining analysis, RNFL and GCL+ data were statistically treated in order to see differences between HCs and MS patients and among different age groups. It was observed that both layers were thinner in MS patients and this result was obtained for all age groups. These results are in accordance with previous investigations using spectral domain OCT [8][29][26][30]. However, differences between age groups have not been previously described. In

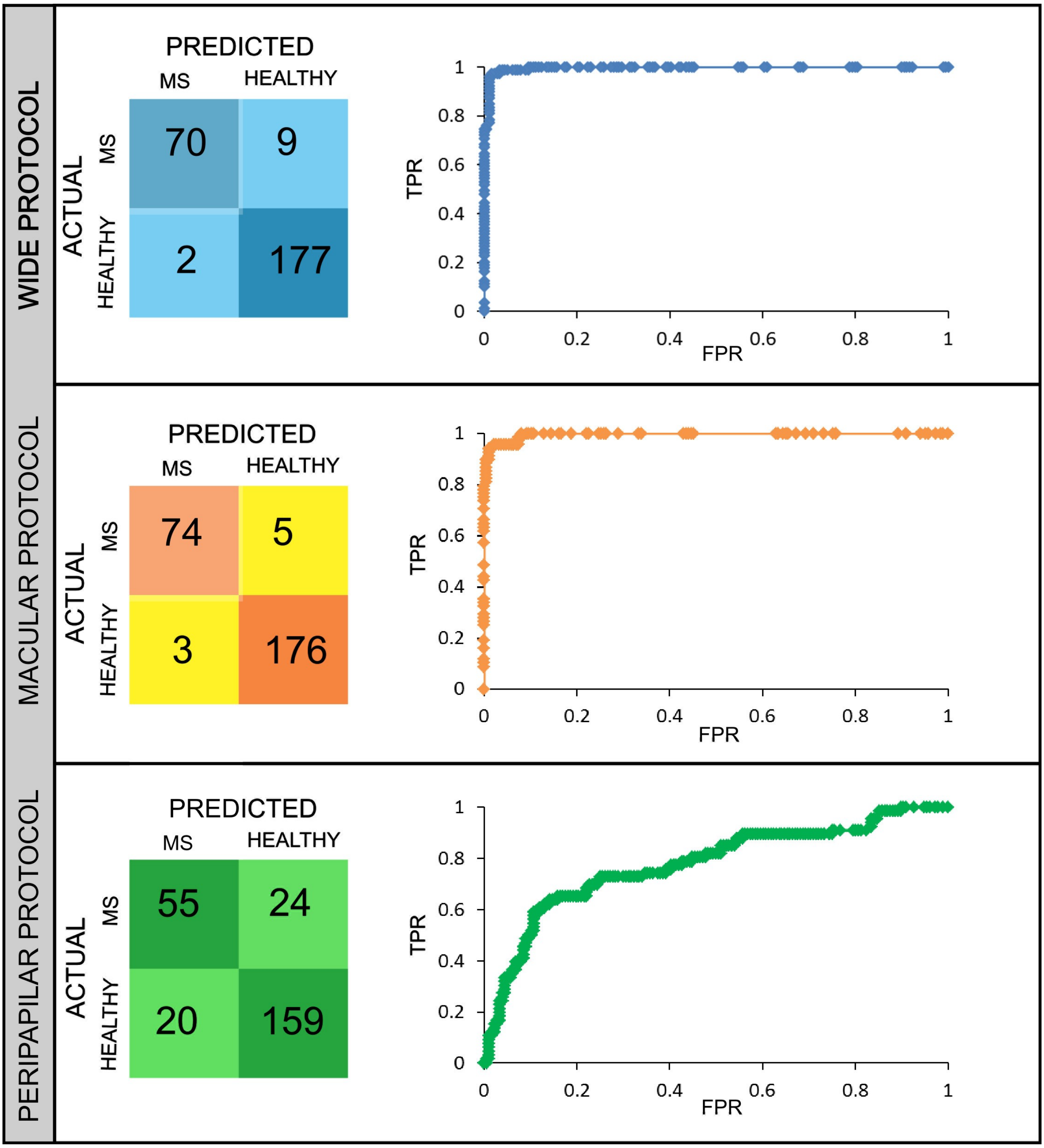

WIDE PROTOCOL

ACTUAL \ PREDICTED	MS	HEALTHY
MS	70	9
HEALTHY	2	177

MACULAR PROTOCOL

ACTUAL \ PREDICTED	MS	HEALTHY
MS	74	5
HEALTHY	3	176

PERIPAPILAR PROTOCOL

ACTUAL \ PREDICTED	MS	HEALTHY
MS	55	24
HEALTHY	20	159

Fig 4. Confusion matrix and ROC curve of the best algorithm for each protocol. On the left, confusion matrix is shown for wide, macular and peripapilar protocol. On the right, receiver-operating characteristic (ROC) curve [on the x-axis the false positive rate (FPR) and on the y-axis the true positive rate (TPR) are represented] for each protocol. In detail, for this representation, the random forest algorithm results have been selected for wide and macular protocol using retinal nerve fiber layer (RNFL) data. For peripapilar protocol, the logistic model tree (LMT) with GCL+ data has been chosen.

https://doi.org/10.1371/journal.pone.0216410.g004

Table 2. Different precision parameters are listed for each protocol. Only the best algorithms (highlighted in Fig 3) are shown. Accuracy is calculated as (TP+TN)/total; Sensitivity is TP/actual MS; Specificity as TN/actual Healthy; Precision as TP/predicted MS; Error rate as 1 –accuracy and Prevalence as Actual MS/total with total = TN + TP + FP + FN. Abbreviations: TP, true positives; TN, true negatives; FP, false positives; FN, false negatives; MS, multiple sclerosis.

PROTOCOL	ACCURACY	SENSITIVITY	SPECIFITY	PRECISION	ERROR RATE	PREVALENCE
Wide	95.74%	97.22%	95.16%	88.61%	4.26%	27.91%
Macular	97.24%	95.52%	97.86%	94.12%	2.76%	26.38%
Peripapilar	80.99%	67.24%	85.33%	59.09%	19.01%	23.97%

https://doi.org/10.1371/journal.pone.0216410.t002

our study, more significant differences were obtained between patients and controls using data from macular and peripapilar protocols than from wide protocol. For this comparison, average thickness and standard deviation was used and this simplification does not seem to be suitable when the analyzed region is large, as happens for wide protocol. Attending to age groups, significant differences in GCL+ thickness between groups were obtained for patients older than 35 years old, while for RNFL these differences were more significant for younger people (20–50 years old). Although this work is a cross-sectional study, these results seem to be in accordance with Petzold et al. [8] who observed that the highest annual atrophy rate was found in MS patients with shorter disease duration. Thus, these patients (groups 1 and 2) would have more intact neuroaxonal tissue to lose than patients with longer disease duration [31], and therefore the thickness reduction in patients from 20 to 50 years old would be more significant. In the same line, Balk et al. [10] demonstrated in a longitudinal study that injury in the

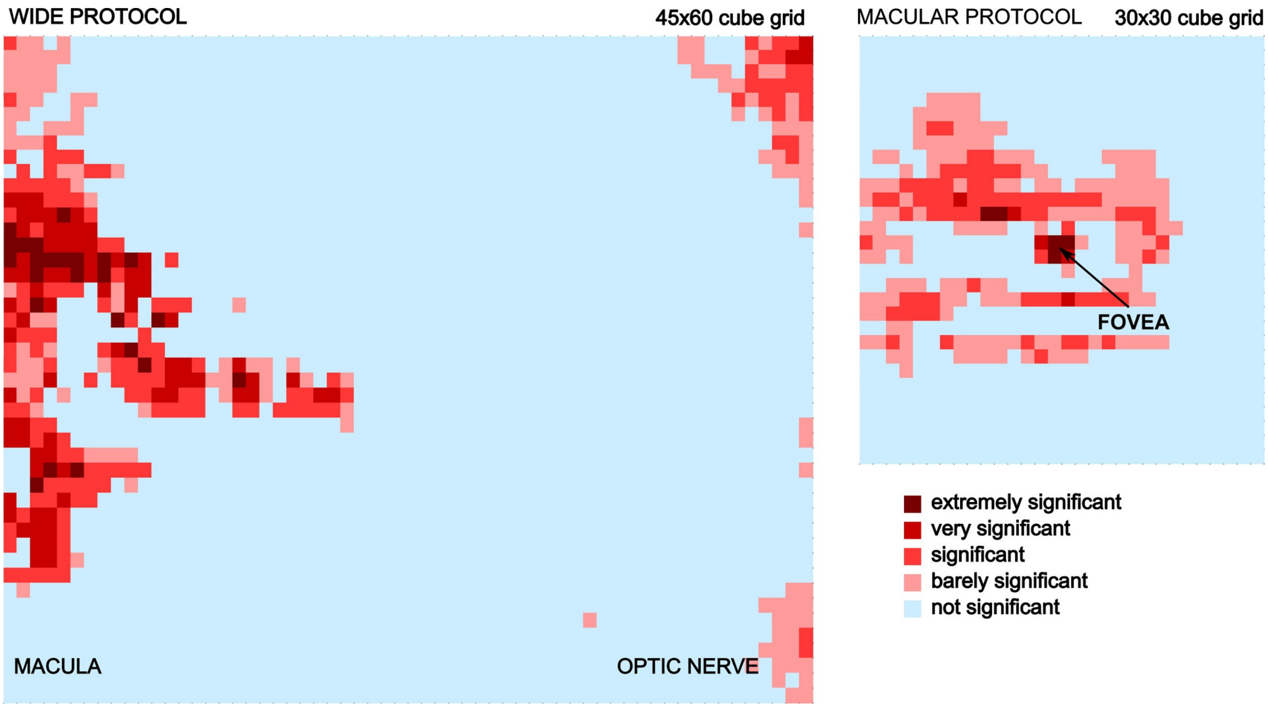

Fig 5. Significance of each cube of the grid for wide and macular protocols for retinal nerve fiber layer (RNFL) to predict multiple sclerosis (MS) disease. On the left the grid of the wide protocol is shown and the most significant areas to predict the disease located at the macula are plotted. On the right, the grid of the macular protocol is shown, and the fovea is highlighted as the most determinant area to detect the disease.

https://doi.org/10.1371/journal.pone.0216410.g005

innermost retinal layers is found in MS and that this damage occurs most rapidly during the early stages of disease. However, it seems clear that the differences between patients and controls are present in all age groups, and both RNFL and GCL+ thicknesses would give valuable information to predict MS disease.

To deeply investigate on these differences, different data mining algorithms were used. This analysis was made using three different protocols provided by DRI OCT Triton. DRI OCT Triton presents one advantage respect to other OCT devices. The information of retinal layers thickness is very precise since the values of the layer thickness is computed in each box of the grid. Thus, the information of each box can be used for the analysis and no average value has to be computed. The highest measure accuracy is obtained for denser grids with smallest box size (200μmx200μm). Therefore, the selected protocols were those centered in the macula (macular protocol), in the papilla (peripapilar protocol) and an extended one covering macular and papilla area (wide protocol). Only measures of RNFL and GCL+ were treated.

Different machine learning algorithms were used for each protocol, and different accuracies were obtained. However, the same two conclusions can be obtained. The first one, is that RNFL data provide more information to classify between MS and healthy patients than GCL + data. The second conclusion is that both macular and wide protocols are more useful for data mining analysis than peripapilar protocol.

In general, the best accuracy was obtained for the decision tree algorithms. As it can be seen in the supplementary material a wide range of algorithms have been tested for every protocol. For instance, Multilayer Perceptron does not give high accuracy (82.2% for macular protocol using RNFL data). On the other hand, support vector machines (SVM) are supposed to be the best binary classifiers because theoretically SVM get the best possible solution and avoid local minima related solutions. However, in our calculations, the highest SVM accuracy was 90.94% (for macular protocol using RNFL data) and ROC area of 0.931. These values are very far from decision tree results: 95.73% accuracy and 0.998 ROC area for wide protocol and 97.24% accuracy and 0.995 ROC area for macular protocol. These results were obtained using the random forest algorithm combined with Adaboost algorithm for both protocols. Although, this type of algorithm cannot be easily represented, S2 Fig shows a C4.5 decision tree for macular protocol using RNFL data. It can be appreciated which boxes of the grid are determinant to predict the disease, and it was obtained that only 8 boxes were used to obtain an accuracy of the classification algorithm of 92.92% and ROC Area of 0.934.

Attending to the best precision obtained, this was obtained for macular protocol using RNFL data, and with the combination of an attribute classifier, Adaboost algorithm and random forest algorithm. The use of Adaboost algorithm improves significantly the accuracy of the algorithms, in special of the decision trees.

As previously mentioned, macular area of the retinal nerve fiber layer provides relevant data to construct a classification between healthy and MS patients. Therefore, an analysis of which specific areas are more significant to predict the disease was performed. Fig 5 shows a color map indicating the most significant areas both for macular and wide protocols. It can be seen how the macular zone is determinant to detect MS disease. Furthermore, the significance of each cube of the grid can be analyzed, and the temporal and superior zones of the macula were very significant to predict the disease. These locations correspond to the location of small RGCs which are more susceptible to be damaged than larger ones [32]. Our results are totally in accordance with other works [33][34].

On the other hand, GCL+ did not contribute to predict MS and the different machine learning techniques performed worse in this layer than in RNFL. Although this result may result surprising since GCL+ thickness in MS patients has been shown to correlate better than RNFL thickness with EDSS score [12][31], it has been previously reported [29][35][36].

Notwithstanding the fact, that the thickness of both layers (RNFL and GCL+) decreases for MS patients (see Fig 2 and Table 1), in this work, the data mining process obtained more reliable rates when using RNFL data. Considering that, the purpose of this research is to construct a classifier to distinguish between MS patient or HC, the EDSS score was not considered as an input of the algorithm. Therefore, the possible relation between disease disability and GCL+ or RNFL thickness could not be taken into account.

In this work, an exhaustive evaluation of different machine learning algorithms was performed. This kind of research has only be made before using MRI data to predict MS course [37][38], and in these papers, SVM and k-nearest neighbors (kNN) respectively performed better than other classifiers. Our work is the first which analyses swept-source OCT data to classify between MS patients and healthy controls, and the decision trees performed as powerful classifiers. The quality of the data obtained by the OCT platforms is influenced by retinal pigment epithelium status and media opacity. In addition, swept-source OCT gives real thickness values in each grid box and therefore the number of inputs for the data mining process is higher than in spectral domain OCT measurements. Thus, the use of decision trees could correctly identify a high percentage of MS subjects. In our study, we selected only good-quality scans, but in clinical practice, this is not always possible. These limitations must be taken into account when interpreting OCT and data mining results.

We have found that the combination of some RNFL thickness measurements obtained with swept-source OCT provides high precision to detect the disease using machine learning algorithms. This can be considered as a practical tool to help clinicians for discriminating between normal and MS patients with early diagnosis or nondefinitive MS diagnosis. Here, promising results have been obtained, however, MS cohort has average disease duration of 7.12 years and therefore the classification between healthy controls and MS patients is easier than using only data from the onset of the disease. Thus, MS cohort should be modified in the future only considering patients with at least only one year of disease duration.

In spite of the relevant information that can be extracted from OCT measures, nowadays the diagnosis of MS is determined by a neurologist based on standard clinical and neuroimaging criteria (2017 Mc Donald criteria) [15]. Even though MRI is a reliable tool to diagnose MS, the definite diagnosis can take years since not every patient's symptoms and signs fit with McDonald criteria's parameters. Thus, without a single 'gold standard' diagnostic test, MS is a difficult disease to describe precisely. Moreover, there are new disease-modifying treatments (alemtuzumab, cladribina or ocrelizumab) that would help to stop MS progression and neural damage if an early diagnosis could be made. Several authors have proposed that MS diagnostic criteria should include OCT parameters [7] [9][39]. Our work confirms that the use of OCT parameters (specifically RNFL thickness) can predict the disease with a precision higher than 95%.

In conclusion, a review of MS diagnostic criteria, including RNFL measurements provided by OCT and machine learning analysis, may improve the sensitivity–specificity balance in diagnostic performance.

Supporting information

S1 Table. The accuracy and the receiver-operating characteristic (ROC) area obtained for different machine learning algorithms for wide, macular and peripapilar protocols. The following notation has been used: **AC**: Attribute classifier; **ADA**: Adaboost; **C4.5**: Decision Tree; **BAG**: Bagging; **DS**: Decision Stump; **HT**: Hoeffding Tree; **LMT**: Logistic model tree; **MLP**: Multilayer Perceptron; **RepTree**: Fast Decision Tree Learner; **RF**: Random Forest; **RT**: Random Tree; **SVM (C-SVC)**: Support Vector Machine with c value ranging from 0 to

infinity; **SVM (NU-SVC)**: Support Vector Machine with nu value ranging from 0 to 1.
(DOCX)

S1 Fig. Average RNFL and GCL+ thickness for healthy controls and MS patients. Average thickness of retina nerve fiber layer (RNFL) and the complex ganglion cell layer–inner plexiform layer (GCL+) for wide, macular and peripapilar protocols. On the left, data for the healthy patients are shown; on the right, data correspond to multiple sclerosis (MS) patients. The median and the quartiles are shown.
(TIF)

S2 Fig. Scheme of C4.5 decision tree using RNFL data to classify between healthy controls (HC) and multiple sclerosis (MS) patients. C4.5 decision tree for macular protocol (30x30 cube grid centered on the macula) using retinal nerve fiber layer (RNFL) data. The accuracy of the classification algorithm is 92.92% and receiver-operating characteristic (ROC) Area 0.934. It can be seen that the first test corresponds to the component 14_15 of the grid (shown on the right part of the picture), and the algorithm is able to predict 29 multiple sclerosis (MS) patients. The next level is constructed based on the value of the 10_13 box. Depending on this vale, two new branches appear. Continuing like this, the decision tree classifies healthy patients (H) and MS patients. The value of each attribute is normalized. It can be seen that the most significant box is 14_15 which corresponds to fovea location.
(TIF)

Acknowledgments

The authors would like to thank Dr. Tanima Bose for her helpful and constructive comments that greatly contributed to improving the final version of the paper.

Author Contributions

Conceptualization: Amaya Pérez del Palomar, José Cegoñino, Elvira Orduna, Elisa Vilades, Berta Sebastián, Luis E. Pablo, Elena Garcia-Martin.

Data curation: Amaya Pérez del Palomar, José Cegoñino, Alberto Montolío, Elvira Orduna, Elisa Vilades, Berta Sebastián, Luis E. Pablo, Elena Garcia-Martin.

Formal analysis: Amaya Pérez del Palomar, José Cegoñino, Alberto Montolío, Elvira Orduna, Elisa Vilades, Berta Sebastián, Luis E. Pablo, Elena Garcia-Martin.

Funding acquisition: Amaya Pérez del Palomar, José Cegoñino, Luis E. Pablo, Elena Garcia-Martin.

Investigation: Amaya Pérez del Palomar, José Cegoñino, Alberto Montolío, Elvira Orduna, Elisa Vilades, Luis E. Pablo, Elena Garcia-Martin.

Methodology: Amaya Pérez del Palomar, José Cegoñino, Alberto Montolío, Elena Garcia-Martin.

Project administration: Amaya Pérez del Palomar, José Cegoñino, Elena Garcia-Martin.

Resources: Amaya Pérez del Palomar, José Cegoñino, Elena Garcia-Martin.

Software: Amaya Pérez del Palomar, José Cegoñino, Elena Garcia-Martin.

Supervision: Amaya Pérez del Palomar, José Cegoñino, Elvira Orduna, Elisa Vilades, Berta Sebastián, Luis E. Pablo, Elena Garcia-Martin.

Validation: Amaya Pérez del Palomar, José Cegoñino, Alberto Montolío, Berta Sebastián, Luis E. Pablo, Elena Garcia-Martin.

Visualization: Amaya Pérez del Palomar, José Cegoñino, Alberto Montolío, Berta Sebastián, Elena Garcia-Martin.

Writing – original draft: Amaya Pérez del Palomar, José Cegoñino.

Writing – review & editing: Amaya Pérez del Palomar, José Cegoñino, Elena Garcia-Martin.

References

1. Joy JE, Johnston R. Multiple Sclerosis. Current status and strategies for the future. Washington: National Academy Press; 2001. 1–413 p.
2. Rovira À, Swanton Jo, Tintoré M, Huerga E, Barkhof F, Filippi M, et al. A Single, Early Magnetic Resonance Imaging Study in the Diagnosis of Multiple Sclerosis. Arch Neurol [Internet]. 2009 May 1; 66 (5):587–92. Available from: http://archneur.jamanetwork.com/article.aspx?doi=10.1001/archneurol.2009.49 PMID: 19433658
3. Alonso R. Optical coherence tomography as a biomarker of neurodegeneration in multiple sclerosis: A review. Mult Scler Relat Disord [Internet]. 2018; 22(December 2017):77–82. Available from: https://doi.org/10.1016/j.msard.2018.03.007 PMID: 29605802
4. Lambe J, Murphy OC, Saidha S. Can Optical Coherence Tomography Be Used to Guide Treatment Decisions in Adult or Pediatric Multiple Sclerosis? Curr Treat Options Neurol [Internet]. 2018 Mar 21; 20 (4):9. Available from: http://link.springer.com/10.1007/s11940-018-0493-6 PMID: 29564662
5. Martinez-Lapiscina EH, Arnow S, Wilson JA, Saidha S, Preiningerova JL, Oberwahrenbrock T, et al. Retinal thickness measured with optical coherence tomography and risk of disability worsening in multiple sclerosis: A cohort study. Lancet Neurol [Internet]. 2016; 15(6):574–84. Available from: http://dx.doi.org/10.1016/S1474-4422(16)00068-5 PMID: 27011339
6. London A, Benhar I, Schwartz M. The retina as a window to the brain—from eye research to CNS disorders. Nat Rev Neurol [Internet]. 2012 Nov 20; 9:44. Available from: https://doi.org/10.1038/nrneurol.2012.227 PMID: 23165340
7. Satue M, Obis J, Rodrigo MJ, Otin S, Fuertes MI, Vilades E, et al. Optical Coherence Tomography as a Biomarker for Diagnosis, Progression, and Prognosis of Neurodegenerative Diseases. J Ophthalmol. 2016; 2016.
8. Petzold A, Balcer LJ, Calabresi PA, Costello F, Frohman TC, Frohman EM, et al. Retinal layer segmentation in multiple sclerosis: a systematic review and meta-analysis. Lancet Neurol. 2017; 16:797–812. https://doi.org/10.1016/S1474-4422(17)30278-8 PMID: 28920886
9. Serbecic N, Aboul-Enein F, Beutelspacher SC, Vass C, Kristoferitsch W, Lassmann H, et al. High Resolution Spectral Domain Optical Coherence Tomography (SD-OCT) in Multiple Sclerosis: The First Follow Up Study over Two Years. Kleinschnitz C, editor. PLoS One [Internet]. 2011 May 17; 6(5):e19843. Available from: https://dx.plos.org/10.1371/journal.pone.0019843 PMID: 21611198
10. Balk LJ, Cruz-Herranz A, Albrecht P, Arnow S, Gelfand JM, Tewarie P, et al. Timing of retinal neuronal and axonal loss in MS: a longitudinal OCT study. J Neurol. 2016; 263(7):1323–31. https://doi.org/10.1007/s00415-016-8127-y PMID: 27142714
11. Parisi V, Manni G, Spadaro M, Colacino G, Restuccia R, Marchi S, et al. Correlation between morphological and functional retinal impairment in multiple sclerosis patients. Investig Ophthalmol Vis Sci. 1999; 40(11):2520–7.
12. Saidha S, Syc SB, Durbin MK, Eckstein C, Oakley JD, Meyer SA, et al. Visual dysfunction in multiple sclerosis correlates better with optical coherence tomography derived estimates of macular ganglion cell layer thickness than peripapillary retinal nerve fiber layer thickness. Mult Scler J [Internet]. 2011 Aug 24; 17(12):1449–63. Available from: https://doi.org/10.1177/1352458511418630
13. Garcia-Martin E, Pablo LE, Herrero R, Ara JR, Martin J, Larrosa JM, et al. Neural networks to identify multiple sclerosis with optical coherence tomography. Acta Ophthalmol. 2013; 91(8):628–34.
14. Garcia-Martin E, Herrero R, Bambo MP, Ara JR, Martin J, Polo V, et al. Artificial Neural Network Techniques to Improve the Ability of Optical Coherence Tomography to Detect Optic Neuritis. Semin Ophthalmol [Internet]. 2015 Jan 2; 30(1):11–9. Available from: http://www.tandfonline.com/doi/full/10.3109/08820538.2013.810277 https://doi.org/10.3109/08820538.2013.810277 PMID: 23952910
15. Thompson AJ, Banwell BL, Barkhof F, Carroll WM, Coetzee T, Comi G, et al. Diagnosis of multiple sclerosis: 2017 revisions of the McDonald criteria. Lancet Neurol. 2018; 17(2):162–73. https://doi.org/10.1016/S1474-4422(17)30470-2 PMID: 29275977

16. Garcia-Martin E, Pueyo V, Ara JR, Almarcegui C, Martin J, Pablo L, et al. Effect of optic neuritis on progressive axonal damage in multiple sclerosis patients. Mult Scler J [Internet]. 2011; 17(7):830–7. Available from: https://doi.org/10.1177/1352458510397414
17. Chylack LT, Wolfe JK, Singer DM, Leske MC, Bullimore MA, Bailey IL, et al. The Lens Opacities Classification System III. The Longitudinal Study of Cataract Study Group. Arch Ophthalmol (Chicago, Ill 1960) [Internet]. 1993 Jun 1; 111(6):831–6. Available from: http://dx.doi.org/10.1001/archopht.1993.01090060119035
18. Armstrong RA. Statistical guidelines for the analysis of data obtained from one or both eyes. Ophthalmic Physiol Opt. 2013; 33:7–14. https://doi.org/10.1111/opo.12009 PMID: 23252852
19. Witten IH, Frank E, Hall MA, Pal CJ. Data Mining, Fourth Edition: Practical Machine Learning Tools and Techniques. 4th ed. San Francisco, CA, USA: Morgan Kaufmann Publishers Inc.; 2016.
20. Baum EB. On the capabilities of multilayer perceptrons. J Complex [Internet]. 1988 Sep; 4(3):193–215. Available from: http://linkinghub.elsevier.com/retrieve/pii/0885064X88900209
21. Cortes C, Vapnik V. No Title. Mach Learn [Internet]. 1995; 20(3):273–97. Available from: http://link.springer.com/10.1023/A:1022627411411
22. Quinlan JR. C4.5: Programs for Machine Learning. San Mateo, Californmia: Morgan Kaufman Publishers; 1993. 299 p.
23. Breiman L. Random Forests. Mach Learn. 2001; 45:5–32.
24. Freund Y, Schapire RE. A Decision-Theoretic Generalization of On-Line Learning and an Application to Boosting. J Comput Syst Sci [Internet]. 1997 Aug; 55(1):119–39. Available from: http://link.springer.com/10.1007/3-540-59119-2_166
25. Cruz JA, Wishart DS. Applications of machine learning in cancer prediction and prognosis. Cancer Inform. 2006; 2:59–77.
26. Kruppa J, Ziegler A, König IR. Risk estimation and risk prediction using machine-learning methods. Hum Genet. 2012; 131(10):1639–54. https://doi.org/10.1007/s00439-012-1194-y PMID: 22752090
27. Kourou K, Exarchos TP, Exarchos KP, Karamouzis MV., Fotiadis DI. Machine learning applications in cancer prognosis and prediction. Comput Struct Biotechnol J [Internet]. 2015; 13:8–17. Available from: http://dx.doi.org/10.1016/j.csbj.2014.11.005 PMID: 25750696
28. Weng SF, Reps J, Kai J, Garibaldi JM, Qureshi N. Can Machine-learning improve cardiovascular risk prediction using routine clinical data? PLoS One [Internet]. 2017; 12(4):1–14. Available from: http://dx.doi.org/10.1371/journal.pone.0174944
29. Garcia-Martin E, Polo V, Larrosa JM, Marques ML, Herrero R, Martin J, et al. Retinal layer segmentation in patients with multiple sclerosis using spectral domain optical coherence tomography. Ophthalmology [Internet]. 2014; 121(2):573–9. Available from: http://dx.doi.org/10.1016/j.ophtha.2013.09.035 PMID: 24268855
30. Jankowska-Lech I, Wasyluk J, Palasik W, Terelak-Borys B, Grabska-Liberek I. Peripapillary Retinal Nerve Fiber Layer Thickness Measured by Optical Coherence Tomography in Different Clinical Subtypes of Multiple Sclerosis. Mult Scler Relat Disord [Internet]. 2018 Nov; Available from: https://linkinghub.elsevier.com/retrieve/pii/S2211034818304887
31. Costello F, Burton J. Retinal imaging with optical coherence tomography: a biomarker in multiple sclerosis? Eye Brain [Internet]. 2018 Jul; Volume 10:47–63. Available from: http://www.ncbi.nlm.nih.gov/pubmed/30104912%0Ahttp://www.pubmedcentral.nih.gov/articlerender.fcgi?artid=PMC6074809%0Ahttps://www.dovepress.com/retinal-imaging-with-optical-coherence-tomography-a-biomarker-in-multi-peer-reviewed-article-EB https://doi.org/10.2147/EB.S139417 PMID: 30104912
32. Evangelou N, Konz D, Esiri MM, Palace J, Matthews PM, Smith S, et al. Size-selective neuronal changes in the anterior optic pathways suggest a differential susceptibility to injury in multiple sclerosis. Brain [Internet]. 2001; 124(Pt 9):1813–20. Available from: internal-pdf://251.0.9.69/Evangelou et al. 2001. Size-selective neuronal.pdf PMID: 11522583
33. Fjeldstad C, Bemben M, Pardo G. Reduced retinal nerve fiber layer and macular thickness in patients with multiple sclerosis with no history of optic neuritis identified by the use of spectral domain high-definition optical coherence tomography. J Clin Neurosci [Internet]. 2011 Nov; 18(11):1469–72. Available from: http://dx.doi.org/10.1016/j.jocn.2011.04.008 PMID: 21917458
34. Birkeldh U, Manouchehrinia A, Hietala MA, Hillert J, Olsson T, Piehl F, et al. The Temporal Retinal Nerve Fiber Layer Thickness Is the Most Important Optical Coherence Tomography Estimate in Multiple Sclerosis. Front Neurol [Internet]. 2017 Dec 13; 8(DEC). Available from: http://journal.frontiersin.org/article/10.3389/fneur.2017.00675/full
35. Britze J, Jette GP, Frederiksen L. Retinal ganglion cell analysis in multiple sclerosis and optic neuritis: a systematic review and meta-analysis. J Neurol. 2017; 264(9):1837–53. https://doi.org/10.1007/s00415-017-8531-y PMID: 28567539

36. Cipres Alastuey M, Vilades Palomar E, Garcia Martín E, Satué M, Rodrigo MJ, Obis Alfaro J. Retinal nerve fiber layer measurements in multiple sclerosis patients using new Swetpt-Source Optical coherence tomography Triton device. Acta Ophthalmol [Internet]. 2016 Oct 14; 94(S256). Available from: https://doi.org/10.1111/j.1755-3768.2016.0586

37. Zhao Y, Healy BC, Rotstein D, Guttmann CRG, Bakshi R, Weiner HL, et al. Exploration of machine learning techniques in predicting multiple sclerosis disease course. PLoS One [Internet]. 2017; 12(4): e0174866. Available from: http://www.ncbi.nlm.nih.gov/pubmed/28379999%0Ahttp://www.pubmedcentral.nih.gov/articlerender.fcgi?artid=PMC5381810 PMID: 28379999

38. Zhang Y, Lu S, Zhou X, Yang M, Wu L, Liu B, et al. Comparison of machine learning methods for stationary wavelet entropy-based multiple sclerosis detection: decision tree, k -nearest neighbors, and support vector machine. Simulation [Internet]. 2016 Sep 5; 92(9):861–71. Available from: https://doi.org/10.1177/0037549716666962

39. Martínez-Lapiscina EH, Fraga-Pumar E, Gabilondo I, Martínez-Heras E, Torres-Torres R, Ortiz-Pérez S, et al. The multiple sclerosis visual pathway cohort: understanding neurodegeneration in MS. BMC Res Notes [Internet]. 2014; 7(1):910. Available from: http://bmcresnotes.biomedcentral.com/articles/10.1186/1756-0500-7-910

2.2.2 MS diagnosis and prognosis using Cirrus HD-OCT

Manuscript 3: Machine learning in diagnosis and disability prediction of multiple sclerosis using optical coherence tomography

Alberto Montolío, Alejandro Martín-Gallego, José Cegoñino, Elvira Orduna, Elisa Vilades, Elena Garcia-Martin, Amaya Pérez del Palomar

Abstract

Background

Multiple sclerosis (MS) is a neurodegenerative disease that affects the central nervous system, especially the brain, spinal cord, and optic nerve. Diagnosis of this disease is a very complex process and generally requires a lot of time. In addition, treatments are applied without any information on the disability course in each MS patient. For these two reasons, the objective of this study was to improve the MS diagnosis and predict the long-term course of disability in MS patients based on clinical data and retinal nerve fiber layer (RNFL) thickness, measured by optical coherence tomography (OCT).

Material and methods

A total of 104 healthy controls and 108 MS patients, 82 of whom had a 10-year follow-up, were enrolled. Classification algorithms such as multiple linear regression (MLR), support vector machines (SVM), decision tree (DT), k-nearest neighbours (k-NN), Naïve Bayes (NB), ensemble classifier (EC) and long short-term memory (LSTM) recurrent neural network were tested to develop two predictive models: MS diagnosis model and MS disability course prediction model.

Results

For MS diagnosis, the best result was obtained using EC (accuracy: 87.7%; sensitivity: 87.0%; specificity: 88.5%; precision: 88.7%; AUC: 0.8775). In line with this good performance, the accuracy was 85.4% using k-NN and 84.4% using SVM. And, for long-term prediction of MS disability course, LSTM recurrent neural network was the most appropriate classifier (accuracy: 81.7%; sensitivity: 81.1%; specificity: 82.2%; precision: 78.9%; AUC: 0.8165). The use of MLR, SVM and k-NN also showed a good performance (AUC ≥ 0.8).

Conclusions

This study demonstrated that machine learning techniques, using clinical and OCT data, can help establish an early diagnosis and predict the course of MS. This ad-

vance could help clinicians select more specific treatments for each MS patient. Therefore, our findings underscore the potential of RNFL thickness as a reliable MS biomarker.

Computers in Biology and Medicine 133 (2021) 104416

Contents lists available at ScienceDirect

Computers in Biology and Medicine

journal homepage: www.elsevier.com/locate/compbiomed

Machine learning in diagnosis and disability prediction of multiple sclerosis using optical coherence tomography

Alberto Montolío [a,b], Alejandro Martín-Gallego [a,b], José Cegoñino [a,b], Elvira Orduna [c,d], Elisa Vilades [c,d], Elena Garcia-Martin [c,d], Amaya Pérez del Palomar [a,b,*]

[a] Group of Biomaterials, Aragon Institute of Engineering Research (I3A), University of Zaragoza, Zaragoza, Spain
[b] Department of Mechanical Engineering, University of Zaragoza, Zaragoza, Spain
[c] Ophthalmology Department, Miguel Servet University Hospital, Zaragoza, Spain
[d] GIMSO Research and Innovative Group, Aragon Institute for Health Research (IIS Aragon), Zaragoza, Spain

ARTICLE INFO

Keywords:
Multiple sclerosis
Machine learning
Optical coherence tomography
Retinal nerve fiber layer
Expanded disability status scale

ABSTRACT

Background: Multiple sclerosis (MS) is a neurodegenerative disease that affects the central nervous system, especially the brain, spinal cord, and optic nerve. Diagnosis of this disease is a very complex process and generally requires a lot of time. In addition, treatments are applied without any information on the disability course in each MS patient. For these two reasons, the objective of this study was to improve the MS diagnosis and predict the long-term course of disability in MS patients based on clinical data and retinal nerve fiber layer (RNFL) thickness, measured by optical coherence tomography (OCT).

Material and methods: A total of 104 healthy controls and 108 MS patients, 82 of whom had a 10-year follow-up, were enrolled. Classification algorithms such as multiple linear regression (MLR), support vector machines (SVM), decision tree (DT), k-nearest neighbours (k-NN), Naïve Bayes (NB), ensemble classifier (EC) and long short-term memory (LSTM) recurrent neural network were tested to develop two predictive models: MS diagnosis model and MS disability course prediction model.

Results: For MS diagnosis, the best result was obtained using EC (accuracy: 87.7%; sensitivity: 87.0%; specificity: 88.5%; precision: 88.7%; AUC: 0.8775). In line with this good performance, the accuracy was 85.4% using k-NN and 84.4% using SVM. And, for long-term prediction of MS disability course, LSTM recurrent neural network was the most appropriate classifier (accuracy: 81.7%; sensitivity: 81.1%; specificity: 82.2%; precision: 78.9%; AUC: 0.8165). The use of MLR, SVM and k-NN also showed a good performance (AUC $\geq$ 0.8).

Conclusions: This study demonstrated that machine learning techniques, using clinical and OCT data, can help establish an early diagnosis and predict the course of MS. This advance could help clinicians select more specific treatments for each MS patient. Therefore, our findings underscore the potential of RNFL thickness as a reliable MS biomarker.

1. Introduction

Multiple sclerosis (MS) is a neurodegenerative disease characterized by inflammation, demyelination, and axonal degeneration in the central nervous system (CNS) [1,2]. Diagnosis of MS is a slow and complicated process, since the most commonly used diagnostic approach is mainly based on excluding other diseases using paraclinical methods that are often prolonged, costly, and invasive [3].

While axonal loss is considered the main cause of functional disability in MS patients [4], detection of axonal damage is challenging. Magnetic resonance imaging (MRI) is used to detect inflammation and lesions [5], but is not sufficiently sensitive or specific to reveal the extent and severity of axonal damage [6]. The incorporation of cerebrospinal fluid (CSF) analysis into the McDonald criteria [3] for MS diagnosis increased diagnostic sensitivity but also decreased specificity and accuracy. Moreover, CSF analysis is highly invasive owing to the need for lumbar puncture to collect CSF samples. Another complementary test is evoked potential (EP) monitoring, which measures electrical activity induced in parts of the brain in response to light, sound and touch. The main disadvantages of EP are the length of time taken (about 2 h) and

---

[*] Corresponding author. Escuela de Ingeniería y Arquitectura. Campus Río Ebro, Edificio Betancourt. C/Maria de Luna s/n, 50018, Zaragoza, Spain.
E-mail address: amaya@unizar.es (A.P. Palomar).

https://doi.org/10.1016/j.compbiomed.2021.104416
Received 27 December 2020; Received in revised form 25 March 2021; Accepted 16 April 2021

remaining doubts among clinicians as to whether the observed CNS alterations are specifically due to MS or to other conditions [3].

A faster alternative method for the diagnosis and monitoring of MS based on the assessment of axonal damage in the neuroretina has recently emerged [7–9]. The most recent optical coherence tomography (OCT) techniques allow specific measurement of the thickness of the retinal nerve fiber layer (RNFL) and even the ganglion cell layer (GCL) [10–12]. Thinning of these layers, which are not covered by myelin, constitutes a direct readout of axonal damage [7,13,14].

Studies have shown that RNFL thickness, measured by OCT, is a useful parameter to distinguish MS patients from healthy controls [4,15]. Garcia-Martin et al. [4,16] used an artificial neural network (ANN) in combination with OCT data to diagnose MS. Pérez del Palomar et al. [17] also demonstrated that machine learning techniques, specially decision tree (DT), combined with OCT data could be used to diagnose this disease. In the same vein, Cavaliere et al. [18] test the usefulness of support vector machine (SVM) in the MS diagnosis. Recently, another study compared the ability of SVM and feed-forward neural networks to detect MS using OCT recordings, and reported satisfactory results [19].

Next, the authors assessed the potential of machine learning techniques to predict the disease course in MS patients, which would help clinicians select patient-specific treatments [20]. Zhao et al. [21] evaluated the utility of SVM and logistic regression to predict the progression of MS-associated disability using brain MRI data acquired over 5 years. In another study, MRI data were also used to predict short-term disease progression using parallel convolutional pathways [22]. The work performed by Yperman et al. [23] analysed random forests and logistic regression to predict disability progression after 2 years using EP time series. Pinto et al. [24] trained classifiers such as linear regression, k-nearest neighbours (k-NN), DT and SVM to predict the progression of the disease severity after 6 and 10 years. To do that, these authors used data obtained by MRI, CSF analysis and EP. The study conducted by Seccia et al. [25] incorporated the Liquor analysis in testing different machine learning approaches to predict the course of MS in the short term.

It can be seen that most of the works limited the data to those obtained by means of the common tests included in McDonald criteria. Only a few authors have used the RNFL thickness to predict the disability course in MS patients, and they approached it from traditional statistical analysis. Rothman et al. [10] evaluated the capability of OCT data to predict the disability status 10 years later in 172 MS patients, applying linear regression models. Bsteh et al. [26,27] conducted a 3-year longitudinal study on 151 MS patients with RNFL measurements and tested also a linear regression model to predict the physical and cognitive disability progression. Following this work, these authors demonstrated that retinal thinning is associated with disability progression independent of relapse activity [28].

However, to date no studies have examined the use of machine learning techniques and RNFL data for long-term prediction of MS disease course. In this study, we tested several classification algorithms to develop a predictive model using OCT data obtained from 82 MS patients over 10 years of follow-up. Our goal was to verify RNFL thickness as MS biomarker and know in advance the progression of MS-associated disability using machine learning techniques instead of traditional statistical analysis.

2. Material and methods

2.1. Study population

Our cohort consisted of 108 MS patients and 104 healthy controls from the Miguel Servet University Hospital (Zaragoza, Spain) who underwent evaluations by ophthalmologists to perform OCT measurements and, in case of MS patients, by neurologists to determine their expanded disability status cale (EDSS) score. Moreover, a longitudinal study was carried out in 82 of these 108 MS patients who completed a total of seven visits: a baseline visit, 5 annual follow-up visits and a final visit at 10 years. From these 212 subjects of white European origin, one eye from each subject was randomly selected [29]. The diagnosis of MS was based on standard clinical and neuroimaging criteria (i.e. objective demonstration of lesions in both time and space) [30]. This study was performed in accordance with the Declaration of Helsinki and the protocol was approved by the Aragon Ethics Committee for Clinical Research (CEICA). All subjects provided written informed consent before inclusion in the study.

Table 1

Clinical characteristics of healthy controls and multiple sclerosis (MS) patients, and retinal nerve fiber layer (RNFL) thickness measured by Cirrus high definition optical coherence tomography (HD-OCT) at baseline visit. P-value, based on Student's *t*-test, shows the significance of the comparison between healthy controls and MS patients. Statistically significant differences ($p < 0.05$) are represented in bold. (BCVA: best-corrected visual acuity; RRMS: relapsing-remitting multiple sclerosis; SPMS: secondary-progressive multiple sclerosis; PPMS: primary-progressive multiple sclerosis; EDSS: expanded disability status scale).

	Healthy controls (n = 104)	MS patients (n = 108)	P-value
Visit 0			
General parameters			
Age [years]	40.74 ± 13.13	43.16 ± 10.95	0.146
Sex (M − F)	35–69	34–74	
BCVA [Snellen]	0.84 ± 0.38	0.91 ± 0.28	0.127
OCT parameters – RNFL thickness			
Peripapillary thickness [µm]	100.16 ± 10.09	86.08 ± 16.10	**<0.001**
Superior thickness [µm]	125.63 ± 16.70	108.67 ± 20.84	**<0.001**
Nasal thickness [µm]	74.70 ± 15.95	71.69 ± 17.04	0.186
Inferior thickness [µm]	130.45 ± 17.69	109.99 ± 26.90	**<0.001**
Temporal thickness [µm]	69.51 ± 13.69	55.60 ± 14.82	**<0.001**
Foveal thickness [µm]	235.46 ± 42.26	271.94 ± 28.52	**<0.001**
MS parameters			
MS duration [years]	-	10.15 ± 8.30	
MS subtype (RRMS – SPMS – PPMS)	-	85–17–6	
Optic neuritis antecedent (Yes – No)	-	34–74	
Relapse in preceding year (Yes – No)	-	32–76	
EDSS score	-	2.65 ± 1.97	

The following inclusion criteria were applied: best-corrected visual acuity (BCVA) of 20/40 or higher; refractive error within ±5.00 diopters equivalent sphere and ±2.00 diopters astigmatism; and transparent ocular media (nuclear color/opalescence, cortical or posterior subcapsular lens opacity <1), according to the Lens Opacities Classification System III [31]. Exclusion criteria included prior intraocular surgery, diabetes or other diseases affecting the visual field or nervous system, and ongoing use of medications that could affect visual function.

Clinical data can be divided into general parameters and MS parameters. Age, sex and BCVA were considered as general parameters. For MS patients, MS duration, MS subtype (relapsing-remitting [RRMS], secondary-progressive [SPMS] and primary-progressive [PPMS]), optic neuritis antecedent, relapses in the preceding year and EDSS score were also recorded (see Table 1). These features, in combination with RNFL thicknesses, were the inputs of our predictive models, since they may significantly influence the classification decision [15,32].

2.2. OCT protocol

Cirrus HD-OCT (model 4000; Carl Zeiss Meditec, Dublin, CA, USA) is a digital retinal imaging technology used to monitor axonal loss in MS patients. Depending on the protocol used, RNFL thickness can be measured in different areas of the retina: the peripapillary area (around the optic nerve) or the macular area (around the fovea). Specifically, we used the Optic Disc Cube 200 × 200 study protocol, which generates

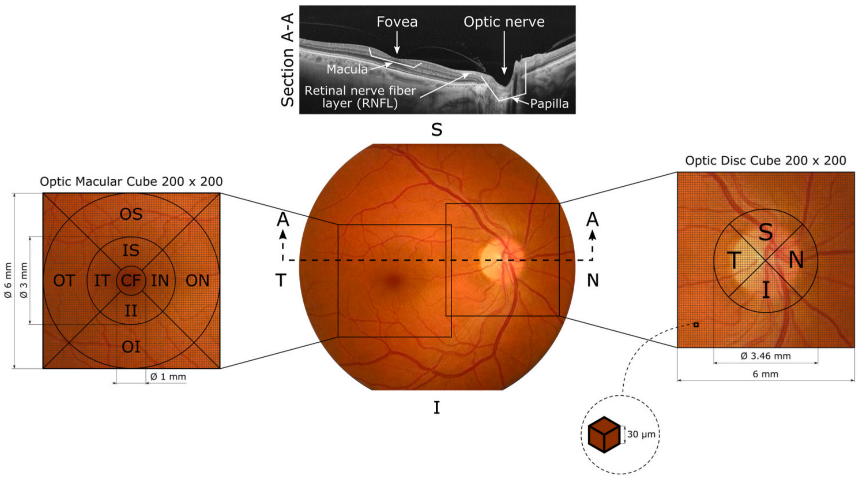

Fig. 1. Schematic representation of the protocols used to measure the retinal nerve fiber layer (RNFL) thickness. Middle: cross section of a right eye retina to indicate the location of the optical coherence tomography (OCT) protocols in the macula and in the peripapillary area. Left: Optic Macular cube 200 × 200 based on early treatment diabetic retinopathy study (ETDRS) grid to measure 9 macular areas (CF: central fovea; IS: inner superior; IN: inner nasal; II: inner inferior; IT: inner temporal; OS: outer superior; ON: outer nasal; OI: outer inferior; OT: outer temporal). Right: Optic Disc Cube 200 × 200 to analyse peripapillary area and 4 quadrants into which this area is divided (S: superior; N: nasal; I: inferior; T: temporal).

200 × 200 cube images enabling analysis of a 6 mm^3 volume around the optic nerve (Fig. 1). The OCT system automatically identifies the centre of the papilla and creates a circle-shaped sweep of 3.46 mm in diameter. This protocol calculates mean RNFL thickness by first determining the values corresponding to each of 4 quadrants into which the peripapillary area is divided (superior, nasal, inferior and temporal). In addition, we used the Macular Cube 200 × 200 study protocol, which scans an area of 6 × 6 mm covering the macula. As can be seen in Fig. 1, early treatment diabetic retinopathy study (ETDRS) grid is automatically centered on the fovea with fovea finder. With this grid, 9 macular areas can be measured (central fovea, inner superior, inner nasal, inner inferior, inner temporal, outer superior, outer nasal, outer inferior and outer temporal). However, for this study only foveal thickness was collected.

The image quality of the OCT device is based on the signal strength measurement, which combines the signal-to-noise ratio with the uniformity of the signal within a scan. The quality score ranges from 0 (poor) to 10 (excellent). Only images with a quality score of ≥7 were included in our analysis.

2.3. Machine learning

The performance of different classification algorithms for classifying between healthy controls and MS patients, and for predicting disability course of MS patients was tested. These algorithms were implemented using the Statistics and Machine Learning Toolbox and Deep Learning Toolbox in Matlab (version R2020b, Mathworks Inc., Natick, MA).

2.3.1. Data preprocessing

First, the dataset was divided into two subgroups: one to build the algorithm (training set) and another to validate it (validation set). The normalization used for numerical features begins with the training set normalization (mean of 0 and standard deviation of 1) and continues with the validation set normalization using mean and standard deviation from the training set. This procedure implies that algorithms do not have access to future information. Since machine learning algorithms need to work with numerical features, the categorical features (sex, MS subtype, optic neuritis antecedent and relapse in preceding year) were encoded into numerical values using one-hot encoding [33].

2.3.2. Feature selection

In machine learning, a rule of the thumb is to have a number of cases per class of at least ten times the number of features. Therefore, feature selection was used in order to reduce the risk of overfitting and increase the model interpretability [34]. To do this selection, two method were tested: sequential forward selection (SFS) and least absolute shrinkage and selection operator (LASSO).

SFS method attempts to minimize an objective function, the misclassification rate for classification models, over all feasible subsets of features. To do this, this sequential search algorithm adds features while evaluating the criterion until the addition of more features does not decrease the criterion. SFS is widely used for its simplicity and speed [35].

LASSO regression imposes a constraint on the model features that produces regression coefficients for some of these features to shrink toward zero taking into account the output of the model. Features with a regression coefficient equal to zero after the shrinkage process were removed from the dataset. By contrast, features with non-zero regression coefficients are strongly associated with the output [36,37].

2.3.3. Classifiers

We tested several algorithms to analyse which one works best with our data. For each model, the optimal hyperparameters of the different classifiers were determined by hyperparameter optimization. This optimization attempts to minimize the cross-validation loss by varying the hyperparameters.

2.3.3.1. Multiple linear regression. Multiple linear regression (MLR) is used to model the linear relationship between a dependent variable (response) and one or more independent variables (predictors). It is necessary that the independent variables are not highly correlated with each other. In case of two independent variables are highly correlated, only one of them should be used [38].

2.3.3.2. Support vector machine. Support vector machine is a robust binary classifier that calculates the optimal hyperplane separating different data classes [39]. This algorithm uses kernel functions to increase the dimension of original data, increasing the possibility of hyperplane separability for non-separable problems [40]. For separable classes, the optimal hyperplane maximizes the space that does not contain any observations. For non-separables classes, the objective is the same, but the algorithm imposes a penalty for each observation that is on the wrong side, which helps to prevent overfitting. This penalty factor is represented by C and is called box constraint. In a dual optimization problem, the Lagrange multipliers are bounded to be within the range [0, C], so C poses a box constraint. The kernel function was linear with a fixed value of kernel scale, the classifier divides all inputs by this value. Then, the algorithm applies the appropriate kernel norm to compute the Gram matrix. Using this procedure, SVM finds the

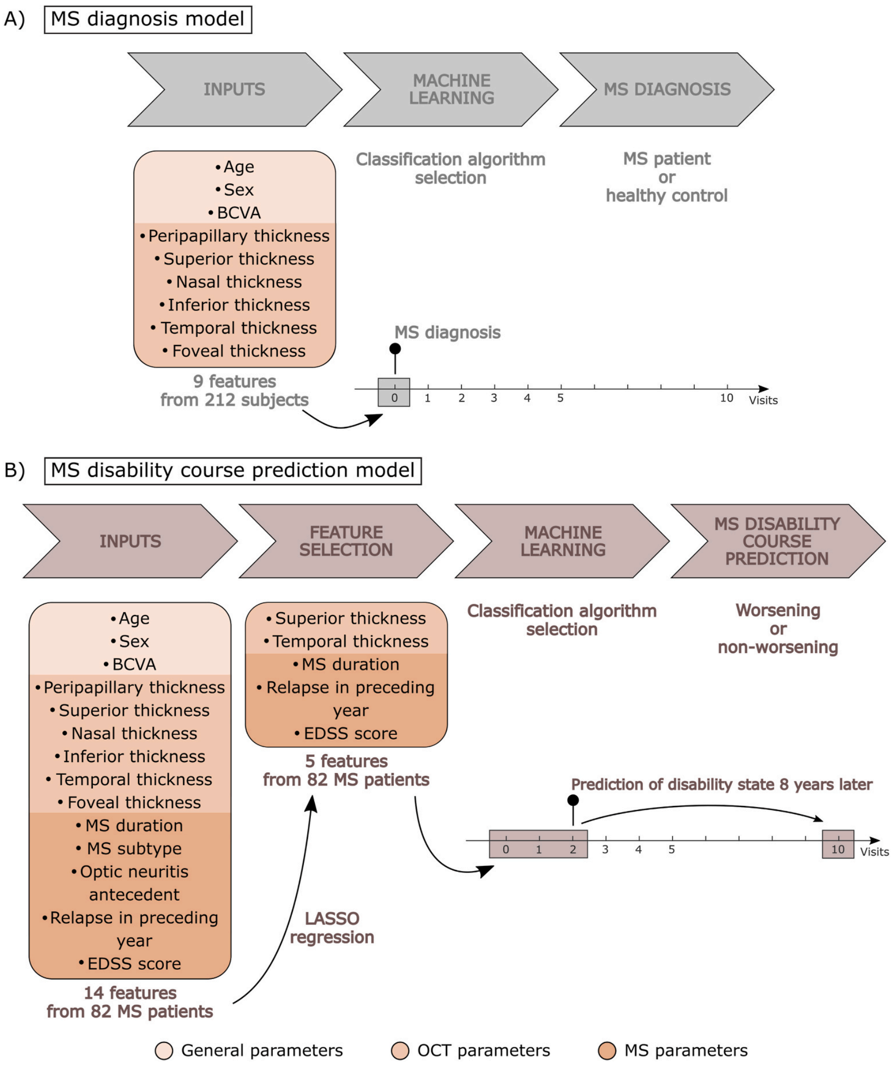

Fig. 2. Schematic diagram of the inputs and outputs of the predictive models. A) Model for diagnosis of multiple sclerosis (MS). The input data consists of 9 features from 108 MS patients and 104 healthy controls at the baseline visit. B) Model to predict the evolution of disability state. The input data consists of 5 features from 82 MS patients at the baseline visit and the first two annual follow-up visits. These 5 features were selected after applying a feature selection by least absolute shrinkage and selection operator (LASSO) regression algorithm.

optimal hyperplane in the transformed predictor space.

2.3.3.3. Decision tree. A decision tree classifier is composed of a root node, several internal nodes and several leaf nodes. The root node and the internal nodes include the test conditions of the features to distinguish between subjects having different qualities. The algorithm uses entropy to evaluate the degree of homogeneity of the sample. The construction of decision tree consists of finding a feature that returns the highest information gain [41]. As hyperparameters to control the depth of the trees, it is necessary to set the minimum number of leaf node observations and the minimum number of branch observations.

2.3.3.4. K-nearest neighbours. This algorithm classifies data according to the class of their nearest neighbours. K-NN classification consists of 2 stages: determination of the nearest neighbours and determination of the class based on those neighbours [42]. In this algorithm, the number of nearest neighbours and the distance metric between neighbours were the hyperparameters to optimize the structure. The number of neighbours it is very important because a very small number of these could be too sensitive to noise, which would increase the risk of overfitting.

2.3.3.5. Naïve Bayes. Naïve Bayes (NB) classifier applies density estimation to the data according to Bayesian theory, which assumes that predictors are conditionally independent [39,43]. There are several data distributions (kernel smoothing density estimation, multinomial, multivariate multinomial or normal) to model the data. One of the most used is kernel density estimation, this distribution is defined by a smoothing parameter called bandwidth. The bandwidth selection defines the smoothness of the density plot. A small bandwidth leads to undersmoothing and a huge bandwidth lead to oversmoothing. Therefore, it is preferable to choose a bandwidth as small as the dataset allows. However, there should be a balance between the bias of the estimator and its variance.

2.3.3.6. Ensemble classifier. Ensemble classifier (EC) is a combination of multiple learning algorithms to allow a more flexible structure, obtaining a better performance [44]. The EC used here was boosting with several classification trees, so that each individual model learns from mistakes made by the previous one. For this binary classification, LogitBoost was the ensemble aggregation algorithm for training the ensemble of boosted classification trees using adaptive logistic regression [45]. The optimization searched over the number of ensemble

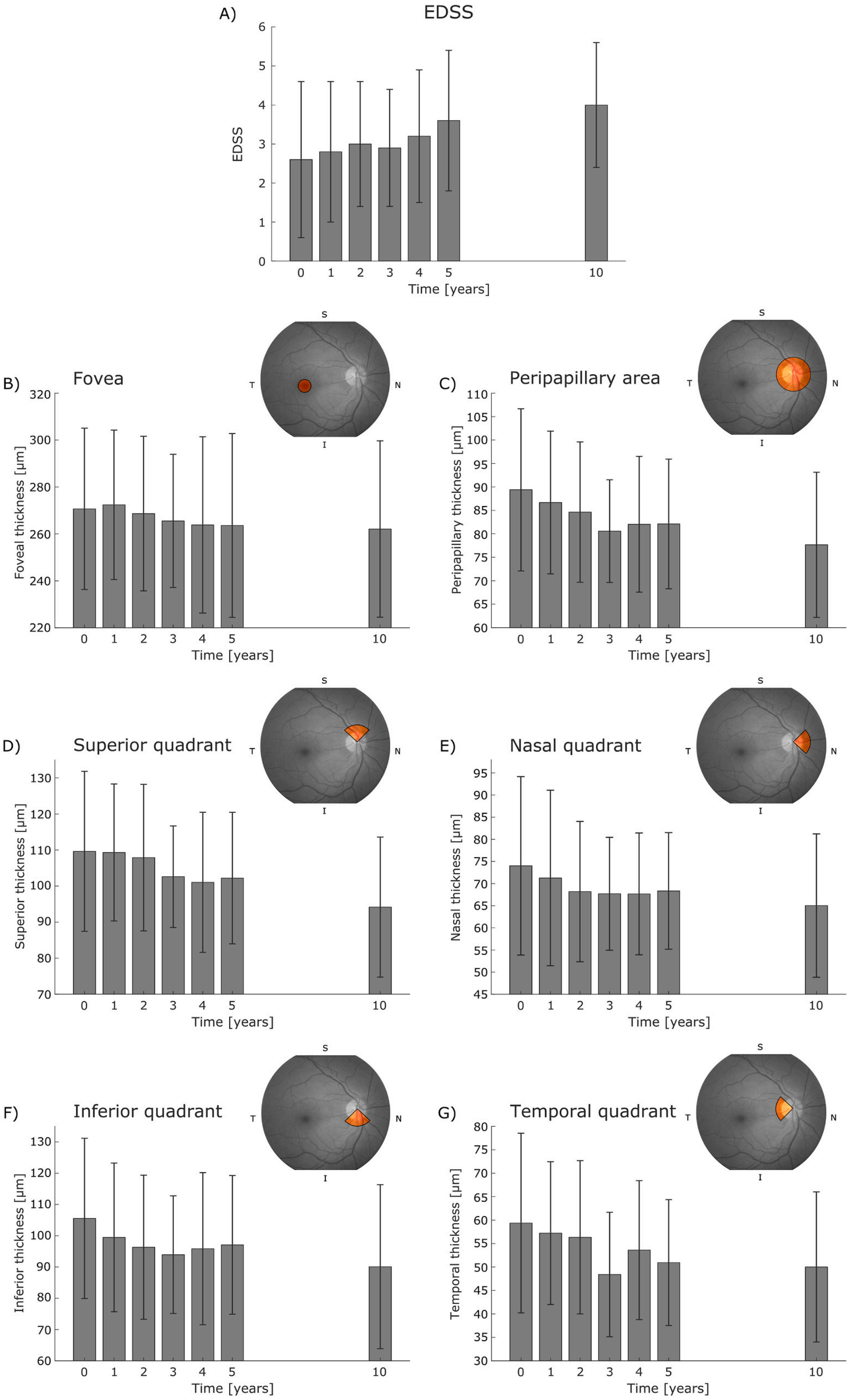

Fig. 3. A) Evolution of expanded disability status scale (EDSS) score from 82 patients with multiple sclerosis over 10 years of follow-up. B-G) Evolution of retinal nerve fiber layer (RNFL) thickness, which was analysed in the fovea and in the peripapillary area by optical coherence tomography (OCT), using Cirrus HD-OCT device, over the 10-year follow-up. Peripapillary area is divided into 4 quadrants (S: superior; N: nasal; I: inferior; T: temporal).

Table 2
Clinical characteristics and retinal nerve fiber layer (RNFL) measurements of both multiple sclerosis (MS) patient populations (non-worsening and worsening) at visits 0, 1 and 2. P-value, based on Student's *t*-test, shows the significance of the comparison between non-worsening patients and worsening patients. Statistically significant differences ($p < 0.05$) are represented in bold. (BCVA: best-corrected visual acuity; OCT: optical coherence tomography; RRMS: relapsing-remitting multiple sclerosis; SPMS: secondary-progressive multiple sclerosis; PPMS: primary-progressive multiple sclerosis; EDSS: expanded disability status scale).

	Non-worsening (n = 45)	Worsening (n = 37)	P-value	Non-worsening (n = 45)	Worsening (n = 37)	P-value	Non-worsening (n = 45)	Worsening (n = 37)	P-value
	Visit 0			Visit 1			Visit 2		
General parameters									
Age [years]	45.10 ± 11.01	39.16 ± 9.29	**0.011**	46.64 ± 10.98	40.38 ± 9.24	**0.007**	47.85 ± 11.50	41.50 ± 8.26	**0.006**
Sex (M – F)	15–30	12–25		15–30	12–25		15–30	12–25	
BCVA [Snellen]	0.91 ± 0.26	0.90 ± 0.29	0.920	0.89 ± 0.28	0.90 ± 0.30	0.944	0.89 ± 0.27	0.89 ± 0.29	0.984
OCT parameters – RNFL thickness									
Peripapillary thickness [µm]	84.88 ± 15.69	94.09 ± 16.05	**0.011**	80.81 ± 13.68	90.19 ± 14.32	**0.003**	77.46 ± 12.70	86.84 ± 12.89	**0.001**
Superior thickness [µm]	103.89 ± 22.69	116.78 ± 18.47	**0.007**	102.56 ± 18.09	114.68 ± 17.18	**0.003**	97.12 ± 18.05	112.24 ± 17.62	**<0.001**
Nasal thickness [µm]	70.24 ± 19.43	73.68 ± 17.54	0.408	65.46 ± 16.13	70.59 ± 19.20	0.192	62.91 ± 13.86	67.78 ± 14.34	0.123
Inferior thickness [µm]	113.16 ± 20.94	121.14 ± 26.99	0.136	105.96 ± 20.37	115.57 ± 23.92	0.053	101.62 ± 19.31	110.22 ± 21.22	0.059
Temporal thickness [µm]	53.71 ± 15.64	64.78 ± 16.75	**0.003**	49.36 ± 13.97	61.59 ± 12.46	**<0.001**	47.82 ± 13.85	56.41 ± 13.69	**0.006**
Foveal thickness [µm]	278.60 ± 30.49	279.86 ± 25.85	0.842	274.87 ± 23.61	280.81 ± 25.73	0.842	266.31 ± 23.88	268.84 ± 29.64	0.670
MS parameters									
MS duration [years]	12.98 ± 9.06	6.70 ± 5.72	**<0.001**	14.40 ± 9.14	7.82 ± 5.68	**<0.001**	15.62 ± 9.33	9.05 ± 5.71	**<0.001**
MS subtype (RRMS – SPMS – PPMS)	40–5–0	36–0–1		40–5–0	36–0–1		40–5–0	36–0–1	
Optic neuritis antecedent (Yes – No)	14–31	11–26		14–31	11–26		14–31	11–26	
Relapse in preceding year (Yes – No)	9–36	11–26		2–43	9–28		4–40	7–30	
EDSS score	3.52 ± 2.02	1.58 ± 1.27	**<0.001**	3.64 ± 2.03	1.65 ± 1.56	**<0.001**	4.04 ± 2.13	1.88 ± 1.68	**<0.001**

learning cycles, over the learning rate for shrinkage and over the minimum number of leaf node observations. The learning rate shrinks the contribution of each new classification tree that is added in the series. The output of this optimization was the EC with the minimum estimated cross-validation loss.

2.3.3.7. *Long short-term memory.*

Long short-term memory (LSTM) is a supervised recurrent neural network, characterized by implementation memory, which can be used to classify sequential data [46]. A bidirectional LSTM layer learns bidirectional long-term dependencies between time steps of sequence data. These dependencies help the network learn from the complete time series at each time step. In this study, LSTM models were trained using back-propagation through time to predict the disability evolution using the time series of the 10-year follow-up. The architecture of the LSTM network consists of 5 layers. The network starts with a sequence input layer, which inputs the time series data into the network, followed by a bidirectional LSTM layer with several hidden units. The number of hidden layers corresponds to the information that is remembered between time steps. The network ends with a fully connected layer, a softmax layer and a classification output layer. The size of the input layer corresponds to the number of features of the input data. The size of the fully connected layer is the number of classes. The softmax layer is a function that converts a vector of real values into a vector of real values that sum to 1, so that they can be interpreted as probabilities. In this way, the scores are converted into a normalized probability distribution, which can be displayed to a user.

The stochastic gradient descent algorithm evaluates the gradient and updates the parameters at each iteration using a subset of the training data, called mini-batch. The complete passage of the training algorithm over the entire training set using mini-batches is an epoch. A sensitivity analysis was performed to determine the value of the adjustable parameters (hidden layers, epochs and mini-batch size). This sensitivity analysis consisted of performing several experiments to know whether the results change when something changes in the way the data analysis is approached. To determine the optimal value of each parameter, it was varied while the rest of the parameters were left fixed.

2.3.4. *Cross-validation*

Since our dataset was not very large, the use of hold-out validation would not be appropriate. As is well known in machine learning, the smaller the data, the higher the probability of overfitting. In this respect, cross-validation was used to minimize the risk of overfitting. Furthermore, k-fold cross-validation ensures that the final results were independent of the initial division [45]. This method consists of dividing the initial dataset into k groups, using k-1 groups to train the algorithm and the remaining group to validate it. The validation group changes k times and the final precision is determined by computing the mean precision of these k validation groups. Following the general consensus in the data mining community, 10-fold cross-validation was performed since this method constitutes an effective compromise between accuracy and computational cost [47].

2.3.5. *Model performance*

Confusion matrix and receiver operating characteristic (ROC) curve were generated in order to quantify the predictive performance of each model. In this way, accuracy, sensitivity, specificity and precision were determined. The area under the curve (AUC) was used to select the best machine learning algorithm. Classifier performance was quantified based on the AUC as follows: excellent (0.9–1), good (0.8–0.9), moderate (0.7–0.8) and fair (<0.7). Moreover, false positives (FP) and false negatives (FN) were analysed to identify which input data were more critical for a misclassification.

2.4. *MS diagnosis model*

This first model was developed to validate the use of RNFL thickness as MS biomarker. It can be said that our dataset is balanced since there are almost the same number of healthy controls and MS patients. Data from 108 MS patients and 104 healthy controls collected at the baseline visit (visit 0) were used. These data were general parameters and OCT

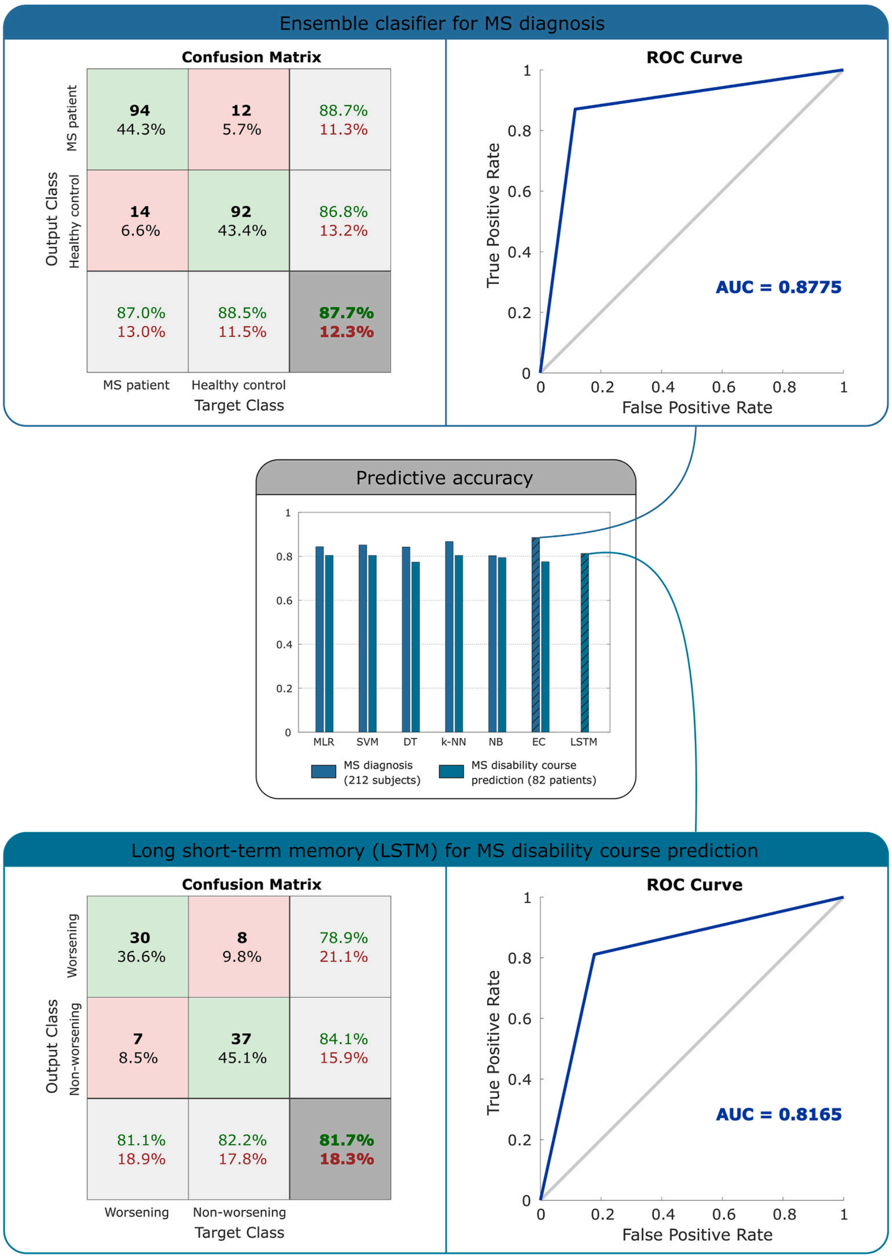

Fig. 4. Confusion matrix and receiver operating characteristic (ROC) curve, with area under curve (AUC), of the best algorithm for each predictive model. Middle: predictive accuracy for multiple sclerosis (MS) diagnosis model and MS disability course prediction model using 7 machine learning techniques: multiple linear regression (MLR), support vector machine (SVM), decision tree (DT), k-nearest neighbours (k-NN), Naïve Bayes (NB), ensemble classifier (EC) and long short-term memory (LSTM). The best algorithm for each model is highlighted by striped bars. LSTM was only tested for MS disability course prediction. Top: results using EC for MS diagnosis (accuracy: 87.7%; sensitivity: 87.0%; specificity: 88.5%; AUC: 0.8775). Bottom: results using LSTM for MS disability course prediction (accuracy: 81.7%; sensitivity: 81.1%; specificity: 82.2%; AUC: 0.8165).

parameters: age, sex, BCVA and the 6 RNFL thicknesses measured by OCT (Fig. 2A). Therefore, we characterized each subject using a total of 9 features. Comparison between data from MS patients and healthy controls was performed using Student's *t*-test (see Table 1). In this case, we had more than 90 subjects in each class, so feature selection was not necessary.

2.5. *MS disability course prediction model*

The next step was to develop a predictive model to assess the ability of RNFL thickness to accurately predict the progression of MS-associated disability in the long term. To do that, a 10-year longitudinal study was performed in 82 MS patients. Fig. 3 shows the evolution of EDDS score and RNFL data. An increase in EDSS score (Fig. 3A) and a decrease in RNFL thickness (Fig. 3B–G) were observed during follow-up. This model used data collected at the baseline visit (visit 0) and the first two annual follow-up visits (visits 1 and 2), and was designed to predict the disability course of MS patients at the final visit of the 10-year follow-up (i.e. 8 years later) (Fig. 2B). The features for this predictive model were general parameters, OCT parameters and MS parameters: age, sex, BCVA, the 6 RNFL thicknesses, MS duration, MS subtype, optic neuritis antecedent, relapse in preceding year and EDSS. Whereas age, sex, MS duration, MS subtype, optic neuritis antecedent were introduced only at baseline visit; BCVA, relapse in preceding year, EDSS score and the 6 RNFL thickness were taken into account at visits 0, 1 and 2.

In this prediction, the output was "worsening" or "non-worsening" in

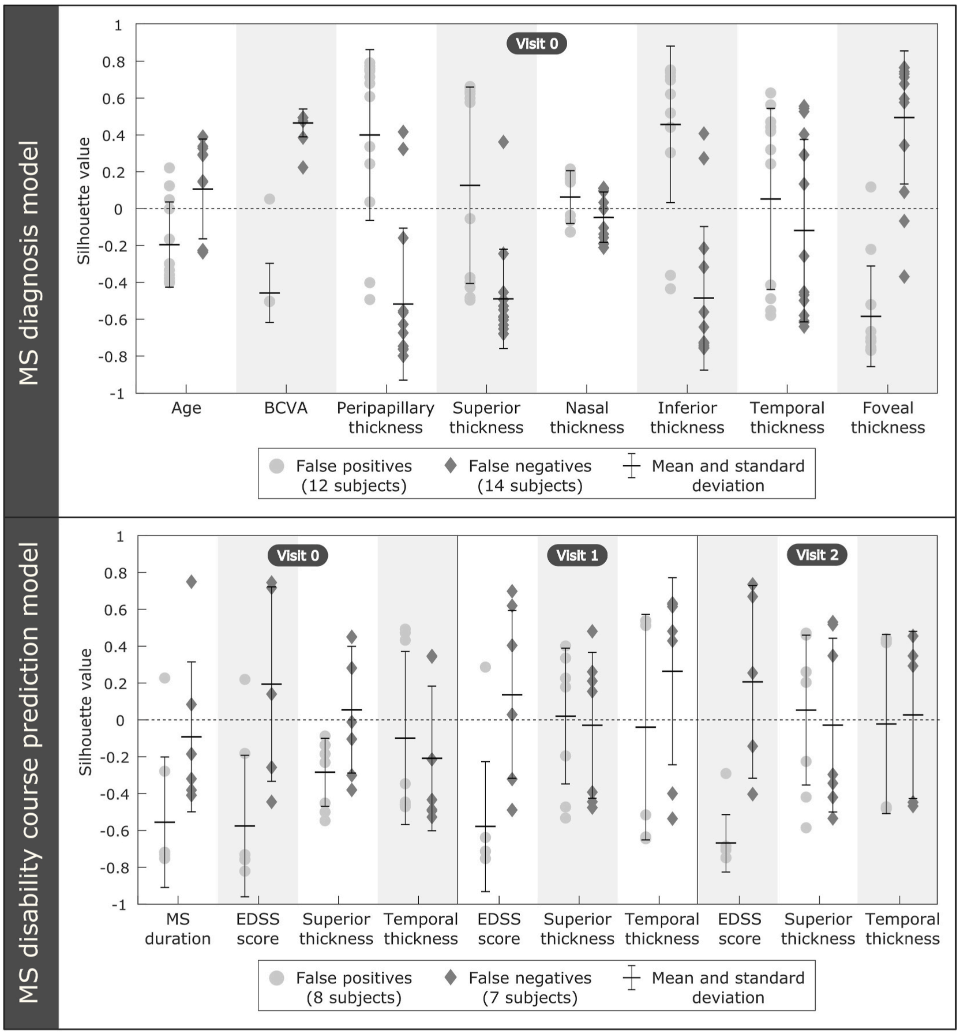

Fig. 5. Numerical feature analysis of false positives and false negatives for multiple sclerosis (MS) diagnosis model and MS disability course prediction model. The Silhouette value of each feature was calculated to compare false positives and false negatives with healthy controls and MS patients for MS diagnosis model, and with worsening and non-worsening for MS disability course prediction model (see Supplementary Material Fig. S1). Values close to +1 suggest that the subject is well matched to the assigned cluster, values close to 0 indicate that the subject coincides with the boundary between the two clusters and values close to −1 suggest that the subject may be assigned to the wrong cluster.

EDSS score at the target visit. We defined "worsening" as an increase of 1 or more points in EDSS between visit 2 and the final visit of the 10-year follow-up ($\Delta EDSS \geq 1$). And "non-worsening" represented patients whose EDSS value increased less than 1 point or decreased ($\Delta EDSS < 1$). In our dataset, 37 patients were worsening and 45 patients were non-worsening, so these classes were balanced. The statistical analysis of the input features of these two classes can be seen in Table 2, where significant differences ($p < 0.05$) are represented in bold.

As mentioned before, there were 14 inputs and we had less than 140 MS patients per class, so feature selection was necessary. Both SFS and LASSO were used to perform the feature selection and the resulting dataset after applying LASSO showed the best model performance (see Fig. S1). In this way, 5 features were chosen: MS duration, relapse in preceding year, EDSS score, temporal RNFL thickness and superior RNFL thickness (Fig. 2B). In this way, the reduced dataset was MS duration at baseline visit; relapse in preceding year, EDSS score, temporal RNFL thickness and superior RNFL thickness at visits 0, 1 and 2.

3. Results

As described above, 7 different classification algorithms were used to analyse the predictive accuracy of these two models. LSTM was only used for MS disability course prediction. While only the most relevant findings are discussed here, the complete results obtained for each classification algorithm are summarized in Fig. 4. The optimal value of the hyperparameters of each algorithm is shown in Table S1.

3.1. MS diagnosis model

The model for MS diagnosis was designed to classify subjects as MS patients or healthy controls based on age, sex, BCVA and RNFL measurements (9 features) acquired at the baseline visit. Whereas age, sex, BCVA and nasal thickness did not differ significantly between classes, the differences in peripapillary, superior, inferior, temporal and foveal thickness were significant (Table 1). The best result was obtained using EC, this algorithm correctly classified 186 out of 212 subjects (12 FP and

Table 3

Quantitative performance comparison of the best diagnostic methods for multiple sclerosis (MS) disease. Results of MS diagnosis using optical coherence tomography (OCT) from related works are compared. The following data are shown: OCT device, study population, classifier and model assessment. We indicated n/a when data were not available in the study. (ANN: artificial neural network; DT: decision tree; SVM: support vector machine; EC: ensemble classifier).

Study	Data type	MS patients	Healthy controls	Classifier	Accuracy (%)	Sensitivity (%)	Specificity (%)	Precision (%)	AUC (%)
MS diagnosis model									
Garcia-Martin et al. (2013) [4]	Spectralis OCT	106	115	ANN	n/a	n/a	n/a	n/a	94.5
Garcia-Martin et al. (2015) [16]	Spectralis OCT	112	105	ANN	88.5	89.3	87.6	88.5	n/a
Pérez del Palomar et al. (2019) [17]	SS-OCT Triton	80	180	DT	97.2	95.5	97.8	94.1	99.5
Cavaliere et al. (2019) [18]	SS-OCT Triton	48	48	SVM	90.6	89.8	91.5	91.7	97.0
Garcia-Martin et al. (2021) [19]	SS-OCT Triton	48	48	ANN	97.9	97.9	97.9	97.9	n/a
Our work	Cirrus HD-OCT	108	104	EC	87.7	87.0	88.5	88.7	87.8

14 FN, see confusion matrix in Fig. 4). Thus, the best accuracy for MS diagnosis was 87.7% (sensitivity: 87.0%; specificity: 88.5%; precision: 88.7%; AUC: 0.8775). The optimal hyperparameters of EC were: 100 classification trees, 0.196 learning rate and 1 minimum observation for leaf nodes.

The k-NN algorithm showed an accuracy of 85.4% with the use of 7 nearest neighbours and the Euclidean distance as distance metric between them (sensitivity: 83.3%; specificity: 87.5%; precision: 87.4%; AUC: 0.8542). With SVM the accuracy was 84.4% (sensitivity: 85.2%; specificity: 83.7%; precision: 84.4%; AUC: 0.8442). After optimizing the hyperparameters, box constraint was set to 1.752 and kernel scale to 0.055.

3.2. *MS disability course prediction model*

In this model, we evaluated the ability of the model to predict whether the degree of disability of a given MS patient would worsen or not. This predictive model used data from 82 MS patients acquired at 3 consecutive visits (baseline and annual follow-up visits 1 and 2) to predict the disability course of each patient at year 10. It can be seen that the reduced dataset, after the application of LASSO regression, corresponds to the input features whose difference was the most significant ($p < 0.001$) (see Table 2). The predictions generated by LSTM neural network were correct in 67 of 82 cases (8 FP and 7 FN, see confusion matrix in Fig. 4) giving an accuracy of 81.7% (sensitivity: 81.1%; specificity: 82.2%; precision: 78.9%; AUC: 0.8165). This result was obtained with the following structure: 30 hidden layers, 30 epochs and a mini-batch size of 20. Regarding hidden layers, the performance increased as the number of hidden layers increased up to 30 layers, from that point the performance was constant. For epochs and mini-batch size, the performance increased until reaching 30 epochs and a size of 20, and then the performance started to decrease.

SVM, MLR and k-NN also showed a good performance, correctly classifying 66 out of 82 MS patients. The optimal SVM structure was a box constraint of 2.120 and a kernel scale of 2.610 (accuracy: 80.5%; sensitivity: 83.8%; specificity: 77.8%; precision: 75.6%; AUC: 0.8078). In the case of k-NN, the hyperparameter optimization showed 13 neighbours as the optimal number of nearest neighbours and standardized Euclidean distance as the distance metric between neighbours (accuracy: 80.5%; sensitivity: 75.7%; specificity: 84.4%; precision: 80.0%; AUC: 0.8006). As can be seen in Fig. 4, the same accuracy was obtained using MLR (accuracy: 80.5%; sensitivity: 78.4%; specificity: 82.2%; precision: 78.4%; AUC: 0.8030). The rest of the classifiers showed moderate performance ($AUC < 0.8$).

3.3. *Misclassified subjects*

In order to understand why some subjects were misclassified, the features of each individual subject were analysed. Each input feature of a specific subject was studied to check if its value was more related to one class or the other, i.e. healthy control or MS patient for the first model and non-worsening or worsening for the second one. To do that, Silhouette value of each numerical input variable was calculated to compare the 12 FP and 14 FN with healthy controls and MS patients in case of MS diagnosis model, and the 8 FP and the 7 FN with worsening and non-worsening for MS disability course prediction. The Silhouette method measures how close each data point is to its own cluster compared to other clusters, this measure ranges from -1 to $+1$ [48]. A Silhouette value near $+1$ indicates that the data point is well matched to its own cluster and poorly matched to neighbouring clusters, a value of 0 suggests that the data point is on the decision boundary between two neighbouring clusters and negative values indicate that those data points might have been assigned to the wrong cluster. The Silhouette value of each numerical input variable, for each visit used in our predictive models, of FP and FN is available in the Supplementary Material. These data are summarized in Fig. 5.

The features whose mean Silhouette value was negative could cause a misclassification in our models because their values would be more related to the opposite group. First, paying attention to MS diagnosis model, the features with lowest Silhouettes values were: BCVA and foveal thickness for FP, and peripapillary, superior and inferior thickness for FN. Second, in the MS course prediction model, MS duration and EDSS score had values near -1 for FP. However, there are no features with values close to -1 for FN.

4. Discussion

Machine learning is based on the use of mathematical algorithms that seek to match input and output data, and is emerging as a very useful tool in many scientific fields. These algorithms can be used to improve the diagnosis of certain diseases and to aid clinicians in selecting the most appropriate therapy for a given patient [18,41,49]. More specifically, classification algorithms can use clinical data to improve diagnosis and predict the disease progression in MS patients [17,23]. In the present study, we evaluate the utility of machine learning techniques to diagnose MS disease and provide long-term predictions of the degree of disability in MS patients based on clinical data and RNFL thickness measurements acquired by OCT. This imaging technique offers certain advantages over other techniques, such as MRI, since it provides a rapid, cost-effective, and non-invasive means to evaluate RNFL thickness [17].

It is known that RNFL thickness is a very useful parameter to diagnose this disease [50] and, with our results, this fact has been corroborated, establishing this layer of the retina as a MS biomarker [51]. In addition, the significance of each RNFL thickness was analysed to find out which are the most important areas for MS diagnosis. The difference of RNFL thickness between MS patients and healthy controls was statistically significant in peripapillary area where superior, inferior

Table 4
Quantitative performance comparison of the best methods for disability course prediction in multiple sclerosis (MS) patients. Data type indicates the source of the data used. Data from represents the data points used to train the predictive model and prediction time is the time from the last data point to the output time. The studies had different output types, these are based on the variation of the expanded disability status scale (**Δ**EDSS) or on the evolution from relapse-remitting (RR) to secondary-progressive (SP) form of the disease. Study population, classifier and model assessment are also shown. We indicated n/a when data were not available in the study. (MRI: magnetic resonance imaging; EP: evoked potential; CSF: cerebrospinal fluid; OCT: optical coherence tomography; SVM: support vector machine; CNN: convolutional neural network; RF: random forest; LSTM: long short-term memory).

Study	Data type	Data from	Pred. time	Output type (positives vs negatives)	Positive patients	Negative patients	Classifier	Accuracy (%)	Sensitivity (%)	Specificity (%)	Precision (%)	AUC (%)
MS disability course prediction model												
Zhao et al. (2017) [21]	MRI	3 years	2 years	ΔEDSS ≥ 1.5 vs ΔEDSS < 1.5	212	362	SVM	71.0	65.0	74.0	n/a	n/a
Tousignant et al. (2019) [22]	MRI	1 year	1 year	ΔEDSS $\geq$ 1.5/1/0.5 vs ΔEDSS $<$ 1.5/1/0.5	103	980	CNN	n/a	n/a	n/a	n/a	70.1
Yperman et al. (2020) [23]	EP	2 years	2 years	ΔEDSS $\geq$ 1/0.5 vs ΔEDSS $<$ 1/0.5	46	373	RF	n/a	n/a	n/a	n/a	75.0
Pinto et al. (2020) [24]	MRI CSF EP	2 years	4 years	RR to SP vs otherwise	21	166	SVM	n/a	76.0	0.77	n/a	86.0
	MRI CSF EP	2 years	4 years	EDSS ≥ 3 vs EDSS < 3	38	107	SVM	n/a	84.0	81.0	n/a	89.0
Seccia et al. (2020) [25]	MRI Liquor	1 year	2 years	RR to SP vs otherwise	1168	207	SVM	87.8	77.3	87.9	9.3	n/a
	MRI Liquor	6 years	2 years	RR to SP vs otherwise	1168	207	LSTM	98.0	67.3	98.5	42.7	n/a
Our work	OCT	3 years	8 years	ΔEDSS ≥ 1 vs ΔEDSS < 1	37	45	LSTM	81.7	81.1	82.2	78.9	81.7

and temporal quadrants were also significant, highlighting the temporal quadrant. This difference turned out to be significant in the fovea, corroborating the importance of macular area [17].

Our results are totally in accordance with other works [52–54]. These studies establish that, although axonal loss diffusely affects RNFL thickness throughout the peripapillary area, the temporal quadrant is the most affected area in MS patients from early stages of the disease, even without previous optic neuritis episodes. Some authors suggest that, because the temporal quadrant of the optic disc is relatively thinner than other quadrants, atrophy is noted from earlier stages [52]. Other authors, including our group, suggest that this temporal thinning reflects a predominant involvement of the fovea and the papillomacular bundle, which is the structure that transmits information from the fovea. The fovea is the central macular structure and is primarily responsible for detailed visual and color functions, which are affected in MS. Therefore, a reduction in macular volume is also observed in these patients, especially in the nasal sectors of the macula, which correspond to the papillomacular bundle [55].

As can be seen in Table 3, RNFL thickness, measured by different OCT devices, has been evaluated to train classifiers for MS diagnosis. Garcia-Martin et al. used Spectralis OCT in combination with ANN, obtaining an AUC of 94.5% [4] and an accuracy of 88.5% [16]. Other studies employed SS-OCT Triton to measure the RNFL thickness and the results were: an accuracy of 97.2% with DT [17], 90.6% with SVM [18] and 97.9% with ANN [19]. Whereas we have used RNFL thickness measured by Cirrus HD-OCT and the best classifier was EC with an accuracy of 87.7%. The results of these studies could indicate that the best OCT device for MS diagnosis, using machine learning techniques, would be SS-OCT Triton. However, the study populations with this OCT device were either too small or imbalanced. Therefore, a more significant result would be an accuracy of 88.5%, obtained by Garcia-Martin et al. [16] with ANN, very similar to ours.

Previous studies [7,26,56] have reported associations between RNFL thickness and MS disability course, suggesting that the retina may also be a reliable biomarker of the progression of this neurodegenerative disease. However, it was not possible to establish a direct relationship between disability and RNFL thickness. First, RNFL thinning is not caused exclusively by MS, but is also affected by aging [57–59]. Second, there is marked variation in RNFL thickness among MS patients [7,27,60]. For these reasons, we examined the potential utility of machine learning techniques to predict the progression of disability in MS patients.

In this study, for MS disability course prediction, it has been distinguished between two classes (worsening versus non-worsening). As can be seen in Table 2, input features such as age, MS duration, EDSS, peripapillary, superior and temporal thicknesses were significant ($p < 0.05$). However, after feature selection by LASSO, only the most significant features were used ($p < 0.001$). These results are in line with the findings of the work by Birkeldh et al. [54] in which it was shown that the temporal quadrant was highly associated with the EDSS score. Higher EDSS values correspond to a significant RNFL reduction in peripapillary, superior and temporal thicknesses for non-worsening patients. The reason for that was well explained in our previous study [7], MS patients with greater disability have a lower RNFL thickness because the most part of this thinning occurs during the initial stages of the disease (before the onset of significant disability).

Several studies have assessed the ability of machine learning techniques to predict the short-term progression of MS. These studies used datasets with information from MRI, EP or CSF analysis and tested different classifiers to predict the disability progression in MS patients (see Table 4). However, none of these studies has evaluated the use of RNFL thickness to predict the long-term progression of MS-associated disability. Therefore, our study is the first to apply machine learning techniques to OCT data obtained from a 10-year longitudinal study. The progression was based on the variation of EDSS score in the majority of the works [21–24], although some studies also predicted the progression or not from RRMS to SPMS form of the disease [24,25]. The time from the last data point used to train the predictive model to the output time

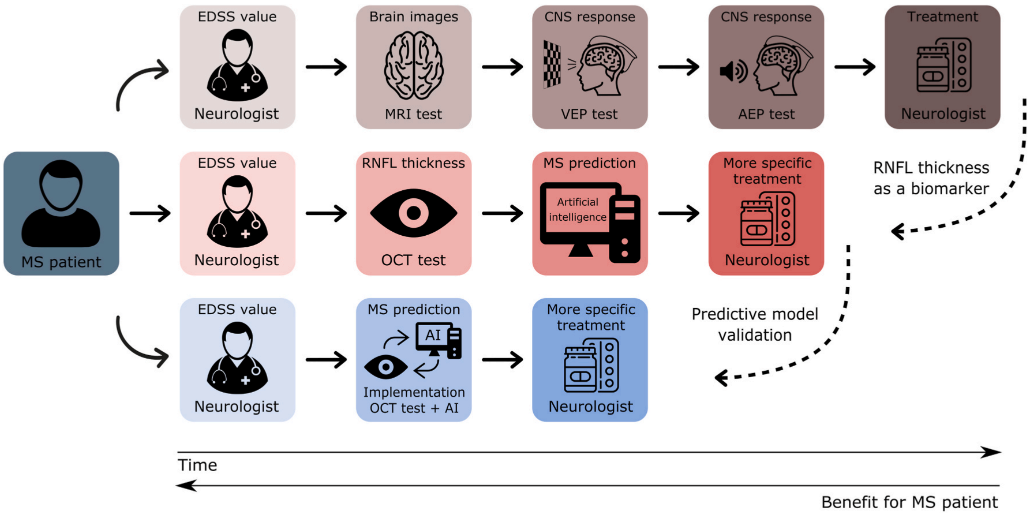

Fig. 6. Flowchart of the treatment process for MS patients. The top row shows the methodology currently implemented in most hospitals: magnetic resonance imaging (MRI) to detect changes in brain volume; visual evoked potential (VEP) and auditory evoked potential (AEP) tests to analyse central nervous system (CNS) response. The middle row shows our proposed method, based on the use of retinal nerve fiber layer (RNFL) thickness together with artificial intelligence (AI) to predict the progression of MS-associated disability and thus to be able to apply a more specific treatment. The bottom row depicts the proposed method following incorporation of classification algorithms into optical coherence tomography (OCT) devices after prior validation of our predictive models. In all cases, a neurologist must establish the disability state using the expanded disability status scale (EDSS).

was usually 1 or 2 years, but Pinto et al. predicted the disability course 4 years later with an AUC of 89% using SVM [24]. Seccia et al. tested LSTM trained with 6 data points to predict the disability course 2 year later obtaining a high accuracy and specificity but low sensitivity and precision because their data were class-imbalanced [25]. To obtain a significant result, several factors should be taken into account. First, it is necessary a balance between the data points used for training and the prediction time since it is desirable to achieve a good prediction with the lowest number of progression years. Secondly, the dataset should be balanced to obtain a good performance in all parameters of the predictive model evaluation. For these reasons, we have used 3 data points from a class-balanced dataset to predict the disability progression 8 years later with an accuracy of 81.7% using LSTM.

While our findings constitute an important step towards patient-specific prediction of the course of MS, our results should be interpreted considering several limitations. Our predictive models are largely based on OCT data. However, the use of OCT devices in combination with other techniques such as MRI, EP or CSF analysis could improve the model performance. Given that the quality of OCT data directly influences the results, the precision of the OCT device must also be considered. Moreover, these data should be used in combination with clinical data, such as the EDSS score. Although EDSS score is considered the most useful tool for measurement of MS progression and is assumed by many neurologists to directly determine worsening/non-worsening, this variable has some drawbacks in terms of reliability and sensitivity [61]. Our progression prediction was defined as a variation in EDSS score (ΔEDSS), so it is a qualitative prediction because the value of the disability state is not predicted. Besides, it should be borne in mind that the treatment regimens of MS patients, which were not considered when developing our models, could potentially influence disease course.

The heterogeneity of our sample population should also be noted. Patients began the follow-up at different stages of disease progression and, therefore, there was considerable variation among patients in MS duration at baseline and consequently in EDSS score. However, since MS progression in each patient was measured relative to their baseline EDSS score, this variation would not affect our results. Furthermore, although our study population included patients with all subtypes of this disease, RRMS clearly predominated, as shown in Table 1.

Taking into account the numerical input features used in the models, we analysed the reasons why some subjects could have been incorrectly classified. As can be seen in Fig. 5, for MS diagnosis model, BCVA and foveal thickness for FP; and peripapillary, superior and inferior thickness for FN had values closer to the wrong class than the correct one (i.e. Silhouette values near -1), and this fact could confuse algorithms. In case of MS disability course prediction, MS duration and EDSS score were the most confusing variables for FP, while there are no features with mean Silhouette value near -1 for FN. These results could indicate that subjects with values closer to those of the opposite class in some significant variable could be misclassified. Machine learning techniques have great potential to improve the diagnosis and treatment of MS, but it is important that they are used in conjunction with large datasets that appropriately represent all cases.

Although more longitudinal studies of MS patients from other parts of the world will be required to validate the predictive models presented here, our results indicate that RNFL thickness measured by OCT is a useful biomarker to establish an early diagnosis and predict the progression of MS, in line with the findings of previous studies [62,63]. For this reason, we support the proposal of several authors to review the approach for MS diagnosis [64]. Currently, MS diagnosis requires a large number of tests, including MRI to detect MS lesions in the brain tissue, the analysis of CSF samples and multiple EP tests to detect possible decreases in the rate of neurotransmission in the CNS. Visual evoked potential (VEP) and auditory evoked potential (AEP) are measures of CNS activity in response to light and acoustic stimuli, respectively. Another less commonly used test is somatosensory evoked potential (SSEP) testing, which is used to detect deficits in electrical activity in the spinal cord by applying electrical stimuli to the wrist, the back of the knee, or other locations. These all procedures are time-consuming.

The same happens to design an appropriate treatment for a MS patient. First, a neurologist evaluates the disability state by establishing the EDSS value. Then, MRI and EP tests are performed to detect lesions in the CNS. Thus, the neurologist prescribes a treatment without any prior information of the MS progression for that specific patient. In this work, we propose that OCT data should be used in combination with artificial intelligence to MS diagnose and predict MS course (see Fig. 6). OCT is an objective and reproducible test that can be completed in as little as 2 min by non-specialized personnel without exposing the patient to radiation or causing any discomfort [18]. Moreover, OCT devices are available in practically any hospital and even in some outpatient centres.

This would be of significant benefit to clinicians, who could select more specific and appropriate treatments based on the predicted disease course for a given patient. Moreover, as can be seen in Fig. 6, this approach would help to reduce waiting times and improve the overall quality of life of MS patients. To make this possible, it will be necessary to validate the predictive models presented here in other populations in order to incorporate these algorithms into OCT devices, improving the diagnosis and disability prediction of MS.

Declaration of competing interest

The authors state that there are no conflicts of interest.

Acknowledgements

This work was supported by the Spanish Ministry of Economy and Competitiveness (project DPI 2016-79302-R), the Spanish Ministry of Science, Innovation and Universities (grant BES-2017-080384), and the Instituto de Salud Carlos III (PI17/01726).

Appendix A. Supplementary data

Supplementary data to this article can be found online at https://doi.org/10.1016/j.compbiomed.2021.104416.

References

[1] B. Ferguson, M.K. Matyszak, M.M. Esiri, V.H. Perry, Axonal damage in acute multiple sclerosis lesions, Brain 120 (1997) 393–399, https://doi.org/10.1093/brain/120.3.393.

[2] Y. You, M.H. Barnett, C. Yiannikas, J. Parratt, J. Matthews, S.L. Graham, A. Klistorner, Chronic demyelination exacerbates neuroaxonal loss in patients with MS with unilateral optic neuritis, Neurol. Neuroimmunol. Neuroinflammation. 7 (2020), https://doi.org/10.1212/NXI.0000000000000700.

[3] C.H. Polman, S.C. Reingold, G. Edan, M. Filippi, H.-P. Hartung, L. Kappos, F. D. Lublin, L.M. Metz, H.F. McFarland, P.W. O'Connor, M. Sandberg-Wollheim, A. J. Thompson, B.G. Weinshenker, J.S. Wolinsky, Diagnostic criteria for multiple sclerosis: 2005 revisions to the "McDonald Criteria," Ann, Neurol. 58 (2005) 840–846, https://doi.org/10.1002/ana.20703.

[4] E. Garcia-Martin, L.E. Pablo, R. Herrero, J.R. Ara, J. Martin, J.M. Larrosa, V. Polo, J. Garcia-Feijoo, J. Fernandez, Neural networks to identify multiple sclerosis with optical coherence tomography, Acta Ophthalmol. 91 (2013) e628–e634, https://doi.org/10.1111/aos.12156.

[5] S. Roy, D. Bhattacharyya, S.K. Bandyopadhyay, T.H. Kim, An effective method for computerized prediction and segmentation of multiple sclerosis lesions in brain MRI, Comput. Methods Progr. Biomed. 140 (2017) 307–320, https://doi.org/10.1016/j.cmpb.2017.01.003.

[6] Y. Fu, T.M. Talavage, J.-X. Cheng, New imaging techniques in the diagnosis of multiple sclerosis, Expert Opin. Med. Diagn. 2 (2008) 1055–1065, https://doi.org/10.1517/17530050802361161.

[7] A. Montolío, J. Cegoñino, E. Orduna, B. Sebastian, E. Garcia-Martin, A. Pérez del Palomar, A mathematical model to predict the evolution of retinal nerve fiber layer thinning in multiple sclerosis patients, Comput. Biol. Med. 111 (2019) 103357, https://doi.org/10.1016/j.compbiomed.2019.103357.

[8] L.J. Balk, A. Cruz-Herranz, P. Albrecht, S. Arnow, J.M. Gelfand, P. Tewarie, J. Killestein, B.M.J. Uitdehaag, A. Petzold, A.J. Green, Timing of retinal neuronal and axonal loss in MS: a longitudinal OCT study, J. Neurol. 263 (2016) 1323–1331, https://doi.org/10.1007/s00415-016-8127-y.

[9] F. Eslami, M. Ghiasian, E. Khanlarzade, E. Moradi, Retinal nerve fiber layer thickness and total macular volume in multiple sclerosis subtypes and their relationship with severity of disease, a cross-sectional study, Eye Brain 12 (2020) 15–23, https://doi.org/10.2147/EB.S229814.

[10] A. Rothman, O.C. Murphy, K.C. Fitzgerald, J. Button, E. Gordon-Lipkin, J. N. Ratchford, S.D. Newsome, E.M. Mowry, E.S. Sotirchos, S.B. Syc-Mazurek, J. Nguyen, N.G. Caldito, L.J. Balcer, E.M. Frohman, T.C. Frohman, D.S. Reich, C. Crainiceanu, S. Saidha, P.A. Calabresi, Retinal measurements predict 10-year disability in multiple sclerosis, Ann. Clin. Transl. Neurol. 6 (2019) 222–232, https://doi.org/10.1002/acn3.674.

[11] A.U. Brandt, E.H. Martinez-Lapiscina, R. Nolan, S. Saidha, Monitoring the course of MS with optical coherence tomography, Curr. Treat. Options Neurol. 19 (2017) 15, https://doi.org/10.1007/s11940-017-0452-7.

[12] S. Saidha, O. Al-Louzi, J.N. Ratchford, P. Bhargava, J. Oh, S.D. Newsome, J. L. Prince, D. Pham, S. Roy, P. van Zijl, L.J. Balcer, E.M. Frohman, D.S. Reich, C. Crainiceanu, P.A. Calabresi, Optical coherence tomography reflects brain atrophy in multiple sclerosis: a four-year study, Ann. Neurol. 78 (2015) 801–813, https://doi.org/10.1002/ana.24487.

[13] G. Kitsos, E.T. Detorakis, S. Papakonstantinou, A.P. Kyritsis, S.H. Pelidou, Perimetric and peri-papillary nerve fibre layer thickness findings in multiple sclerosis, Eur. J. Neurol. 18 (2011) 719–725, https://doi.org/10.1111/j.1468-1331.2010.03256.x.

[14] E. Garcia-Martin, J.R. Ara, J. Martin, C. Almarcegui, I. Dolz, E. Vilades, L. Gil-Arribas, F.J. Fernandez, V. Polo, J.M. Larrosa, L.E. Pablo, M. Satue, Retinal and optic nerve degeneration in patients with multiple sclerosis followed up for 5 years, Ophthalmology 124 (2017) 688–696, https://doi.org/10.1016/j.ophtha.2017.01.005.

[15] E. Garcia-Martin, L.E. Pablo, R. Herrero, M. Satue, V. Polo, J.M. Larrosa, J. Martin, J. Fernandez, Diagnostic ability of a linear discriminant function for spectral-domain optical coherence tomography in patients with multiple sclerosis, Ophthalmology 119 (2012) 1705–1711, https://doi.org/10.1016/j.ophtha.2012.01.046.

[16] E. Garcia-Martin, R. Herrero, M.P. Bambo, J.R. Ara, J. Martin, V. Polo, J. M. Larrosa, J. Garcia-Feijoo, L.E. Pablo, Artificial neural network techniques to improve the ability of optical coherence tomography to detect optic neuritis, Semin. Ophthalmol. 30 (2015) 11–19, https://doi.org/10.3109/08820538.2013.810277.

[17] A. Pérez del Palomar, J. Cegoñino, A. Montolío, E. Orduna, E. Vilades, B. Sebastián, L.E. Pablo, E. Garcia-Martin, Swept source optical coherence tomography to early detect multiple sclerosis disease. The use of machine learning techniques, PloS One 14 (2019), e0216410, https://doi.org/10.1371/journal.pone.0216410.

[18] C. Cavaliere, E. Vilades, M. Alonso-Rodríguez, M. Rodrigo, L. Pablo, J. Miguel, E. López-Guillén, E. Morla, L. Boquete, E. Garcia-Martin, Computer-Aided diagnosis of multiple sclerosis using a support vector machine and optical coherence tomography features, Sensors 19 (2019) 5323, https://doi.org/10.3390/s19235323.

[19] E. Garcia-Martin, M. Ortiz, L. Boquete, E.M. Sánchez-Morla, R. Barea, C. Cavaliere, E. Vilades, E. Orduna, M.J. Rodrigo, Early diagnosis of multiple sclerosis by OCT analysis using Cohen`s d method and a neural network as classifier, Comput. Biol. Med. 129 (2021), https://doi.org/10.1016/j.compbiomed.2020.104165.

[20] E. Garcia-Martin, D. Rodriguez-Mena, R. Herrero, C. Almarcegui, I. Dolz, J. Martin, J.R. Ara, J.M. Larrosa, V. Polo, J. Fernández, L.E. Pablo, Neuro-ophthalmologic evaluation, quality of life, and functional disability in patients with MS, Neurology 81 (2013) 76–83, https://doi.org/10.1212/WNL.0b013e318299ccd9.

[21] Y. Zhao, B.C. Healy, D. Rotstein, C.R.G. Guttmann, R. Bakshi, H.L. Weiner, C. E. Brodley, T. Chitnis, Exploration of machine learning techniques in predicting multiple sclerosis disease course, PloS One 12 (2017), e0174866, https://doi.org/10.1371/journal.pone.0174866.

[22] A. Tousignant, M. Paul LemâitreLemâıtre, C. Doina Precup, D.L. Arnold, Prediction of disease progression in multiple sclerosis patients using deep learning analysis of MRI data tal arbel 3, Proc. Mach. Learn. Res. 102 (2019) 483–492, in: http://proceedings.mlr.press/v102/tousignant19a.html.

[23] J. Yperman, T. Becker, D. Valkenborg, V. Popescu, N. Hellings, B. Van Wijmeersch, L.M. Peeters, Machine learning analysis of motor evoked potential time series to predict disability progression in multiple sclerosis, BMC Neurol. 20 (2020) 1–15, https://doi.org/10.1186/s12883-020-01672-w.

[24] M.F. Pinto, H. Oliveira, S. Batista, L. Cruz, M. Pinto, I. Correia, P. Martins, C. Teixeira, Prediction of disease progression and outcomes in multiple sclerosis with machine learning, Sci. Rep. 10 (2020) 1–13, https://doi.org/10.1038/s41598-020-78212-6.

[25] R. Seccia, D. Gammelli, F. Dominici, S. Romano, A.C. Landi, M. Salvetti, A. Tacchella, A. Zaccaria, A. Crisanti, F. Grassi, L. Palagi, Considering patient clinical history impacts performance of machine learning models in predicting course of multiple sclerosis, PloS One 15 (2020) 1–18, https://doi.org/10.1371/journal.pone.0230219.

[26] G. Bsteh, H. Hegen, B. Teuchner, M. Amprosi, K. Berek, F. Ladstätter, S. Wurth, M. Auer, F. Di Pauli, F. Deisenhammer, T. Berger, Peripapillary retinal nerve fibre layer as measured by optical coherence tomography is a prognostic biomarker not only for physical but also for cognitive disability progression in multiple sclerosis, Mult. Scler. J. 25 (2019) 196–203, https://doi.org/10.1177/1352458517740216.

[27] G. Bsteh, H. Hegen, B. Teuchner, K. Berek, S. Wurth, M. Auer, F. Di Pauli, F. Deisenhammer, T. Berger, Peripapillary retinal nerve fibre layer thinning rate as a biomarker discriminating stable and progressing relapsing–remitting multiple sclerosis, Eur. J. Neurol. 26 (2019) 865–871, https://doi.org/10.1111/ene.13897.

[28] G. Bsteh, H. Hegen, P. Altmann, M. Auer, K. Berek, F. Di Pauli, S. Wurth, A. Zinganell, P. Rommer, F. Deisenhammer, F. Leutmezer, T. Berger, Retinal layer thinning is reflecting disability progression independent of relapse activity in multiple sclerosis, Mult. Scler. J. - Exp. Transl. Clin. 6 (2020), https://doi.org/10.1177/2055217320966344.

[29] R.A. Armstrong, Statistical guidelines for the analysis of data obtained from one or both eyes, Ophthalmic Physiol. Opt. 33 (2013) 7–14, https://doi.org/10.1111/opo.12009.

[30] W.I. McDonald, A. Compston, G. Edan, D. Goodkin, H.P. Hartung, F.D. Lublin, H. F. McFarland, D.W. Paty, C.H. Polman, S.C. Reingold, M. Sandberg-Wollheim, W. Sibley, A. Thompson, S. van den Noort, B.Y. Weinshenker, J.S. Wolinsky, Recommended diagnostic criteria for multiple sclerosis: guidelines from the International Panel on the diagnosis of multiple sclerosis, Ann. Neurol. 50 (2001) 121–127, https://doi.org/10.1002/ana.1032.

[31] L.T. Chylack, J.K. Wolfe, D.M. Singer, M.C. Leske, M.A. Bullimore, I.L. Bailey, J. Friend, D. McCarthy, S.Y. Wu, The lens Opacities classification system III. The longitudinal study of cataract study group, Arch. Ophthalmol. (Chicago, Ill. 111

(1960) 831–836, https://doi.org/10.1001/archopht.1993.01090060119035, 1993.

[32] A. Minneboo, B. Jasperse, F. Barkhof, B.M.J. Uitdehaag, D.L. Knol, V. De Groot, C. H. Polman, J.A. Castelijns, Predicting short-term disability progression in early multiple sclerosis: added value of MRI parameters, J. Neurol. Neurosurg. Psychiatry 79 (2008) 917–923, https://doi.org/10.1136/jnnp.2007.124123.

[33] K. Potdar, T. S, C. D, A comparative study of categorical variable encoding techniques for neural network classifiers, Int. J. Comput. Appl. 175 (2017) 7–9, https://doi.org/10.5120/ijca2017915495.

[34] P. Peduzzi, J. Concato, E. Kemper, T.R. Holford, A.R. Feinstein, A simulation study of the number of events per variable in logistic regression analysis, J. Clin. Epidemiol. 49 (1996) 1373–1379, https://doi.org/10.1016/S0895-4356(96)00236-3.

[35] M. Tan, J. Pu, B. Zheng, Optimization of breast mass classification using sequential forward floating selection (SFFS) and a support vector machine (SVM) model, Int. J. Comput. Assist. Radiol. Surg. 9 (2014) 1005–1020, https://doi.org/10.1007/s11548-014-0992-1.

[36] R. Tibshirani, Regression shrinkage and selection via the lasso, J. R. Stat. Soc. Ser. B. 58 (1996) 267–288, https://doi.org/10.1111/j.2517-6161.1996.tb02080.x.

[37] E.M. Mowry, A.K. Hedström, M.A. Gianfrancesco, X. Shao, C.A. Schaefer, L. Shen, K.H. Bellesis, F.B.S. Briggs, T. Olsson, L. Alfredsson, L.F. Barcellos, Incorporating machine learning approaches to assess putative environmental risk factors for multiple sclerosis, Mult. Scler. Relat. Disord. 24 (2018) 135–141, https://doi.org/10.1016/j.msard.2018.06.009.

[38] J. Mata, Interpretation of concrete dam behaviour with artificial neural network and multiple linear regression models, Eng. Struct. 33 (2011) 903–910, https://doi.org/10.1016/j.engstruct.2010.12.011.

[39] T. Hastie, R. Tibshirani, J. Friedman, The Elements of Statistical Learning, Springer, New York, New York, NY, 2009, https://doi.org/10.1007/978-0-387-84858-7.

[40] A. Mathur, G.M. Foody, Multiclass and binary SVM classification: implications for training and classification users, Geosci. Rem. Sens. Lett. IEEE 5 (2008) 241–245, https://doi.org/10.1109/LGRS.2008.915597.

[41] N.I.R. Yassin, S. Omran, E.M.F. El Houby, H. Allam, Machine learning techniques for breast cancer computer aided diagnosis using different image modalities: a systematic review, Comput. Methods Progr. Biomed. 156 (2018) 25–45, https://doi.org/10.1016/j.cmpb.2017.12.012.

[42] P. Cunningham, S.J. Delany, k-Nearest neighbour classifiers, Mult. Classif. Syst. 34 (2007) 1–17.

[43] P.C. Cheeseman, M. Self, J. Kelly, W. Taylor, D. Freeman, J.C. Stutz, Bayesian classification, in: Proc. 7th Natl. Conf. Artif. Intell. St. Paul, MN, USA, August 21-26, 1988, 1988, pp. 607–611.

[44] H. Bonab, F. Can, Less is more: a comprehensive framework for the number of components of ensemble classifiers, IEEE Trans. Neural Networks Learn. Syst. 30 (2019) 2735–2745, https://doi.org/10.1109/TNNLS.2018.2886341.

[45] M. Kuhn, K. Johnson, Applied Predictive Modeling, Springer New York, New York, NY, 2013, https://doi.org/10.1007/978-1-4614-6849-3.

[46] Z.C. Lipton, D.C. Kale, C. Elkan, R. Wetzel, Learning to diagnose with LSTM recurrent neural networks, in: 4th Int. Conf. Learn. Represent, ICLR, 2016, pp. 1–18, 2016, http://arxiv.org/abs/1511.03677.

[47] J.D. Rodriguez, A. Perez, J.A. Lozano, Sensitivity analysis of k-fold cross validation in prediction error estimation, IEEE Trans. Pattern Anal. Mach. Intell. 32 (2010) 569–575, https://doi.org/10.1109/TPAMI.2009.187.

[48] F. Wang, H.-H. Franco-Penya, J.D. Kelleher, J. Pugh, R. Ross, in: P. Perner (Ed.), An Analysis of the Application of Simplified Silhouette to the Evaluation of K-Means Clustering Validity, Springer International Publishing, Cham, 2017, pp. 291–305, https://doi.org/10.1007/978-3-319-62416-7_21.

[49] C.C. Wu, W.C. Yeh, W.D. Hsu, M.M. Islam, P.A. (Alex) Nguyen, T.N. Poly, Y. C. Wang, H.C. Yang, Y.C. (Jack) Li, Prediction of fatty liver disease using machine learning algorithms, Comput. Methods Progr. Biomed. 170 (2019) 23–29, https://doi.org/10.1016/j.cmpb.2018.12.032.

[50] F. London, H. Zéphir, E. Drumez, J. Labreuche, N. Hadhoum, J. Lannoy, J. Hodel, P. Vermersch, J.-P. Pruvo, X. Leclerc, O. Outteryck, Optical coherence tomography: a window to the optic nerve in clinically isolated syndrome, Brain 142 (2019) 903–915, https://doi.org/10.1093/brain/awz038.

[51] F. Costello, J. Burton, Retinal imaging with optical coherence tomography: a biomarker in multiple sclerosis? Eye Brain 10 (2018) 47–63, https://doi.org/10.2147/EB.S139417.

[52] S. Noval, I. Contreras, S. Muñoz, C. Oreja-Guevara, B. Manzano, G. Rebolleda, Optical coherence tomography in multiple sclerosis and neuromyelitis optica: an update, Mult. Scler. Int. 2011 (2011) 1–11, https://doi.org/10.1155/2011/472790.

[53] C. Fjeldstad, M. Bemben, G. Pardo, Reduced retinal nerve fiber layer and macular thickness in patients with multiple sclerosis with no history of optic neuritis identified by the use of spectral domain high-definition optical coherence tomography, J. Clin. Neurosci. 18 (2011) 1469–1472, https://doi.org/10.1016/j.jocn.2011.04.008.

[54] U. Birkeldh, A. Manouchehrinia, M.A. Hietala, J. Hillert, T. Olsson, F. Piehl, I. S. Kockum, L. Brundin, O. Zahavi, M. Wahlberg-Ramsay, R. Brautaset, M. Nilsson, The temporal retinal nerve fiber layer thickness is the most important optical coherence tomography estimate in multiple sclerosis, Front. Neurol. 8 (2017), https://doi.org/10.3389/fneur.2017.00675.

[55] A.A. Khanifar, G.J. Parlitsis, J.R. Ehrlich, G.D. Aaker, D.J. D'Amico, S.A. Gauthier, S. Kiss, Retinal nerve fiber layer evaluation in multiple sclerosis with spectral domain optical coherence tomography, Clin. Ophthalmol. 4 (2010) 1007–1013, https://doi.org/10.2147/OPTH.S13278.

[56] A. Klistorner, E.C. Graham, C. Yiannikas, M. Barnett, J. Parratt, R. Garrick, C. Wang, Y. You, S.L. Graham, Progression of retinal ganglion cell loss in multiple sclerosis is associated with new lesions in the optic radiations, Eur. J. Neurol. 24 (2017) 1392–1398, https://doi.org/10.1111/ene.13404.

[57] E. Viladés, A.P. Del Palomar, J. Cegoñino, J. Obis, M. Satue, E. Orduna, L.E. Pablo, M. Ciprés, E. GarciaMartin, Physiological changes in retinal layers thicknesses measured with swept source optical coherence tomography, PloS One 15 (2020) 1–14, https://doi.org/10.1371/journal.pone.0240441.

[58] B. Alamouti, J. Funk, Retinal thickness decreases with age: an OCT study, Br. J. Ophthalmol. 87 (2003) 899–901, https://doi.org/10.1136/bjo.87.7.899.

[59] C.K.S. Leung, M. Yu, R.N. Weinreb, C. Ye, S. Liu, G. Lai, D.S.C. Lam, Retinal nerve fiber layer imaging with spectral-domain optical coherence tomography: a prospective analysis of age-related loss, Ophthalmology 119 (2012) 731–737, https://doi.org/10.1016/j.ophtha.2011.10.010.

[60] E.S. Sotirchos, N. Gonzalez Caldito, A. Filippatou, K.C. Fitzgerald, O.C. Murphy, J. Lambe, J. Nguyen, J. Button, E. Ogbuokiri, C.M. Crainiceanu, J.L. Prince, P. A. Calabresi, S. Saidha, Progressive multiple sclerosis is associated with faster and specific retinal layer atrophy, Ann. Neurol. (2020), https://doi.org/10.1002/ana.25738.

[61] S. Meyer-Moock, Y.-S. Feng, M. Maeurer, F.-W. Dippel, T. Kohlmann, Systematic literature review and validity evaluation of the expanded disability status scale (EDSS) and the multiple sclerosis functional composite (MSFC) in patients with multiple sclerosis, BMC Neurol. 14 (2014) 58, https://doi.org/10.1186/1471-2377-14-58.

[62] M. Satue, J. Obis, M.J. Rodrigo, S. Otin, M.I. Fuertes, E. Vilades, H. Gracia, J. R. Ara, R. Alarcia, V. Polo, J.M. Larrosa, L.E. Pablo, E. Garcia-Martin, Optical coherence tomography as a biomarker for diagnosis, progression, and prognosis of neurodegenerative diseases, J. Ophthalmol. (2016) 1–9, https://doi.org/10.1155/2016/8503859, 2016.

[63] R. Alonso, D. Gonzalez-Moron, O. Garcea, Optical coherence tomography as a biomarker of neurodegeneration in multiple sclerosis: a review, Mult. Scler. Relat. Disord. 22 (2018) 77–82, https://doi.org/10.1016/j.msard.2018.03.007.

[64] A.J. Thompson, B.L. Banwell, F. Barkhof, W.M. Carroll, T. Coetzee, G. Comi, J. Correale, F. Fazekas, M. Filippi, M.S. Freedman, K. Fujihara, S.L. Galetta, H. P. Hartung, L. Kappos, F.D. Lublin, R.A. Marrie, A.E. Miller, D.H. Miller, X. Montalban, E.M. Mowry, P.S. Sorensen, M. Tintoré, A.L. Traboulsee, M. Trojano, B.M.J. Uitdehaag, S. Vukusic, E. Waubant, B.G. Weinshenker, S.C. Reingold, J. A. Cohen, Diagnosis of multiple sclerosis: 2017 revisions of the McDonald criteria, Lancet Neurol. 17 (2018) 162–173, https://doi.org/10.1016/S1474-4422(17)30470-2.

2.2.3 MS diagnosis and prognosis using Spectralis OCT

Manuscript 4: Comparison of machine learning methods using Spectralis OCT for diagnosis and disability progression prognosis in multiple sclerosis

Alberto Montolío, José Cegoñino, Elena Garcia-Martin, Amaya Pérez del Palomar

Abstract

Machine learning approaches in diagnosis and prognosis of multiple sclerosis (MS) were analysed using retinal nerve fiber layer (RNFL) thickness, measured by optical coherence tomography (OCT). A cross-sectional study (72 MS patients and 30 healthy controls) was used for diagnosis. These 72 MS patients were involved in a 10-year longitudinal follow-up study for prognostic purposes. Structural measurements of RNFL thickness were performed using different Spectralis OCT protocols: fast macular thickness protocol to measure macular RNFL, and fast RNFL thickness protocol and fast RNFL-N thickness protocol to measure peripapillary RNFL. Binary classifiers such as multiple linear regression (MLR), support vector machines (SVM), decision tree (DT), k-nearest neighbours (k-NN), Naïve Bayes (NB), ensemble classifier (EC) and long short-term memory (LSTM) recurrent neural network were tested. For MS diagnosis, the best acquisition protocol was fast macular thickness protocol using k-NN (accuracy: 95.8%; sensitivity: 94.4%; specificity: 97.2%; precision: 97.1%; AUC: 0.958). For MS prognosis, our model with a 3-year follow up to predict disability progression 8 years later was the best predictive model. DT performed best for fast macular thickness protocol (accuracy: 91.3%; sensitivity: 90.0%; specificity: 92.5%; precision: 92.3%; AUC: 0.913) and SVM for fast RNFL-N thickness protocol (accuracy: 91.3%; sensitivity: 87.5%; specificity: 95.0%; precision: 94.6%; AUC: 0.913). This work concludes that measurements of RNFL thickness obtained with Spectralis OCT have a good ability to diagnose MS and to predict disability progression in MS patients. This machine learning approach would help clinicians to have valuable information.

Annals of Biomedical Engineering (© 2022)
https://doi.org/10.1007/s10439-022-02930-3

Original Article

Comparison of Machine Learning Methods Using Spectralis OCT for Diagnosis and Disability Progression Prognosis in Multiple Sclerosis

Alberto Montolío,[1,2,5] José Cegoñino,[1,2] Elena Garcia-Martin,[3,4] and Amaya Pérez del Palomar[1,2]

[1]Group of Biomaterials, Aragon Institute of Engineering Research (I3A), University of Zaragoza, Zaragoza, Spain; [2]Department of Mechanical Engineering, University of Zaragoza, Zaragoza, Spain; [3]Ophthalmology Department, Miguel Servet University Hospital, Zaragoza, Spain; [4]GIMSO Research and Innovative Group, Aragon Institute for Health Research (IIS Aragon), Zaragoza, Spain; and [5]Escuela de Ingeniería y Arquitectura, Campus Río Ebro, Edificio Betancourt, C/Maria de Luna s/n, 50018 Zaragoza, Spain

(Received 6 October 2021; accepted 10 February 2022)

Associate Editor Jane Grande-Allen oversaw the review of this article.

Abstract—Machine learning approaches in diagnosis and prognosis of multiple sclerosis (MS) were analysed using retinal nerve fiber layer (RNFL) thickness, measured by optical coherence tomography (OCT). A cross-sectional study (72 MS patients and 30 healthy controls) was used for diagnosis. These 72 MS patients were involved in a 10-year longitudinal follow-up study for prognostic purposes. Structural measurements of RNFL thickness were performed using different Spectralis OCT protocols: fast macular thickness protocol to measure macular RNFL, and fast RNFL thickness protocol and fast RNFL-N thickness protocol to measure peripapillary RNFL. Binary classifiers such as multiple linear regression (MLR), support vector machines (SVM), decision tree (DT), k-nearest neighbours (k-NN), Naïve Bayes (NB), ensemble classifier (EC) and long short-term memory (LSTM) recurrent neural network were tested. For MS diagnosis, the best acquisition protocol was fast macular thickness protocol using k-NN (accuracy: 95.8%; sensitivity: 94.4%; specificity: 97.2%; precision: 97.1%; AUC: 0.958). For MS prognosis, our model with a 3-year follow up to predict disability progression 8 years later was the best predictive model. DT performed best for fast macular thickness protocol (accuracy: 91.3%; sensitivity: 90.0%; specificity: 92.5%; precision: 92.3%; AUC: 0.913) and SVM for fast RNFL-N thickness protocol (accuracy: 91.3%; sensitivity: 87.5%; specificity: 95.0%; precision: 94.6%; AUC: 0.913). This work concludes that measurements of RNFL thickness obtained with Spectralis OCT have a good ability to diagnose MS and to predict disability progression in MS patients. This machine learning approach would help clinicians to have valuable information.

Keywords—Multiple sclerosis, Machine learning, Optical coherence tomography, Retinal nerve fiber layer.

INTRODUCTION

Multiple sclerosis (MS) is a chronic inflammatory demyelinating autoimmune disease of the central nervous system (CNS) in which axonal loss is considered the main cause of disability.[61] Despite its high heterogeneity and unpredictable course, this disease is characterized by relapses with reversible neurological problems. After each relapse, a gradual neurological worsening is often observed.[34]

Axonal damage in MS patients is also widespread in the neuroretina. The visual pathway is one of the most affected systems, where inflammation, demyelination and axonal degeneration cause visual symptoms. This fact highlights the importance of studying neuroretina as a possible MS biomarker.[13,45] Optical coherence tomography (OCT) is a non-invasive, objective and reproducible method to monitor retinal damage. OCT devices provide measurements of each retinal layer and, therefore, show great potential for quantifying axonal damage by measuring peripapillary retinal nerve fiber layer (pRNFL) and macular RNFL (mRNFL) thicknesses.[30]

The use of Fourier-domain OCT (FD-OCT) provided higher resolution in relation to time-domain OCT (TD-OCT), which required long acquisition times. FD-OCT is divided into spectral-domain OCT

Address correspondence to Alberto Montolío, Escuela de Ingeniería y Arquitectura, Campus Río Ebro, Edificio Betancourt, C/Maria de Luna s/n, 50018 Zaragoza, Spain. Electronic mail: amontolio@unizar.es

(SD-OCT) and swept-source OCT (SS-OCT). Current SD-OCT and SS-OCT devices use lasers of different wavelengths to acquire OCT images in the same way. Some commercially available SD-OCT devices are RTVue (Optovue, Fremont, CA, USA), Spectralis OCT (Heidelberg Engineering, Heidelberg, Germany), SOCT Copernicus (Optopol Technology, Zawiercie, Poland), Cirrus HD-OCT (Carl Zeiss Meditec, Dublin, CA, USA), and 3D OCT-1000 (Topcon, Paramus, NJ, USA). And others with SS-OCT technology are Triton SS-OCT (Topcon, Tokyo, Japan) and Plex Elite 9000 (Carl Zeiss Meditec, Dublin, CA, USA).

OCT technique allows correlating retinal neurodegeneration and MS disability.[2,12,55] In this way, some authors demonstrated its potential, in combination with artificial intelligence (AI), as an early diagnostic tool. Garcia-Martin *et al.*[16] applied artificial neural network (ANN) to pRNFL thickness in order to analyse the ability of Spectralis OCT to diagnose MS. Cavaliere *et al.*[9] designed a computer-aided diagnosis method using support vector machine (SVM) with mRNFL and pRNFL measurements performed by Triton SS-OCT from 48 MS patients and 48 healthy controls. These database was also used by Garcia-Martin *et al.*[17] with a feed-forward neural network as a deep learning technique. Pérez del Palomar *et al.*[41] used machine learning techniques for MS diagnosis using mRNFL and pRNFL thicknesses measured by Triton SS-OCT. With a sample of 80 MS patients and 180 healthy controls, the results were promising with an accuracy of 97.2% using decision tree (DT) and mRNFL.

To analyse disability progression, there are two approaches. The first approach is to observe whether secondary-progressive (SPMS) development occurs in patients with relapse-remitting type (RRMS) such that the neurological state continues to worsen. The second approach, which is widely used, is based on the variation of expanded disability status scale (EDSS). This scale ranges from 0 (healthy control) to 10 (patient died from MS).[31,56] The disability progression depends on the EDSS measurement as a reference and the EDSS variation (ΔEDSS) over time, these standard criteria represent a relevant worsening of disability state.[22]

Most studies have based their prognosis on correlations and statistical analysis. Rothman *et al.*[47] showed that lower baseline macular volume was associated with higher 10-year EDSS scores. Paying attention to RNFL thickness, the study conducted by Schurz *et al.*[51] demonstrated how a pRNFL thinning > 1.5 μm/year was related to a higher likelihood of disability worsening. The same annual pRNFL thinning rate was used to discriminate between stable and progressing MS patients, and was associated with a 15-fold increased risk of disability progression.[8] Moreover, a baseline pRNFL thickness <88 μm was reflected in a 3-fold increased risk of EDSS progression.[7] Also ganglion cell-inner plexiform layer (GCIPL) showed promise for this purpose, where a baseline GCIPL thickness < 70 μm was independently associated with long-term disability worsening in MS.[26] Similar result was obtained by Bsteh *et al.*[6] who set the baseline macular GCIPL (mGCIPL) barrier at 77 μm and the annual mGCIPL loss rate barrier at 1 μm. Other authors reached the same conclusion, showing that GCIPL thinning >1 μm/year represented an increased risk of disability worsening.[51]

As shown above, several longitudinal studies demonstrated the relationship between RNFL thickness and disability progression. After proving the good performance of AI with OCT data for the diagnosis of this disease, the next step could be to apply AI using OCT data for MS prognosis. However, more recent studies have limited the data to those obtained using the tests included in McDonald criteria such as magnetic resonance imaging (MRI) or evoked potential (EP)[53]. Zhao *et al.*[65] compared SVM, logistic regression (LR), random forest (RF) and several ensemble classifiers (EC) to predict ΔEDSS up to 5 years after the baseline using MRI data acquired in the first 2 years. The work performed by Yperman *et al.*[62] used RF and LR to predict disability progression after 2 years using 2-year EP time series. Seccia *et al.*[52] predicted whether the disease would progress from RRMS to SPMS applying different machine learning approaches to MRI and Liquor analysis data from the last available visit or the whole clinical history. Another study evaluated LR, SVM, DT and EC for MS prognosis between 2-year follow-up and baseline also using MRI data.[27]

As can be seen, previous studies predicted disability progression in the short term and did not focus machine learning approaches on OCT data for MS prognosis.[40] However, we proposed the use of AI to predict long-term disability state using OCT data. In our previous work,[36] RNFL thickness measured by Cirrus HD-OCT showed a high performance for MS prognosis. Along the same lines, in this work, different AI approaches were applied to RNFL thicknesses measured by Spectralis OCT in order to analyse which acquisition protocol and which classifier works best for predicting disability progression in the long term.

TABLE 1. General data and retinal nerve fiber layer (RNFL) data, measured by Spectralis optical coherence tomography (OCT), from 72 patients with multiple sclerosis (MS) and 30 healthy controls.

	MS patients (n = 72)	Healthy controls (n = 30)	p-value
General data			
Age [years]	45.94 ± 10.85	48.78 ± 14.70	0.247
Sex [M–F]	19–53	5–25	
BCVA [Snellen]	0.90 ± 0.24	1.00 ± 0.11	0.020
Fast macular thickness protocol			
Total volume [mm^3]	0.78 ± 0.16	0.96 ± 0.11	< 0.001
Central fovea th. [μm]	12.32 ± 2.78	12.40 ± 1.77	0.818
Inner nasal th. [μm]	19.83 ± 4.86	22.50 ± 2.70	< 0.001
Outer nasal th. [μm]	39.89 ± 13.68	52.53 ± 6.82	< 0.001
Inner superior th. [μm]	21.32 ± 4.18	24.43 ± 2.11	< 0.001
Outer superior th. [μm]	31.15 ± 7.36	38.50 ± 5.10	< 0.001
Inner temporal th. [μm]	17.65 ± 2.06	17.97 ± 1.52	0.488
Outer temporal th. [μm]	18.31 ± 2.14	19.67 ± 1.94	< 0.001
Inner inferior th. [μm]	22.50 ± 4.46	27.13 ± 3.20	< 0.001
Outer inferior th. [μm]	31.69 ± 8.13	40.70 ± 7.95	< 0.001
Fast RNFL thickness protocol			
Mean th. [μm]	84.39 ± 15.15	101.37 ± 8.60	< **0.001**
Temporal th. [μμμμm]	59.53 ± 16.69	73.13 ± 12.85	< **0.001**
Superotemporal th. [μm]	115.36 ± 23.50	134.77 ± 19.87	**0.001**
Inferotemporal th. [μm]	118.78 ± 27.44	146.40 ± 19.00	< **0.001**
Nasal th. [μm]	67.56 ± 18.39	75.63 ± 12.73	**0.005**
Superonasal th. [μm]	90.38 ± 21.85	118.20 ± 27.33	< **0.001**
Inferonasal th. [μm]	96.51 ± 26.95	115.00 ± 17.88	< **0.001**
Fast RNFL-N thickness protocol			
Mean th. [μm]	83.77 ± 17.69	101.55 ± 9.69	0.172
PMB th. [μm]	44.73 ± 12.91	55.83 ± 8.84	< **0.001**
N/T ratio	1.29 ± 0.46	1.14 ± 0.35	0.082
Superonasal th. [μm]	96.62 ± 27.13	107.34 ± 22.90	**0.010**
Nasal th. [μm]	67.61 ± 19.73	79.62 ± 15.36	< **0.001**
Inferonasal th. [μm]	100.68 ± 28.01	118.14 ± 24.77	**0.005**
Inferotemporal th. [μm]	114.25 ± 29.19	147.72 ± 23.17	< **0.001**
Temporal th. [μm]	55.15 ± 14.87	73.03 ± 13.35	< **0.001**
Superotemporal th. [μm]	112.79 ± 28.63	135.28 ± 18.39	< **0.001**

p value, based on Wilcoxon test, is used to compare data between MS patients and healthy controls. Statistically significant differences ($p < 0.05$) are represented in bold.

BCVA best-corrected visual acuity, *th* thickness, *PMB* papillomacular bundle, *N/T* nasal/temporal.

MATERIAL AND METHODS

Study Population

The study procedure was approved by the Ethics Committee of Clinic Research in Aragon (CEICA) and by the Ethics Committee of Miguel Servet University Hospital (Zaragoza, Spain). This work was performed in accordance with the tenets of the Declaration of Helsinki. All participants provided written informed consent to participate in the study.

This work includes a cross-sectional study and a longitudinal study. The cross-sectional study enrolled 72 MS patients (19 males and 53 females) and 30 healthy controls (5 males and 25 females). The age of MS patients ranged from 25 to 72 years with a mean of 45.94 years, while for healthy controls if ranged from 26 to 73 with a mean of 48.78 years (see Table 1). MS patients were diagnosed by a neurologist based on the 2010 revision of the McDonald Criteria [43]. In the longitudinal study, 72 MS patients were evaluated at several visits until the 10-year follow-up was completed. The participants had no concomitant ocular diseases, nor any history of retinal pathology or systemic conditions that could affect the visual function. All participants underwent neuro-ophthalmological evaluations, including best-corrected visual acuity (BCVA) to quantify the level of vision and EDSS to register MS-associated disability.

The required inclusion criteria were: BCVA of 20/40 or higher, refractive error within ±5.00 diopters equivalent sphere and ± 2.00 diopters astigmatism, transparent ocular media (nuclear colour/opalescence, cortical or posterior subcapsular lens opacity <1), according to the Lens Opacities Classification System III[11]. From these 102 subjects of white European origin, one randomly selected eye was analysed to avoid potential bias by interrelation between eyes of the same subject. In subjects with exclusion criteria in one eye, the other eye was selected.

OCT Evaluation

Structural measurements of RNFL were performed using the Spectralis OCT (Heidelberg Engineering, Inc., Heidelberg, Germany). The Spectralis OCT uses a blue quality bar in the image to indicate signal strength. The quality score ranges from 0 (poor quality) to 40 (excellent quality). Only images with quality higher than 25 were analysed. A real-time eye-tracking system measures eye movements and provides feedback to the scanning mechanism to stabilize the retinal position on the B-scan. This system enables sweep averaging at each B-scan location to reduce speckle noise. The average number of scans to produce each circular B-scan was nine. The TruTrack eye tracking technology (Heidelberg Engineering) recognizes, locks onto, follows the patient's retina during scanning and automatically places follow-up scans to ensure accurate monitoring of disease progression.[19] All scans were obtained by operators with extensive experience in the use of the OCT device. Databases were performed in accordance to the quality control criteria (OSCAR-IB) and the Advised Protocol for OCT Study Terminology and Elements (APOSTEL) criteria.[14,50]

This OCT device allows to measure the RNFL thickness in different areas depending on the protocol used (see Fig. 1). Spectralis OCT directly provides RNFL thickness data from OCT images. This automated segmentation was performed with the manufacturer's software Heidelberg Eye Explorer (HEYEX) which consist of a multilayer segmentation algorithm (Heidelberg Engineering). **Fast macular thickness protocol**: a map around the fovea showing the total volume and the mRNFL thickness in nine sectors (central fovea, inner nasal, outer nasal, inner superior, outer superior, inner temporal, outer temporal, inner inferior and outer inferior). Three concentric circles (1 mm, 3 mm and 6 mm) define these nine macular sectors established by the Early Treatment Diabetic Retinopathy Study (ETDRS). **Fast RNFL thickness protocol**: a 3.5 mm diameter circle scan centred on the optic disc showing the mean pRNFL thickness and the pRNFL thickness in six sectors (superonasal, nasal, inferonasal, inferotemporal, temporal and superotemporal). This protocol also generates a database with pRNFL thickness measurements at all 768 points registered during circular peripapillary scan acquisition. The image sweep is done from temporal to temporal. **Fast RNFL-N thickness protocol:** like fast RNFL thickness protocol, a map around the optic disc with the mean pRNFL thickness and the pRNFL thickness in six sectors, and also the 768 sector pRNFL thicknesses. Two extra data are the papillomacular bundle (PMB) thickness and nasal/temporal (N/T) ratio. In this protocol, unlike fast RNFL thickness protocol, the sweep is done from nasal to nasal.

FIGURE 1. Schematic representation of Spectralis OCT▶ acquisition protocols on a right eye retina. Fast macular thickness protocol measures total volume and macular RNFL (mRNFL) thickness in nine sectors (*CF* central fovea, *IN* inner nasal, *ON* outer nasal, *IS* inner superior, *OS* outer superior, *IT* inner temporal, *OT* outer temporal, *II* inner inferior, *OI* outer inferior). Fast RNFL thickness protocol measures peripapillary RNFL (pRNFL) thickness by providing mean pRNFL thickness (G) and pRNFL thickness in six sectors *NS* superonasal, *N* nasal, *NI* inferonasal, *TI* inferotemporal, *T* temporal, *TS* superotemporal. This protocol also generates 768 pRNFL thickness measurements with a circular sweep from temporal to temporal (counterclockwise). Fast RNFL-N thickness protocol differs from the previous one in two aspects: it adds papillomacular bundle (PMB) thickness and nasal/temporal (N/T) ratio, and the circular sweep is performed from nasal to nasal (clockwise). *OD* right eye, *OCT* optical coherence tomography, *RNFL* retinal nerve fiber layer.

Statistical Analysis

Statistical analysis was performed with Matlab (version 2020b, Mathworks Inc., Natick, MA). The Kolmogorov-Smirnov test was used to analyse the normality of numerical variables. Comparison between groups was performed using the Wilcoxon test as an alternative to the Student's t-test due to the non-normality of the variables. A p-value < 0.05 was considered statistically significant.

Machine Learning Pipeline

The aim of this work was to diagnose MS disease and predict the disability progression in MS patients using clinical data and OCT data in combination with machine learning techniques. To solve these problems, it is necessary to divide the method into five steps: data preprocessing, Variable selection, model building, cross-validation and model assessment (see Fig. 2).

Data Preprocessing

Data preprocessing is a very important step in machine learning. Data cleaning, missing data resolution and data balancing are included here. We had to eliminate those subjects with incomplete data and remove from the study those variables that had not been collected in a large number of subjects.

Given a binary classification problem, the data are class-imbalanced when the majority of the subjects represent one class. In this way, many classification algorithms have low predictive accuracy for the infre-

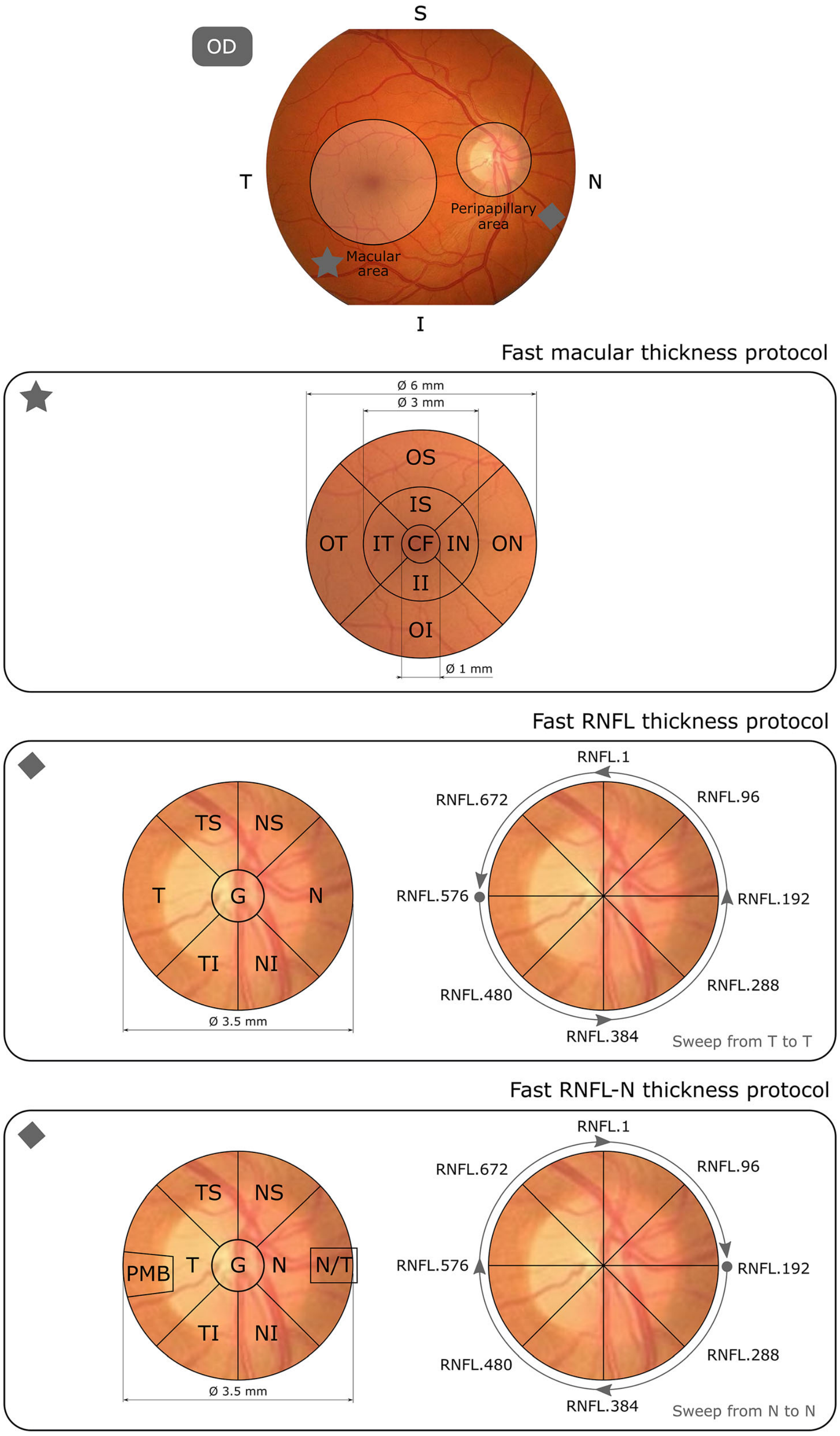
S
OD
T
N
Peripapillary area
Macular area
I
Fast macular thickness protocol
Ø 6 mm
Ø 3 mm
OS
IS
OT
IT
CF
IN
ON
II
OI
Ø 1 mm
Fast RNFL thickness protocol
TS
NS
T
G
N
TI
NI
Ø 3.5 mm
RNFL.1
RNFL.672
RNFL.96
RNFL.576
RNFL.192
RNFL.480
RNFL.288
RNFL.384
Sweep from T to T
Fast RNFL-N thickness protocol
TS
NS
PMB
T
G
N
N/T
TI
NI
Ø 3.5 mm
RNFL.1
RNFL.672
RNFL.96
RNFL.576
RNFL.192
RNFL.480
RNFL.288
RNFL.384
Sweep from N to N

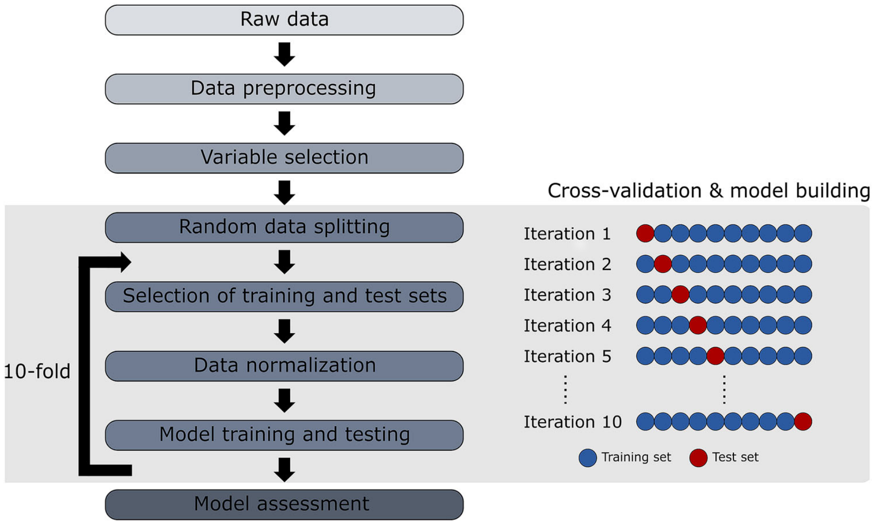

FIGURE 2. Machine learning pipeline of the proposed method consists of five steps: data preprocessing, variable selection, 10-fold cross-validation, model building and model assessment.

quent class. The problem of class imbalance is closely related to cost-sensitive learning, in which the costs of errors, per class, are not equal. It is much worse to falsely diagnose a MS patient as healthy control (false negative) than to misdiagnose a healthy control as MS patient (false positive). A false negative could result in the loss of life, so is much more expensive than a false positive.

In order to improve the classification performance of class-imbalanced data, synthetic minority over-sampling technique (SMOTE) was used. SMOTE is widely used to balanced clinical data in machine learning approaches.[60] This method works by resampling the minority class so that the resulting dataset contains an equal number of positive and negative subjects. To increase the sample of the minority class, SMOTE synthesises new cases. To do so, a data point is randomly selected from the minority class and its k-nearest neighbours (k-NN) are determined. Following the consensus, 5 neighbours were used. The new synthetic subject is a combination of the randomly selected data point and its neighbours.[24]

Variable Selection

In the development of predictive models, the selection of relevant variables has several advantages such as reducing overfitting, improving predictive accuracy and reducing computational cost. In machine learning, a rule of thumb is to have a number of subjects per class of at least ten time the number of variables.[39] To perform this variable selection, least absolute shrinkage and selection operator (LASSO) and sequential forward selection (SFS) were used to remove the irrelevant variables. LASSO regression imposes a constraint on the model variables that produces regression coefficients so that some of these variables are reduced to zero and removed from the dataset, retaining only the good features of the data.[57] SFS method is based on trying to minimize the objective function called misclassification rate over all possible subsets of features. To minimize this rate, this sequential forward algorithm incorporates features while evaluating the objective function until adding more features does not decrease the objective function.[54]

Model Building

The predictive models were developed for two purposes: MS diagnosis and MS prognosis. The classifiers used for model building were implemented in Matlab (version 2020b, Mathworks Inc., Natick, MA) using the Statistics and Machine Learning Toolbox. Classifier performance was optimised by hyperparameter optimization, which attempts to minimise the cross-validation loss.

Multiple Linear Regression Multiple linear regression (MLR) is used to estimate the relationship between one or more explanatory variables and a response variable by fitting a linear equation to observed data. MLR can be very useful in understanding the role that predictors play in the predictive model.[38] This is the simplest linear model to be tested in a binary classification problem.[32]

Support Vector Machine In a binary classification problem, SVM seeks the optimal hyperplane that separates two different classes with the maximum margins. SVM supports the mapping of predictor data using kernel functions with an optimised kernel scale value to increase the separability of the hyperplane for non-separable problems.[58] In case of non-separable classes, this classifier imposes a penalty factor, called box constraint, whose aim is to avoid overfitting. This classifier has been extensively tested in the literature, both for MS diagnosis[9,41] and MS prognosis.[65]

K-Nearest Neighbours The k-NN algorithm is one of the most used classifiers in machine learning.[10,21,33] This algorithm consists in associating the training data with a distance function and the class choice function based on the classes of nearest neighbours. Before classifying a new subject, it should be compared with another subject using a similarity measure. Its k-nearest neighbours are considered and the class that appears most among them is assigned to the new subject. In general, a number of neighbours greater than one is used, since such a small number could lead to overfitting. The neighbours are weighted by the distance from the new subjects to be classified.[63]

Decision Tree In the DT classifier, a tree is developed and it contains a predefined target variable. The structure of a DT contains a root node, several internal nodes and several leaf nodes. This tree is traversed from root to leaf for decision making and this process is carried out until the criteria are met.[10] The minimum number of leaf node observations and the minimum number of branch observations are the parameters with which the depth of the trees can be controlled. The ability of DT to accurately classify between MS patients and healthy controls and to predict the short-term course of MS has also been previously investigated.[3,63]

Naïve Bayes Based on Bayesian theory for density estimation, the Naïve Bayes (NB) classifier assumes that predictor variables are independent of each other. This assumption of independence increases the simplicity of the model. Kernel density estimation, defined by the smoothing parameter called bandwidth, is one of the most commonly used data distributions. The choice of this hyperparameter determines the smoothness of the density plot, so it is preferable to choose a bandwidth as small as the data allow. The performance of the NB algorithm is comparable to that of the DT due to its high accuracy and speed, as well as fast training and low computational complexity.[20]

Ensemble Classifier Another possibility is to combine several algorithms using ensemble methods. EC generates several base classifiers from which a new classifier is derived which works better than any constituent classifier. The motivation is to combine weak models to produce a powerful ensemble.[24] LogitBoost was used as the ensemble aggregation algorithm to train the set of boosted classification trees. There are several hyperparameters to optimize the performance of this classifier: number of learning cycles, learning rate and minimum number of leaf node observations.[5] In this structure, the number of learning cycles corresponds to the number of classification trees. The learning rate limits the contribution of each new classification tree added in the algorithm. These type of ensemble learning approaches showed good performance in previous studies with the same purposes as this work.[36,65]

Long Short-Term Memory Recurrent neural network (RNN), particularly those that work by learning sequences, such as long short-term memory (LSTM), are very useful in the context of disability course prediction. In previous works comparing several classifiers with this objective, this method showed the best results.[36,52] LSTM models are able to work with long-range dependencies and non-linear dynamics. Another sequence models, such as Markov models, conditional random fields and Kalman filters, deal with sequential data but fail to learn the long-range dependencies. However, this RNN can learn representations and can discover unexpected structures.[28] The LSTM neural network implemented in this work had the following structure: a sequence input layer, a bidirectional LSTM layer with predefined hidden layers containing the information recalled between time steps, a fully connected layer, a softmax layer and a final classification output layer. The input layer inputs the features into the network. The size of the fully connected layer correspond to the number of classes. Finally, softmax layer converts a vector of real values into a vector of probabilities. This structure can be improved by optimising the number of hidden layers, the epochs and the mini-batch size. A mini-batch is a subset of the training set used to evaluate the gradient of the loss function and update the weights. An epoch is the complete passage of the algorithm over the entire training set using mini-batches.

Cross-Validation

Since our dataset was not large enough to use hold-out validation, k-fold cross-validation was used to reduce the risk of overfitting. In addition, this method ensures that the result is independent of the initial division.[46] The data set was randomly divided into equal k-fold, using 1-fold as a test set and the remaining folds as training set. This process is repeated k-times until each fold has been used as a test set and the overall performance is calculated by the combination of these k-iterations. A 10-fold cross-validation was used, as it is the general recommendation in the machine learning field due to its balance between performance and computational cost.[20]

Data normalization was performed to improve the quality of our dataset. The normalization used for numerical variables consists of the normalization of the training set (mean of 0 and standard deviation of 1) and the normalization of the test set using the mean and standard deviation of the training set. With this method, the classification algorithms do not have access to future information. Since these algorithms work with numerical variables, categorical variables, such as sex, MS subtype, optic neuritis antecedent and relapse in preceding year, had to be encoded into numerical values using one-hot encoding.[44]

Model Assessment

Confusion matrix was used as a performance measurement because it is extremely useful to determine accuracy, sensitivity, specificity, precision and negative predictive value (NPV). First, four parameters have to be defined: true positives (TPs) are the positive data correctly classified and true negatives (TNs) are the negative data correctly classified, false positives (FPs) are the negatives classified as positives and false negatives (FNs) are the positives classified as negatives. Accuracy provides the percentage of correctly classified subjects. Sensitivity is used to determine the proportion of positives that are correctly identified and specificity is used to determine the proportion of negatives that are correctly identified. Precision expresses the percentage of the predicted positives that are actually positive and NPV is the percentage of the predicted negatives that are actually negatives.

$$\mathrm{Accuracy(acc)} = \frac{\mathrm{TP}+\mathrm{TN}}{\mathrm{TP}+\mathrm{TN}+\mathrm{FP}+\mathrm{FN}}, \tag{1}$$

$$\mathrm{Sensitivity(sens)} = \frac{\mathrm{TP}}{\mathrm{TP}+\mathrm{FN}}, \tag{2}$$

$$\mathrm{Specificity(spec)} = \frac{\mathrm{TN}}{\mathrm{TN}+\mathrm{FP}}, \tag{3}$$

$$\mathrm{Precision(prec)} = \frac{\mathrm{TP}}{\mathrm{TP}+\mathrm{FP}}, \tag{4}$$

$$\mathrm{Negativepredictivevalue(NPV)} = \frac{\mathrm{TN}}{\mathrm{TN}+\mathrm{FN}}, \tag{5}$$

There are more parameters to evaluate a binary classification. F1 score is the harmonic mean of precision and sensitivity and Fowkles–Mallows index (FM) is the geometric mean of precision and sensitivity. However, these parameters do not take into account TN and give equal importance to precision and sensitivity when, in practice, different misclassifications cause different costs. For example, a FN (MS patient classified as healthy control) is worse than a FP (healthy control classified as MS patient). To solve that, we used Matthews correlation coefficient (MCC), which is a correlation coefficient between actual values and predicted values. It ranges from -1 to 1, where 0 indicates a random classification. Since there is no perfect way to describe the confusion matrix by a single number, this parameter is one of the most informative because it takes into account true and false positives and true and false negatives.

$$F1\,\mathrm{score} = 2\frac{\mathrm{Prec}*\mathrm{Sens}}{\mathrm{Prec}+\mathrm{Sens}}, \tag{6}$$

$$\mathrm{FM} = \sqrt{\mathrm{Prec}*\mathrm{Sens}}, \tag{7}$$

$$\mathrm{MCC} = \frac{\mathrm{TP}*\mathrm{TN}-\mathrm{FP}*\mathrm{FN}}{\sqrt{(\mathrm{TP}+\mathrm{FP})(\mathrm{TP}+\mathrm{FN})(\mathrm{TN}+\mathrm{FP})(\mathrm{TN}+\mathrm{FN})}}, \tag{8}$$

Another interesting parameter is Cohen's kappa coefficient (κ), which is used to determine the degree of agreement between actual and predicted values. It is a more robust measure because it takes into account the possibility of a correct classification by chance.

$$\kappa = \frac{\mathrm{Acc}-\mathrm{Random\,acc}}{1-\mathrm{Random\,acc}}, \tag{9}$$

$$\mathrm{Random\,Acc} = \frac{(\mathrm{TN}+\mathrm{FP})(\mathrm{TN}+\mathrm{FN})+(\mathrm{FN}+\mathrm{TP})(\mathrm{FP}+\mathrm{TP})}{(\mathrm{TP}+\mathrm{TN}+\mathrm{FP}+\mathrm{FN})^2}, \tag{10}$$

The receiver operating characteristic (ROC) curve, a graph that illustrates the diagnostic ability of a classification algorithm, was also analysed. The ROC curve is drawn by plotting the true positive rate (TPR) or sensitivity against the false positive rate (FPR) as the discrimination threshold is varied. The area under the curve (AUC) provides a measurement of performance at all possible classification threshold.

MS Diagnosis Model

A MS diagnosis model was developed using the data from 72 MS patients and 30 healthy controls evaluated in our cross-sectional study. For this model, we used three datasets, one per each protocol. **Dataset 1**: general data and fast macular thickness protocol (13 features). **Dataset 2**: general data and fast RNFL thickness protocol (778 features). **Dataset 3**: general data and fast RNFL-N thickness protocol (780 features).

This cross-sectional study was class-imbalanced, so SMOTE was used to resample healthy controls class. In this way, the data turned out to be 72 MS patients and 72 healthy control, a total of 144 subjects. It can be seen that these three datasets contained too many variables compared to the number of subjects per class, so it was necessary to perform variable selection. LASSO was applied to reduce the datasets to five, six or seven variables, depending on the dataset (see Fig. 3). As previous works also demonstrated,[29,36,37] the reduced datasets after applying LASSO showed a better model performance. Finally, the six classifiers were tested using the 10-fold cross-validation for model assessment. The LSTM was not used in this model because it is designed to work with time series.

MS Prognosis Model

Here, the data from our longitudinal study were used to develop a model capable or predicting the long-term course of disability state in MS patients. The 72 MS patients were evaluated in seven visits: a baseline visit followed by five annual visits and a final visit 10 year after the start of the follow-up. This model was carried to know the disability state of MS patients in the future, distinguishing between patients whose disability state will get worse and patients whose disability state will remain in a similar neurological state. We established, following the standard definition of disability progression,[22] that a MS patient gets worse when the criteria shown in Table 2 are met between the target future time and the time the prediction is made. In contrast, MS patients whose EDSS values do not meet the standard criteria are considered patients who remain in a similar disability state. We proposed to make a prediction as soon as possible, for this reason, we developed a first model using the data from the first 2 years of the follow-up to predict the disability state 9 years later. These two data points are the minimum necessary for the classifiers to have a sequence to work with. We developed a second model using data from the first 3 years to evaluate whether delaying the prediction by 1 year leads to an increase in the model performance. With this second model, the disability state is predicted 8 years later.

Taking into account these considerations, MS patients turned out to be 32 patients with disability progression and 40 patients without disability progression in both models. Therefore, we used six datasets, one per protocol in each model. **Dataset 4**: general data, MS data and fast macular thickness protocol (19 features with 2-year follow-up). **Dataset 5**: general data, MS data and fast RNFL thickness protocol (784 features with 2-year follow-up). **Dataset 6**: general data, MS data and fast RNFL-N thickness protocol (786 features with 2-year follow-up). **Dataset 7**: general data, MS data and fast macular thickness protocol (19 features with 3-year follow-up). **Dataset 8**: general data, MS data and fast RNFL thickness protocol (784 features with 3-year follow-up). **Dataset 9**: general data, MS data and fast RNFL-N thickness protocol (786 features with 3-year follow-up).

As in MS diagnosis model, SMOTE was applied to resample the minority class, in these models, it was the patients with ΔEDSS $\geq$ criteria. Therefore, the class-balanced data was 40 patients with ΔEDSS $\geq$ criteria and 40 patients with ΔEDSS $<$ criteria. Another point was the variable selection, in this longitudinal study we had fewer subjects so we had to minimize the number of features, reducing the risk of overfitting and increasing the interpretability. As can be seen in Fig. 4, thanks to LASSO regression, the datasets were reduced to four or even three features.

After the variable selection process, all seven classifiers were evaluated, using 10-fold cross-validation, to determine their capability to predict the long-term course of disability state in MS patients.

RESULTS

Several classifiers were tested to analyse the model performance of these two predictive models using three Spectralis OCT acquisition protocols. The accuracy obtained for all classification algorithms are summarised in Fig. 5.

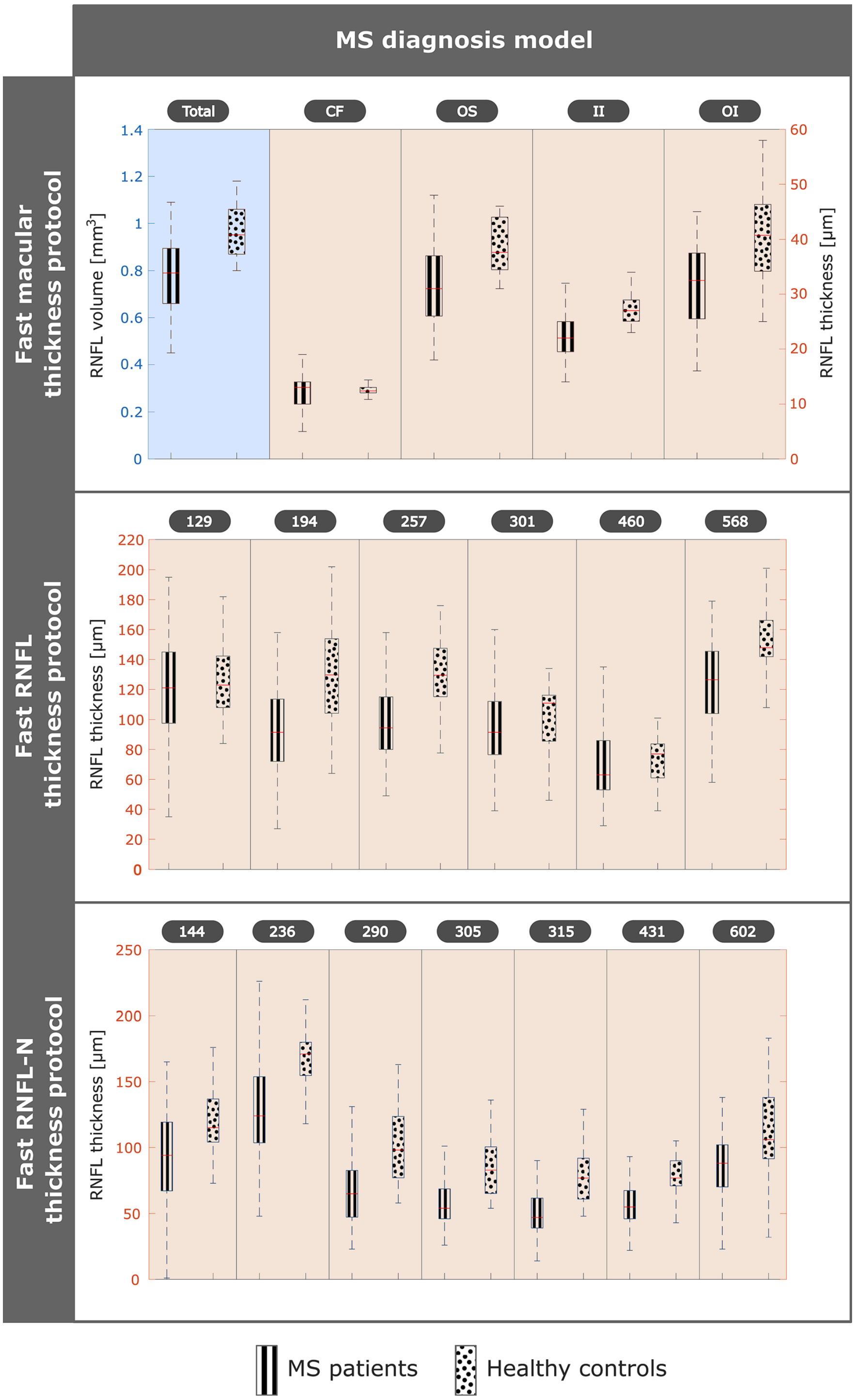

FIGURE 3. Variable selection for multiple sclerosis (MS) diagnosis model after applying least absolute shrinkage and selection operator (LASSO) to balanced data with 72 MS patients and 72 healthy controls. Raw dataset 1 included general data and fast macular thickness protocol (13 features), raw dataset 2 included general data and fast retinal nerve fiber layer (RNFL) thickness protocol (778 features), and raw dataset 3 included general data and fast RNFL-N thickness protocol (780 features). *CF* central fovea, *OS* outer superior, *II* inner inferior, *OI* outer inferior.

TABLE 2. Standard criteria for disability progression in multiple sclerosis patients based on expanded disability status scale (EDSS).

Reference EDSS	Criteria
0	An increase of 1.5 or more points in EDSS (ΔEDSS ≥ 1.5)
1 to 5.5	An increase of 1 or more points in EDSS (ΔEDSS ≥ 1)
6 and up	An increase of 0.5 or more points in EDSS (ΔEDSS ≥ 0.5)

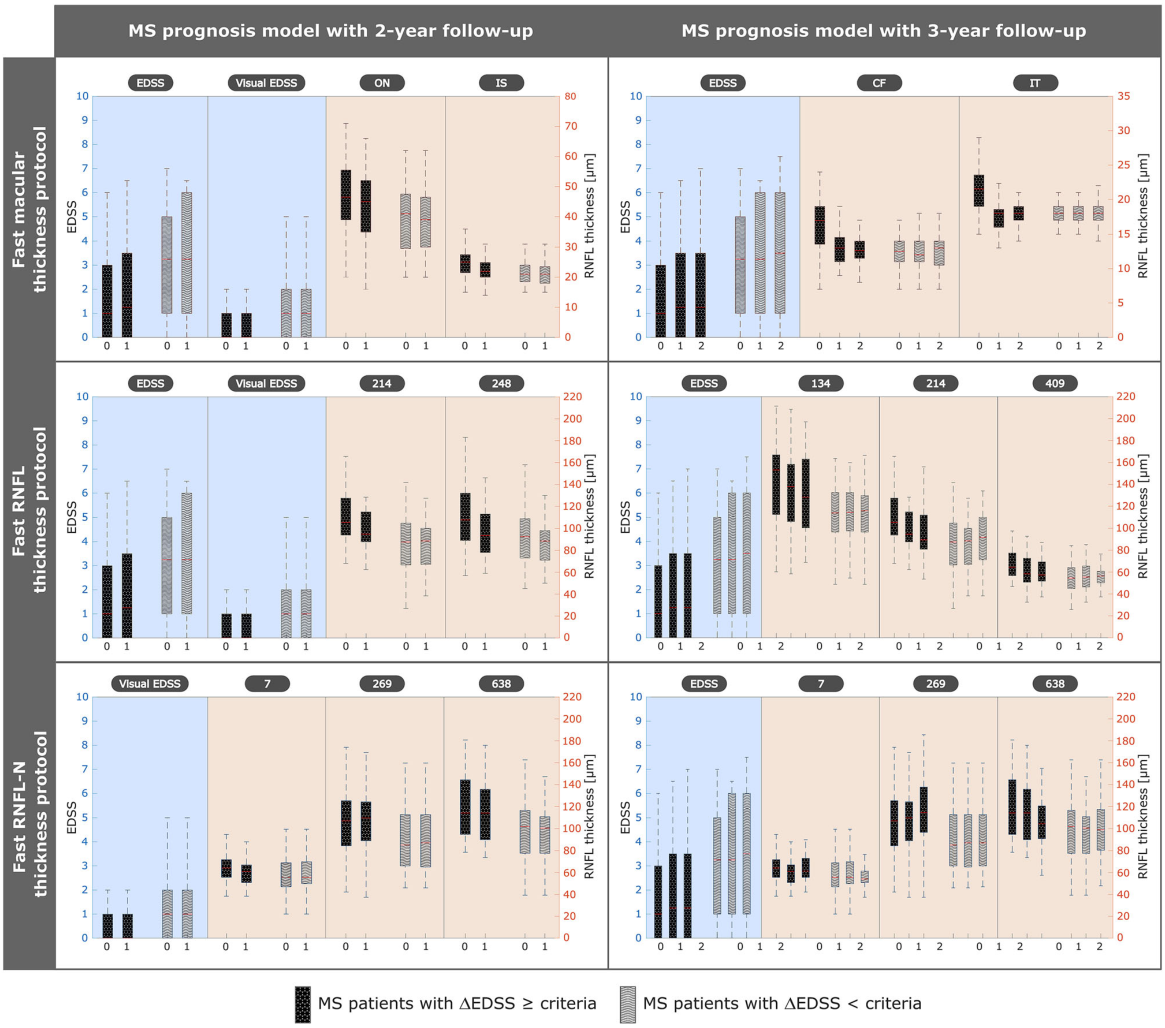

FIGURE 4. Variable selection for multiple sclerosis (MS) prognosis models after applying least absolute shrinkage and selection operator (LASSO) to balanced data with 40 MS patients with ΔEDSS ≥ criteria and 40 MS patients with ΔEDSS < criteria. Raw dataset 4 included general data, MS data and fast macular thickness protocol (19 features with 2-year follow-up); raw dataset 5 included general data, MS data and fast retinal nerve fiber layer (RNFL) thickness protocol (784 features with 2-year follow-up): and raw dataset 6 included general data, MS data and fast RNFL-N thickness protocol (786 features with 2-year follow-up). Raw dataset 7 included general data, MS data and fast macular thickness protocol (19 features with 2-year follow-up); raw dataset 8 included general data, MS data and fast retinal nerve fiber layer (RNFL) thickness protocol (784 features with 2-year follow-up): and raw dataset 9 included general data, MS data and fast RNFL-N thickness protocol (786 features with 2-year follow-up). Values 0, 1 and 2 on the x-axis represent the years of the 10-year follow-up. *EDSS* expanded disability status scale, *ON* outer nasal, *IS* inner superior, *CF* central fovea, *IT* inner temporal.

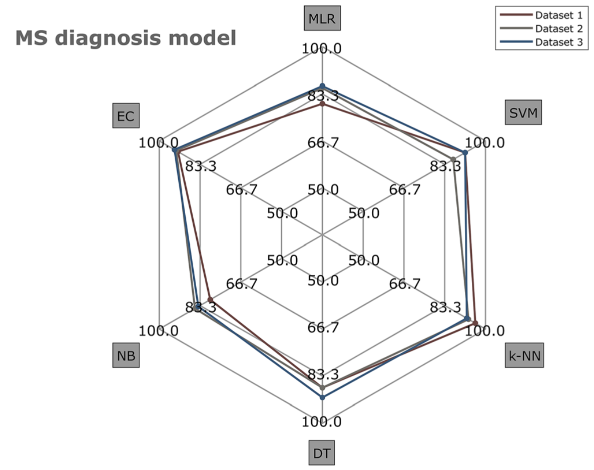
MS diagnosis model
MLR
SVM
k-NN
DT
NB
EC
Dataset 1
Dataset 2
Dataset 3
50.0
66.7
83.3
100.0

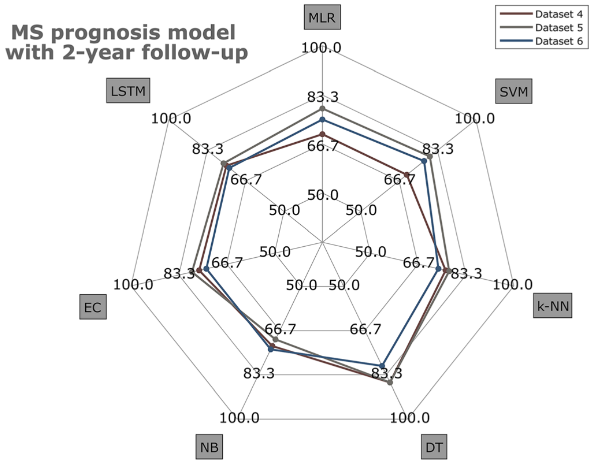
MS prognosis model
with 2-year follow-up
MLR
SVM
k-NN
DT
NB
EC
LSTM
Dataset 4
Dataset 5
Dataset 6
50.0
66.7
83.3
100.0

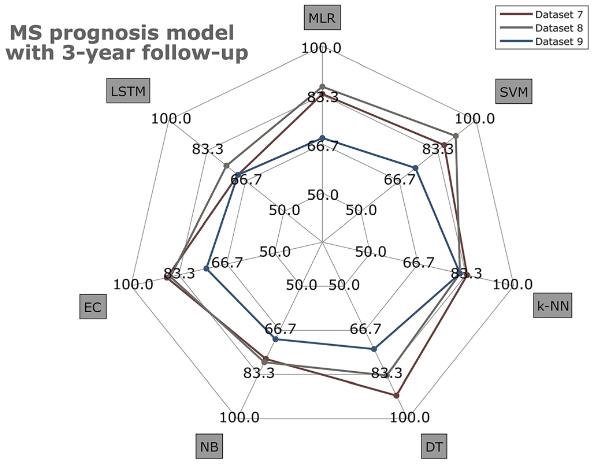
MS prognosis model
with 3-year follow-up
MLR
SVM
k-NN
DT
NB
EC
LSTM
Dataset 7
Dataset 8
Dataset 9
50.0
66.7
83.3
100.0

◀FIGURE 5. Accuracy of different classifiers for multiple sclerosis (MS) diagnosis and MS prognosis models. Datasets 1, 4 and 7 (brown colour) correspond to clinical data and fast macular thickness protocol. Datasets 2, 5 and 8 (grey colour) correspond to clinical data and fast retinal nerve fiber layer (RNFL) thickness protocol. Datasets 3, 6 and 9 (blue colour) correspond to clinical data and fast RNFL-N thickness protocol. The tested algorithms were: *MLR* multiple linear regression, *SVM* support vector machine, *k-NN* k-nearest neighbours, *DT* decision tree, *NB* Naïve Bayes, *EC* ensemble classifier, *LSTM* long short-term memory, neural network.

MS Diagnosis Model

After balancing the cross-sectional data by SMOTE, variable selection was performed using data from 72 MS patients and 72 healthy controls. As can be seen in Fig. 3, the result obtained with LASSO was as follows: five features (total volume, CF, OS, II and OI) for dataset 1, six features (points 129, 194, 257, 301, 460 and 568) for dataset 2, and seven features (points 144, 236, 290, 305, 315, 431 and 602) for dataset 3. The location of all these features is shown in Fig. 1.

For dataset 1, the best accuracy (95.8%) was obtained using k-NN with 4 as number of nearest neighbours and Euclidean distance as distance metric between neighbours. Looking at Table 1, the variables chosen by LASSO showed a statistically significant difference ($p < 0.05$) between MS patients and healthy controls. In case of dataset 2, k-NN and EC correctly classified 134 out of 144 (4 FPs and 6 FNs, see confusion matrix in Fig. 6), giving an accuracy of 93.1%. The optimal hyperparameters were: 3 nearest neighbours with cosine distance metric for k-NN, and 100 learning cycles, 0.487 learning rate and the minimum of 1 leaf node observation for EC. Finally, for dataset 3, the best classifier was EC with an AUC of 0.951 (see ROC curve in Fig. 7). In this case, its optimal configuration was 65 classification trees, a learning rate of 0.033 and a minimum of 4 observations per leaf node. It can be seen that AUC is equal to accuracy since raw data was balanced in the data preprocessing step.

MS Prognosis Model

For MS prognosis, two predictive models were proposed: the first used data from the first two years of follow-up to predict disability state 9 years later and the second added one more data point to predict disability progression 8 years later. With this second model, it can be assessed whether delaying the prediction by 1 year increases the model performance. After resampling the minority class, the class-balanced data was 40 MS patients with ΔEDSS $\geq$ criteria and 40 MS patients with ΔEDSS $<$ criteria.

For clinical data and fast macular thickness protocol, variable selection turned out to be four features (EDSS, visual EDSS, ON and IS) for the first model (dataset 4) and three features (EDSS, CF and IT) for the second model (dataset 7). As can be seen in Fig. 4, EDSS was chosen for both models. The difference between patients with disability progression and without disability progression was significant for EDSS and visual EDSS at the three data points, while for ON, IS, CF and IT was significant only at the baseline (see Table 3). For datasets with fast RNFL thickness protocol, four features (EDSS, visual EDSS, points 214 and 248) were selected in dataset 5 using 2-year follow-up and four features (EDSS, points 134, 214 and 409) in dataset 8 using 3-year follow-up. In these two datasets, both EDSS and point 214 were in the feature selection performed by LASSO. Finally, with data from fast RNFL-N thickness protocol, variable selection was almost the same for both models: four features (visual EDSS, points 7, 269 and 638) to predict disability progression 9 years later (dataset 6) and four features (EDSS, points 7, 269 and 638) to predict 8 years later (dataset 9).

First, we evaluated the ability of these classifiers to predict whether or not a MS patient will get worse using data from three Spectralis OCT acquisition protocols collected at the first 2 years (see Fig. 5 for accuracy of all classifiers). The best result was an 86.3% accuracy obtained by DT in dataset 4 (minimum of 1 observation per leaf node and 10 observations per branch) and in dataset 5 (minimum of 4 observations per leaf node and 10 observations per branch). As can be seen in the confusion matrices, there were 3 FNs in dataset 4 compared to 5 FNs in dataset 5. For dataset 6, the best classifier was also DT with an accuracy of 80.0% and its hyperparameters were a minimum of 6 leaf node observations and 10 branch observations.

Second, adding an additional data point to the previous model, we tested whether delaying the prediction by 1 year results in an increase in the model performance. For dataset 7, the predictions generated by DT were correct in 73 of 80 cases (3 FPs and 4 FNs, see confusion matrix in Figure 6) giving an accuracy of 91.3%. The same accuracy and AUC were obtained for dataset 8 using SVM whose optimal structure was a box constraint of 0.431 and a kernel scale of 0.109. Finally, k-NN correctly classified 68 out of 80 MS patients using dataset 9 with an AUC of 0.850 (see Fig. 7). The hyperparameter optimization showed 4 neighbours as the optimal number of nearest neighbours and Euclidean distance as the distance metric between them.

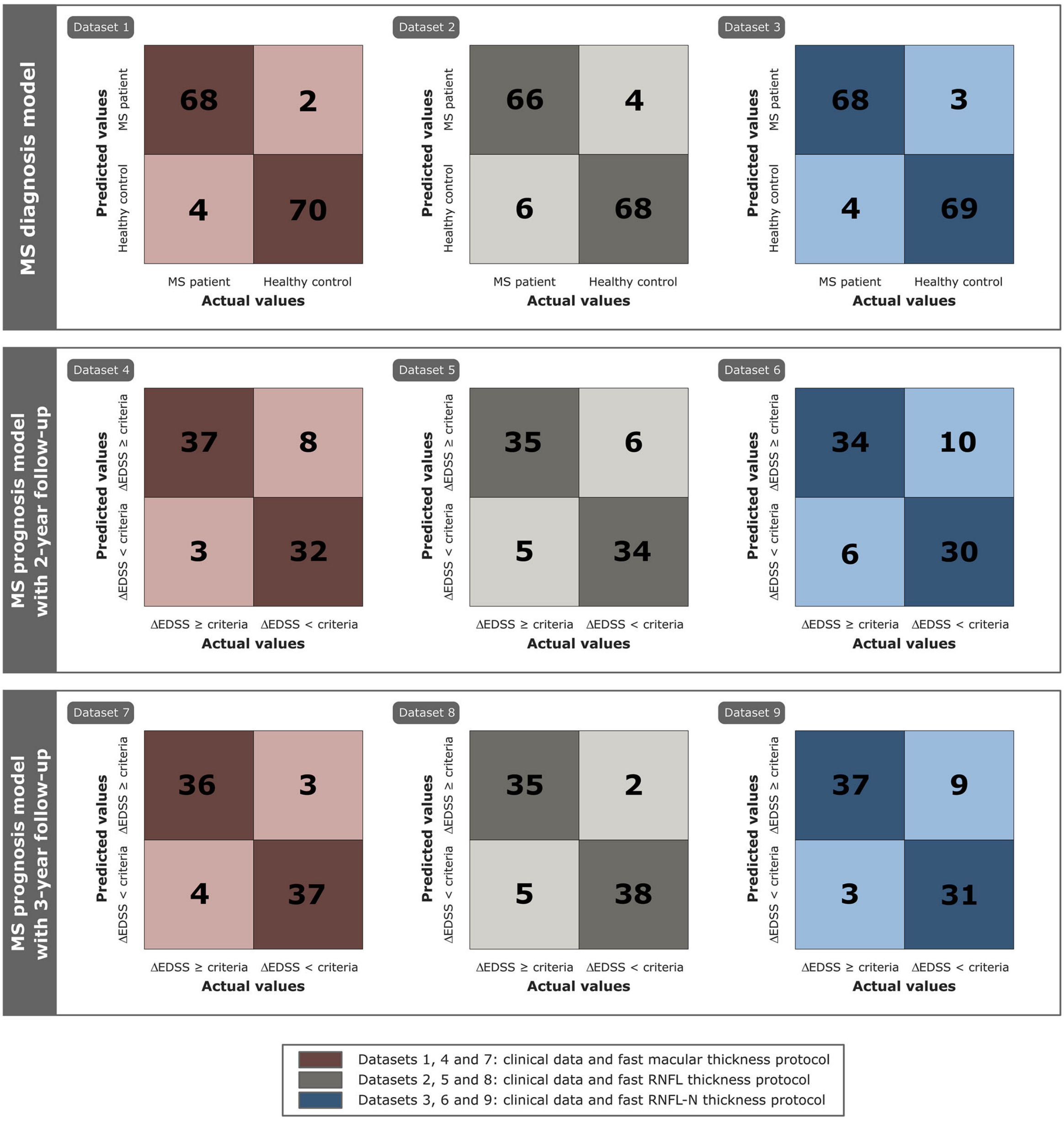

FIGURE 6. Confusion matrix of the best classifier for each predictive model using different datasets. Top: results for multiple sclerosis (MS) diagnosis. Middle: results for MS prognosis with 2-year follow-up. Bottom: results for MS prognosis with 3-year follow-up. The best classifier and several parameters to analyse the model performance for each dataset were shown in Table 4. (*ΔEDSS* expanded disability status scale variation).

DISCUSSION

In MS, many factors influence the development and progression of this disease so that even large correlational studies have come to weak conclusions.[48] Therefore, it is time to take advantage of the potential of data-driven ML analysis. Most ML approaches were based on the MRI examination to diagnose MS or to predict disease progression, following the emerging use of image analysis.[1] However, we propose a ML approach to diagnose MS and provide long-term predictions of disability progression based on RNFL

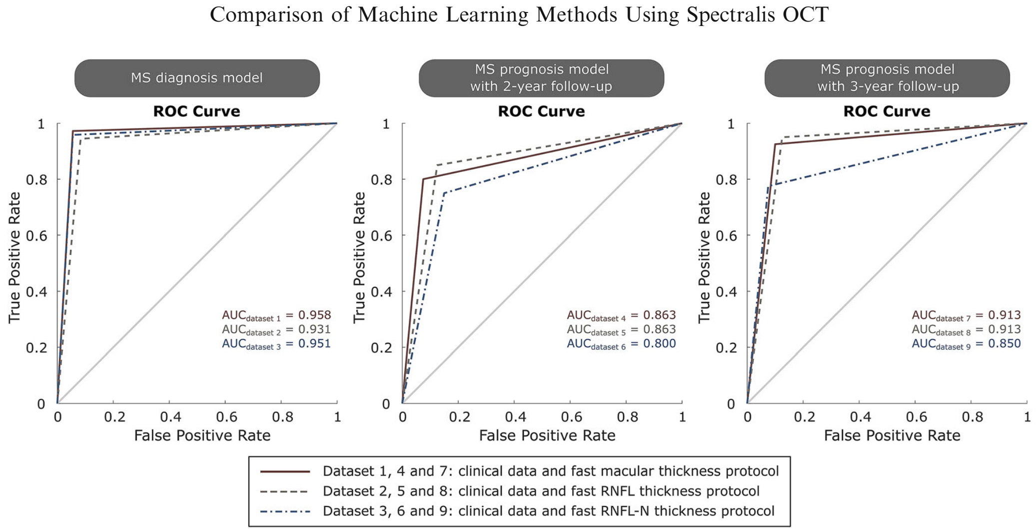

FIGURE 7. Receiver operating characteristic (ROC) curve with area under curve (AUC) of the best classification algorithm for multiple sclerosis (MS) diagnosis and MS prognosis using different datasets. The best classifier and several parameters to analyse the model performance for each dataset were shown in Table 4.

thickness measured by OCT. This imaging technique has some advantages over MRI since it is a fast, cost-effective and non-invasive test.

Paying attention to the statistical analysis of raw data between MS patients and healthy controls (see Table 1), the difference was significant in almost all features (not for CF and IT) for fast macular thickness protocol, in all features for fast RNFL thickness protocol and in most features (not for mean thickness and N/T ratio) for fast RNFL-N thickness protocol. In relation to general data, the difference was also significant in BCVA. As previous studies have shown,[4,15] axonal loss affects the entire pRNFL, with the temporal quadrant being the most affected area in MS patients. It can also be observed that mRNFL showed a significant decrease in this disease. Fig. 3 shows the variables selected by LASSO to develop the MS diagnosis model after balancing our raw data. As expected, the general trend was that both volume and thickness were higher in healthy controls than in MS patients. It is well known that RNFL thinning occurs as part of normal aging,[59] but an additional thinning occurs as a pathological consequence of MS. In the early stages of the disease, demyelination and axonal transection occur. And, as the pathology progresses, inflammation and axonal degeneration predominate.[25,35]

In our MS diagnosis model, the best accuracy was obtained with fast macular thickness protocol (database 1), very similar to that obtained with fast RNFL-N thickness protocol (database 3). And the best classifiers for this purpose were k-NN and EC (see Table 4). This result (acc: 95.8%; AUC: 0.958) was better than that obtained in previous works by Garcia-Martin *et al.* who also used Spectralis OCT: an AUC of 0.945[18] and an accuracy of 88.5%[16] using ANN. Compared to studies that used SS-OCT Triton to measure RNFL, Pérez del Palomar *et al.*[41] obtained an accuracy of 97.2% using DT, Cavaliere *et al.*[9] 90.6% using SVM and Garcia-Martin *et al.* [17] 97.9 using ANN. In our previous work[36], the best result was an accuracy of 87.7% using also EC with Cirrus HD-OCT data.

For MS prognosis, MS patients of our longitudinal study were divided into two classes based on standard criteria for disability progression (Table 2). Table 3 shows the statistical analysis of clinical data and RNFL data performed between 32 MS patients with disability progression and 40 MS patients without disability progression at the first 3 year of our follow-up (the first two for the first model and the first three for the second model). For MS data, the difference was significant in EDSS and visual EDSS at the 3 years. In fast macular thickness protocol, the difference turned to be significant in all features at baseline, while only in total volume, OS and OI at visits 1 and 2. In fast RNFL thickness protocols, the difference between classes was found to be significant in mean thickness, T, ST, N, SN at baseline; in mean thickness, ST and SN at year 1; and in ST at year 2. Finally, for fast RNFL-N thickness protocol, the difference was significant in mean thickness, SN, N, IT and ST at baseline, and in IT and ST at years 1 and 2. With these results, it could be said that the difference in RNFL thickness was higher at the baseline visit of our 10-year follow-up.

After applying LASSO regression to the class-balanced data (40 MS patients with ΔEDSS $\geq$ criteria and 40 MS patients with ΔEDSS $<$ criteria), the variable

TABLE 3. General data, multiple sclerosis (MS) data and retinal nerve fiber layer (RNFL) data, measured by Spectralis optical coherence tomography (OCT), from 32 MS patients with ΔEDSS $\geq$ 1 and 40 MS patients with ΔEDSS < 1 at the first three years of the 10-year follow-up.

	MS patients ΔEDSS˚ crit. ($n = 32$)	MS patients ΔEDSS < crit. ($n = 40$)	*p*-value	MS patients ΔEDSS˚ crit.($n = 32$)	MS patients ΔEDSS < crit. ($n = 40$)	*p*-value	MS patients ΔEDSS˚ crit. ($n = 32$)	MS patients ΔEDSS < crit. ($n = 40$)	*p*-value
	Baseline			1 year			2 years		
General data									
Age (years)	44.01 ± 10.30	44.77 ± 12.51	0.905	45.11 ± 9.19	45.93 ± 12.21	0.9413	46.38 ± 9.76	47.14 ± 11.74	0.887
Sex (M–F)	12–20	7–33		12–20	7–33		12–20	7–33	
BCVA (Snellen)	0.93 ± 0.24	0.90 ± 0.27	0.235	0.96 ± 0.12	0.89 ± 0.27	0.073	0.97 ± 0.13	0.92 ± 0.28	0.538
MS data									
MS duration (years)	11.09 ± 5.65	12.19 ± 8.24	0.716	12.37 ± 5.98	13.35 ± 8.05	0.860	13.46 ± 6.23	14.47 ± 8.33	0.977
MS subtype (RRMS–SPMS–PPMS)	29–2–1	36–3–1		29–2–1	35–4–1		29–2–1	35–4–1	
Optic neuritis antecedent (Yes–No)	6–26	9–31		6–26	10–30		7–25	10–30	
Relapse in preceding year (Yes–No)	4–28	6–34		3–29	7–33		1–31	6–34	
EDSS	1.88 ± 1.89	3.45 ± 2.34	**0.004**	1.92 ± 1.87	3.41 ± 2.44	**0.011**	1.97 ± 2.09	3.59 ± 2.45	**0.005**
Visual EDSS	0.63 ± 0.94	1.20 ± 1.16	**0.013**	0.63 ± 0.91	1.15 ± 1.10	**0.014**	0.63 ± 0.87	1.18 ± 1.11	**0.011**
Fast macular thickness protocol									
Total volume (mm^3)	0.85 ± 0.17	0.72 ± 0.14	**0.002**	0.81 ± 0.17	0.73 ± 0.14	**0.034**	0.82 ± 0.17	0.74 ± 0.13	**0.015**
Central fovea th. (μm)	16.09 ± 3.92	12.73 ± 3.12	**< 0.001**	12.88 ± 2.49	12.30 ± 2.72	0.301	12.41 ± 2.21	12.28 ± 2.82	0.833
Inner nasal th. (μm)	23.31 ± 4.26	20.48 ± 3.88	**0.001**	19.94 ± 3.16	20.10 ± 3.61	0.815	19.78 ± 3.22	19.83 ± 3.07	0.873
Outer nasal th. (μm)	44.75 ± 14.02	39.48 ± 10.55	**0.033**	42.91 ± 11.09	39.13 ± 10.34	0.110	43.19 ± 12.45	38.93 ± 9.45	0.089
Inner superior th. (μm)	24.97 ± 4.84	21.35 ± 3.70	**0.001**	21.97 ± 3.90	21.28 ± 3.66	0.403	21.28 ± 3.79	20.98 ± 4.94	0.964
Outer superior th. (μm)	35.88 ± 8.46	26.15 ± 10.79	**< 0.001**	32.22 ± 9.66	26.08 ± 10.66	**0.016**	32.56 ± 7.97	26.55 ± 10.53	**0.029**
Inner temporal th. (μm)	21.50 ± 3.77	18.50 ± 2.62	**< 0.001**	17.44 ± 4.04	18.33 ± 1.91	0.341	17.78 ± 1.86	18.13 ± 2.02	0.474
Outer temporal th. (μm)	22.41 ± 3.49	18.73 ± 2.03	**< 0.001**	18.63 ± 3.92	18.58 ± 1.58	0.216	18.09 ± 3.74	18.73 ± 1.69	0.959

TABLE 3. continued

	MS patients ΔEDSS˚ crit. (n = 32)	MS patients ΔEDSS < crit. (n = 40)	*p*-value	MS patients ΔEDSS˚ crit.(n = 32)	MS patients ΔEDSS < crit. (n = 40)	*p*-value	MS patients ΔEDSS˚ crit. (n = 32)	MS patients ΔEDSS < crit. (n = 40)	*p*-value
		Baseline			1 year			2 years	
Inner inferior th. [μm]	26.59 ± 4.54	22.65 ± 3.86	**< 0.001**	23.16 ± 4.06	22.28 ± 3.71	0.465	23.13 ± 4.55	22.10 ± 4.04	0.244
Outer inferior th. (μm)	36.81 ± 10.78	27.18 ± 12.49	**0.001**	33.59 ± 9.86	27.50 ± 11.54	**0.019**	34.22 ± 10.50	28.95 ± 9.35	**0.015**
Fast RNFL thickness protocol									
Mean th. (μm)	96.19 ± 22.67	82.85 ± 16.36	**0.002**	91.41 ± 22.50	81.58 ± 15.78	**0.034**	89.31 ± 23.31	81.15 ± 16.13	0.130
Temporal th. (μm)	64.78 ± 20.42	55.23 ± 14.95	**0.039**	59.53 ± 20.03	54.13 ± 14.56	0.310	58.47 ± 18.37	52.13 ± 12.23	0.156
Superotemporal th. (μm)	133.06 ± 41.01	107.13 ± 27.04	**0.002**	127.34 ± 41.06	106.18 ± 25.52	**0.009**	125.59 ± 40.34	104.73 ± 24.81	**0.007**
Inferotemporal th. (μm)	128.53 ± 42.54	112.90 ± 26.86	0.053	124.00 ± 42.69	110.03 ± 28.16	0.132	128.19 ± 43.93	112.83 ± 27.10	0.115
Nasal th. (μm)	77.84 ± 22.37	68.25 ± 23.23	**0.033**	73.75 ± 21.30	66.88 ± 22.44	0.145	69.59 ± 21.68	67.53 ± 22.46	0.555
Superonasal th. (μm)	110.69 ± 23.85	91.70 ± 20.92	**0.002**	103.19 ± 22.98	91.10 ± 20.11	**0.041**	99.34 ± 24.31	92.25 ± 22.61	0.292
Inferonasal th. (μm)	112.19 ± 34.56	103.10 ± 28.32	0.324	109.78 ± 34.60	102.38 ± 29.39	0.518	105.22 ± 34.52	98.98 ± 30.46	0.830
Fast RNFL-N thickness protocol									
Mean th. (μm)	93.88 ± 20.50	81.89 ± 15.12	**0.009**	90.34 ± 20.04	81.58 ± 14.71	0.093	86.78 ± 24.63	77.82 ± 19.61	0.062
PMB th. [μm)	49.38 ± 15.53	44.84 ± 11.49	0.233	46.13 ± 14.75	44.29 ± 11.21	0.688	44.41 ± 13.40	43.45 ± 11.08	0.813
N/T ratio	1.36 ± 0.53	1.27 ± 0.40	0.560	1.28 ± 0.68	1.19 ± 0.52	0.795	1.32 ± 0.69	1.25 ± 0.48	0.855
Superonasal th. (μm)	110.56 ± 32.16	94.50 ± 21.73	**0.018**	105.88 ± 31.77	93.47 ± 23.51	0.139	99.81 ± 32.64	88.92 ± 28.34	0.273
Nasal th. (μm)	77.97 ± 24.77	65.37 ± 15.42	**0.024**	74.06 ± 24.56	66.18 ± 14.31	0.209	70.28 ± 26.27	63.58 ± 18.44	0.342
Inferonasal th. (μm)	108.75 ± 33.08	104.92 ± 26.86	0.958	105.00 ± 34.06	103.74 ± 25.51	0.773	103.06 ± 27.77	97.11 ± 31.90	0.571
Inferotemporal th. (μm)	126.09 ± 28.19	108.63 ± 28.80	**0.007**	123.97 ± 27.31	109.32 ± 29.81	**0.020**	126.63 ± 28.07	109.00 ± 33.24	**0.027**
Temporal th. (μm)	60.97 ± 16.49	55.03 ± 15.17	0.122	58.03 ± 15.78	53.47 ± 14.35	0.186	57.66 ± 16.94	52.42 ± 13.44	0.144
Superotemporal th. (μm)	127.50 ± 30.17	106.21 ± 26.83	**0.003**	123.81 ± 30.07	106.74 ± 26.29	**0.012**	123.94 ± 30.56	107.13 ± 26.29	**0.019**

ΔEDSS represents the variation of expanded disability status scale (EDSS) between the target future time and the time the prediction is made. The criteria for disability progression are show in Table 2. P-value, obtained by Wilcoxon test, is used to compare data between MS patients with ΔEDSS ≥ criteria and MS patients with ΔEDSS < criteria. Statistically significant differences ($p < 0.05$) are represented in bold..

BCVA best-corrected visual acuity, *RRMS* relapsing-remitting multiple sclerosis, *SPMS* secondary-progressive multiple sclerosis, *PPMS* primary-progressive multiple sclerosis, *th* thickness, *PMB* papillomacular bundle, *N/T* nasal/temporal.

TABLE 4. Model assessment for each dataset, only the best classifier is shown.

Dataset	Features	Classifier	Acc (%)	Sens (%)	Spec (%)	Prec (%)	NPV (%)	F1 score	FM	MCC	κ	AUC
MS diagnosis model												
1	5	k-NN	95.8	94.4	97.2	97.1	94.6	0.958	0.958	0.917	0.917	0.958
2	6	k-NN/EC	93.1	91.7	94.4	94.3	91.9	0.930	0.930	0.861	0.861	0.931
3	7	EC	95.1	94.4	95.8	95.8	94.5	0.951	0.951	0.903	0.903	0.951
MS prognosis model with 2-year follow-up												
4	4	DT	86.3	92.5	80.0	82.2	91.4	0.871	0.872	0.731	0.725	0.863
5	4	DT	86.3	87.5	85.0	85.4	87.2	0.864	0.864	0.725	0.725	0.863
6	4	DT	80.0	85.0	75.0	77.3	83.3	0.810	0.810	0.603	0.600	0.800
MS prognosis model with 3-year follow-up												
7	3	DT	91.3	90.0	92.5	92.3	90.2	0.911	0.911	0.825	0.825	0.913
8	4	SVM	91.3	87.5	95.0	94.6	88.4	0.909	0.910	0.827	0.825	0.913
9	4	k-NN	85.0	92.5	77.5	80.4	91.2	0.860	0.863	0.708	0.700	0.850

As can be seen in Eqs. [1–9], the following parameters are calculated: accuracy (acc), sensitivity (sens), specificity (spec), precision (prec), negative predictive value (NPV), F1 score, Fowkles-Mallows index (FM), Matthews correlation coefficient (MCC), Cohen's Kappa coefficient (κ). Area under curve (AUC) is the area under the receiver operating characteristic (ROC) curve.
k-NN k-nearest neighbours, *EC* ensemble classifier, *DT* decision tree, *SVM* support vector machine.

selection was shown in Fig. 4. On the one hand, EDSS and visual EDSS were chosen and it can be seen how MS patients with ΔEDSS $<$ criteria had higher values while the progression was very similar in both groups. On the other hand, the RNFL data of the three Spectralis OCT protocols chosen showed the same overall behaviour. RNFL thickness was higher in MS patients with ΔEDSS $\geq$ criteria and these patients experienced a greater RNFL thinning because in MS patients without disability progression RNFL thickness was constant or subtly decreased. In this way, we corroborate the conclusion obtained in one of our previous works,[35] establishing that axonal damage occurs cumulatively from the onset of MS and that most of the RNFL thinning occurs before the appearance of significant disability. MS patients with disability progression show a RNFL thinning while MS patients without disability progression (patients with greater disability) had this thinning in the past (during the early stages of disability).

In our first MS prognosis model with a 2-year follow-up, the best accuracy was 86.3% and it was obtained with fast macular thickness protocol (dataset 4) and with fast RNFL thickness protocol (dataset 5) using DT in both cases. Using an additional data point to the first model, we developed our second MS prognosis model with a 3-year follow-up. In this second model, the performance increased compared to the first model: an accuracy of 91.3% with fast macular thickness protocol (dataset 7) and DT, and with fast RNFL thickness protocol (dataset 8) and SVM. This result obtained in the prediction of disability progression 8 years later (acc: 91.3%; AUC: 0.913) improved our previous result (acc: 81.7%; AUC: 0.816) obtained by LSTM using Cirrus HD-OCT.[36]

Pending further studies that use OCT data in combination with AI for MS prognosis, we have to compare our results with those of studies that used test such as MRI or EP.[53] Zhao *et al.*[64] used MRI data to predict disability progression after 2 years using 3-year follow-up and the best result was an accuracy of 71.0% with SVM. Recently, Zhao *et al.*[65] also achieved an AUC of 0.83 using MRI data from the first 2 years to predict disease course 3 years later. Using EP, Yperman *et al.*[62] predicted disability progression after 2 years using 2-year time series with an AUC of 0.75. Pinto *et al.*[42] developed several models to predict disease severity in the 6/10th year of progression using 1-5 years of follow-up with MRI, EP and cerebrospinal fluid (CSF) data. It is clear that model performance increased over time, but it is preferable to achieve a good accuracy with the minimum number of data points. Therefore, these authors considered that the 2-year model (AUC: 0.89) was the most suitable to predict disease severity 4 years later.

As can be seen in Table 4, the results of this work could indicate some conclusions. For MS diagnosis, the best acquisition protocols of Spectralis OCT were fast macular thickness and fast RNFL-N thickness. In addition, the best performing binary classifiers for this task were k-NN and EC, while simpler methods such as MLR or NB showed a performance not as good as the previous ones (see accuracy for MS diagnosis model in Fig. 5). Our results are totally in accordance with our previous work,[36] in which the behaviour of the tested algorithms was similar. For both MS prognosis models, the best performance was obtained using datasets with fast macular thickness protocol and fast RNFL thickness protocol in combination with DT or SVM. For prognosis purposes, the accuracy increased from 86.3% to 91.3% using one more data point.

Therefore, it seems worthwhile to delay the prediction by 1 year to increase the model performance. In this case, Fig. 5 shows how the behaviour of each classifier strongly depends on the acquisition protocol used and the model developed, and no determining conclusion can be drawn. This fact highlights the need for further machine learning studies using RNFL thickness for MS prognosis. Alternatively, as mentioned above, several studies used data from other tests such as MRI, EP or CSF analysis. Zhao *et al.* compared SVM, LR, RF and EC.[64,65] Seccia *et al.* tested SVM, RF, k-NN, EC and LSTM.[52] Pinto *et al.* used MLR, SVM, k-NN and DT.[42] All of them, together with this work, concluded that SVM is one of the best classifiers to predict MS disease course.

Although our results represent a major step forward in the use of OCT to provide valuable information that could help clinician to treat MS better and faster, this work has several limitations. In our study, only good quality scans were selected, but it is not always possible in clinical practice. The models developed are heavily based on OCT data. However, if these data are combined with other previously studied tests such as MRI, EP or CSF analysis, the model performance could be improved. Although the EDSS score is considered the most useful tool to measure MS disability progression, this scale has low reliability and sensitivity.[34] Our prediction of progression is based on the variation of EDSS score (ΔEDSS), so the output of our models is a qualitative and not a quantitative prediction.

Another highly limiting aspect is the sample population of our study (72 MS patients and 30 healthy controls) which is too small to establish our results as a gold standard. It can be said that the dataset detailed in this work could be representative of the subjects affected by MS since these data follow the trend of this pathology: 73.6% of MS patients were females and RRMS was the most predominant MS subtype. Moreover, the size of our raw data and characteristics such as age or MS duration were similar to those of previous studies.[36,42] However, more cross-sectional and longitudinal studies with the same aims and with larger sample population will be required to confirm RNFL thickness as a biomarker for early diagnosis and prediction of the disability progression in MS patients.

We must also take into account our class-imbalanced data and the method used to solve this issue. The use of any method of handling imbalanced datasets actually changes the nature of the dataset, and this fact could imply the generality of the results. However, by generating examples similar to existing minority subjects, SMOTE creates broader and less specific decision boundaries that increase the generalizability of the classifiers, increasing their performance.[23,49] Thus, the risk of overfitting for the majority class and underfitting for the minority class is reduced.

With this work, we support the idea of several authors to use AI in MS and take advantage of its benefits.[1] For our particular goal, OCT is an objective, reproducible, cost-effective and non-invasive test that can be performed by any clinician in a couple of minutes, without causing any discomfort to the patient. This study can be considered as a proof of concept on the possibility of diagnosing MS and predicting MS disability progression using a machine learning approach with Spectralis OCT data. This work used data from a hospital with the aim of developing models that are ready to test new patients who are undiagnosed or whose progression is unknown. In addition, disease progression was also analysed by accumulating information based on consecutive years. This would be of great benefit to doctors, who would be able to make an early diagnosis and select more specific treatments according to the predicted disability progression of each MS patient.

FUNDING

Open Access funding provided thanks to the CRUE-CSIC agreement with Springer Nature.

CONFLICT OF INTEREST

The authors state that there are no conflicts of interest.

ACKNOWLEDGMENTS

This work was supported by the Spanish Ministry of Economy and Competitiveness (Project DPI 2016-79302-R), the Spanish Ministry of Science, Innovation and Universities (Grant BES-2017-080384), and the Instituto de Salud Carlos III (PI17/01726).

OPEN ACCESS

REFERENCES

[1]Afzal, H. M. R., S. Luo, S. Ramadan, and J. Lechner-Scott. The emerging role of artificial intelligence in multiple sclerosis imaging. *Mult. Scler. J.* 2020. https://doi.org/10.1177/1352458520966298.

[2]Avery, R. L., D. J. Pieramici, M. D. Rabena, A. A. Castellarin, M. A. Nasir, and M. J. Giust. Intravitreal BEVACIZUMAB (Avastin) for neovascular age-related macular degeneration. *Ophthalmology*. 113:363–372, 2006.

[3]Bejarano, B., M. Bianco, D. Gonzalez-Moron, J. Sepulcre, J. Goñi, J. Arcocha, O. Soto, U. Del Carro, G. Comi, L. Leocani, and P. Villoslada. Computational classifiers for predicting the short-term course of Multiple sclerosis. *BMC Neurol*. 11:67, 2011.

[4]Birkeldh, U., A. Manouchehrinia, M. A. Hietala, J. Hillert, T. Olsson, F. Piehl, I. S. Kockum, L. Brundin, O. Zahavi, M. Wahlberg-Ramsay, R. Brautaset, and M. Nilsson. The temporal retinal nerve fiber layer thickness is the most important optical coherence tomography estimate in multiple sclerosis. *Front. Neurol.* 8:8, 2017.

[5]Bonab, H., and F. Can. Less is more: a comprehensive framework for the number of components of ensemble classifiers. *IEEE Trans. Neural Netw. Learn. Syst*. 30:2735–2745, 2019.

[6]Bsteh, G., K. Berek, H. Hegen, P. Altmann, S. Wurth, M. Auer, A. Zinganell, F. Di Pauli, P. Rommer, F. Leutmezer, F. Deisenhammer, and T. Berger. Macular ganglion cell–inner plexiform layer thinning as a biomarker of disability progression in relapsing multiple sclerosis. *Mult. Scler. J.* 2020. https://doi.org/10.1177/1352458520935724.

[7]Bsteh, G., H. Hegen, B. Teuchner, M. Amprosi, K. Berek, F. Ladstätter, S. Wurth, M. Auer, F. Di Pauli, F. Deisenhammer, and T. Berger. Peripapillary retinal nerve fibre layer as measured by optical coherence tomography is a prognostic biomarker not only for physical but also for cognitive disability progression in multiple sclerosis. *Mult. Scler. J.* 25:196–203, 2019.

[8]Bsteh, G., H. Hegen, B. Teuchner, K. Berek, S. Wurth, M. Auer, F. Di Pauli, F. Deisenhammer, and T. Berger. Peripapillary retinal nerve fibre layer thinning rate as a biomarker discriminating stable and progressing relapsing–remitting multiple sclerosis. *Eur. J. Neurol.* 26:865–871, 2019.

[9]Cavaliere, C., E. Vilades, M. Alonso-Rodríguez, M. Rodrigo, L. Pablo, J. Miguel, E. López-Guillén, E. Morla, L. Boquete, and E. Garcia-Martin. Computer-aided diagnosis of multiple sclerosis using a support vector machine and optical coherence tomography features. *Sensors*. 19:5323, 2019.

[10]Choudhury, A., and D. Gupta. A Survey on Medical Diagnosis of Diabetes Using Machine Learning Techniques. Singapore: Springer, pp. 67–78, 2019.

[11]Chylack, L. T., J. K. Wolfe, D. M. Singer, M. C. Leske, M. A. Bullimore, I. L. Bailey, J. Friend, D. McCarthy, and S. Y. Wu. The lens opacities classification system III: the longitudinal study of cataract study group. *Arch. Ophthalmol.* 111:831–836, 1993.

[12]Cordón, B., J. Pérez, M. J. Vicente, E. Viladés, E. Orduna, A. Pérez del Palomar, J. Cegoñino, A. Montolío, J. R. Ara, M. J. Rodrigo, M. Satué, and E. García-Martín. Evaluation with angiography by optical coherence tomography of patients with multiple sclerosis. *Acta Ophthalmol.* 97:1755–3768, 2019.

[13]Costello, F., and J. Burton. Retinal imaging with optical coherence tomography: a biomarker in multiple sclerosis? *Eye Brain*. 10:47–63, 2018.

[14]Cruz-Herranz, A., L. J. Balk, T. Oberwahrenbrock, S. Saidha, E. H. Martinez-Lapiscina, W. A. Lagreze, J. S. Schuman, P. Villoslada, P. Calabresi, L. Balcer, A. Petzold, A. J. Green, F. Paul, A. U. Brandt, and P. Albrecht. The APOSTEL recommendations for reporting quantitative optical coherence tomography studies. *Neurology*. 86:2303–2309, 2016.

[15]Fjeldstad, C., M. Bemben, and G. Pardo. Reduced retinal nerve fiber layer and macular thickness in patients with multiple sclerosis with no history of optic neuritis identified by the use of spectral domain high-definition optical coherence tomography. *J. Clin. Neurosci.* 18:1469–1472, 2011.

[16]Garcia-Martin, E., R. Herrero, M. P. Bambo, J. R. Ara, J. Martin, V. Polo, J. M. Larrosa, J. Garcia-Feijoo, and L. E. Pablo. Artificial neural network techniques to improve the ability of optical coherence tomography to detect optic neuritis. *Semin. Ophthalmol.* 30:11–19, 2015.

[17]Garcia-Martin, E., M. Ortiz, L. Boquete, E. M. Sánchez-Morla, R. Barea, C. Cavaliere, E. Vilades, E. Orduna, and M. J. Rodrigo. Early diagnosis of multiple sclerosis by OCT analysis using Cohen's d method and a neural network as classifier. *Comput. Biol. Med.* 129:104165, 2021.

[18]Garcia-Martin, E., L. E. Pablo, R. Herrero, J. R. Ara, J. Martin, J. M. Larrosa, V. Polo, J. Garcia-Feijoo, and J. Fernandez. Neural networks to identify multiple sclerosis with optical coherence tomography. *Acta Ophthalmol.* 91:e628–e634, 2013.

[19]Garcia-Martin, E., V. Pueyo, I. Pinilla, J. R. Ara, J. Martin, and J. Fernandez. Fourier-Domain OCT in multiple sclerosis patients: Reproducibility and ability to detect retinal nerve fiber layer atrophy. *Investig. Ophthalmol. Vis. Sci.* 52:4124–4131, 2011.

[20]dos Gruginskie, L. A. S., and G. L. R. Vaccaro. Lawsuit lead time prediction: Comparison of data mining techniques based on categorical response variable. *PLoS ONE*. 13:1–26, 2018.

[21]Islam, M. M., H. Iqbal, M. R. Haque, and M. K. Hasan. Prediction of breast cancer using support vector machine and K-Nearest neighbors. *5th IEEE Reg. 10 Humanit. Technol. Conf. 2017, R10-HTC 2017* 2018-Janua: pp 26–229, 2018.

[22]Kalincik, T., et al. Defining reliable disability outcomes in multiple sclerosis. *Brain*. 138:3287–3298, 2015.

[23]Karlık, B., A. M. Yibre, and B. Koçer. Comprising feature selection and classifier methods with SMOTE for prediction of male infertility. *Int. J. Fuzzy Syst. Adv. Appl.* 3:1–6, 2016.

[24]Kuhn, M., and K. Johnson. Applied Predictive Modeling. New York: Springer, pp. 1–600, 2013.

[25]Kutzelnigg, A., and H. Lassmann. Pathology of multiple sclerosis and related inflammatory demyelinating diseases.

In: Handbook of Clinical Neurology. Elsevier B.V., 2014, pp. 15–58.

[26] Lambe, J., K. C. Fitzgerald, O. C. Murphy, A. G. Filippatou, E. S. Sotirchos, G. Kalaitzidis, E. Vasileiou, N. Pellegrini, E. Ogbuokiri, B. Toliver, N. J. Luciano, S. Davis, N. Fioravante, O. Kwakyi, H. Risher, C. M. Crainiceanu, J. L. Prince, S. D. Newsome, E. M. Mowry, S. Saidha, and P. A. Calabresi. Association of spectral-domain OCT with long-term disability worsening in multiple sclerosis. *Neurology*. 96:2058, 2021.

[27] Law, M. T. K., A. L. Traboulsee, D. K. B. Li, R. L. Carruthers, M. S. Freedman, S. H. Kolind, and R. Tam. Machine learning in secondary progressive multiple sclerosis: an improved predictive model for short-term disability progression. *Mult. Scler. J.* 5:45, 2019.

[28] Lipton, Z. C., D. C. Kale, C. Elkan, and R. Wetzel. Learning to diagnose with LSTM recurrent neural networks. , 2016.at <http://arxiv.org/abs/1511.03677>.

[29] Liu, Z., B. Ji, Y. Zhang, G. Cui, L. Liu, S. Man, L. Ding, X. Yang, H. Mao, and L. Wang. Machine learning assisted MRI characterization for diagnosis of neonatal acute bilirubin encephalopathy. *Front. Neurol.* 10:1–11, 2019.

[30] London, F., H. Zéphir, E. Drumez, J. Labreuche, N. Hadhoum, J. Lannoy, J. Hodel, P. Vermersch, J.-P. Pruvo, X. Leclerc, and O. Outteryck. Optical coherence tomography: a window to the optic nerve in clinically isolated syndrome. *Brain*. 142:903–915, 2019.

[31] Lublin, F. D., et al. Defining the clinical course of multiple sclerosis: the 2013 revisions. *Neurology*. 83:278–286, 2014.

[32] Mata, J. Interpretation of concrete dam behaviour with artificial neural network and multiple linear regression models. *Eng. Struct.* 33:903–910, 2011.

[33] Md Isa, N. E. Z. A. Amir, M. Z. Ilyas, and M. S. Razalli. The Performance Analysis of K-Nearest Neighbors (K-NN) Algorithm for Motor Imagery Classification Based on EEG Signal. *MATEC Web Conf.* 140:0–5, 2017.

[34] Meyer-Moock, S., Y.-S. Feng, M. Maeurer, F.-W. Dippel, and T. Kohlmann. Systematic literature review and validity evaluation of the expanded disability status scale (EDSS) and the multiple sclerosis functional composite (MSFC) in patients with multiple sclerosis. *BMC Neurol.* 14:58, 2014.

[35] Montolío, A., J. Cegoñino, E. Orduna, B. Sebastian, E. Garcia-Martin, and A. Pérez del Palomar. A mathematical model to predict the evolution of retinal nerve fiber layer thinning in multiple sclerosis patients. *Comput. Biol. Med.* 111:103357, 2019.

[36] Montolío, A., A. Martín-Gallego, J. Cegoñino, E. Orduna, E. Vilades, E. Garcia-Martin, and A. Pérez del Palomar. Machine learning in diagnosis and disability prediction of multiple sclerosis using optical coherence tomography. *Comput. Biol. Med.* 133:104416, 2021.

[37] Mowry, E. M., A. K. Hedström, M. A. Gianfrancesco, X. Shao, C. A. Schaefer, L. Shen, K. H. Bellesis, F. B. S. Briggs, T. Olsson, L. Alfredsson, and L. F. Barcellos. Incorporating machine learning approaches to assess putative environmental risk factors for multiple sclerosis. *Mult. Scler. Relat. Disord.* 24:135–141, 2018.

[38] Nathans, L. L., F. L. Oswald, and K. Nimon. Interpreting multiple linear regression: A guidebook of variable importance. . *Pract. Assess. Res. Eval.* 17:1–19, 2012.

[39] Peduzzi, P., J. Concato, E. Kemper, T. R. Holford, and A. R. Feinstein. A simulation study of the number of events per variable in logistic regression analysis. *J. Clin. Epidemiol.* 49:1373–1379, 1996.

[40] Pellegrini, F., M. Copetti, M. P. Sormani, F. Bovis, C. de Moor, T. P. A. Debray, and B. C. Kieseier. Predicting disability progression in multiple sclerosis: Insights from advanced statistical modeling. *Mult. Scler. J.* 26:1828–1836, 2020.

[41] Pérez del Palomar, A., J. Cegoñino, A. Montolío, E. Orduna, E. Vilades, B. Sebastián, L. E. Pablo, and E. Garcia-Martin. Swept source optical coherence tomography to early detect multiple sclerosis disease: the use of machine learning techniques. *PLoS ONE*. 14:0216410, 2019.

[42] Pinto, M. F., H. Oliveira, S. Batista, L. Cruz, M. Pinto, I. Correia, P. Martins, and C. Teixeira. Prediction of disease progression and outcomes in multiple sclerosis with machine learning. *Sci. Rep.* 10:1–13, 2020.

[43] Polman, C. H., S. C. Reingold, B. Banwell, M. Clanet, J. A. Cohen, M. Filippi, K. Fujihara, E. Havrdova, M. Hutchinson, L. Kappos, F. D. Lublin, X. Montalban, P. O'Connor, M. Sandberg-Wollheim, A. J. Thompson, E. Waubant, B. Weinshenker, and J. S. Wolinsky. Diagnostic criteria for multiple sclerosis: 2010 revisions to the McDonald criteria. *Ann. Neurol.* 69:292–302, 2011.

[44] Potdar, K., T. S. Pardawala, and C. D. Pai. A comparative study of categorical variable encoding techniques for neural network classifiers. *Int. J. Comput. Appl.* 175:7–9, 2017.

[45] Povedano-Montero, F. J., R. N. Weinreb, I. Raga-Martínez, A. Romero, and F. López-Muñoz. Detection of neurological and ophthalmological pathologies with optical coherence tomography using retinal thickness measurements: a bibliometric study. *Appl. Sci.* 10:5477, 2020.

[46] Rodriguez, J. D., A. Perez, and J. A. Lozano. Sensitivity analysis of k-fold cross validation in prediction error estimation. *IEEE Trans. Pattern Anal. Mach. Intell.* 32:569–575, 2010.

[47] Rothman, A., O. C. Murphy, K. C. Fitzgerald, J. Button, E. Gordon-Lipkin, J. N. Ratchford, S. D. Newsome, E. M. Mowry, E. S. Sotirchos, S. B. Syc-Mazurek, J. Nguyen, N. G. Caldito, L. J. Balcer, E. M. Frohman, T. C. Frohman, D. S. Reich, C. Crainiceanu, S. Saidha, and P. A. Calabresi. Retinal measurements predict 10-year disability in multiple sclerosis. *Ann. Clin. Transl. Neurol.* 6:222–232, 2019.

[48] Rotstein, D., and X. Montalban. Reaching an evidence-based prognosis for personalized treatment of multiple sclerosis. *Nat. Rev. Neurol.* 15:287–300, 2019.

[49] Santos, M. S., J. P. Soares, P. H. Abreu, H. Araujo, and J. Santos. Cross-validation for imbalanced datasets: Avoiding overoptimistic and overfitting approaches. *IEEE Comput. Intell. Mag.* 13:59–76, 2018.

[50] Schippling, S., L. J. Balk, F. Costello, P. Albrecht, L. Balcer, P. A. Calabresi, J. L. Frederiksen, E. Frohman, A. J. Green, A. Klistorner, O. Outteryck, F. Paul, G. T. Plant, G. Traber, P. Vermersch, P. Villoslada, S. Wolf, and A. Petzold. Quality control for retinal OCT in multiple sclerosis: validation of the OSCAR-IB criteria. *Mult. Scler. J.* 21:163–170, 2015.

[51] Schurz, N., L. Sariaslani, P. Altmann, F. Leutmezer, C. Mitsch, B. Pemp, P. Rommer, T. Zrzavy, T. Berger, and G. Bsteh. Evaluation of retinal layer thickness parameters as biomarkers in a real-world multiple sclerosis cohort. *Eye Brain*. 13:59–69, 2021.

[52] Seccia, R., D. Gammelli, F. Dominici, S. Romano, A. C. Landi, M. Salvetti, A. Tacchella, A. Zaccaria, A. Crisanti, F. Grassi, and L. Palagi. Considering patient clinical history impacts performance of machine learning models in

predicting course of multiple sclerosis. *PLoS ONE*. 15:1–18, 2020.

[53] Seccia, R., S. Romano, M. Salvetti, A. Crisanti, L. Palagi, and F. Grassi. Machine learning use for prognostic purposes in multiple sclerosis. *Life*. 11:1–18, 2021.

[54] Tan, M., J. Pu, and B. Zheng. Optimization of breast mass classification using sequential forward floating selection (SFFS) and a support vector machine (SVM) model. *Int. J. Comput. Assist. Radiol. Surg*. 9:1005–1020, 2014.

[55] Thabit, M. N., M. M. Farouk, M. Awni, and A. A. B. Mohamed. Early disability in ambulatory patients with multiple sclerosis: optical coherence tomography versus visual evoked potentials, a comparative study Egypt. *J. Neurol. Psychiatry Neurosurg*. 56:1–9, 2020.

[56] Thompson, A. J., et al. Diagnosis of multiple sclerosis: 2017 revisions of the McDonald criteria. *Lancet Neurol*. 17:162–173, 2018.

[57] Tibshirani, R. Regression shrinkage and selection via the lasso. *J. R. Stat. Soc. Ser. B*. 58:267–288, 1996.

[58] Vapnik, V. N. An overview of statistical learning theory. *IEEE Trans. Neural Netw*. 10:988–999, 1999.

[59] Viladés, E., A. Pérez del Palomar, J. Cegoñino, J. Obis, M. Satue, E. Orduna, L. E. Pablo, M. Ciprés, and E. GarciaMartin. Physiological changes in retinal layers thicknesses measured with swept source optical coherence tomography. *PLoS ONE*. 15:1–14, 2020.

[60] Wu, C. C., W. C. Yeh, W. D. Hsu, M. M. Islam, P. A. Nguyen, T. N. Poly, Y. C. Wang, H. C. Yang, and Y. C. Li. Prediction of fatty liver disease using machine learning algorithms. *Comput. Methods Programs Biomed*. 170:23–29, 2019.

[61] You, Y., M. H. Barnett, C. Yiannikas, J. Parratt, J. Matthews, S. L. Graham, and A. Klistorner. Chronic demyelination exacerbates neuroaxonal loss in patients with MS with unilateral optic neuritis. *Neurol. Neuroimmunol. Neuroinflammation*. 7:3, 2020.

[62] Yperman, J., T. Becker, D. Valkenborg, V. Popescu, N. Hellings, B. Van Wijmeersch, and L. M. Peeters. Machine learning analysis of motor evoked potential time series to predict disability progression in multiple sclerosis. *BMC Neurol*. 20:1–15, 2020.

[63] Zhang, Y., S. Lu, X. Zhou, M. Yang, L. Wu, B. Liu, P. Phillips, and S. Wang. Comparison of machine learning methods for stationary wavelet entropy-based multiple sclerosis detection: decision tree, k -nearest neighbors, and support vector machine. *Simulation*. 92:861–871, 2016.

[64] Zhao, Y., B. C. Healy, D. Rotstein, C. R. G. Guttmann, R. Bakshi, H. L. Weiner, C. E. Brodley, and T. Chitnis. Exploration of machine learning techniques in predicting multiple sclerosis disease course. *PLoS ONE*. 12:e0174866, 2017.

[65] Zhao, Y., T. Wang, R. Bove, B. Cree, R. Henry, H. Lokhande, M. Polgar-Turcsanyi, M. Anderson, R. Bakshi, H. L. Weiner, and T. Chitnis. Ensemble learning predicts multiple sclerosis disease course in the SUMMIT study. *Digit. Med*. 3:135, 2020.

2.3 Glaucoma monitoring with vitreous imaging

2.3.1 Vitreous parainflammation analysis in glaucoma

Manuscript 5: Analysis of Parainflammation in Chronic Glaucoma Using Vitreous-OCT Imaging

María Jesús Rodrigo, Manuel Subías, Alberto Montolío, Silvia Méndez-Martínez, Teresa Martínez-Rincón, Lorena Arias, David García-Herranz, Irene Bravo-Osuna, Julian Garcia-Feijoo, Luis Pablo, José Cegoñino, Rocio Herrero-Vanrell, Ana Carretero, Jesus Ruberte, Elena Garcia-Martin, Amaya Pérez del Palomar

Abstract

Glaucoma causes blindness due to the progressive death of retinal ganglion cells. The immune response chronically and subclinically mediates a homeostatic role. In current clinical practice, it is impossible to analyse neuroinflammation non-invasively. However, analysis of vitreous images using optical coherence tomography detects the immune response as hyperreflective opacities. This study monitors vitreous parainflammation in two animal models of glaucoma, comparing both healthy controls and sexes over six months. Computational analysis characterizes in vivo the hyperreflective opacities, identified histologically as hyalocyte-like Iba-1+ (microglial marker) cells. Glaucomatous eyes showed greater intensity and number of vitreous opacities as well as dynamic fluctuations in the percentage of activated cells (50–250 microns2) vs. non-activated cells (10–50 microns2), isolated cells (10 microns2) and complexes (>250 microns2). Smaller opacities (isolated cells) showed the highest mean intensity (intracellular machinery), were the most rounded at earlier stages (recruitment) and showed the greatest change in orientation (motility). Study of vitreous parainflammation could be a biomarker of glaucoma onset and progression.

biomedicines

Article

Analysis of Parainflammation in Chronic Glaucoma Using Vitreous-OCT Imaging

María Jesús Rodrigo [1,2,3,*,†], Manuel Subías [1,2], Alberto Montolío [4,5], Silvia Méndez-Martínez [1,2], Teresa Martínez-Rincón [1,2], Lorena Arias [1,2], David García-Herranz [6,7,8], Irene Bravo-Osuna [8], Julian Garcia-Feijoo [9], Luis Pablo [1,2,3], José Cegoñino [4,5], Rocio Herrero-Vanrell [3,8], Ana Carretero [10,11,12], Jesus Ruberte [10,11,12], Elena Garcia-Martin [1,2,3] and Amaya Pérez del Palomar [4,5]

[1] Department of Ophthalmology, Miguel Servet University Hospital, 50009 Zaragoza, Spain; manusubias@gmail.com (M.S.); oftalmosmm@gmail.com (S.M.-M.); teresamrincon@gmail.com (T.M.-R.); LorAriCam@hotmail.com (L.A.); lpablo@unizar.es (L.P.); egmvivax@yahoo.com (E.G.-M.)
[2] Miguel Servet Ophthalmology Research Group (GIMSO), Aragon Health Research Institute (IIS Aragon), 50009 Zaragoza, Spain
[3] National Ocular Pathology Network (OFTARED), Carlos III Health Institute, 28040 Madrid, Spain; rociohv@farm.ucm.es
[4] Biomaterials Group, Aragon Engineering Research Institute (I3A), University of Zaragoza, 50018 Zaragoza, Spain; amontolio@unizar.es (A.M.); jcegoni@unizar.es (J.C.); amaya@unizar.es (A.P.d.P.)
[5] Department of Mechanical Engineering, University of Zaragoza, 50018 Zaragoza, Spain
[6] Innovation, Therapy and Pharmaceutical Development in Ophthalmology (InnOftal) Research Group, UCM 920415, Department of Pharmaceutics and Food Technology, Faculty of Pharmacy, Complutense University of Madrid (UCM), 28040 Madrid, Spain; davgar07@ucm.es
[7] Health Research Institute of the San Carlos Clinical Hospital (IdISSC), 28040 Madrid, Spain
[8] University Institute of Industrial Pharmacy (IUFI), School of Pharmacy, Complutense University of Madrid, 28040 Madrid, Spain; ibravo@ucm.es
[9] Department of Ophthalmology, San Carlos Clinical Hospital, UCM, 28040 Madrid, Spain; jgarciafeijoo@hotmail.com
[10] Centre for Animal Biotechnology and Gene Therapy (CBATEG), Universitat Autònoma de Barcelona, 08193 Bellaterra, Spain; ana.carretero@uab.cat (A.C.); jesus.ruberte@uab.cat (J.R.)
[11] CIBER for Diabetes and Associated Metabolic Diseases (CIBERDEM), 28029 Madrid, Spain
[12] Department of Animal Health and Anatomy, School of Veterinary Medicine, Universitat Autònoma de Barcelona, 08193 Bellaterra, Spain
* Correspondence: mariajesusrodrigo@hotmail.es; Tel.: +34-976765558; Fax: +34-976566234
† Postal address: C/Padre Arrupe. Servicio de Oftalmología, Edificio de Consultas Externas, Planta 1., 50009 Zaragoza, Spain.

check for updates

Citation: Rodrigo, M.J.; Subías, M.; Montolío, A.; Méndez-Martínez, S.; Martínez-Rincón, T.; Arias, L.; García-Herranz, D.; Bravo-Osuna, I.; Garcia-Feijoo, J.; Pablo, L.; et al. Analysis of Parainflammation in Chronic Glaucoma Using Vitreous-OCT Imaging. *Biomedicines* **2021**, *9*, 1792. https://doi.org/10.3390/biomedicines9121792

Academic Editor: Erich Knop

Received: 21 October 2021
Accepted: 25 November 2021
Published: 29 November 2021

Abstract: Glaucoma causes blindness due to the progressive death of retinal ganglion cells. The immune response chronically and subclinically mediates a homeostatic role. In current clinical practice, it is impossible to analyse neuroinflammation non-invasively. However, analysis of vitreous images using optical coherence tomography detects the immune response as hyperreflective opacities. This study monitors vitreous parainflammation in two animal models of glaucoma, comparing both healthy controls and sexes over six months. Computational analysis characterizes in vivo the hyperreflective opacities, identified histologically as hyalocyte-like Iba-1+ (microglial marker) cells. Glaucomatous eyes showed greater intensity and number of vitreous opacities as well as dynamic fluctuations in the percentage of activated cells (50–250 microns^2) vs. non-activated cells (10–50 microns^2), isolated cells (10 microns^2) and complexes (>250 microns^2). Smaller opacities (isolated cells) showed the highest mean intensity (intracellular machinery), were the most rounded at earlier stages (recruitment) and showed the greatest change in orientation (motility). Study of vitreous parainflammation could be a biomarker of glaucoma onset and progression.

Keywords: optical coherence tomography; biomedical imaging; image analysis and processing; vitreous body; glaucoma; animal models; inflammation

1. Introduction

Chronic glaucoma is the leading cause of irreversible blindness in the developed world [1]. Increased intraocular pressure (IOP) is the modifiable risk factor most strongly associated with the onset and progression of the disease [2]. This pathology causes progressive retinal ganglion cell (RGC) death, resulting in irreversible visual field impairment [3,4]. Campimetric alteration is detected when 25–30% of RGCs have died, leading to late diagnosis. It is therefore necessary to develop new tools and markers for early diagnosis. With the aim of better understanding the pathogenesis of glaucoma, different models of ocular hypertension have been developed in animals, either by genetic engineering [5,6], or by injection of neurotoxic substances [7,8], or by increasing IOP using pre- and post-trabecular mechanisms [9–11]. At the same time, there is also a known progression in glaucoma of neurodegeneration not dependent on IOP, which has been related to cellular and humoral immune-mediated response [12–15].

The eye has traditionally been considered an immunoprivileged organ. This condition allows a transparent optical visual axis to be maintained by preventing neural destruction followed by repair, scarring and subsequent irreversible visual loss in the event of noxa [16]. It is a complex balance of regional immune system specializations based on a baseline immunoinhibitory microenvironment. Multiple components act by regulating the function and activation of innate (monocyte-macrophage) and adaptive cells (cellular and humoral response) [17–19]. In pathological situations such as non-infectious uveitis, the eye is subject to acute adaptive inflammatory processes. However, parainflammatory processes characterized by slow and insidious inflammation, mainly with the involvement of innate immune elements, have also been recognized in processes previously thought to be purely degenerative, such as age-related macular degeneration, diabetic retinopathy and glaucoma [20–22]. In glaucoma, several signs suggestive of inflammation have been described, such as more acidic pH with increased immune proteins in the aqueous humour and vitreous, as well as activation of astrocytes and microglia and deposits of immunocomplexes and immunoglobulins in the retina identified by histological techniques [23–30]. Microglia are cells of innate immunity derived from blood-borne monocyte-macrophages that migrate during development to the central nervous system and retina where effector functions are acquired to maintain serosal homeostasis and immune surveillance. In the effector organs, these cells present different morphologies depending on their state of activation [28,31,32]. Soma size, assessed using automated in vivo fluorescence image analysis, has been proposed as a significant morphological marker of microglial activation in the neocortex [31]—and subsequently corroborated in glaucomatous mouse retinas—and a positive linear correlation was found with Iba1 staining (specific for microglia) [33]. Microglial activation appears to be the earliest detectable change in the retina [34] that strongly correlates with and predicts the severity of neurodegeneration following acute and chronic damage in glaucoma [35].

The vitreous body is a transparent three-dimensional structure that participates in the cushioning and transmission of light and plays an important role in the metabolism of the different ocular structures under physiological and pathological conditions [36–38]. Very few studies have delved into analysis of the vitreous in entities with parainflammation [39]. The vitreous body is composed mainly of water, collagen fibres, hyaluronic acid and hyalocytes. Hyalocytes are hematopoietic cells of monocyte/macrophage lineage (as microglia) that are located at the periphery of the vitreous cavity, mainly at the anterior base of the vitreous next to the ciliary body and in the vicinity of the optic nerve head [40]. Their functions include synthesis of extracellular matrices, participation in immune regulation of vitreous cavity-associated immune deviation (as inhibitors) through phagocytic activity and contractile properties, and modulation of intraocular inflammation with surface receptors for immunoglobulins and complements. Hyalocytes are highly sensitive to local and systemic physiological perturbations. In response to noxa, they are replaced by reproduction, increasing their mitotic activity, and their changes are postulated as early indicators of value in ocular disease [41]. Imaging-based study of changes in the vitreous under conditions of parainflammation could provide a better understanding of the pathophysiology of these diseases.

Most glaucoma studies have focused on neuroretinal analysis (using either histological or imaging techniques) and very few have focused on vitreous analysis, possibly due to the risk derived from the vitreous sampling process [42,43]. Histological studies are time-consuming, susceptible to human bias and not conducive to analysis of large databases. In contrast, optical coherence tomography (OCT) is an objective, fast and cost-efficient technological tool that allows in vivo acquisition of high-resolution cross-sectional images in the order of microns. Latest-generation OCT systems allow users to study the vitreous in a non-invasive manner under normal conditions and in acute and chronic inflammatory processes, it also being possible to evaluate the changes that occur after treatment [44–46]. Vitreous opacities analysed using OCT can provide rapid correlation with vitreous and intraretinal ocular inflammation and do not require any correction factor for vitreous histological correlation [47,48]. Recently, our group described for the first time an increase in vitreous signal intensity using OCT after induction of ocular hypertension in an animal model of chronic glaucoma [49]. Our group hypothesizes that, thanks to the optical transparency of the vitreous, the activation and/or increase in the number of hyperreflective vitreous opacities detected in OCT images corresponding to immune cells can be identified more easily than intraretinal ones. Moreover, unlike other techniques, it does not require modification of the animal's genetics, nor does it require contrast injection to express fluorescence and, therefore, it has greater potential for application in clinical settings. To our knowledge, OCT analysis of the vitreous has not previously been studied in situations of parainflammation in glaucoma. This paper analyses the changes in vitreous signal in rat eyes, measured using OCT and differentiated by sex, in two models of chronic glaucoma induced by ocular hypertension over 6 months. Computational analysis characterizes the hyperreflective opacities at the vitreoretinal interface and their dynamics over time by means of changes in number, size, intensity, eccentricity and orientation.

2. Materials and Methods

2.1. Data Collection

Images of the vitreoretinal interface were obtained, using OCT (HR-OCT Spectralis, Heidelberg® Engineering, Germany), in previous interventional studies carried out by our research group detailing the methodology used for the generation of two different animal models of chronic glaucoma (MEPI and Ms) [50]. The experiment was previously approved by the Ethics Committee for Animal Research (PI34/17) of the University of Zaragoza (Spain) and was carried out in strict accordance with the Association for Research in Vision and Ophthalmology's Statement on the Use of Animals. The widely used Morrison model [11] was generated with sclerosing injections of episcleral veins (MEPI) of the right eye of Long–Evans rats, performed biweekly for 6 months. The second model (Ms) was generated by injecting a 2 microlitre suspension (10% w) of 20/10 biodegradable PLGA [51] microspheres into the anterior chamber of the right rat eye at 0, 2, 4, 8, 12, 16 and 20 weeks. The left eyes did not undergo intervention. IOP (with Tonolab® rebound tonometer) and OCT scans of both eyes were performed at 0, 2, 4, 6, 8, 12, 18 and 24 weeks. A cohort that did not undergo intervention served as control and was scanned at 0, 12 and 24 weeks.

2.2. Image Analysis

Images were acquired using a high-resolution OCT device (OCT Spectralis for research on animals) with a plane power polymethylmethacrylate contact lens (thickness 270 µm, diameter 5.2 mm) (Cantor+Nissel®, Northamptonshire, UK) adapted to the rats' cornea to obtain higher quality images [52], in every scan examination. This neutral dioptric power lens (no positive or negative dioptric addition) allowed continuous hydration of the cornea preventing desiccation and kept the refractive state stable during the examination. The retinal posterior pole protocol with automatic segmentation, eye-tracking software and follow-up application were used to ensure that the same points were re-scanned throughout the study. The "Enhance depth imaging" mode was disabled in all cases.

The OCT images were exported as Audio Video Interleave (AVI) videos. These videos were composed of cross-sectional images acquired by means of 61 b-scans measuring around 3 mm in length and centred on the optic nerve. These cross-sectional images are 3 mm in length and 0.969 mm in height, so the image area is 2.906 mm^2. Image resolution was 3 microns per pixel generated. Each cross-sectional image has a total of 1536 × 496 pixels. Therefore, each pixel has an area of 3.815 µm^2. These videos were analysed using a custom program implemented in Matlab (version R218a, Mathworks Inc., Natick, MA, USA). The imaging data were analysed by a masked reader. OCT segmentation was performed by two different researchers, likewise masked, to verify reproducibility.

Vitreous/retinal pigment epithelium (VIT/RPE) relative intensity was quantified as an indirect measure of immune response [44,48,49]. Our custom program finds the internal limiting membrane (ILM) and the inner and outer layers of the RPE by greyscale conversion, obtaining the segmentation of vitreous and RPE (Figure 1). The vitreous and RPE intensity value was calculated as the mean of the intensity of all pixels within each region, giving the VIT/RPE relative intensity in each b-scan. Thus, the VIT/RPE relative intensity of each eye is the mean of the 61 b-scans.

The vitreous opacities, closely related to the immune cells, were analysed. This technique focuses on the analysis of hyperreflective opacities in the vitreoretinal interface using OCT, which does not require a correction factor for histological correlation [47] and ensures characterization of the actual opacity. These opacities were studied according to their size, taking as a reference previous studies of morphological analysis of microglia in the retina and histological analysis of hyalocytes [53]. It is possible to discriminate between non-activated and activated cellularity according to the size of the soma, since microglia morphology differs depending on their state of activation. The smallest cells (early growth) have a rounded or amoeboid morphology. Resting cells (non-activated) are characterized by a thin cell body with ramified cellular processes; and reactive cells (activated) have a larger somatic size with phagocytic activity and motility [28,31].

Individual hyperreflective opacities, extrapolated as soma areas, were automatically measured and classified into groups according to size: isolated cells (<10 µm^2), non-activated cells (10–50 µm^2), activated cells (50–250 µm^2) and cell complexes (>250 µm^2). Our custom program determined the size of the opacities in each b-scan by calculating the number of pixels in each opacity. It is necessary to convert the greyscale image to binary image in order to identify all regions in the vitreous. First, the greyscale image was filtered with a multidimensional filter that emphasizes horizontal edges by approximating a vertical gradient; and second, the filtered image was converted to a binary image using the global image threshold, specified as a scalar luminance value, determined by Otsu's method [54]. This method chooses a threshold that minimizes the intraclass variance of the thresholded black and white pixels. To ensure the measurement, the background speckle noise was deleted using a denoising filter. Using grey scale and binary images, this filter distinguishes between hyperreflective opacities and background noise because the opacity intensity is greater than the background intensity (see Figure 1). In our custom denoising filter, individual hyperreflective opacities correspond to areas whose intensity exceeds the noise intensity. To quantify that, we computed the upper outliers of the intensity of the areas in the vitreous for each cross-sectional image. Those areas with intensity lower than this limit were removed, while the most reflective areas were extrapolated as soma areas. Thus, only the cellularity was quantified, eliminating the physiological phenomena of the eye [55]. In this way, opacity intensity was obtained from the grey scale image using the binary image as a mask to detect the regions. Moreover, number, size, eccentricity and orientation of these opacities were obtained from the binary image.

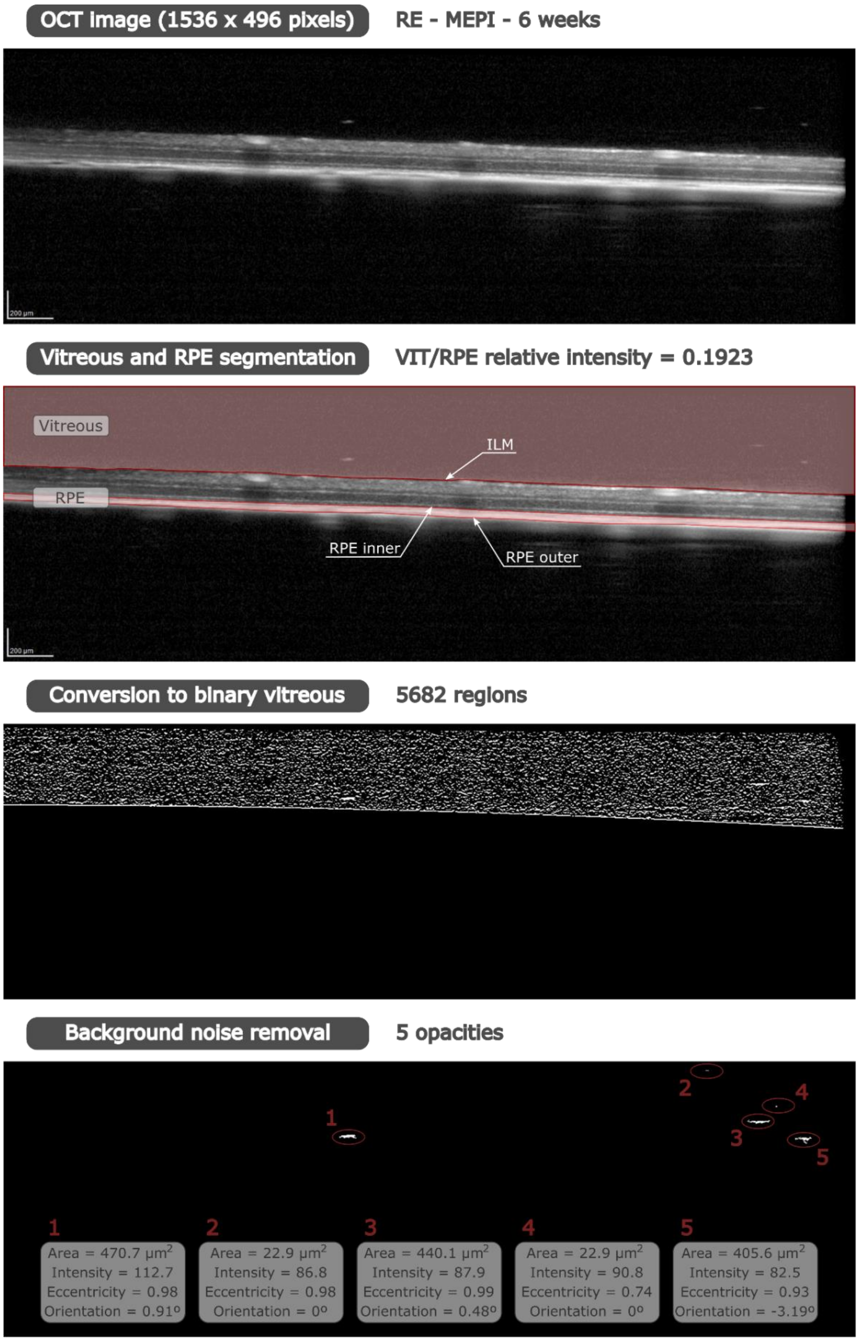

Figure 1. Methodology of the custom program implemented in Matlab (version R218a, Mathworks Inc., Natick, MA, USA). From an OCT (HR-OCT Spectralis, Heidelberg® Engineering, Heidelberg, Germany) image of a right eye with the MEPI model at 6 weeks, VIT/RPE relative intensity was quantified after vitreous and RPE segmentation. To analyse the opacities/cells, it is necessary to remove the background noise of the vitreous. Our denoising filter was applied to the grey scale image intensity in those regions identified in the binary image. Therefore, intensity was obtained from the grey scale image, while area, eccentricity and orientation were computed from the binary image. Abbreviations: OCT: optical coherence tomography; RE: right eye; MEPI: glaucoma model induced by sclerosing the episcleral veins; VIT: vitreous; RPE: retinal pigment epithelium.

Once each opacity was detected, several parameters could be computed for each eye at different stages of follow-up. As a measurement of the overall immune response to the induced model vs. physiological conditions, the total cell area was calculated by the number of opacities and the area of each opacity. The mean number of opacities was an indicator of immunity to noxa over time that allowed analysis of in situ resident immune cellularity and intra- or extra-ocular recruitment [56–59]. The mean area of opacities was calculated for all cells and for each group according to cell area, obtaining reliable reproducibility of the cell soma. By computing the cell percentage for each group, we studied the dynamic relationship between activated and non-activated cell populations.

The mean intensity of opacities is of great importance since immune activation involves gene-protein expression prior to soma remodelling. This parameter is the mean of the intensity values of each pixel in the opacity. Eccentricity is the ratio of the distance between the foci of an ellipse and the length of its major axis. An ellipse with an eccentricity of 0 is actually a circle, while an ellipse with an eccentricity of 1 is a line segment. Therefore, the eccentricity indicates if the cell morphology is more linear, elongated or flat (values closer to 1) or, on the contrary, more rounded (values further from 1). Finally, the orientation of opacities was analysed as a quantification of the motility or active displacement of immunity towards the noxa [28,33,35,60,61]. This orientation is the angle between the x-axis and the major axis of the corresponding ellipse of each opacity and its value is represented in degrees.

2.3. Histological Analysis

To investigate the nature of vitreous hyperreflective opacities observed by OCT during glaucoma, six rat eyes, in three of which episcleral veins were sclerosed producing ocular hypertension (>20 mmHg) for 24 weeks, were analysed. Paraffin-embedded eyes were sectioned (3 µm) along the eye axis, deparaffinized and rehydrated. After several washes in phosphate buffered saline (PBS), sections were incubated overnight at 4 °C with goat anti-human Iba1 (Abcam, Cambridge, UK) at 1:100 dilution. After washing the sections in PBS, they were incubated for 2 h at room temperature with rabbit anti-goat Alexa 568 (Invitrogen, Carlsbad, CA, USA). SYTOX Green Nucleic Acid Stain (Invitrogen) diluted in PBS (1:500 dilution) was incubated for 10 min for nuclear counterstaining. Slides were mounted in Fluoromount (Sigma-Aldrich, St. Louis, MO, USA) medium for further analysis using a laser scanning confocal microscope (TCS SP5; Leica Microsystems GmbH, Heidelberg, Germany). Immunohistochemistry controls were conducted by omission of the primary antibody in a sequential tissue section. Hematoxylin/eosin stain was also performed to study the morphology and presence of intravitreal cells on the surface of the retina.

2.4. Statistical Analysis

All data were recorded in an Excel database, and statistical analysis was performed using SPSS software version 20.0 (SPSS Inc., Chicago, IL, USA). The variables under study were as follows: eye (intervened right eye vs. non-intervened left eye), sex (male vs. female), type of chronic glaucoma model (MEPI vs. Ms) and control, number of injections performed per model, intraocular pressure and vitreous signal intensity (VIT/RPE) measured using OCT.

After checking for variable normality with the Kolmogorov–Smirnov test, we performed parametric test using multiple comparisons by ANOVA and Tukey post-hoc analysis (to identify between which groups there are statistical differences) and analysis of correlations with Pearson's p test. All values were expressed as means ± standard deviations. Although values of $p < 0.05$ were considered to indicate statistical significance, but also the Bonferroni correction for multiple comparisons was calculated to avoid a high false-positive rate.

3. Results

3.1. Descriptive Data

A total of 271 OCT videos, extracted from 95 animals (40% males/60% females) at different times of study follow-up, were analysed. Episcleral model (n = 35 animals): 72 videos from the right eye (RE)/47 videos from the left eye (LE); Ms model (n = 28): 38 RE/26 LE; healthy controls (n = 32): 31 RE/57 LE. The number of eye injections inducing each glaucoma model, and the IOP curves they generated compared to healthy controls, are shown in Figure 2. Glaucomatous and healthy males had higher IOP levels than females throughout the study (data extracted from [50,62]).

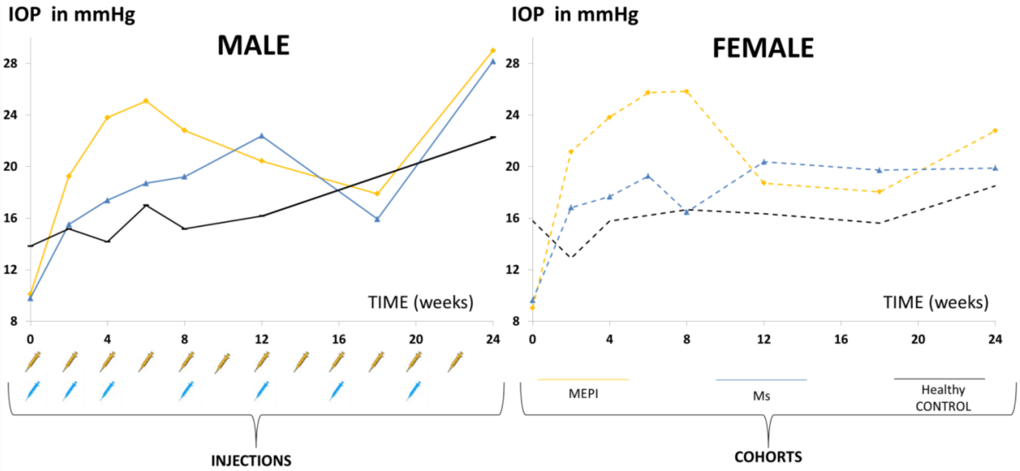

Figure 2. Intraocular pressure curves (right eyes) in two models of chronic glaucoma and healthy controls. Abbreviations: MEPI: glaucoma model induced by sclerosing the episcleral veins; Ms: glaucoma model induced by injection of PLGA microspheres; IOP: intraocular pressure (data extracted from [50,62]).

3.2. Descriptive Data

OCT analysis of the vitreous detected higher vitreous/retinal pigment epithelium (VIT/RPE) intensities in chronic glaucoma. After the first hypertensive injection, the MEPI model presented the highest initial vitreous signal intensity value, coinciding with the greatest initial fluctuation in IOP increase. This trend was maintained until 12 weeks (Figure 3a). The Ms model presented lower initial vitreous signal intensity, equalled the MEPI model at week 8 (even when IOP still remained at ocular normotension levels (<20 mmHg)) and, from week 12 onwards, the Ms model surpassed the MEPI model. Non-injected left eyes also showed a slight increase in vitreous signal with respect to healthy controls (Figure 3b). Healthy control animals' IOP and vitreous signal intensity curves showed lower levels than both chronic glaucoma models (Figures 2 and 3).

In addition, the influence of sex on vitreous signal was analysed. In general, females of both chronic glaucoma models showed slightly higher VIT/RPE OCT intensity than males and their healthy female counterparts. However, under physiological conditions (healthy control) males showed a peak of vitreous intensity at week 12 (16 weeks of life) that declined in later phases of the study (Figure 3c,d).

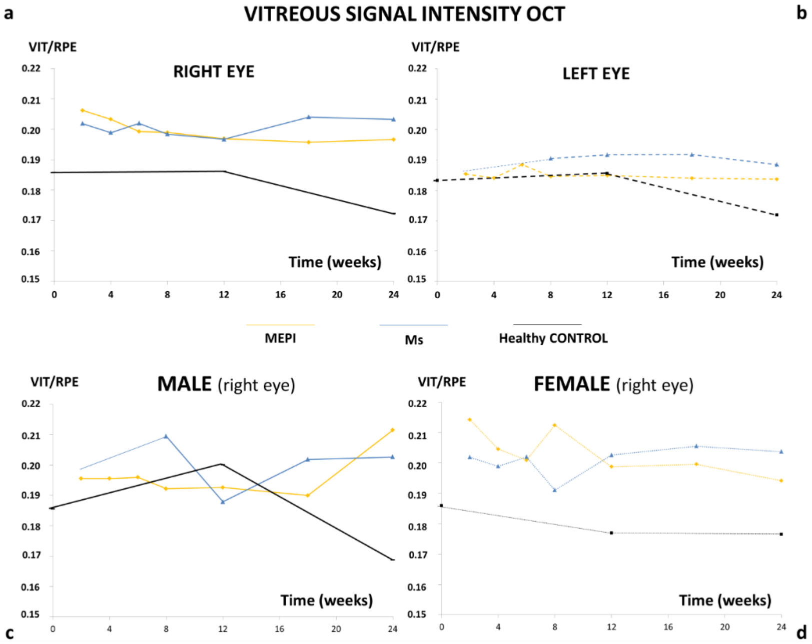

Figure 3. VIT/RPE signal intensity. (**a**) Right eye (both sexes); (**b**) left eye (both sexes); (**c**) males (right eye); (**d**) females (right eye). MEPI: episcleral vein sclerosis model (yellow); Ms: microsphere intraocular injection model (blue); healthy CONTROL: cohort of healthy animals without intervention (black); VIT: vitreous; RPE: retinal pigment epithelium.

3.3. Correlation Analysis

A correlation study was performed to determine the influence of the model on the VIT/RPE intensity analysed using OCT, as a marker of immunity. The MEPI model generates higher early IOPs (but without intraocular injection) than the Ms model, which has slower and progressive IOPs but is induced by intraocular injections with rupture of the ocular barrier and, therefore, induction of anterior chamber associated immune deviation (ACAID) [19,63]. The most relevant results and the strongest statistically significant correlations are shown (in bold) for all animals (Table 1) and by sex (Figure 4).

3.3.1. MEPI Model

Males presented higher IOPs at 4 weeks (r = 0.713, p = 0.014) and 6 weeks (r = 0.759, p = 0.007) as the number of injections increased (Figure 2). This correlation was not found in females. Males with higher IOPs after the first injection (2 w) also showed a later correlation (6 w) with higher IOPs (r = 0.832, p = 0.001) (Figure 4). In both sexes, week 6 OCT intensity correlates with week 12 intensity (r = 0.762, p = 0.001) (Figure 4). In the episcleral model, the presence of inflammation detectable by vitreous OCT signal at week 6 was maintained and even increased at later stages.

Table 1. Correlations in both chronic glaucoma models and healthy controls. Abbreviations: INJ: injections; IOP: intraocular pressure; OCT: optical coherence tomography; w: week; RE: right eyes; LE: left eyes; MEPI: model induced by sclerosing the episcleral veins; Ms: model induced by injecting microspheres into the anterior chamber; HC: healthy controls; im: inverse moderate correlation; m: moderate correlation. In bold: statistically high correlations.

	RIGHT EYE			**LEFT EYE**		
	MEPI	**Ms**	**HC**	**MEPI**	**Ms**	**HC**
INJ/IOP	Inj/6 w (m)	Inj/8 w (m)				
IOP/IOP	0 w/8 w (im) 2 w/4–6–8 w (m) **2 w/24 w** (r = 0.816, p = 0.025)	2 w/4 w (m) 8 w/12 w (m) **8 w/24 w** (r = 0.917, p = 0.028)	**4 w/8 w** (r = 0.934, p = 0.020)	0 w/8 w (im)	**4 w/12 w** (r = 0.800, p = 0.004)	
IOP/OCT	**2 w/2 w** (r = 0.812, p = 0.027)			**0 w/18 w** (r = −0.979 p = 0.004) **24 w/24 w** (r = 0.885, p = 0.008)	**18 w/18 w** (r = 0.890 p = 0.043)	
OCT/OCT	6 w/12 w (m) (r = 0.762, p = 0.001)					

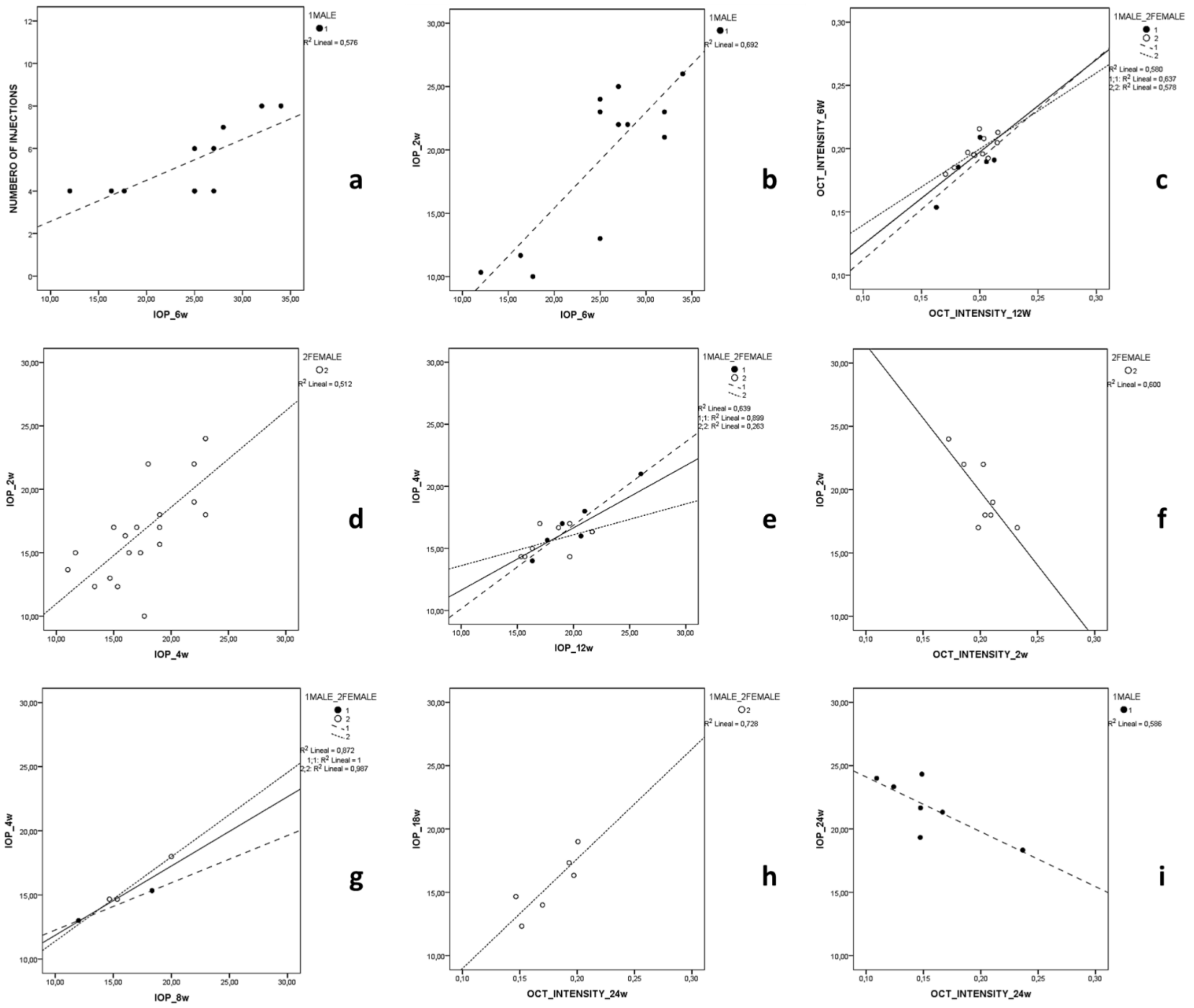

Figure 4. Significant correlations by sex in the two models of chronic glaucoma (episcleral model: (**a**–**c**); Ms model: (**d**–**f**)); and healthy controls (**g**–**i**). Abbreviations: IOP: intraocular pressure; OCT: optical coherence tomography; w: week.

3.3.2. Ms Model

In this model, both sexes presented a moderate direct correlation in IOPs between early (Figure 4d) and intermediate stages of the study (r = 0.716, $p < 0.001$) (Figure 4e). This became strong between weeks 8 and 24 (milestone reached later than in MEPI 2 w/24 w) (Table 1). However, in this model, an inverse correlation was found at week 2 between IOP and OCT (r = −0.775, $p = 0.024$) (Figure 4f), between IOP 2 w and OCT 12 w (r = −0.999, r = 0.026) and between IOP 12 w and OCT 18 w (r = −0.998, $p = 0.045$), mainly at the expense of females. Even when IOP did not reach ocular hypertension values (lower IOP levels) (higher) vitreous OCT signal was generated in that same week and later.

3.3.3. Healthy Control Cohort

Physiologically, a positive IOP correlation at early stages of the study (IOP4w-IOP8w r = 0.934, $p = 0.020$) was observed in both sexes (Table 1 and Figure 4g). Furthermore, in females, an inverse correlation IOP baseline -IOP 6 w (r = −0.999, $p = 0.021$) and direct correlations between IOP and OCT at intermediate (IOP 12 w-OCT 12 w; r = 0.997, $p = 0.049$, in the left eye) and late stages (IOP 18 w-OCT 24 w; r = 0.854, $p = 0.031$, in the right eye) were observed (Figure 4h). In females, the age-related degenerative process (possible neoepitope generation) [64,65] produces higher vitreous OCT intensity (reflex of immune involvement and/or activation) correlated with IOP even in a situation of ocular normotension. However, in males, moderate inverse correlation was found at the end of the study (IOP 24 w-OCT 24 w; r = −0.766, $p = 0.045$). In healthy control animals, no statistically significant strong correlation was found between OCT intensities, suggesting lower inflammatory influence under physiological conditions compared to glaucoma conditions.

Analysis of VIT/RPE signal intensity (as an indirect measure of vitreous parainflammation) showed different behaviour according to glaucoma model, inducing injections and sex. IOP levels correlated with vitreous intensity using OCT directly at early and late stages of the study. In addition, contralateral non-induced eyes also showed higher vitreous signal using OCT than healthy controls.

3.4. Histology

Based on the hypothesis of considering vitreous OCT intensity a reflection of the activity of the vitreous immune population, histological studies were performed to cellularly characterize the hyperreflective opacities.

An increased number of cells in the vitreous cavity was observed in the glaucomatous eyes (Figure 5). This was in accordance with a previous paper showing that the number of intravitreal cells was higher when IOP was experimentally elevated in adult mice [34]. Preretinal localization of intravitreal cells close to the internal limiting membrane, as well as their round shape, suggested that these cells could be hyalocytes [66] (Figure 5). Hyalocytes exhibit many phenotypic characteristics of macrophages and have a well-described phagocytic function that likely aids in maintaining vitreal transparency through the clearance of cellular and extracellular debris [67]. Hyalocyte-like cells in hypertensive rat eyes showed positive for ionized calcium-binding adaptor molecule 1 (Iba1) (Figure 6), a 17-kDa protein whose expression is restricted to macrophages [68], including hyalocytes [41]. As expected, the Iba1 antibody also marked activated microglia embedded in the retina of hypertensive eyes (Figure 6) [69]. Similarly, as occurs in other models of ocular inflammation [41], examination of the ciliary body in hypertensive eyes revealed that the ciliary body was surrounded by many hyalocyte-like cells (Figure 6), some of which seemed to have migrated from the ciliary body, crossing its outer non-pigmented epithelium (Figure 6). This could suggest that, as has been postulated by other authors [41], the ciliary body could be a potent source of vitreal macrophages during eye inflammation. Hyalocyte-like cells in hypertensive rat eyes were never related with protruding glial membranes that, from the internal limiting membrane, penetrate the vitreous body (Figures 5 and 6), suggesting that the migration of microglia through the internal limiting membrane as proposed by Santos et al. [70] in a model of photoreceptor degeneration would not be a common phenomenon in hypertensive rat eyes. However, this cannot be ruled out.

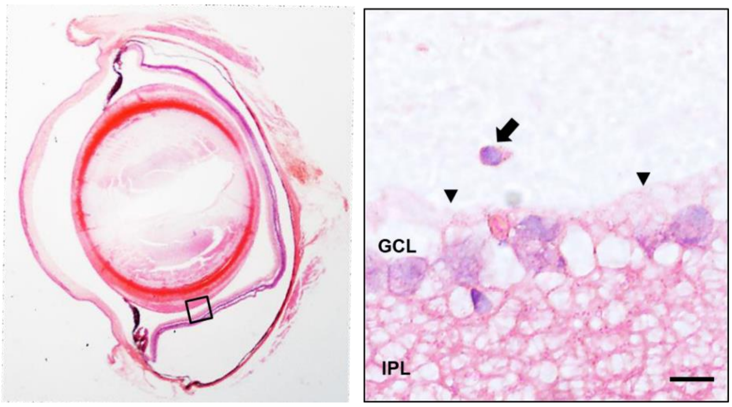

Figure 5. Localization of intravitreal cells (arrow) close to the internal limiting membrane (arrowhead) in hypertensive rat eyes. GCL: ganglion cell layer; IPL: internal plexiform layer. Scale bar: 12.5 µm.

Once the existence of vitreous changes detected by OCT (VIT/RPE signal) was evidenced in glaucoma models, and the vitreous hyperreflective opacities were corroborated by histological studies as cell-like Iba-1+ hyalocytes with phagocytic activity, the vitreous signal was studied as an indirect representation of the immune population by analysing the size of the hyperreflective opacities [31,33].

3.5. In Vivo Analysis of Vitreous Immunity Detected Using OCT

The individual hyperreflective opacities detected using OCT and characterized as Iba1+ cell-like hyalocytes were analysed. As a representation of overall immune response, the total area of opacities/cells was quantified. In the glaucoma models, right eyes showed significantly increased total areas (MEPI > Ms), and left non-induced eyes showed increase (no significantly) compared to healthy controls (Figure 7). To ascertain whether the increase in total cell area was due to an increased number of cells and/or an increase in cell size, and thus an increase in activated cells, the following was performed:

3.5.1. Quantification of the Mean Number of Opacities/Cells

Under physiological conditions, the number of opacities remained at 10–20; however, glaucoma-induced right eyes had a higher number of hyperreflective opacities/cells that fluctuated with a mean of approximately 70 opacities/cell. The highest quantification occurred early in the MEPI model. The Ms model showed an initial peak, coinciding with the first intraocular injection, and achieved elevated levels at later stages. The left eyes from both models also showed a slight increase in cell number (Figure 7). The results of these two in-depth analyses are in agreement with previous results for relative VIT/EPR intensity [49].

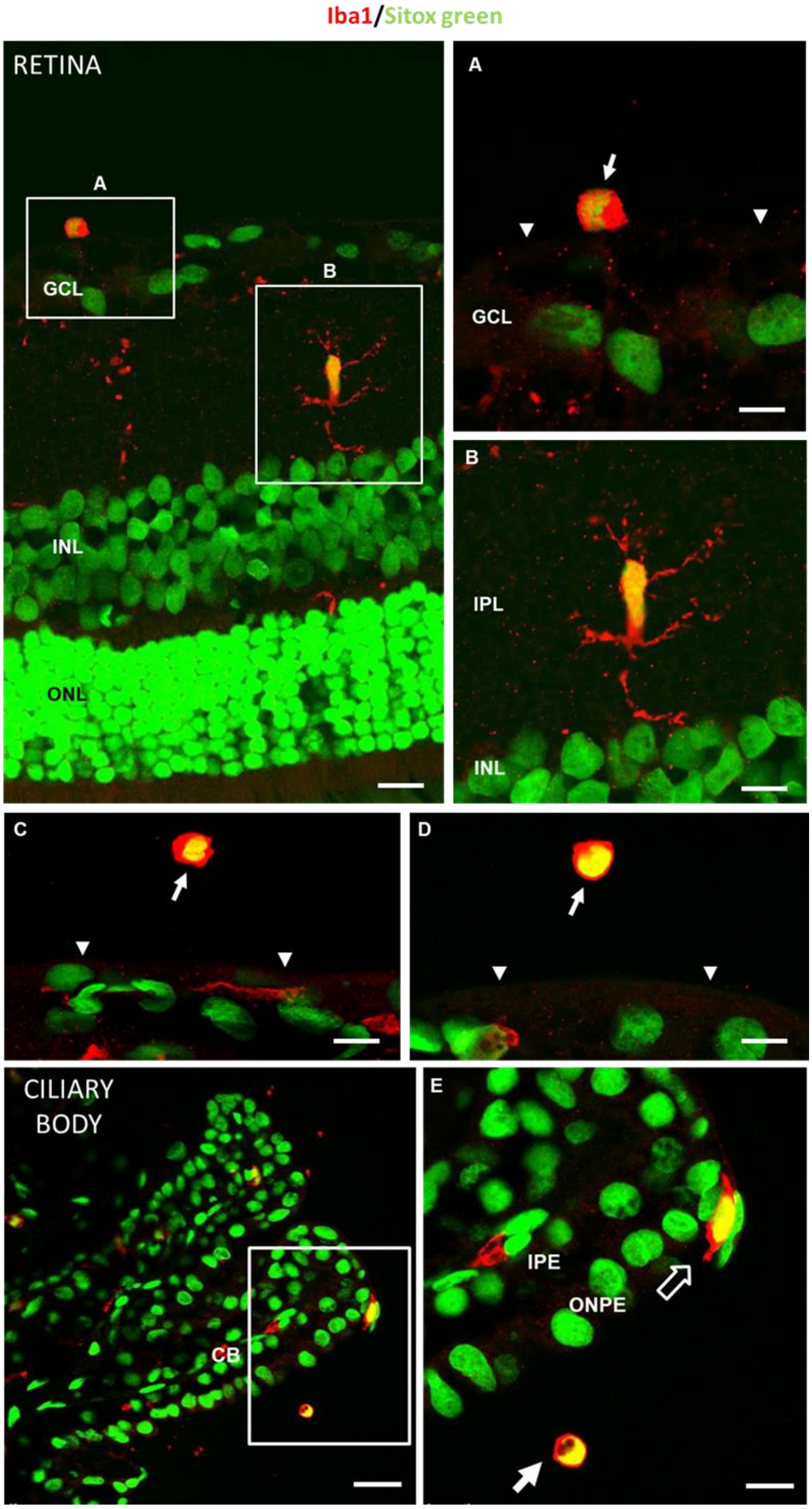

Figure 6. Hyalocyte-like cells in hypertensive rat eyes showed positive for Iba1 (arrows). (**A**,**C**,**D**,**E**): Examples of Iba1 positive hyalocyte-like cells. (**B**): Activated microglia embedded in the retina also showed, as expected, positive for Iba1. (**E**): The presence of Iba1 positive cells crossing the outer

non-pigmented epithelium could suggest that hyalocytes migrate from the ciliary body to the vitreous. GCL: ganglion cell layer; IPL: internal plexiform layer; INL: inner nuclear layer; ONL: outer nuclear layer; arrowhead: internal limiting membrane; CB: ciliary body; ONPE: outer non-pigmented epithelium; IPE: inner pigmented epithelium; open arrow: Iba1 positive cell crossing the outer non-pigmented epithelium; white arrow: Iba1 positive hyalocyte. Scale bar: Retina: 12.19 µm; (**A**): 6.25 µm; (**B**): 7.24 µm; (**C**): 10 µm; (**D**): 8.3 µm; Ciliary body: 23.81 µm; (**E**): 9.92 µm.

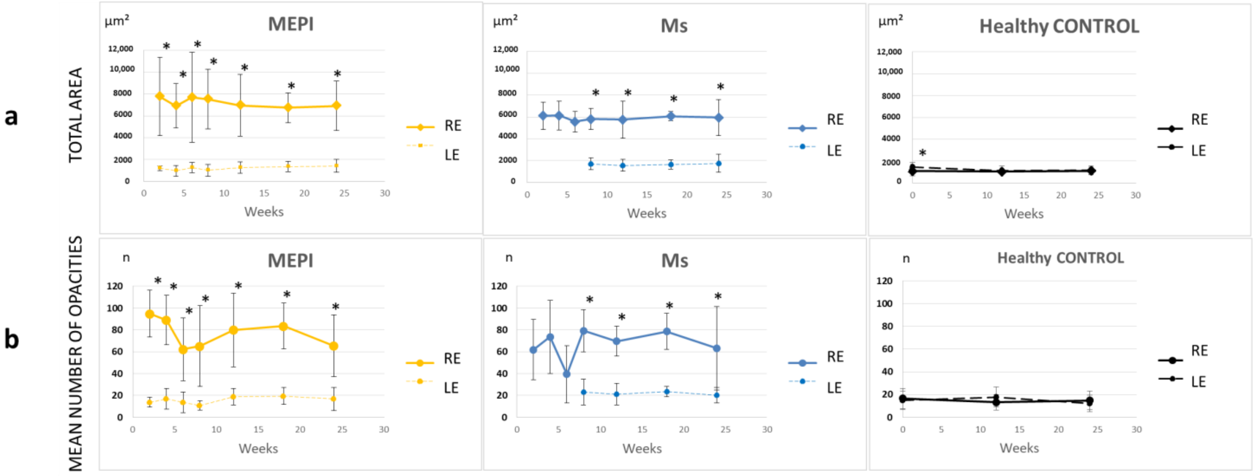

Figure 7. Changes in total immune response (**a**) and cellular quantification (**b**) in both glaucoma models and healthy controls. Abbreviations: RE: right eyes; LE: left eyes; MEPI: model induced by sclerosing the episcleral veins; Ms: model induced by injecting microspheres into the anterior chamber; n: number; *: statistical significance, $p < 0.05$, using ANOVA test.

3.5.2. Percentage of Opacities/Cells by Size

The set of hyperreflective opacities or vitreous cell populations was divided into isolated cells (<10 microns^2), non-activated cells (10–50 microns^2), activated cells (50–250 microns^2) and cell complexes (>250 microns^2) [31,33] (Figure 8) with the aim of determining the changes in the population ratio in the non-activated and activated state in glaucoma vs. healthy eyes (Figure 9). Study at the vitreoretinal interface does not require a correction factor and the histological similarity can be measured directly [47]. Under physiological conditions, a population ratio ordered from lowest to highest representation was found: isolated cells (<10 microns^2) < complexes (>250 microns^2) < activated cells (50–250 microns^2) < non-activated cells (10–50 microns^2). Under glaucoma conditions, a specular response was found between opacities of 50–250 microns^2 (activated cells) and 10–50 microns^2 (non-activated cells), respectively. Dynamic fluctuations were observed, but approximately 40–50% on average were opacities >50 microns^2 in size (activated cells). In addition, the onset of damage generated an early peak in complexes (>250 microns^2). The Ms model (induced by intraocular injection) produced a higher proportion of opacities in the 50–250 microns^2 range, suggesting early vitreous activation.

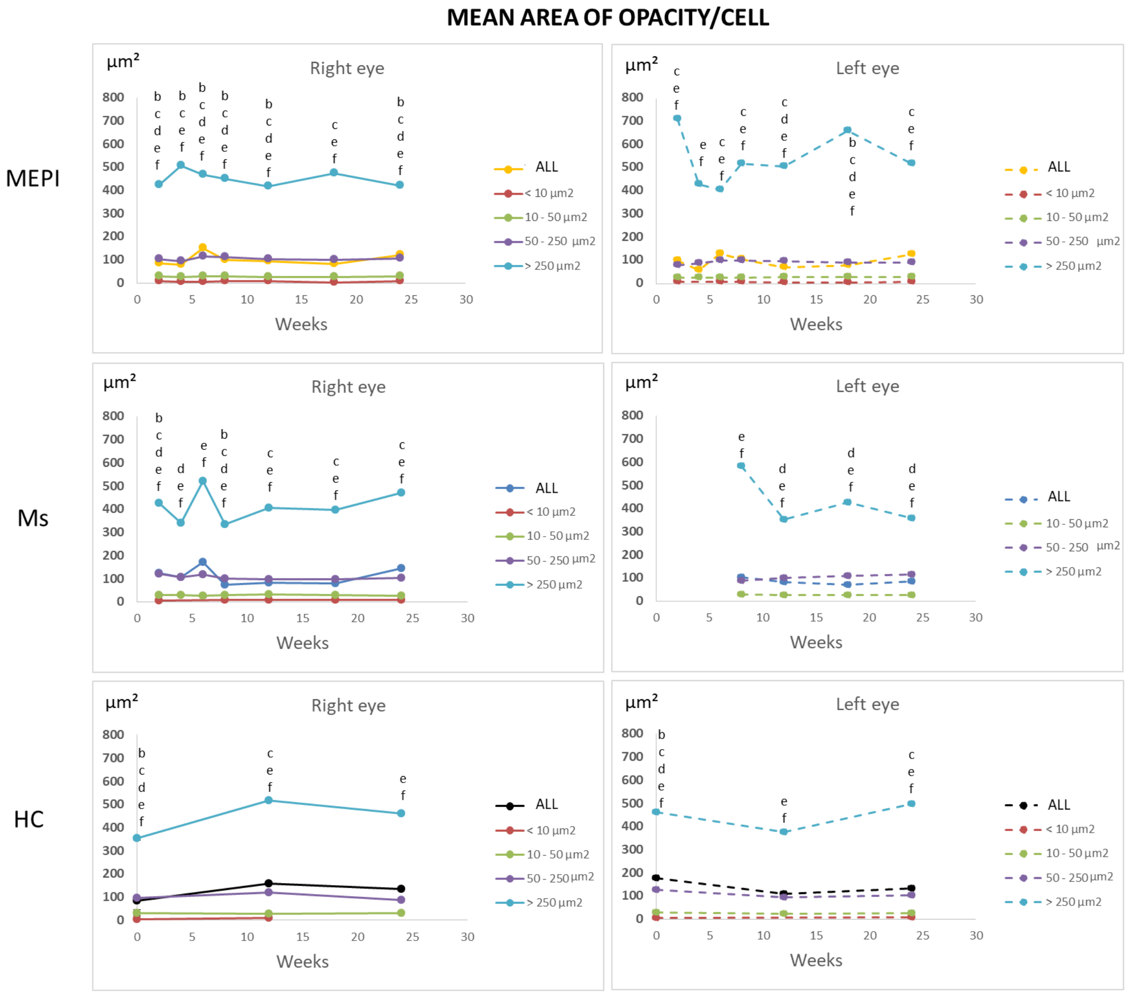

Figure 8. Cell subdivisions based on the mean area of vitreous opacities measured using OCT. Abbreviations: MEPI: model induced by sclerosing the episcleral veins; Ms: model induced by injecting microspheres into the anterior chamber; isolated cells: <10 microns^2 (group 1); non-activated cells: 10–50 microns^2 (group 2); activated cells: 50–250 microns^2 (group 3); cell complexes: >250 microns^2 (group 4). Cell populations maintain similar sizes over time, implying reliability of measurement. Complexes > 250 microns^2 undergo the greatest variations with peaks at the onset of noxa in both eyes. Statistically significant differences ($p < 0.05$) were highlighted with alphabetic markers as follows: a (group 1-group 2); b (group 1-group 3); c (group 1-group 4); d (group 2-group 3); e (group 2-group 4); f (group 3-group 4).

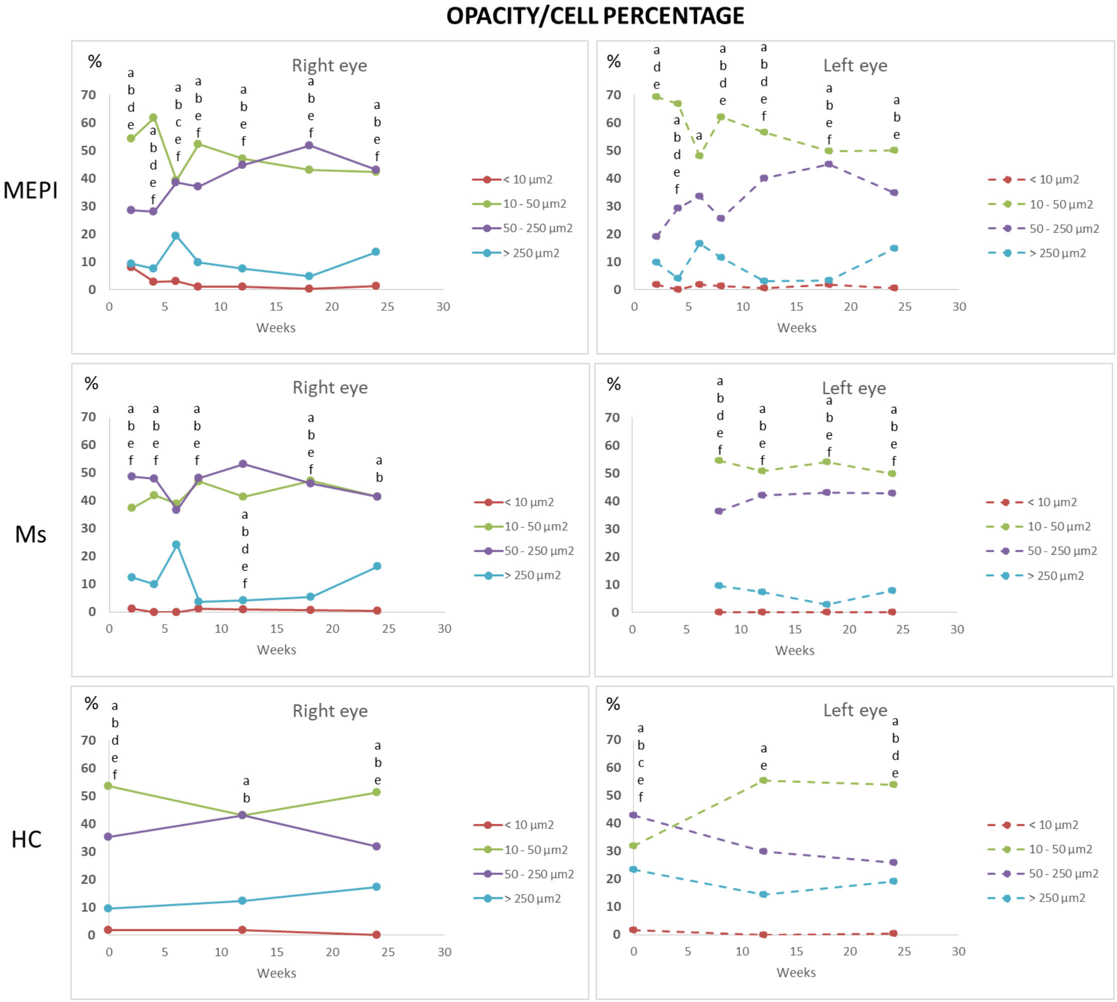

Figure 9. Changes in the vitreous immune population (opacities) in both chronic glaucoma models and healthy controls over 6 months. Abbreviations: MEPI: model induced by sclerosing the episcleral veins; Ms: model induced by injecting microspheres into the anterior chamber; isolated cells: opacities < 10 microns^2 (group 1); non-activated cells: 10–50 microns^2 (group 2); activated cells: 50–250 microns^2 (group 3); cell complexes: > 250 microns^2 (group 4). Data represented in percentages. Statistically significant differences ($p < 0.05$) were highlighted with alphabetic markers as follows: a (group 1-group 2); b (group 1-group 3); c (group 1-group 4); d (group 2-group 3); e (group 2-group 4); f (group 3-group 4).

3.5.3. Mean Intensity of Opacities/Cells

Under physiological conditions, the lowest intensity was quantified in isolated opacities/cells (<10 microns^2) and progressively increased with size: opacities of 10–50 microns^2 (non-activated cells) followed by opacities of 50–250 microns^2 (activated cells). However, under glaucomatous noxa, this trend reversed and a greater variation in intensity was quantified in the smallest opacities/cells (<10 microns^2) (Figure 10) prior to the increase in size. Subsequently, with increased soma size (activated cells with pseudopod formation) [40,53,67,71], a relative decreased mean intensity was quantified.

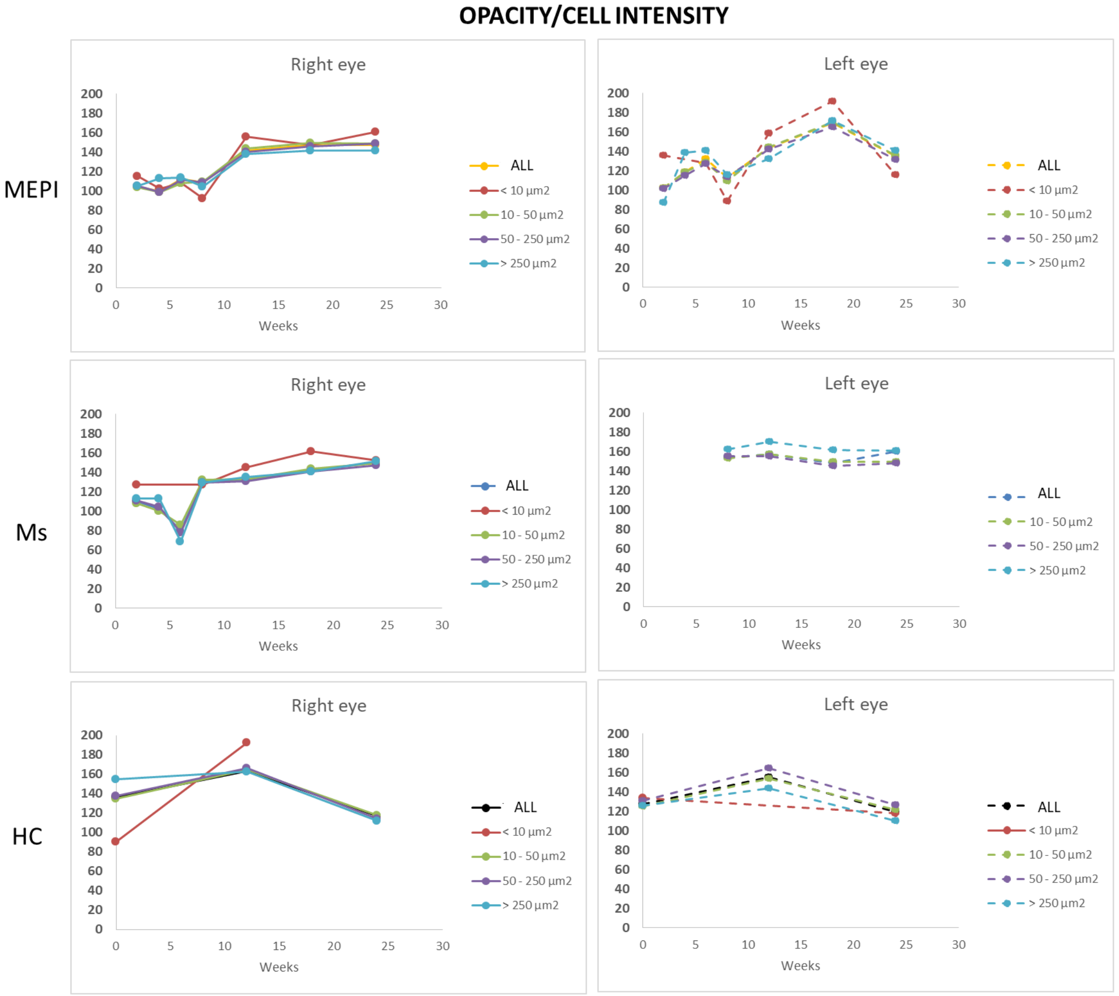

Figure 10. Mean intensity of opacities/cells based on size in both chronic glaucoma models and healthy controls. Abbreviations: MEPI: model induced by sclerosing the episcleral veins; Ms: model induced by injecting microspheres into the anterior chamber; isolated cells: opacities < 10 microns^2; non-activated cells: 10–50 microns^2; activated cells: 50–250 microns^2; cell complexes: > 250 microns^2. There were no statistically significant differences.

3.5.4. Average Eccentricity of the Opacities/Cells

This analysis allows observation of cell morphology. Linear or flat morphology (eccentricity close to 1) vs. rounded morphology (eccentricity far from 1). Under physiological conditions, isolated opacities/cells (<10 microns^2) presented the most rounded or amoeboid morphology (eccentricity 0.85) as opposed to opacities/cells with progressively larger sizes of 10–50 microns^2 (non-activated), followed by 50–250 microns^2 (activated cells) and <250 microns^2 (cell complexes), these being increasingly flat (eccentricity 0.95–1). Under conditions of glaucomatous noxa, this same trend was maintained. However, at early stages of the study, mean eccentricity was even lower than under healthy conditions (and was lower in the Ms model with intraocular injection) (Figure 11).

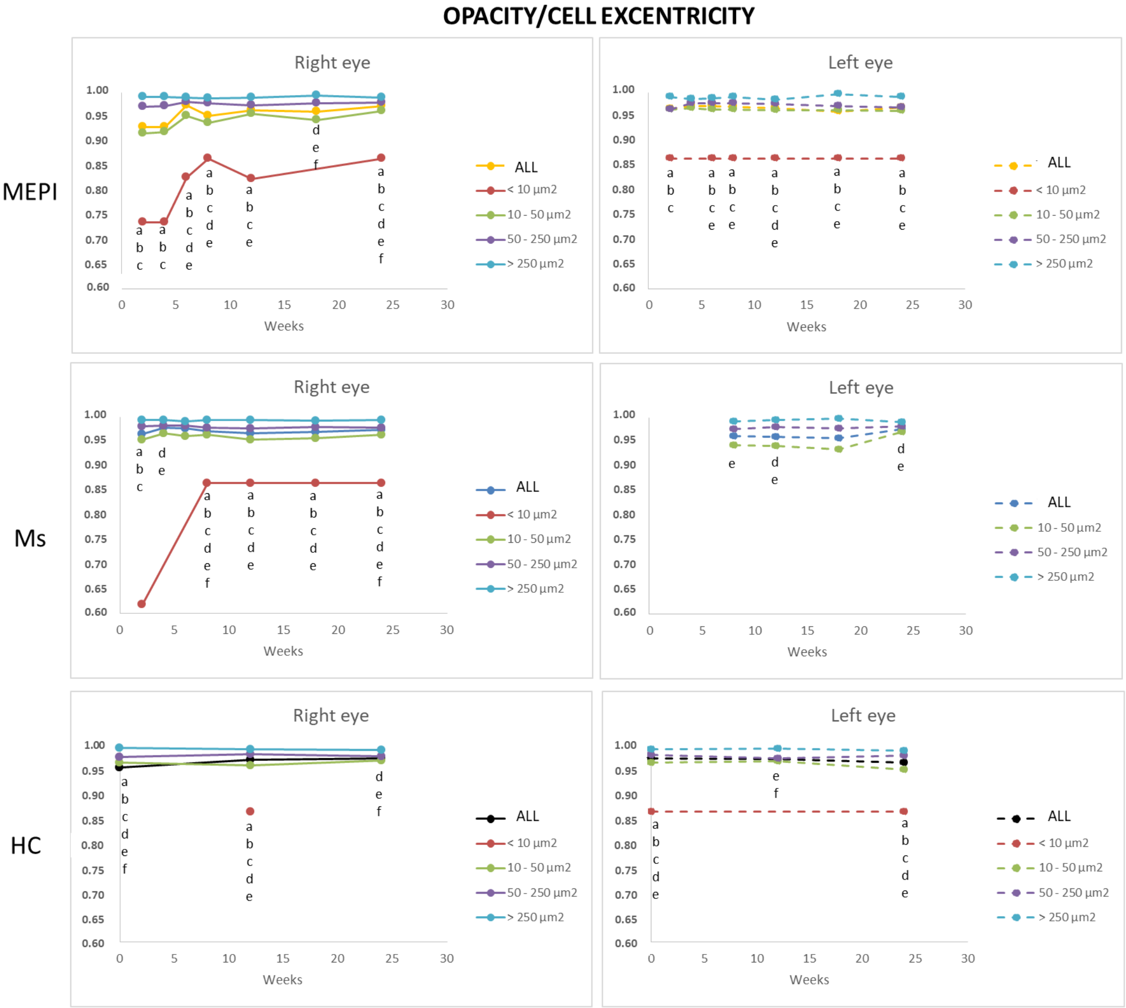

Figure 11. Mean eccentricity of vitreous opacity detected using OCT, according to size, in both glaucoma models and healthy controls. Indirect in vivo analysis of cell soma morphology. Abbreviations: MEPI: model induced by sclerosing the episcleral veins; Ms: model induced by injecting microspheres into the anterior chamber; isolated cells: opacities < 10 microns^2 (group 1); non-activated cells: 10–50 microns^2 (group 2); activated cells: 50–250 microns^2 (group 3); cell complexes: > 250 microns^2 (group 4). Statistically significant differences ($p < 0.05$) were highlighted with alphabetic markers as follows: a (group 1–group 2); b (group 1–group 3); c (group 1–group 4); d (group 2–group 3); e (group 2–group 4); f (group 3–group 4).

3.5.5. Mean Orientation of the Opacities/Cells

Orientation was analysed to discover if examination of the vitreous OCT made it possible to objectify an active shift (change in mean orientation) of immunity towards the noxa [35,41,60,72]. Under physiological conditions, stability was observed in all sizes of opacities/cell groups. However, under glaucomatous noxa conditions, the smaller opacities (<10 microns^2: isolated ovoid cells) of both models showed an early change in orientation. In addition, the Ms model showed a progressively increasing change in orientation that continued until the later stages of the study (Figure 12). Continuous activation and motility of early vitreous immunity was detected prior to the increase in opacity/soma size, which coincided with the increase in IOP and intraocular injections.

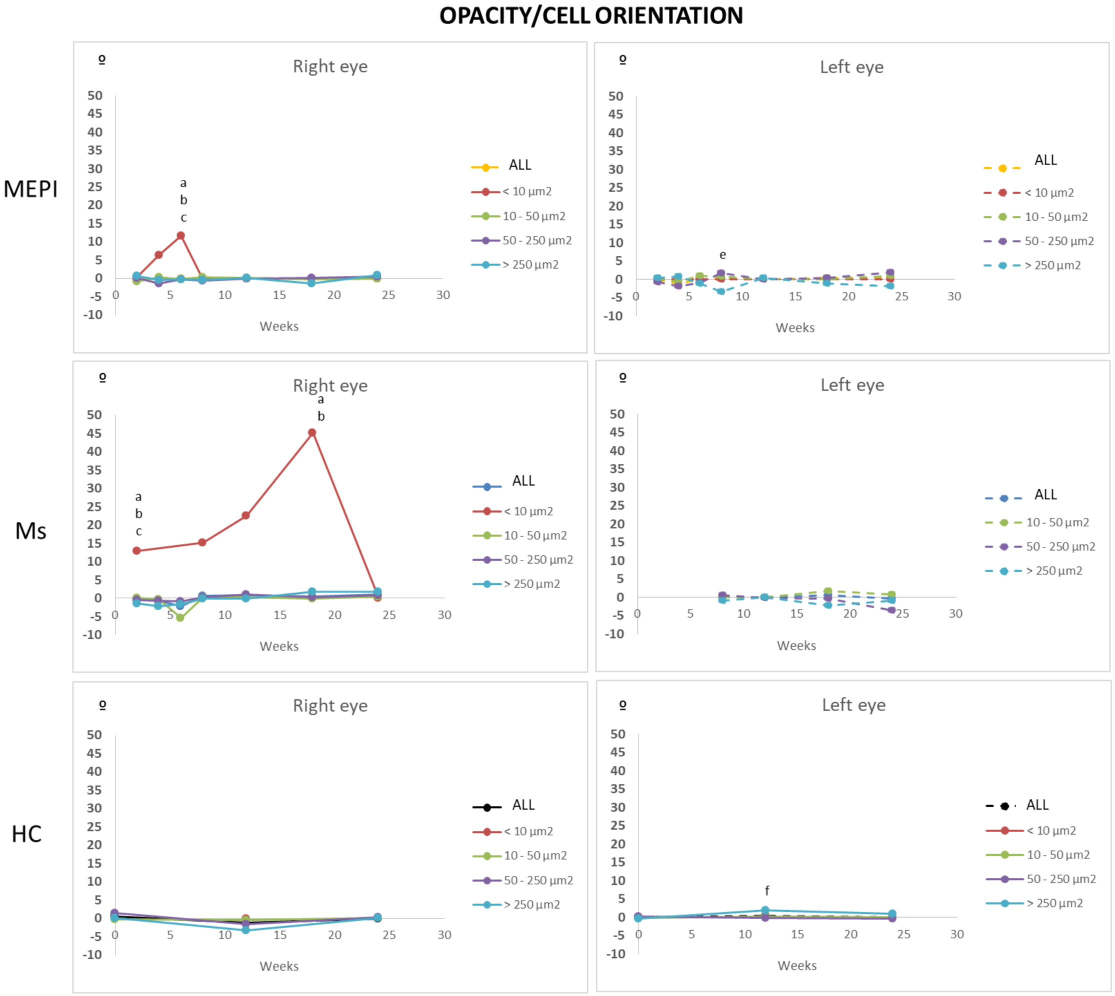

Figure 12. Mean orientation of vitreous opacity detected using OCT, according to size, in both glaucoma models and healthy controls. In vivo analysis of the change in opacity/cell direction for motility. Abbreviations: MEPI: model induced by sclerosing the episcleral veins; Ms: model induced by injecting microspheres into the anterior chamber; isolated cells: opacities < 10 microns^2 (group 1); non-activated cells: 10–50 microns^2 (group 2); activated cells: 50–250 microns^2 (group 3); cell complexes: > 250 microns^2 (group 4). Statistically significant differences ($p < 0.05$) were highlighted with alphabetic markers as follows: a (group 1–group 2); b (group 1–group 3); c (group 1–group 4); d (group 2–group 3); e (group 2–group 4); f (group 3–group 4).

4. Discussion

Imaging study: OCT is a fast, non-invasive tool that provides repeatable analysis of the neuroretinal structure and measurement of different retinal layers [73,74]. However, it has the handicap of not being able to identify the different cell types within the neuroretinal thickness, for example, to differentiate between immune cells and the rest of the neuronal, supporting or vascular cells. Studies that have identified certain cell types either require animals genetically modified to express fluorescence or are technically very complex [75]. OCT is a technology capable of offering almost histological images depending on the light transmitted or reflected as it passes through different structures with differing densities. It can be utilized to identify tissue structure or composition. With the development of more advanced technologies, we have made the leap to vitreous analysis under both normal and inflammatory conditions. The size of the vitreous cells involved (10 microns) is larger than the resolution of OCT (3 microns), which allows the number of cells to be quantified manually or, in our case, by automated image-counting methods [76]. In addition, OCT has the added advantage of having its peak sensitivity in the vitreous over the retina. Evaluating opacities on a background with less diffuse backscattering due to tissue homogeneity of the vitreous (mainly water) allows us to analyse the intensity changes more reliably than in the retina (with tissue heterogeneity and hundreds of neurons, connecting cells, astro/microglial and blood cells). Those areas that light finds it harder to pass through have higher optical densities (intensity in our study) corresponding to lipid or calcium membranes. Related to this idea, Keane et al. [77] published a study demonstrating that the relative intensity of VIT/RPE correlates positively with clinical vitreous turbidity. This technique was validated in subsequent studies [46,78]. Rodrigo et al. [49] described greater vitreous signal in rats with glaucoma than in healthy rats. Recently, a study performed in humans using OCT identified ramified macrophage-like cells on the retinal surface, suggesting a hyalocyte origin (but without histological confirmation), with altered morphology in patients with retinopathies and associated with areas of retinal nerve fibre layer (RNFL) thinning in glaucoma patients. However, this technique is limited by complexity, long acquisition time, axial length correction to correct for ocular magnification, manual cell identification and high cost [72]. To our knowledge, vitreous OCT analysis has not been used in animal research to analyse in depth the vitreous parainflammation caused by different models of ocular hypertension.

Parainflammation is an intermediate state between the basal homeostatic state and the classic inflammatory response, which is more common but of lesser magnitude. An immune response is initially beneficial and necessary to restore tissue homeostasis and promote tissue cleaning, healing and functionality. Glaucoma results in neuroretinal damage and, when mediated by glutamate, damage-associated molecular patterns released by RGCs and glia trigger parainflammatory responses [28]. Retinal response to glaucoma damage appears to be neuroprotective and mediated by myeloid-derived suppressor cells [56]. In the event of damage, astrocytes and retinal microglia release pro- and anti-inflammatory factors [79] capable of activating and regenerating retinal progenitor cell niches [56]. Both are activated at the same time and negotiate the removal of waste, this falling primarily on microglia. However, when microglia are not sufficient, astroglia compensate, albeit in a delayed manner leading to pathological conditions [60]. If there is a defect in immune response pathways due to accumulating risk factors, prolonged or sustained inflammatory stimulation, or to “neo-antigens” generated with ageing, the physiological equilibrium may be impaired and the regulatory mechanisms are altered [75], thereby converting beneficial immunity into a neurodestructive autoimmune process [80]. Microglia and macrophages undergo important dynamic morphological changes in their function. In an inactive situation, they are branched to serve as a sensor to changes in the microenvironment. Upon damage they are activated, upregulate surface and complement receptors, secrete soluble factors and undergo changes in shape, proliferation, migration and phagocytosis through rearrangements of the actin cytoskeleton. The Iba1 protein [69] is a calcium- and actin-binding protein for cell migration and phagocytosis of hematopoietic cells, restricted to microglia and macrophages; therefore, its staining/marking rules out other cell types such as lymphocytes, astrocytes or oligodendrocytes. Microglial activation is one of the first events in glaucomatous neuronal damage that occurs prior to RGC death; low levels of microglial activation induce delayed neurodegeneration and control of its activation reduces optic nerve damage [28].

Vitreous and hyalocytes: The inhibitory vitreous microenvironment is regulated by hyalocyte-like macrophages and mediated by soluble molecules [81]. The vitreous medium, with high water content embedded in the extracellular matrix, is ideal for the transmission of soluble factors, meaning that hyalocytes can detect changes in the microenvironment [82] easily and rapidly to target the noxa. Hyalocytes present secretory granules, lysosomes, a developed Golgi apparatus, a lobulated nucleus, cytoplasmic projections and a moderate number of mitochondria [40]. In a state of activation secondary to changes in the microenvironment, the number/size of intracellular organelles increases and, therefore, the membrane content increases, facilitating its possible detection by imaging tests. Under normal conditions, the vitreous is transparent. Analysing a structure designed to be virtually invisible (vitreous) by non-histological imaging techniques is difficult. Dark-field slit microscopy revealed many spots in the cortex of vitreous that scatter light intensely, the small ones being described as hyalocytes and the larger ones as debris [38]. In the activated state, increased intracellular membranes and organelles may generate increased hyperreflectivity with OCT. A two-week study using OCT detected a higher density of vitreous opacities located near areas of cell death [48]. The nature of these vitreous opacities was unknown and it was posited they were inflammatory cells, cellular debris or other factors migrating through the vitreous. In our 24-week follow-up study, these opacities were analysed in depth and a hyalocyte origin was demonstrated.

Characterization of hyalocytes under physiological and pathological conditions remains unclear.

Under physiological conditions, there is a slow turnover with long half-lives of macrophages resident in the brain, retina [83] and vitreous [40,67]. In a histologic study of healthy guinea pig eyes, Ogawa K [53] describes free hyalocytes of elongated morphology (approximately 50 microns) entangled in the vitreous cortex, and the highest density of small, mostly ovoid, free cells (approximately 20 microns) on the surface of the ciliary body. The abundance in the ciliary body epithelium suggests that it is a site of precursor emigration from the ciliary stroma, consistent with our results (Figure 6). Hyalocytes can enter the vitreous through the ciliary body epithelium and subsequently move along the longitudinal tracts of the vitreous gel into the neuroretinal vicinity. In mice, hyalocytes are concentrated near the papilla and at the vitreous base, with the latter location coinciding with a higher concentration of total proteins [84]. In rats, 90% presented macrophage markers and 15% monocyte/macrophages, which is close to the percentage found in healthy rats in our study, where approximately 95% were in the large cell range (10–250 microns) and approximately 5% in the smaller cell range (<10 microns—monocytes). The higher proportion of vitreous opacities/cells in healthy rats coincided with opacities of sizes corresponding to non-activated (or anti-inflammatory state) cells, consistent with the eye's immune inhibitory privilege state [81,85] and with the control microglia size (20–60 microns^2) identified in retinal studies [33]. A variable number of opacities corresponding to cells activated for the maintenance of homeostasis was also quantified [35] (Figure 9).

Sex: The healthy females in our study showed a linear vitreous signal, unlike the males, in which at around 16 weeks of age (12 weeks of the study) vitreous activation seems to occur, coinciding with an increase in retinal thickness and increased remodelling with subsequent loss [62]. In this regard, variations in microglial density between males/females have been described in different brain areas such as the preoptic area [61], and marked sexual dimorphism has been found in mouse peritoneal macrophages [86]. Hyalocytes share phenotypic characteristics with peritoneal and ependymal macrophages as serous cavity roving macrophages. The replacement rate of peritoneal macrophages was very high in males at 16 weeks of age, after sexual maturation, but was decreased and slow in females, coinciding with our results (Figure 3c,d). In contrast, immune disturbances tend to be more frequent in females, but more severe in males [87–89]. Females have demonstrated an enhanced ability to control infection [86] and less neuroretinal tissue loss in the presence of glaucomatous noxa [90]. The greater vitreous intensity observed in females in the glaucoma models, as well as in healthy animals at later ages (28 weeks of age), suggests a greater immunogenic presence that could act in an initially reparative manner in the presence of hypertensive noxa or age-associated neoepitopes, maintaining retinal structure and function [62,90]. These results highlight the importance of considering the influence of sex (traditionally not taken into account) and age in immune research, due to susceptibility to infectious, inflammatory or age-associated diseases such as glaucoma.

Visualization of neuroinflammation in the CNS and eye: In early stages of chronic neurodegenerative and psychiatric diseases, neuroinflammatory mechanisms initiated by chronic activation of innate immunity alter function and trigger death. As microglial alterations (dynamic changes in density and activation) are detectable in early stages of disease and precede neurodegeneration, they have been established as diagnostic and therapeutic biomarkers of progression [61,91]. Direct visualization of the recruitment of specific immune cells from the periphery to the brain [57] currently requires expensive and invasive techniques such as 2-photon microscopy (T cells), MRI (macrophages) and PET and SPECT (microglia). In the retina [33], in vivo microglia tracking using CSLO imaging has been achieved [92], allowing them to be evaluated independently of other retinal cells. This technique requires animals genetically modified to express fluorescence, and for obvious reasons cannot be performed on humans; however, analysis of the vitreoretinal interface using OCT is now within the reach of conventional ophthalmologic clinics. In addition, the image quality of the Bosco et al. technique [33] is critically dependent on background autofluorescence. In contrast, our vitreous OCT measurement filters and removes smaller-sized cellular elements and therefore ensures correct counting without interference. Comparing the retinal findings from the CSLO microglia study with the vitreous findings from the OCT hyalocyte study, we found comparable cell percentages, although with some key differences. Using CSLO analysis of retina in mice with glaucoma, 200–300 total microglial cells were quantified, and of these 10–180 were activated (approximate mean of 27–34%, with large variation of 5–60%). In our study, a mean of 70 opacities/cell (approximately 40–100) were counted, with a higher activation percentage (approximate mean of 40%) and lower variability (30–50%). It was not possible to analyse histologically whether hyalocyte activation was precocious to retinal microglia, but the higher percentage of vitreous opacities (hyalocytes) in the cell activation range found in our results with respect to retinal cells (microglia) suggests it was. It could thus serve as an indicator of progression or be linked to initial events in glaucoma pathogenesis.

Analysis of the vitreous in two glaucoma models.

The episcleral model alters the aqueous humour outflow pathway by sclerosis of episcleral veins via retrograde hypersaline injection; consequently, the blood–ocular barrier would be altered and activate the perivascular glia [16,93], triggering the inflammatory response. The MEPI results suggest that those animals with the lowest initial IOPs will have the highest IOPs after the onset of repeated episcleral hypertensive stimuli. In this model, the main correlations occur at early stages. The first hypertensive injection triggers an increase in vitreous intensity. The more damage produced at the first injection, the higher the IOP at week 2, which correlates with the OCT-detectable vitreous signal ($r = 0.812$, $p = 0.027$). Greater and earlier involvement of retinal glia was observed by histology in previous studies [50,51]. In addition, in left eyes an inverse correlation was found between baseline IOP levels and vitreous OCT 18 w ($r = -0.979$, $p = 0.004$), reflecting possible higher late contralateral inflammatory vitreous activation in those more hypotensive (susceptible) non-induced eyes, and also higher vitreous OCT signals the higher the IOP at later stages, IOP 24 w-OCT 24 w ($r = 0.885$, $p = 0.008$).

The Ms model triggers an ACAID response [85] to trauma (intraocular injection in the anterior chamber). After cannulation and acute IOP increase, a marked microglial response was observed, with similar increases in vitreous hyalocytes [34], coinciding with our observations of increased vitreous signal with cannulations (Figure 7). The Ms model presented a strong positive correlation in IOP at intermediate stages (IOP 8-24 w: $r = 0.917$, $p = 0.028$), later, therefore, than the episcleral model, where this milestone occurred from 2 w onwards (IOP 2 w-24 w). Likewise, correlation was detected in the non-induced left eye at IOP 4 w-12 w ($r = 0.800$, $p = 0.004$) and IOP 18 w-OCT 18 w ($r = 0.890$, $p = 0.043$), also demonstrating contralateral vitreous inflammatory activation.

Contralateral involvement: In the retina of a glaucoma mouse model with ocular hypertension induced by cauterization, microglial activation was observed in both the induced eye and the contralateral eye, exhibiting lower intensity, but which remained stable over time [94]. Our study produces similar results in the analysis of vitreous opacities/hyalocytes obtained in models of more progressive and chronic hypertension. The contralateral eye also shows vitreous changes with respect to the healthy control. These appear to be resident hyalocytes (without recruitment), as an increase in intensity (Figure 3b) but hardly any increase in number (Figure 7) was detected. Other glaucoma studies examining retinal microglia have shown contralateral activation even at normal IOP values, suggesting that increased IOP may not be a contributing factor in early stages [29], and with the superior colliculus acting as a communicative structure [12]. Individual susceptibility to increased IOP may differ based on the ability to control the immune response, and each individual's immune background may modify disease progression. Our vitreous OCT study is also able to detect early changes even in conditions of ocular normotension.

Affectation prior to IOP increase (normotensive values): Changes in gene expression related to immune response [95], acute stress and proinflammatory markers [12] have been demonstrated with early cytokine dysregulation, independently and prior to IOP increase, detection of RGC loss and axonal degeneration [28,79]. Cooper et al. [95] demonstrated activation of the complement cascade (plasma proteins to opsonize cellular debris by formation of membrane attack complexes, as a bridge between the innate and adaptive response) in retinal degeneration with increased inflammatory response that facilitates apoptotic cell elimination and Iba1 activation at an early stage of IOP increase. It was suggested that IOP increase could later act as an aggravating factor that exacerbates disease progression. In addition, Tsai et al. [14] described, in a model of experimental autoimmune glaucoma, an increase in complement activation after 6 weeks of IOP induction. Our results also showed an increase in larger vitreous opacities (>250 microns^2) at 6 weeks (Figure 9) that could correspond to complement-opsonized apoptotic bodies.

Analysis of vitreous opacities as a biomarker in glaucoma: There is still a long way to go in understanding the actions of immune cells in both healthy and diseased eyes. In the retina, microglia are considered activated when the soma is >50 microns. However, our results detect increased intensity (onset of intracellular machinery) in the vitreous and a change of orientation (onset of displacement) as an expression of activation in the smallest opacities at an early stage. Our findings suggest the smallest cells (<10 microns^2) would be the first in the communication and transformation chain to detect a change in homeostasis or noxa detection in the vitreous. This suggests that small cell analysis could serve as an early marker of vitreous immune activation, prior to the morphological change of the soma. In the episcleral model, the change is mainly observed in the initial hypertension. However, in the Ms model, even without an IOP increase, a marked change of orientation is generated with a progressive increase indicating that more and more cells are oriented towards a certain point (retinal damage). However, at later stages, the mean orientation returns to 0, suggesting that there could be more neuroretinal areas with damage in different locations and, therefore, more orientations to be taken by the cells, annulling the summation effect of the mean orientation. On the other hand, prior studies have also described how in the brain and retina the motility capacity of microglia damaged by chronic stress decreases [61]. In the somatosensory cortex, dystrophic microglia was compensated by microgliosis (increased number of microglia). Accordingly, another possible explanation of our results from both models, concerning the return to 0 orientation of the opacities/hyalocytes, could indicate "ageing or motility damage" due to accumulation, repetition and chronicity of oxidative stress. Reinforcing this idea, in the MEPI model, an increase in the number of opacities/hyalocytes is observed (Figure 7) from week 8 onwards (when the mean orientation is cancelled) (Figure 12). However, in the Ms model, the change in orientation is maintained along with the variation in the number of opacities/hyalocytes, possibly being secondary to the multiple intraocular injections. It has been shown that every intraocular injection (at least in the anterior chamber of the rat eye) triggers vitreous parainflammation, and repeated injections exacerbate this immune response with subsequent neuroretinal damage [33,50,92].

In the event of disease, reactive microgliosis is induced, which may be dependent on infiltration [96] and/or proliferation by self-renewal of adult CNS resident cells [58]. Both systemic and local exposure to harmful molecules can initiate the influx of myeloid cells into the vitreous. Vagaja N et al. [41] demonstrated in mice that after systemic noxa with lipopolysaccharide to simulate infection, an accumulation of hyalocytes is produced in the posterior margin of the ciliary body and inner retinal surface; and after multiple injections, there is much greater abundance in apical ciliary processes. London et al. [56] demonstrated that after glutamate intoxication insult, there is recruitment and activation of innate immune cells in retina on days 1 and 2; however, the increase in IOP produced a milder increase in immune cells. Before macrophages are observed in the retina, there is a proinflammatory profile, which changes to anti-inflammatory. Monocyte-macrophages are essential as anti-inflammatory and neurotrophic elements to support cell renewal of progenitor cells in the ciliary body and contribute to the initiation or resolution of inflammatory and regenerative states by switching functions [28]. Our vitreous opacities/hyalocytes results also show this specular relationship and anti/proinflammatory dynamism (Figure 9). In cell renewal, the primitive or more immature cells are rounded and, as they mature and acquire capabilities, they change their phenotype and morphology to less rounded [40,97]. The eccentricity results show that the Ms model, which has a higher proportion of more rounded or early cells, triggers a call for a higher number of primitive cells (Figure 11) from the ciliary body (Figure 6), or from extraocular circulation. However, the higher number of opacities/hyalocytes quantified in MEPI (Figure 7) suggests that they belong to those located in situ intraocularly.

Limitations and future perspectives: Circulating immune cells from the periphery can rapidly enter the CNS under pathological states and conditions that alter the blood–brain and blood–ocular barrier [79]. The limitations in the histologic phenotyping of our study could not resolve the dilemma of the infiltrative origin [98] (lymphocytic or not) of the increased vitreous opacities.

The authors are aware that many aspects and unknowns remain to be resolved. In our opinion, however, this finding paves the way for in vivo analysis of the immune side of glaucoma (of great importance in normotensive glaucoma and in the progression of glaucoma, even with normal pressure levels) in a non-invasive (without animal sacrifice, histological studies or contrasts), simpler and possibly earlier way than examining astroglial changes [99] in the retina, which are very difficult to detect nowadays.

There is a need to monitor pathological processes and evaluate the therapeutic efficacy of anti-inflammatory and other potential neuroprotective drugs [100]. Designing therapies for glaucoma other than hypotensive mechanisms would be beneficial and neuro-immunomodulatory targeting is emerging as a key to effective new therapies. Mesodermal immune cells could be important candidates for therapeutic interventions without direct impact on neuroectodermal lineage cell types [61]. Our method of analysing vitreous opacities/hyalocytes using OCT could serve as a reliable neuroimaging biomarker to detect disease onset and early progression applicable to glaucoma and potentially other neurodegenerative diseases impacting the retina and optic nerve [101].

5. Conclusions

Glaucoma presents chronic and subclinical inflammation. In a novel way, this study detects and monitors parainflammation non-invasively using optical coherence tomography of the vitreous, while computational analysis characterizes immune cellularity based on morphology.

Author Contributions: Conceptualization, M.J.R., A.M., E.G.-M. and A.P.d.P.; methodology, M.J.R., M.S., A.M., S.M.-M., T.M.-R., L.A., D.G.-H., J.C., A.C., J.R.; software, A.M., A.P.d.P.; validation, M.J.R., L.P., A.P.d.P. and E.G.-M.; formal analysis, M.J.R., M.S., E.G.-M., A.M., A.P.d.P.; investigation, M.J.R., M.S., S.M.-M., T.M.-R., D.G.-H., I.B.-O., J.G.-F., R.H.-V. and E.G.-M.; resources, E.G.-M., A.P.d.P., M.J.R., R.H.-V. and L.P.; data curation, M.J.R., A.M.; writing—original draft preparation, M.J.R., M.S., L.A., A.M., J.R.; writing—review and editing, M.J.R., A.M., E.G.-M., A.P.d.P., J.R. and L.P.; supervision, E.G.-M., A.P.d.P.; project administration, L.P. and A.P.d.P.; funding acquisition, M.J.R., E.G.-M., R.H.-V., L.P., A.P.d.P. All authors have read and agreed to the published version of the manuscript.

Funding: This research was funded by Rio Hortega Research Grants M17/00213, PI17/01726, PI17/01946 and PI20/00437 (Carlos III Health Institute), Research Group UCM 920415, and by MAT2017-83858-C2-2, MAT2017-83858-C2-1 and PID2020-113281RB-C2-2, PID2020-113281RB-C2-1 MINECO/AEI/FEDER, EU.

Institutional Review Board Statement: The study was conducted and approved by the Ethics Committee for Animal Research (PI34/17) of the University of Zaragoza (Spain) and was carried out in strict accordance with the Association for Research in Vision and Ophthalmology's Statement on the Use of Animals.

Informed Consent Statement: Not applicable.

Data Availability Statement: On request to corresponding author.

Conflicts of Interest: The authors declare no conflict of interest. The funders had no role in the design of the study; in the collection, analyses, or interpretation of data; in the writing of the manuscript, or in the decision to publish the results.

References

1. Quigley, H.; Broman, A.T. The number of people with glaucoma worldwide in 2010 and 2020. *Br. J. Ophthalmol.* **2006**, *90*, 262–267. [CrossRef] [PubMed]
2. AGIS Investigators. The advanced glaucoma intervention study (AGIS): 7. the relationship between control of intraocular pressure and visual field deterioration. *Am. J. Ophthalmol.* **2000**, *130*, 429–440. [CrossRef]
3. Jonas, J.B.; Aung, T.; Bourne, R.R.; Bron, A.M.; Ritch, R.; Panda-Jonas, S. Glaucoma. *Lancet* **2017**, *390*, 2183–2193. [CrossRef]
4. Lau, L.I.; Liu, C.J.L.; Chou, J.C.K.; Hsu, W.M.; Liu, J.H. Patterns of visual field defects in chronic angle-closure glaucoma with different disease severity. *Ophthalmology* **2003**, *110*, 1890–1894. [CrossRef]
5. Schlamp, C.L.; Li, Y.; Dietz, J.A.; Janssen, K.T.; Nickells, R.W. Progressive ganglion cell loss and optic nerve degeneration in DBA/2J mice is variable and asymmetric. *BMC Neurosci.* **2006**, *7*, 66. [CrossRef] [PubMed]
6. Chang, B.; Smith, R.S.; Hawes, N.L.; Anderson, M.G.; Zabaleta, A.; Savinova, O.; Roderick, T.H.; Heckenlively, J.R.; Davisson, M.T.; John, S.W.M. Interacting loci cause severe iris atrophy and glaucoma in DBA/2J mice. *Nat. Genet.* **1999**, *21*, 405–409. [CrossRef]
7. Lucas, D.R.; Newhouse, J.P. The Toxic Effect of Sodium L-Glutamate on the Inner Layers of the Retina. *Arch. Ophthalmol.* **1957**, *58*, 193–201. [CrossRef] [PubMed]
8. Neufeld, A.H. Nitric Oxide: A Potential Mediator of Retinal Ganglion Cell Damage in Glaucoma. *Surv. Ophthalmol.* **1999**, *43*, S129–S135. [CrossRef]
9. Dey, A.; Manthey, A.L.; Chiu, K.; Do, C.W. Methods to Induce Chronic Ocular Hypertension: Reliable Rodent Models as a Platform for Cell Transplantation and Other Therapies. *Cell Transplant.* **2018**, *27*, 213–229. [CrossRef] [PubMed]
10. Morgan, J.E.; Tribble, J.R. Microbead models in glaucoma. *Exp. Eye Res.* **2015**, *141*, 9–14. [CrossRef] [PubMed]
11. Morrison, J.C.; Moore, C.G.; Deppmeier, L.M.H.; Gold, B.G.; Meshul, C.K.; Johnson, E.C. A rat model of chronic pressure-induced optic nerve damage. *Exp. Eye Res.* **1997**, *64*, 85–96. [CrossRef]
12. Sapienza, A.; Raveu, A.-L.; Reboussin, E.; Roubeix, C.; Boucher, C.; Dégardin, J.; Godefroy, D.; Rostène, W.; Reaux-Le Goazigo, A.; Baudouin, C.; et al. Bilateral neuroinflammatory processes in visual pathways induced by unilateral ocular hypertension in the rat. *J. Neuroinflamm.* **2016**, *13*, 44. [CrossRef] [PubMed]
13. Chen, H.; Cho, K.S.; Vu, T.H.K.; Shen, C.H.; Kaur, M.; Chen, G.; Mathew, R.; McHam, M.L.; Fazelat, A.; Lashkari, K.; et al. Commensal microflora-induced T cell responses mediate progressive neurodegeneration in glaucoma. *Nat. Commun.* **2018**, *9*, 3209. [CrossRef] [PubMed]
14. Tsai, T.; Reinehr, S.; Maliha, A.M.; Joachim, S.C. Immune Mediated Degeneration and Possible Protection in Glaucoma. *Front. Neurosci.* **2019**, *13*, 931. [CrossRef] [PubMed]
15. Beutgen, V.M.; Perumal, N.; Pfeiffer, N.; Grus, F.H. Autoantibody Biomarker Discovery in Primary Open Angle Glaucoma Using Serological Proteome Analysis (SERPA). *Front. Immunol.* **2019**, *10*, 381. [CrossRef]
16. Streilein, J.W. Ocular immune privilege: The eye takes a dim but practical view of immunity and inflammation. *J. Leukoc. Biol.* **2003**, *74*, 179–185. [CrossRef]
17. Streilein, J.W.; Stein-Streilein, J. Does innate immune privilege exist? *J. Leukoc. Biol.* **2000**, *67*, 479–487. [CrossRef] [PubMed]
18. Jiang, S.; Kametani, M.; Chen, D.F. Adaptive Immunity: New Aspects of Pathogenesis Underlying Neurodegeneration in Glaucoma and Optic Neuropathy. *Front. Immunol.* **2020**, *11*, 65. [CrossRef]
19. Forrester, J.V.; Xu, H. Good news–bad news: The Yin and Yang of immune privilege in the eye. *Front. Immunol.* **2012**, *3*, 338. [CrossRef]
20. Nussenblatt, R.B.; Liu, B.; Wei, L.; Sen, H.N. The Immunological Basis of Degenerative Diseases of the Eye. *Int. Rev. Immunol.* **2013**, *32*, 97–112. [CrossRef]
21. Cruz-Guilloty, F.; Perez, V.L. Defence against oxidative damage. *Nature* **2011**, *478*, 42–43. [CrossRef]
22. Geyer, O.; Levo, Y. Glaucoma is an autoimmune disease. *Autoimmun. Rev.* **2020**, *19*, 102535. [CrossRef]

23. Gala, A. Observations on the hydrogen ion concentration in the vitreous body of the eye with reference to glaucoma. *Br. J. Ophthalmol.* **1925**, *9*, 516–519. [CrossRef]
24. Walsh, M.M.; Yi, H.; Friedman, J.; Cho, K.I.; Tserentsoodol, N.; McKinnon, S.; Searle, K.; Yeh, A.; Ferreira, P.A. Gene and protein expression pilot profiling and biomarkers in an experimental mouse model of hypertensive glaucoma. *Exp. Biol. Med.* **2009**, *234*, 918–930. [CrossRef]
25. Carter-Dawson, L.; Crawford, M.L.J.; Harwerth, R.S.; Smith, E.L.; Feldman, R.; Shen, F.F.; Mitchell, C.K.; Whitetree, A. Vitreal glutamate concentration in monkeys with experimental glaucoma. *Investig. Ophthalmol. Vis. Sci.* **2002**, *43*, 2633–2637.
26. Tong, Y.; Zhou, Y.L.; Zheng, Y.; Biswal, M.; Zhao, P.Q.; Wang, Z.Y. Analyzing cytokines as biomarkers to evaluate severity of glaucoma. *Int. J. Ophthalmol.* **2017**, *10*, 925–930. [CrossRef]
27. Gramlich, O.W.; Beck, S.; Hohenstein-Blaul, N.V.T.U.; Boehm, N.; Ziegler, A.; Vetter, J.M.; Pfeiffer, N.; Grus, F.H. Enhanced Insight into the Autoimmune Component of Glaucoma: IgG Autoantibody Accumulation and Pro-Inflammatory Conditions in Human Glaucomatous Retina. *PLoS ONE* **2013**, *8*, e57557. [CrossRef]
28. Wei, X.; Cho, K.-S.; Thee, E.F.; Jager, M.J.; Chen, D.F. Neuroinflammation and microglia in glaucoma: Time for a paradigm shift. *J. Neurosci. Res.* **2019**, *97*, 70–76. [CrossRef]
29. Gallego, B.I.; Salazar, J.J.; de Hoz, R.; Rojas, B.; Ramírez, A.I.; Salinas-Navarro, M.; Ortín-Martínez, A.; Valiente-Soriano, F.J.; Avilés-Trigueros, M.; Villegas-Perez, M.P.; et al. IOP induces upregulation of GFAP and MHC-II and microglia reactivity in mice retina contralateral to experimental glaucoma. *J. Neuroinflamm.* **2012**, *9*, 586. [CrossRef]
30. Gramlich, O.W.; Teister, J.; Neumann, M.; Tao, X.; Beck, S.; von Pein, H.D.; Pfeiffer, N.; Grus, F.H. Immune response after intermittent minimally invasive intraocular pressure elevations in an experimental animal model of glaucoma. *J. Neuroinflamm.* **2016**, *13*, 82. [CrossRef] [PubMed]
31. Kozlowski, C.; Weimer, R.M. An Automated Method to Quantify Microglia Morphology and Application to Monitor Activation State Longitudinally In Vivo. *PLoS ONE* **2012**, *7*, e31814. [CrossRef] [PubMed]
32. Kettenmann, H.; Hanisch, U.-K.; Noda, M.; Verkhratsky, A. Physiology of Microglia. *Physiol. Rev.* **2011**, *91*, 461–553. [CrossRef] [PubMed]
33. Bosco, A.; Romero, C.O.; Ambati, B.K.; Vetter, M.L. In Vivo Dynamics of Retinal Microglial Activation During Neurodegeneration: Confocal Ophthalmoscopic Imaging and Cell Morphometry in Mouse Glaucoma. *J. Vis. Exp.* **2015**, *2015*, 52731. [CrossRef]
34. Kezic, J.M.; Chrysostomou, V.; Trounce, I.A.; McMenamin, P.G.; Crowston, J.G. Effect of anterior chamber cannulation and acute IOP elevation on retinal macrophages in the adult mouse. *Investig. Ophthalmol. Vis. Sci.* **2013**, *54*, 3028–3036. [CrossRef] [PubMed]
35. Bosco, A.; Romero, C.O.; Breen, K.T.; Chagovetz, A.A.; Steele, M.R.; Ambati, B.K.; Vetter, M.L. Neurodegeneration severity can be predicted from early microglia alterations monitored in vivo in a mouse model of chronic glaucoma. *Dis. Model. Mech.* **2015**, *8*, 443–455. [CrossRef] [PubMed]
36. Holekamp, N.M. The Vitreous Gel: More than Meets the Eye. *Am. J. Ophthalmol.* **2010**, *149*, 32–36. [CrossRef] [PubMed]
37. Siegfried, C.J.; Shui, Y.B. Intraocular Oxygen and Antioxidant Status: New Insights on the Effect of Vitrectomy and Glaucoma Pathogenesis. *Am. J. Ophthalmol.* **2019**, *203*, 12–25. [CrossRef]
38. Sebag, J. Imaging vitreous. *Eye* **2002**, *16*, 429–439. [CrossRef] [PubMed]
39. Boehm, M.R.R.; Oellers, P.; Thanos, S. Inflammation and immunology of the vitreoretinal compartment. *Inflamm. Allergy Drug Targets* **2011**, *10*, 283–309. [CrossRef]
40. Sakamoto, T.; Ishibashi, T. Hyalocytes: Essential cells of the vitreous cavity in vitreoretinal pathophysiology? *Retina* **2011**, *31*, 222–228. [CrossRef] [PubMed]
41. Vagaja, N.N.; Chinnery, H.R.; Binz, N.; Kezic, J.M.; Rakoczy, E.P.; McMenamin, P.G. Changes in murine hyalocytes are valuable early indicators of ocular disease. *Investig. Ophthalmol. Vis. Sci.* **2012**, *53*, 1445–1451. [CrossRef] [PubMed]
42. Mahendradas, P.; Madhu, S.; Kawali, A.; Roy, A.S.; Vala, R.; Vinekar, A.; Shetty, R. Enhanced Vitreous Imaging in Uveitis. *Ocul. Immunol. Inflamm.* **2019**, *27*, 148–154. [CrossRef] [PubMed]
43. Mehta, M.; Rasheed, R.A.; Duker, J.; Reichel, E.; Feinberg, E.; Husain, D.; Foster, C.S.; Laver, N.V. Vitreous evaluation: A diagnostic challenge. *Ophthalmology* **2015**, *122*, 531–537. [CrossRef] [PubMed]
44. Keane, P.A.; Karampelas, M.; Sim, D.A.; Sadda, S.R.; Tufail, A.; Sen, H.N.; Nussenblatt, R.B.; Dick, A.D.; Lee, R.W.; Murray, P.I.; et al. Objective measurement of vitreous inflammation using optical coherence tomography. *Ophthalmology* **2014**, *121*, 1706–1714. [CrossRef]
45. Uji, A.; Yoshimura, N. Microarchitecture of the Vitreous Body: A High-Resolution Optical Coherence Tomography Study. *Am. J. Ophthalmol.* **2016**, *168*, 24–30. [CrossRef] [PubMed]
46. Sreekantam, S.; Macdonald, T.; Keane, P.A.; Sim, D.A.; Murray, P.I.; Denniston, A.K. Quantitative analysis of vitreous inflammation using optical coherence tomography in patients receiving sub-Tenon's triamcinolone acetonide for uveitic cystoid macular oedema. *Br. J. Ophthalmol.* **2017**, *101*, 175–179. [CrossRef] [PubMed]
47. Chu, C.J.; Herrmann, P.; Carvalho, L.S.; Liyanage, S.E.; Bainbridge, J.W.B.; Ali, R.R.; Dick, A.D.; Luhmann, U.F.O. Assessment and In Vivo Scoring of Murine Experimental Autoimmune Uveoretinitis Using Optical Coherence Tomography. *PLoS ONE* **2013**, *8*, e63002. [CrossRef]
48. Korot, E.; Comer, G.; Steffens, T.; Antonetti, D.A. Algorithm for the Measure of Vitreous Hyperreflective Foci in Optical Coherence Tomographic Scans of Patients with Diabetic Macular Edema. *JAMA Ophthalmol.* **2016**, *134*, 15–20. [CrossRef]

49. Rodrigo, M.J.; Del Palomar, A.P.; Montolío, A.; Mendez-Martinez, S.; Subias, M.; Cardiel, M.J.; Martinez-Rincon, T.; Cegoñino, J.; Fraile, J.M.; Vispe, E.; et al. Monitoring new long-lasting intravitreal formulation for glaucoma with vitreous images using optical coherence tomography. *Pharmaceutics* **2021**, *13*, 217. [CrossRef] [PubMed]
50. Rodrigo, M.J.; Garcia-Herranz, D.; Subias, M.; Martinez-Rincón, T.; Mendez-Martínez, S.; Bravo-Osuna, I.; Carretero, A.; Ruberte, J.; Garcia-Feijoo, J.; Pablo, L.E.; et al. Chronic Glaucoma Using Biodegradable Microspheres to Induce Intraocular Pressure Elevation. Six-Month Follow-Up. *Biomedicines* **2021**, *9*, 682. [CrossRef]
51. Garcia-Herranz, D.; Rodrigo, M.J.; Subias, M.; Martinez-Rincon, T.; Mendez-Martinez, S.; Bravo-Osuna, I.; Bonet, A.; Ruberte, J.; Garcia-Feijoo, J.; Pablo, L.; et al. Novel Use of PLGA Microspheres to Create an Animal Model of Glaucoma with Progressive Neuroretinal Degeneration. *Pharmaceutics* **2021**, *13*, 237. [CrossRef]
52. Liu, X.; Wang, C.-H.; Dai, C.; Camesa, A.; Zhang, H.F.; Jiao, S. Effect of Contact Lens on Optical Coherence Tomography Imaging of Rodent Retina. *Curr. Eye Res.* **2013**, *38*, 1235. [CrossRef]
53. Ogawa, K. Scanning electron microscopic study of hyalocytes in the guinea pig eye. *Arch. Histol. Cytol.* **2002**, *65*, 263–268. [CrossRef] [PubMed]
54. Otsu, N. A Threshold Selection Method from Gray-Level Histograms. *IEEE Trans. Syst. Man. Cybern.* **1979**, *9*, 62–66. [CrossRef]
55. Liba, O.; Lew, M.D.; Sorelle, E.D.; Dutta, R.; Sen, D.; Moshfeghi, D.M.; Chu, S.; De La Zerda, A. Speckle-modulating optical coherence tomography in living mice and humans. *Nat. Commun.* **2017**, *8*, 15845. [CrossRef]
56. London, A.; Itskovich, E.; Benhar, I.; Kalchenko, V.; Mack, M.; Jung, S.; Schwartz, M. Neuroprotection and progenitor cell renewal in the injured adult murine retina requires healing monocyte-derived macrophages. *J. Exp. Med.* **2011**, *208*, 23–39. [CrossRef]
57. Jacobs, A.H.; Tavitian, B. Noninvasive Molecular Imaging of Neuroinflammation. *J. Cereb. Blood Flow Metab.* **2012**, *32*, 1393–1415. [CrossRef]
58. Ajami, B.; Bennett, J.L.; Krieger, C.; Tetzlaff, W.; Rossi, F.M.V. Local self-renewal can sustain CNS microglia maintenance and function throughout adult life. *Nat. Neurosci.* **2007**, *10*, 1538–1543. [CrossRef] [PubMed]
59. Ajami, B.; Bennett, J.L.; Krieger, C.; McNagny, K.M.; Rossi, F.M.V. Infiltrating monocytes trigger EAE progression, but do not contribute to the resident microglia pool. *Nat. Neurosci.* **2011**, *14*, 1142–1150. [CrossRef]
60. Damisah, E.C.; Hill, R.A.; Rai, A.; Chen, F.; Rothlin, C.V.; Ghosh, S.; Grutzendler, J. Astrocytes and microglia play orchestrated roles and respect phagocytic territories during neuronal corpse removal in vivo. *Sci. Adv.* **2020**, *6*, eaba3239. [CrossRef]
61. Tay, T.L.; Béchade, C.; D'Andrea, I.; St-Pierre, M.K.; Henry, M.S.; Roumier, A.; Tremblay, M.E. Microglia gone rogue: Impacts on psychiatric disorders across the lifespan. *Front. Mol. Neurosci.* **2018**, *10*, 421. [CrossRef]
62. Rodrigo, M.J.; Martinez-Rincon, T.; Subias, M.; Mendez-Martinez, S.; Luna, C.; Pablo, L.E.; Polo, V.; Garcia-Martin, E. Effect of age and sex on neurodevelopment and neurodegeneration in the healthy eye: Longitudinal functional and structural study in the Long–Evans rat. *Exp. Eye Res.* **2020**, *200*, 108208. [CrossRef]
63. Medawar, P.B. Immunity to homologous grafted skin; the fate of skin homografts. *Br. J. Exp. Pathol.* **1948**, *29*, 58–69.
64. Kehlet, S.N.; Willumsen, N.; Armbrecht, G.; Dietzel, R.; Brix, S.; Henriksen, K.; Karsdal, M.A. Age-related collagen turnover of the interstitial matrix and basement membrane: Implications of age- and sex-dependent remodeling of the extracellular matrix. *PLoS ONE* **2018**, *13*, e0194458. [CrossRef]
65. Perez, V.L.; Caspi, R.R. Immune mechanisms in inflammatory and degenerative eye disease. *Trends Immunol.* **2015**, *36*, 354–363. [CrossRef] [PubMed]
66. Zhu, M.; Provis, J.M.; Penfold, P.L. The human hyaloid system: Cellular phenotypes and inter-relationships. *Exp. Eye Res.* **1999**, *68*, 553–563. [CrossRef] [PubMed]
67. Qiao, H.; Hisatomi, T.; Sonoda, K.H.; Kura, S.; Sassa, Y.; Kinoshita, S.; Nakamura, T.; Sakamoto, T.; Ishibashi, T. The characterisation of hyalocytes: The origin, phenotype, and turnover. *Br. J. Ophthalmol.* **2005**, *89*, 513–517. [CrossRef] [PubMed]
68. Imai, Y.; Ibata, I.; Ito, D.; Ohsawa, K.; Kohsaka, S. A novel gene iba1 in the major histocompatibility complex class III region encoding an EF hand protein expressed in a monocytic lineage. *Biochem. Biophys. Res. Commun.* **1996**, *224*, 855–862. [CrossRef]
69. Ahmed, Z.; Shaw, G.; Sharma, V.P.; Yang, C.; McGowan, E.; Dickson, D.W. Actin-binding proteins coronin-1a and IBA-1 are effective microglial markers for immunohistochemistry. *J. Histochem. Cytochem.* **2007**, *55*, 687–700. [CrossRef]
70. Santos, A.M.; Martin-Oliva, D.; Ferrer-Martãn, R.M.; Tassi, M.; Calvente, R.; Sierra, A.; Carrasco, M.-C.; Marin-Teva, J.L.; Navascues, J.; Cuadros, M.A. Microglial response to light-induced photoreceptor degeneration in the mouse retina. *J. Comp. Neurol.* **2010**, *518*, 477–492. [CrossRef] [PubMed]
71. Noda, Y.; Hata, Y.; Hisatomi, T.; Nakamura, Y.; Hirayama, K.; Miura, M.; Nakao, S.; Fujisawa, K.; Sakamoto, T.; Ishibashi, T. Functional properties of hyalocytes under PDGF-rich conditions. *Investig. Ophthalmol. Vis. Sci.* **2004**, *45*, 2107–2114. [CrossRef]
72. Castanos, M.V.; Zhou, D.B.; Linderman, R.E.; Allison, R.; Milman, T.; Carroll, J.; Migacz, J.; Rosen, R.B.; Chui, T.Y.P. Imaging of Macrophage-Like Cells in Living Human Retina Using Clinical OCT. *Investig. Ophthalmol. Vis. Sci.* **2020**, *61*, 48. [CrossRef]
73. Staurenghi, G.; Sadda, S.; Chakravarthy, U.; Spaide, R.F. Proposed lexicon for anatomic landmarks in normal posterior segment spectral-domain optical coherence tomography: The IN•OCT consensus. *Ophthalmology* **2014**, *121*, 1572–1578. [CrossRef] [PubMed]
74. Choudhry, N.; Duker, J.S.; Freund, K.B.; Kiss, S.; Querques, G.; Rosen, R.; Sarraf, D.; Souied, E.H.; Stanga, P.E.; Staurenghi, G.; et al. Classification and Guidelines for Widefield Imaging: Recommendations from the International Widefield Imaging Study Group. *Ophthalmol. Retin.* **2019**, *3*, 843–849. [CrossRef]

75. Ramírez, A.I.; Fernández-Albarral, J.A.; de Hoz, R.; López-Cuenca, I.; Salobrar-García, E.; Rojas, P.; Valiente-Soriano, F.J.; Avilés-Trigueros, M.; Villegas-Pérez, M.P.; Vidal-Sanz, M.; et al. Microglial changes in the early aging stage in a healthy retina and an experimental glaucoma model. In *Progress in Brain Research*; Elsevier: Amsterdam, The Netherlands, 2020; Volume 256, pp. 125–149. ISBN 9780128211069.
76. Saito, M.; Barbazetto, I.A.; Spaide, R.F. Intravitreal Cellular Infiltrate Imaged as Punctate Spots by Spectral-Domain Optical Coherence Tomography in Eyes with Posterior Segment Inflammatory Disease. *Retina* **2013**, *33*, 559–565. [CrossRef] [PubMed]
77. Keane, P.A.; Balaskas, K.; Sim, D.A.; Aman, K.; Denniston, A.K.; Aslam, T.; Aslam, T. Automated analysis of vitreous inflammation using spectral-domain optical coherence tomography. *Transl. Vis. Sci. Technol.* **2015**, *4*, 4. [CrossRef] [PubMed]
78. Zarranz-Ventura, J.; Keane, P.A.; Sim, D.A.; Llorens, V.; Tufail, A.; Sadda, S.R.; Dick, A.D.; Lee, R.W.; Pavesio, C.; Denniston, A.K.; et al. Evaluation of Objective Vitritis Grading Method Using Optical Coherence Tomography: Influence of Phakic Status and Previous Vitrectomy. *Am. J. Ophthalmol.* **2016**, *161*, 172–180. [CrossRef]
79. Russo, R.; Varano, G.P.; Adornetto, A.; Nucci, C.; Corasaniti, M.T.; Bagetta, G.; Morrone, L.A. Retinal ganglion cell death in glaucoma: Exploring the role of neuroinflammation. *Eur. J. Pharmacol.* **2016**, *787*, 134–142. [CrossRef]
80. Tezel, G. The immune response in glaucoma: A perspective on the roles of oxidative stress. *Exp. Eye Res.* **2011**, *93*, 178–186. [CrossRef]
81. Taylor, A.W.; Ng, T.F. Negative regulators that mediate ocular immune privilege. *J. Leukoc. Biol.* **2018**, *103*, 1179–1187. [CrossRef]
82. Gordon, S.; Plüddemann, A.; Martinez Estrada, F. Macrophage heterogeneity in tissues: Phenotypic diversity and functions. *Immunol. Rev.* **2014**, *262*, 36–55. [CrossRef] [PubMed]
83. Forrester, J.V.; Xu, H.; Kuffová, L.; Dick, A.D.; McMenamin, P.G. Dendritic cell physiology and function in the eye. *Immunol. Rev.* **2010**, *234*, 282–304. [CrossRef]
84. Skeie, J.M.; Mahajan, V.B. Dissection of Human Vitreous Body Elements for Proteomic Analysis. *J. Vis. Exp.* **2011**, *47*, 2455. [CrossRef] [PubMed]
85. Jiang, L.Q.; Streilein, J.W. Immune Privilege Extended to Allogeneic Tumor Cells in the Vitreous Cavity. *Investig. Ophthalmol. Vis. Sci.* **1991**, *32*, 224–228.
86. Bain, C.C.; Gibson, D.A.; Steers, N.J.; Boufea, K.; Louwe, P.A.; Doherty, C.; González-Huici, V.; Gentek, R.; Magalhaes-Pinto, M.; Shaw, T.; et al. Rate of replenishment and microenvironment contribute to the sexually dimorphic phenotype and function of peritoneal macrophages. *Sci. Immunol.* **2020**, *5*, eabc4466. [CrossRef]
87. Hanamsagar, R.; Bilbo, S.D. Sex differences in neurodevelopmental and neurodegenerative disorders: Focus on microglial function and neuroinflammation during development. *J. Steroid Biochem. Mol. Biol.* **2016**, *160*, 127–133. [CrossRef] [PubMed]
88. Klein, S.L.; Flanagan, K.L. Sex differences in immune responses. *Nat. Rev. Immunol.* **2016**, *16*, 626–638. [CrossRef] [PubMed]
89. Ngo, S.T.; Steyn, F.J.; McCombe, P.A. Gender differences in autoimmune disease. *Front. Neuroendocrinol.* **2014**, *35*, 347–369. [CrossRef]
90. Rodrigo, M.J.; Martinez-Rincon, T.; Subias, M.; Mendez-Martinez, S.; Pablo, L.E.; Polo, V.; Aragon-Navas, A.; Garcia-Herranz, D.; Feijoo, J.G.; Osuna, I.B.; et al. Influence of Sex on Neuroretinal Degeneration: Six-Month Follow-Up in Rats with Chronic Glaucoma. *Investig. Ophthalmol. Vis. Sci.* **2021**, *62*, 9. [CrossRef] [PubMed]
91. Zanon-Moreno, V.; Raga-Cervera, J.; García-Medina, J.J.; Benitez-del-Castillo, J.; Vinuesa-Silva, I.; Torregrosa, S.; Pinazo-Durán, M.D. Nuevos horizontes para el tratamiento del glaucoma. I: Neuroinflamación e inflamasomas. *Arch. Soc. Esp. Oftalmol.* **2018**, *93*, e7–e9. [CrossRef] [PubMed]
92. Liu, S.; Li, Z.; Weinreb, R.N.; Xu, G.; Lindsey, J.D.; Ye, C.; Yung, W.; Pang, C.-P.; Lam, D.S.C.; Leung, C.K. Tracking Retinal Microgliosis in Models of Retinal Ganglion Cell Damage. *Investig. Opthalmol. Vis. Sci.* **2012**, *53*, 6254. [CrossRef] [PubMed]
93. Zhou, R.; Caspi, R.R. Ocular immune privilege. *F1000 Biol. Rep.* **2010**, *2*, 3. [CrossRef] [PubMed]
94. Ramírez, A.I.; de Hoz, R.; Fernández-Albarral, J.A.; Salobrar-Garcia, E.; Rojas, B.; Valiente-Soriano, F.J.; Avilés-Trigueros, M.; Villegas-Pérez, M.P.; Vidal-Sanz, M.; Triviño, A.; et al. Time course of bilateral microglial activation in a mouse model of laser-induced glaucoma. *Sci. Rep.* **2020**, *10*, 4890. [CrossRef] [PubMed]
95. Fan, W.; Li, X.; Wang, W.; Mo, J.S.; Kaplan, H.; Cooper, N.G.F. Early Involvement of Immune/Inflammatory Response Genes in Retinal Degeneration in DBA/2J Mice. *Ophthalmol. Eye Dis.* **2010**, *1*, 23. [CrossRef] [PubMed]
96. Hashimoto, D.; Chow, A.; Noizat, C.; Teo, P.; Beasley, M.B.; Leboeuf, M.; Becker, C.D.; See, P.; Price, J.; Lucas, D.; et al. Tissue-Resident Macrophages Self-Maintain Locally throughout Adult Life with Minimal Contribution from Circulating Monocytes. *Immunity* **2013**, *38*, 792–804. [CrossRef]
97. Ling, E.A. Transformation of monocytes into amoeboid microglia and into microglia in the corpus callosum of postnatal rats, as shown by labelling monocytes by carbon particles. *J. Anat.* **1979**, *128*, 847–858.
98. O'Koren, E.G.; Mathew, R.; Saban, D.R. Fate mapping reveals that microglia and recruited monocyte-derived macrophages are definitively distinguishable by phenotype in the retina. *Sci. Rep.* **2016**, *6*, 20636. [CrossRef]
99. Liu, B.; Hong, J.-S. Role of Microglia in Inflammation-Mediated Neurodegenerative Diseases: Mechanisms and Strategies for Therapeutic Intervention. *J. Pharmacol. Exp. Ther.* **2003**, *304*, 1–7. [CrossRef]
100. Venneti, S.; Lopresti, B.J.; Wiley, C.A. Molecular imaging of microglia/macrophages in the brain. *Glia* **2013**, *61*, 10–23. [CrossRef]
101. Coric, D.; Ometto, G.; Montesano, G.; Keane, P.A.; Balk, L.J.; Uitdehaag, B.M.J.; Petzold, A.; Crabb, D.P.; Denniston, A.K. Objective quantification of vitreous haze on optical coherence tomography scans: No evidence for relationship between uveitis and inflammation in multiple sclerosis. *Eur. J. Neurol.* **2020**, *27*, 144. [CrossRef] [PubMed]

2.3.2 Intravitreal formulation for glaucoma

Manuscript 6: Monitoring New Long-Lasting Intravitreal Formulation for Glaucoma with Vitreous Images Using Optical Coherence Tomography

María Jesús Rodrigo, Amaya Pérez del Palomar, Alberto Montolío, Silvia Méndez-Martínez, Manuel Subías, Maria Jose Cardiel, Teresa Martínez-Rincón, José Cegoñino, José Maria Fraile, Eugenio Vispe, José Antonio Mayoral, Vicente Polo, Elena Garcia-Martin

Abstract

Intravitreal injection is the gold standard therapeutic option for posterior segment pathologies, and long-lasting release is necessary to avoid reinjections. There is no effective intravitreal treatment for glaucoma or other optic neuropathies in daily practice, nor is there a non-invasive method to monitor drug levels in the vitreous. Here we show that a glaucoma treatment combining a hypotensive and neuroprotective intravitreal formulation (IF) of brimonidine–Laponite (BRI/LAP) can be monitored non-invasively using vitreoretinal interface imaging captured with optical coherence tomography (OCT) over 24 weeks of follow-up. Qualitative and quantitative characterisation was achieved by analysing the changes in vitreous (VIT) signal intensity, expressed as a ratio of retinal pigment epithelium (RPE) intensity. Vitreous hyperreflective aggregates mixed in the vitreous and tended to settle on the retinal surface. Relative intensity and aggregate size progressively decreased over 24 weeks in treated rat eyes as the BRI/LAP IF degraded. VIT/RPE relative intensity and total aggregate area correlated with brimonidine levels measured in the eye. The OCT-derived VIT/RPE relative intensity may be a useful and objective marker for non-invasive monitoring of BRI/LAP IF.

pharmaceutics

MDPI

Article

Monitoring New Long-Lasting Intravitreal Formulation for Glaucoma with Vitreous Images Using Optical Coherence Tomography

Maria Jesus Rodrigo [1,2,3,*], Amaya Pérez del Palomar [4,5], Alberto Montolío [4,5], Silvia Mendez-Martinez [1,2], Manuel Subias [1,2], Maria Jose Cardiel [6], Teresa Martinez-Rincon [1,2], José Cegoñino [4,5], José Maria Fraile [7], Eugenio Vispe [8], José Antonio Mayoral [7], Vicente Polo [1,2] and Elena Garcia-Martin [1,2,3]

[1] Department of Ophthalmology, Miguel Servet University Hospital, 50009 Zaragoza, Spain; silviamendezmartinez@hotmail.com (S.M.-M.); manusubias@gmail.com (M.S.); teresamrincon@gmail.com (T.M.-R.); vpolo@unizar.es (V.P.); egmvivax@yahoo.com (E.G.-M.)
[2] Miguel Servet Ophthalmology Research Group (GIMSO), Aragon Health Research Institute (IIS Aragon), University of Zaragoza, 50009 Zaragoza, Spain
[3] RETICS: Thematic Networks for Co-Operative Research in Health for Ocular Diseases, 28040 Madrid, Spain
[4] Biomaterials Group, Aragon Institute of Engineering Research (I3A), University of Zaragoza, 50018 Zaragoza, Spain; amaya@unizar.es (A.P.d.P.); amontolio@unizar.es (A.M.); jcegoni@unizar.es (J.C.)
[5] Department of Mechanical Engineering, University of Zaragoza, 50018 Zaragoza, Spain
[6] Department of Pathology, Lozano Blesa University Hospital, 50009 Zaragoza, Spain; mjcardielgarcia@gmail.com
[7] Institute for Chemical Synthesis and Homogeneous Catalysis (ISQCH), Faculty of Sciences, University of Zaragoza-CSIC, C/Pedro Cerbuna 12, 50009 Zaragoza, Spain; jmfraile@unizar.es (J.M.F.); mayoral@unizar.es (J.A.M.)
[8] Chromatography and Spectroscopy Laboratory, Institute for Chemical Synthesis and Homogeneous Catalysis (ISQCH), Faculty of Sciences, University of Zaragoza-CSIC, Pedro Cerbuna 12, 50009 Zaragoza, Spain; evp@unizar.es
* Correspondence: mariajesusrodrigo@hotmail.es; Tel.: +34-619788942 or +34-976765558; Fax: +34-976566234

check for updates

Citation: Rodrigo, M.J.; del Palomar, A.P.; Montolío, A.; Mendez-Martinez, S.; Subias, M.; Cardiel, M.J.; Martinez-Rincon, T.; Cegoñino, J.; Fraile, J.M.; Vispe, E.; et al. Monitoring New Long-Lasting Intravitreal Formulation for Glaucoma with Vitreous Images Using Optical Coherence Tomography. *Pharmaceutics* **2021**, *13*, 217. https://doi.org/10.3390/pharmaceutics13020217

Academic Editor: Anuj Chauhan
Received: 30 November 2020
Accepted: 2 February 2021
Published: 5 February 2021

Abstract: Intravitreal injection is the gold standard therapeutic option for posterior segment pathologies, and long-lasting release is necessary to avoid reinjections. There is no effective intravitreal treatment for glaucoma or other optic neuropathies in daily practice, nor is there a non-invasive method to monitor drug levels in the vitreous. Here we show that a glaucoma treatment combining a hypotensive and neuroprotective intravitreal formulation (IF) of brimonidine–Laponite (BRI/LAP) can be monitored non-invasively using vitreoretinal interface imaging captured with optical coherence tomography (OCT) over 24 weeks of follow-up. Qualitative and quantitative characterisation was achieved by analysing the changes in vitreous (VIT) signal intensity, expressed as a ratio of retinal pigment epithelium (RPE) intensity. Vitreous hyperreflective aggregates mixed in the vitreous and tended to settle on the retinal surface. Relative intensity and aggregate size progressively decreased over 24 weeks in treated rat eyes as the BRI/LAP IF degraded. VIT/RPE relative intensity and total aggregate area correlated with brimonidine levels measured in the eye. The OCT-derived VIT/RPE relative intensity may be a useful and objective marker for non-invasive monitoring of BRI/LAP IF.

Keywords: brimonidine; Laponite; drug delivery; glaucoma; nanomedicine; monitoring; optical coherence tomography; vitreous; intravitreal

1. Introduction

Brimonidine is an ocular hypotension drug widely used in ophthalmological clinical care. For adequate therapeutic control, topical administration is recommended twice a day because of its short half-life (approximately 12 h) [1]. Recently, brimonidine also exhibited a neuroprotective effect in retinal ganglion cells (RGCs), photoreceptors and other retinal cells [2] in animal and human studies [3] and with both topical and intravitreal administration [4]. The short half-life of brimonidine means that periodic intravitreal administration is needed to achieve therapeutic efficacy. However, repeated injection could lead to complications [5]. Therefore, development of sustained drug delivery systems is necessary. Laponite® $Na^{+0.7}[(Si_8Mg_{5.5}Li_{0.3})O_{20}(OH)_4]^{-0.7}$ is a biocompatible and biodegradable clay used in biomedicine [6]. Its safety in intravitreal injection has been demonstrated in animal studies [7–9]. Laponite® forms a transparent gel when dispersed in an aqueous medium. It is able to interact with other molecules, acting as a carrier and releasing the drug in a controlled manner [10]. In this regard, our research group recently demonstrated that an intravitreal formulation (IF) containing brimonidine–Laponite (BRI/LAP) produced a hypotensive and neuroprotective effect in a chronic glaucoma animal model over 6 months of follow-up [9].

The vitreous humour is a 3-D structure mainly composed of water, collagen fibres and hyaluronan that occupies 80% of eye volume. It allows light transmission and intervenes in eye metabolism [11]. A vitreous sample biopsy is a useful means of diagnosing inflammatory, infectious or oncological ocular diseases as well as of carrying out toxicological post-mortem analysis [12,13]. Furthermore, the vitreous humour is becoming increasingly important in clinical practice as it acts as a therapeutic target for posterior pole pathologies involving macular oedema, such as diabetic retinopathy, vascular occlusions or aged-related macular degeneration. However, as an intravitreal treatment for glaucoma is not yet available in clinical practice, many researchers are working to resolve this limitation within a medium-term horizon. The potential interest in using intravitreal administration is to circumvent ocular barriers while avoiding systemic adverse events and, by acting as a reservoir, maintaining therapeutic drug levels near the site of action [14].

Optical coherence tomography (OCT) is an easy-to-handle, cost-efficient, and objective technology that provides high-resolution cross-sectional images. It has long been widely used in clinical practice and research to study neuroretinal structure. Improved OCT devices with swept-source or enhanced vitreous imaging have made it possible to study the vitreous in normal and inflamed states and to study changes to it after treatment [15–17]. However, it has never been used to monitor drug levels in IFs. Currently, loss in IF therapeutic efficacy is evaluated on the basis of changes in neuroretinal structure or decreases in subjective visual acuity measurements, which indicate an increase in disease activity. It would be beneficial, however, to find an objective vitreous monitoring marker with which to quantify the degradation of the injected molecule and which could even anticipate the loss of therapeutic effect before structural retinal changes are detected by OCT, especially as compared with other more expensive or invasive techniques used in research, such as positron emission tomography or magnetic resonance imaging [18,19].

In previous OCT-based studies by this group, BRI/LAP IF was visualised in the vitreous cavity as hyperreflective aggregates [9]. Expanding on this finding, this study uses OCT to analyse changes in the hyperreflectivity signal from the BRI/LAP IF in the vitreous humour in rat eyes over a 24-week period. This paper describes a monitoring marker for the IF, correlates the OCT vitreous signal to drug levels and discusses the therapeutic effect of BRI/LAP IF [9]. It proposes serial OCT as a more affordable and simpler method for monitoring BRI/LAP IF in vivo in animal research.

2. Materials and Methods

2.1. Data Collection

OCT images of the vitreoretinal interface and drug level data were obtained from the experiments carried out in a previous interventional study conducted by the authors [9] (CC BY 4.0 license). In that study, chronic glaucoma was bilaterally induced by biweekly injections of hypertonic solution into the episcleral veins, according to the well-established Morrison model [20], which led to episcleral vein sclerosis and therefore ocular hypertension (OHT). Thereafter, a single 3-µL BRI/LAP IF injection (10 mg BRI/LAP/mL) into the vitreous cavity of right eye (RE) of Long–Evans rats was performed at baseline. Left eyes (LEs) served as non-treated hypertensive controls. Intraocular pressure was measured with a rebound tonometer (Tonolab® iCare, Helsinki, Finland) for rodent research. The material and methods used for the study were deeply detailed in [9]. In this study, OCT examinations of the 43 treated rats at baseline and at weeks 1, 2, 4, 6, 8, 12, 24 after intravitreal injection were analysed to quantify BRI/LAP IF evolution over 6 months. Another 23 non-treated healthy rats were examined for comparison as non-hypertensive controls. The experiment was approved beforehand by the Ethics Committee for Animal Research of Zaragoza University (PI34/17, 27th June 2017) and was carried out in strict accordance with the Association for Research in Vision and Ophthalmology's Statement for the Use of Animals.

2.2. *Optical Coherence Tomography*

Images were acquired using a high-resolution OCT device (HR-OCT Spectralis, Heidelberg® Engineering, Heidelberg, Germany) with a plane power polymethylmethacrylate (PMMA) contact lens of 270 µm thickness and 5.2 mm diameter (Cantor+Nissel®, Northamptonshire, UK) adapted to the rats' cornea to obtain higher quality images. The rodent version of this system acquires cross-sectional images by means of 61 b-scans measuring around 3 mm in length and centred on the optic nerve. It has a resolution of 3 microns per pixel generated. A total of 1536 × 496 pixels per image were analysed. The retinal posterior pole protocol with automatic segmentation, eye-tracking software and follow-up application were used to ensure that the same points were re-scanned throughout the study. The "enhance depth imaging" mode was disabled in all cases.

2.3. *Brimonidine–Laponite (BRI/LAP) Formulation and Analysis*

BRI/LAP was prepared [9] by addition of Laponite (100 mg) to a solution of Brimonidine (10 mg) in ethanol (10 mL) with stirring and then solvent evaporation under a vacuum, to obtain the BRI/LAP formulation in powder form, which was gamma-ray sterilised. BRI/LAP was injected in the form of a yellow colloidal dispersion in balanced saline solution (BSS) (10 mg/mL).

The brimonidine content in the rat eyes was analysed [8,9] using an ultra-high-pressure liquid chromatography mass spectrometer (UHPLC-MS, Waters, Milford, MA, USA). The eyes were first cut into pieces, sonicated with a solution of formic acid in acetonitrile, then with ammonium formate in phosphoric acid and internal standard (2-bromoquinoxaline), centrifuged and the supernatant was cleaned up by solid phase extraction.

2.4. *In Vitro Release of BRI from BRI/LAP Formulation*

Release was studied in a model of vitreous humour made up of 0.5% sodium hyaluronate in saline solution (pH 7.1–7.4). The release tests were performed by dispersing BRI/LAP (5 mg, weight ratio 1/10, brimonidine amount 454.5 µg) in the extraction medium (0.5 g of the vitreous model) under stirring at 120 rpm at 37 °C. After 24 h the dispersion was centrifuged at 14,000 rpm for 20 min. The liquid phase was separated and the solid was re-dispersed in fresh extraction medium for a new cycle. The liquid phase was diluted with acetonitrile (0.5 mL) containing the internal standard, centrifuged again and analysed by HPLC as described above.

2.5. *Analysis of the Intravitreal Formulation Using OCT*

The BRI/LAP IF aggregates present in the OCT scans of the vitreoretinal interface were studied. This technique focuses on the analysis of opacities in the vitreoretinal interface by OCT, which does not require a correction factor for its histological correlation [21] and ensures a characterisation of the actual aggregate. These aggregates were defined as being dots dispersed in the vitreous humour or vitreoretinal interface whose larger size, irregularity or greater signal hyperreflectivity differentiated them from background speckle noise.

OCT image contrast was not adjusted at any time. OCT raw images were exported as Audio Video Interleave (AVI) videos. These videos were analysed using a custom program implemented in Matlab (version R218a, Mathworks Inc., Natick, MA, USA). This code allows us to find the inner limiting membrane (ILM) and the inner and outer layers of the retinal pigment epithelium (RPE) by grayscale conversion. This makes it possible to delimit vitreous space and RPE space in each b-scan (Figure 1). The vitreous was defined as the space between the uppermost extent of the b-scan and the ILM, whereas the RPE was defined as the space between the inner and outer layer of the RPE [16,17]. The mean intensity value of these two spaces was calculated as the average of the intensity of all the pixels within each region, obtaining the VIT/RPE relative intensity in each b-scan. Thus, the VIT/RPE relative intensity of each eye is the average of the 61 b-scans. Furthermore, as the BRI/LAP aggregates tend to be deposited on the ILM–retinal nerve fibre layer (RNFL), the inner and outer limits of the ILM–RNFL were determined to obtain the evolution of ILM–RNFL thickness throughout the 24 weeks of follow-up.

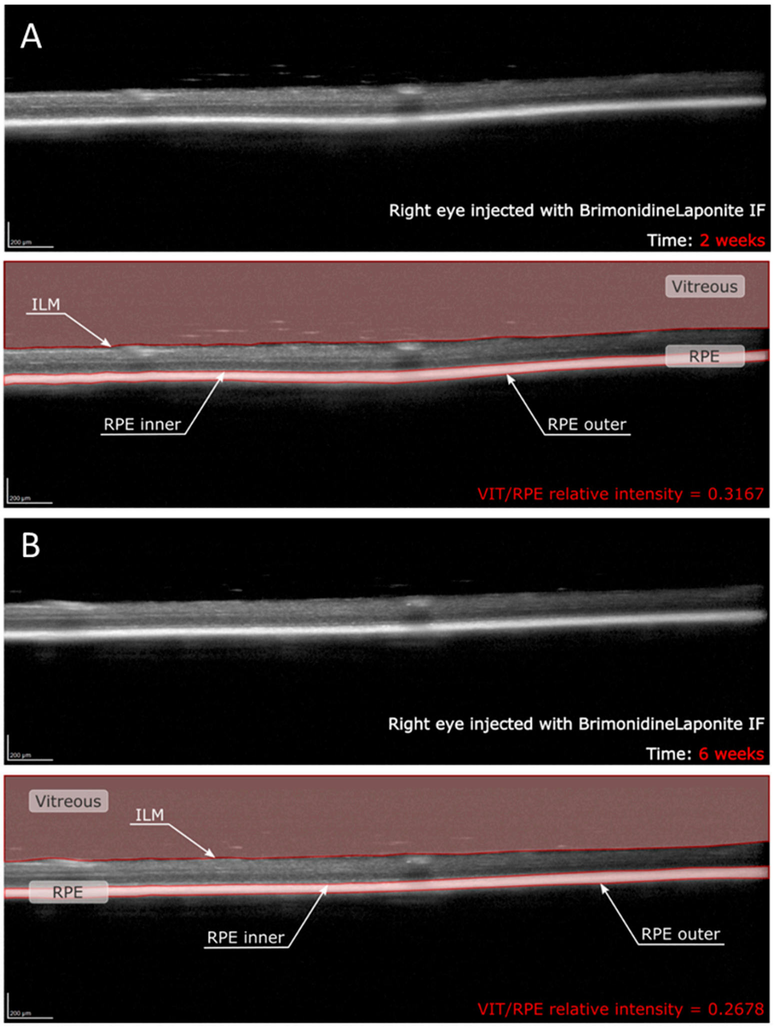

Figure 1. Quantitative assessment of VIT/RPE relative intensity in the same right eye of a rat at (**A**) two weeks and (**B**) six weeks post-injection with brimonidine–Laponite intravitreal formulation. Abbreviations: IF: intravitreal formulation; VIT: vitreous; RPE: retinal pigment epithelium; ILM: inner limiting membrane.

The size of the aggregates in each b-scan was also determined by calculating the number of pixels that each aggregate contains in the image. In the analysed b-scans, there are a total of 761,856 pixels and the image area is 2906 mm^2. Therefore, the ratio is 3815 μm^2/pixel. To calculate that correctly, the background speckle noise of the image was deleted using a denoising filter, which made it possible to distinguish between aggregates and background noise. This filter was implemented in our custom code following the definition of aggregates as larger dots whose intensity is greater than the background intensity. In order to ensure that we only quantify the aggregates produced by the BRI/LAP IF, a minimum limit was established, so that the possible noise [22] due to the physiological components of the eye were not taken into account. This minimum limit was set at 500 μm^2 per aggregate. Once we had calculated the size of each aggregate, we could compute the average area and total area of the BRI/LAP IF in each eye at different stages during the follow-up.

The imaging data were analysed for clinical and drug level information by a masked reader. OCT segmentation was performed by two different researchers, likewise masked, to verify reproducibility.

2.6. Statistical Analysis

All data were recorded in an Excel database, and statistical analysis was performed using SPSS software version 20.0 (SPSS Inc., Chicago, IL, USA). To assess sample distribution, the Kolmogorov–Smirnov test was used. However, given the non-parametric distribution of most of the data, the Mann–Whitney U test was employed to evaluate the differences between both cohorts, and a paired Wilcoxon test was used to compare the changes recorded in each eye over the study period. p values < 0.05 were considered to indicate statistical significance.

3. Results

A total of 186 OCT videos from 43 treated rats (43 hypertensive REs treated with BRI/LAP IF and 29 non-treated hypertensive LEs) and 23 non-treated healthy rats (23 REs/23 LEs) were analysed. The REs injected with the BRI/LAP IF showed hyperreflective dots/aggregates mixing uniformly in the vitreous gel and dispersed as floaters, with a tendency to move toward the vitreoretinal interface during the 24-week follow-up [9]. There was also OCT-guided evidence of the hyperreflective dots crossing the vitreoretinal interface and embedding deeply in the retinal tissue. Particular qualitative characteristics of the behaviour of the BRI/LAP IF observed in several animals are shown in Figure 2.

OCT also detected a progressive decrease over time in the number and size of BRI/LAP aggregates (Figure 3). Figure 4 shows the temporal change in aggregate size. Figure 4A shows that total aggregate area decreased with time over the 24 weeks of follow-up. This drop was very marked during the first 4–6 weeks, after which the change was more gradual. Moreover, total aggregate area increased two weeks after injection. Although a similar trend was observed (aggregate size increased at 2 weeks), this seems to be at the expense of an increase in mean aggregate size. A considerable decrease was then detected around 8 weeks, and from 12 weeks onwards mean aggregate size remained practically constant (Figure 4B).

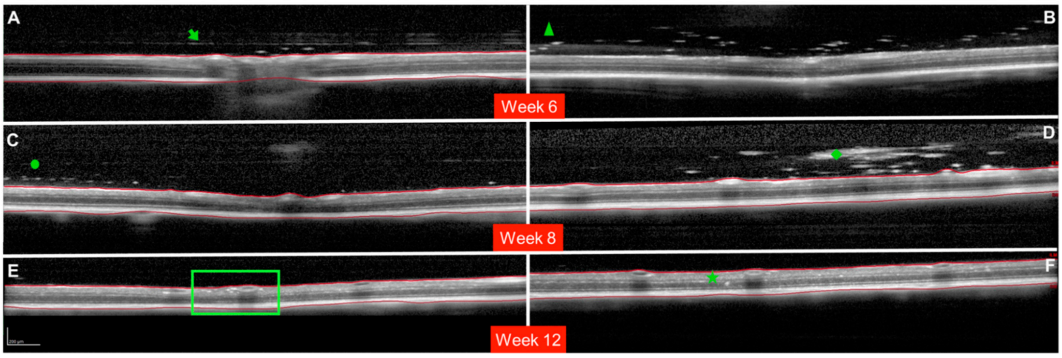

Figure 2. Milestones in the evolution of the brimonidine–Laponite intravitreal formulation (BRI/LAP IF) analysed using optical coherence tomography. (**A**): Cross-sectional image of the optic nerve showing hyper-reflective IF aggregates after crossing the posterior vitreous cortex (PVC). The green arrow points to the posterior vitreous cortex. Three hyper-reflective dots are found in the space between the PVC and the inner limiting membrane (ILM). (**B**): Hyper-reflective aggregates (green triangle) at the moment of crossing the posterior vitreous cortex. (**C**): Hyper-reflective aggregates (green circle) arranged one-by-one in a row. (**D**): Large BRI/LAP IF aggregate (green rhombus) in the vitreous humour. A light optical shadow can be observed (indicating potential perception of floaters) similar to the shadow that retinal vessels produce. (**E**,**F**): Hyper-reflective aggregates penetrating the retinal layers. Deposits in the inner nuclear layer or perivascular (green square). Deposits in the outer nuclear layer (green star). Red lines indicate the ILM and retinal pigment epithelium (RPE) boundaries. (**B**) Shows an example without boundaries (red lines) so as to permit measurement. (**A**,**B**) Show images obtained at 6 weeks of follow-up. (**C**,**D**) Show images obtained at 8 weeks of follow-up. (**E**,**F**) Show images obtained at 12 weeks of follow-up. Representative images are extracted from different animals.

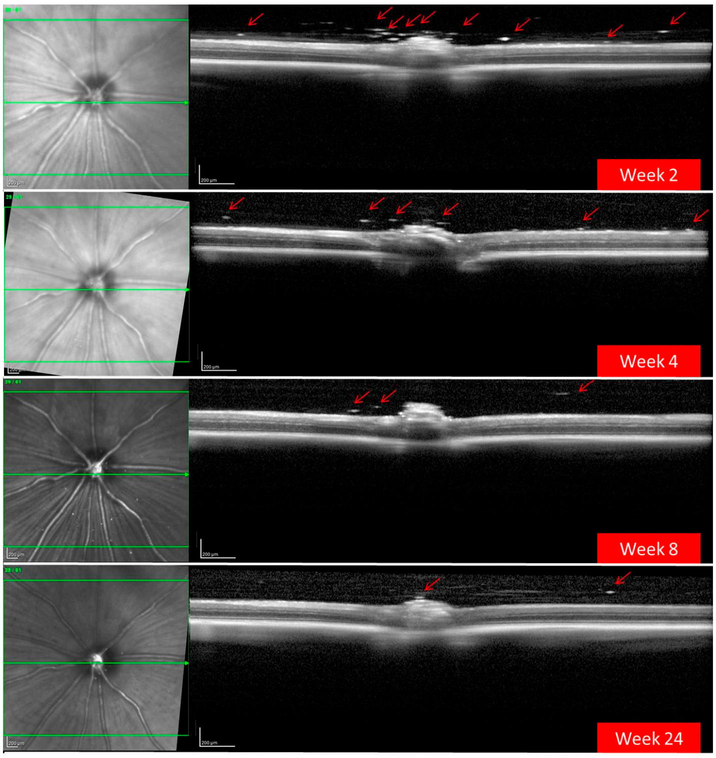

Figure 3. Progressive decrease in hyper-reflective aggregates (red arrows) of the brimonidine–Laponite intravitreal formulation (BRI/LAP IF) detected in the vitreous–retinal interface using optical coherence tomography over 24 weeks of follow-up.

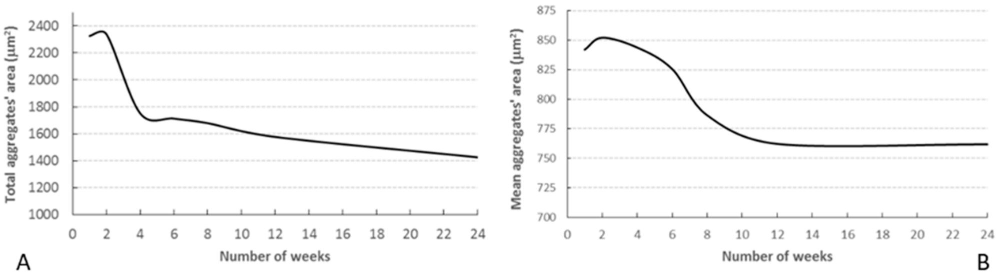

Figure 4. Temporal change in aggregate area. (**A**) Total area of the aggregates located in the vitreous; (**B**) mean area of the aggregates.

OCT analysis revealed the decreasing intensity of the hyperreflective IF aggregates in the vitreous over 24 weeks of follow-up (Figure 5A). The figure shows that the intensity peaked at the end of the second week and then decreased until it stabilised around week 12. It should be noted that the intensity index rose slightly from weeks 4 to 6 and that this coincided with a decrease in total aggregate area (Figure 4A) and a slight increase in mean aggregate area (Figure 4B). Comparison of the intensity indices for REs (treated with BRI/LAP IF) and LEs (non-treated) (Figure 5A) shows that the intensity is very much lower in the LEs (0.30 vs., 0.25; $p < 0.001$). As can be seen, VIT/RPE relative intensity in eyes with glaucoma treated with BRI/LAP IF is higher than in eyes with non-treated glaucoma due to the presence of BRI/LAP IF. Interestingly, the index similarly increased over the first two weeks. This effect could be produced by the induction of glaucoma. Furthermore, the intensity index for non-treated eyes (right and left control eyes; the grey lines in Figure 5A) was also computed. In this case, the intensity value remained constant (0.17). Here, the difference observed in the intensity index between eyes with glaucoma and healthy controls is produced by glaucoma induction. Finally, we observed that the aggregates were initially distributed throughout the vitreous but as time went by (6 to 8 weeks) they settled on top of the ILM–RNFL. It was not possible to distinguish between the aggregates and the ILM–RNFL because the intensity values are very similar. Therefore, this co-layer was segmented in order to measure the deposited aggregates. Figure 5B shows how RE ILM–RNFL thickness increased until it plateaued at week 12. This increase in thickness is directly related to the aggregates' distribution on top of the retina. In the same plot, LE (untreated) ILM–RNFL thickness remained unaltered or decreased slightly during the follow-up if no aggregates were present. Furthermore, we previously not only ruled out that the thickness increase in the treated eye was a consequence of neurodegeneration or cystoid oedema, but also observed functional neuroprotection and a higher RGC count [9].

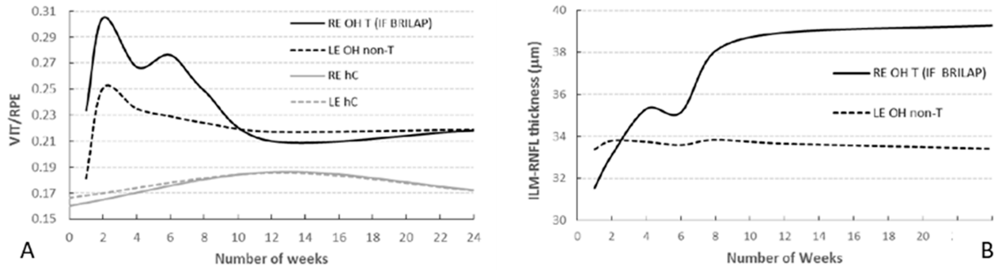

Figure 5. (**A**) Mean VIT/RPE relative intensity in rats with induced bilateral glaucoma (RE treated with brimonidine–Laponite) and healthy controls over 24 weeks of follow-up. (**B**) Segmentation of the ILM–RNFL in rats with induced bilateral glaucoma (RE treated with brimonidine–Laponite) over 24 weeks of follow-up. Abbreviations: RE: right eye; LE: left eye; OH: ocular hypertension; T: treated; BRI/LAP IF: Brimonidine–Laponite intravitreal formulation; non-T: non-treated; hC: healthy control; ILM: inner limiting membrane; RNFL: retinal nerve fibre layer.

Finally, a 3-D reconstruction of the 61 b-scans from a specific rat was performed in order to assess the qualitative decrease in aggregates with time. Figure 6 shows the same eye at 2 weeks of follow-up and then 6 weeks later (8 weeks of follow-up). It clearly shows that the aggregates are widely dispersed 2 weeks post-injection, and that 6 weeks later the aggregates are fewer and smaller and have practically disappeared from the vitreous humour.

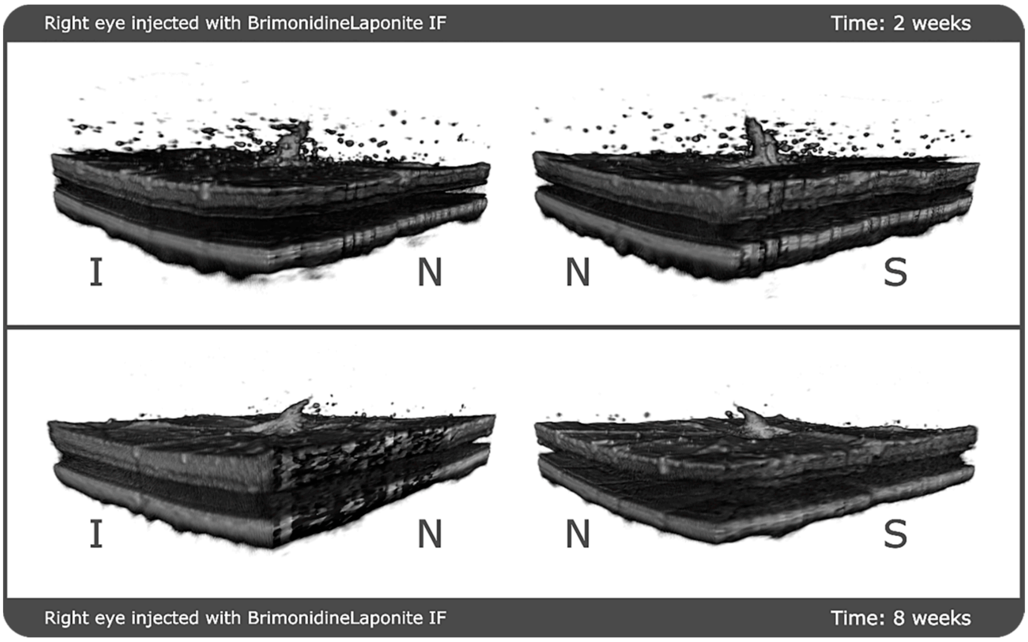

Figure 6. 3-D reconstruction of the evolution of the aggregates at 2 weeks and 8 weeks of follow-up. The reconstruction is shown from two different perspectives at each point in time. Abbreviations: N: nasal; I: inferior; S: superior; IF: intravitreal formulation.

In order to investigate if the vitreous OCT data could serve as an objective marker for non-invasive monitoring of the IF, the curve of the brimonidine levels extracted from our previous study [9] (CC BY 4.0 license) was correlated with the VIT/RPE relative intensities and with the curve of the total aggregate area (as an expression of the total amount of IF injected) obtained using OCT at weeks 1, 4, 8, and 24 after intravitreal injection. Both the brimonidine levels and the VIT/RPE relative intensity curves showed a negative linear tendency with a direct correlation ($y = -0.0003x + 0.1016$ $R^2 = 0.5616$ vs. $y = -0.0002x + 0.2543$ $R^2 = 0.4301$, respectively). Moreover, the logarithmic curves of the brimonidine levels and the total aggregate area were very similar (Figure 7).

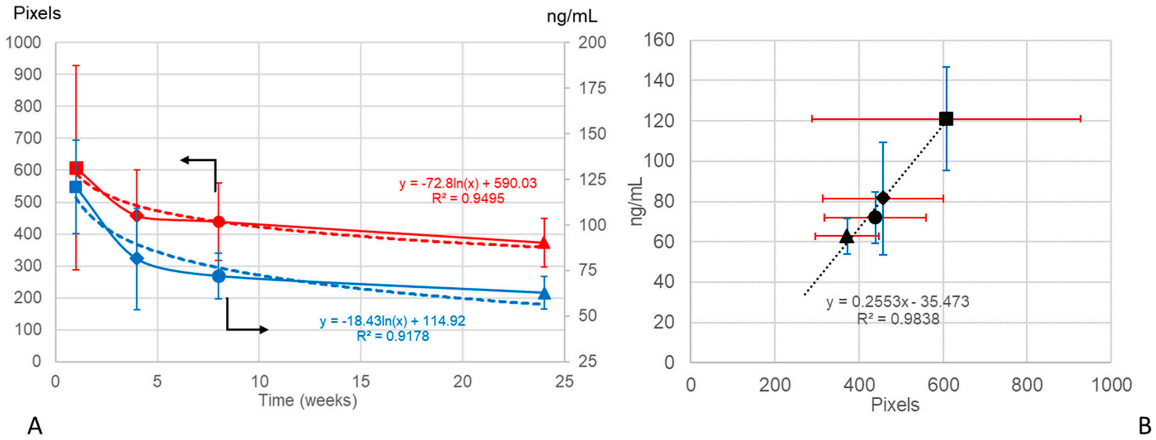

Figure 7. (**A**) Decreasing brimonidine level curves in rat eyes expressed in ng/mL (mean ± standard deviation; n = 3 eyes in each study time) (data from [9] (CC BY 4.0 license)) (in blue) and total aggregate area in the rat eye vitreous expressed in pixels (mean ± standard deviation; n = 9 eyes at week 1, n = 21 eyes at week 4, n = 8 eyes at week 8 and n = 5 eyes at week 24), obtained using optical coherence tomography (in red) over 24 weeks of follow-up. Logarithmic curves in dashes. (**B**) Positive linear correlation between drug levels and total aggregate area. Data are expressed as means ± standard deviation; optical coherence tomography (OCT) data in red; brimonidine data in blue; ■: 1 week; ◆: 4 weeks; ●: 8 weeks; ▲: 24 weeks.

A short in vitro study was performed to compare with the results obtained in the in vivo study. A model for vitreous humour (VHM) formed by sodium hialuronate in saline solution was chosen as medium for release, and the procedure was analogous to our precedent study with the DEX/LAP system [23], with equilibration of the BRI/LAP formulation in the VHM for 24 h, centrifugation to separate the liquid phase with the released BRI for analysis and re-suspension of the solid in a new batch of VHM. As can be seen in Figure 8, the released amount was higher in the first extractions, indicating the presence of a fraction of BRI loosely bound to LAP, whereas the released amount in the successive extractions is much lower, corresponding to the BRI fraction more tightly bound to LAP. In any case, the total amount released after eight extractions is lower than the 22% of the total BRI present in BRI/LAP, confirming in this way the ability of this formulation for a sustained release for a long time period.

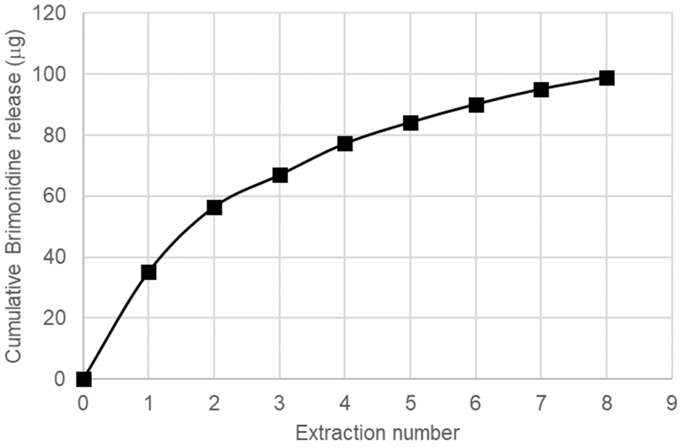

Figure 8. Cumulative release of BRI from BRI/LAP to the model of vitreous humour.

4. Discussion

This paper describes use of OCT to perform non-invasive monitoring of an intravitreal formulation (BRI/LAP) used to treat glaucoma.

Qualitative study made it possible to observe the behaviour of BRI/LAP IF in the vitreous and retina over a 24-week period [9]. In the early stages of the study the BRI/LAP IF was mixed in the vitreous, remaining in suspension in small microaggregates that later showed a tendency to approach and attach to the retina, possibly due to brimonidine tropism towards the alpha-adrenergic receptors present in the ganglion cell layer, inner nuclear layer and outer nuclear layer [24], melanin, the RPE and the choroid. In animal studies, brimonidine has been shown to have both a functional and a structural neuroprotective effect. Intravitreal administration of brimonidine-loaded nanoparticles has shown a neuroprotective effect over 14 days of monitoring [4], a hypotensive and neuroprotective effect lasting 4 weeks in an acute glaucoma model [25] and, recently, our group [9] demonstrated a functional and structural hypotensive and neuroprotective effect lasting 6 months with BRI/LAP IF in a chronic glaucoma model. This was proved not only by analysing the neuroretinal thickness with OCT and the functionally with electroretinography, but also by analysing images of the vitreoretinal interface obtained with OCT, which is a novel measurement method that could provide a non-invasive, objective and reliable means of monitoring the pharmacodynamics of the IF. In addition, brimonidine has been shown to be effective in clinical trials with human patients when administered topically to treat diabetic retinopathy [3] and intravitreally with a brimonidine drug delivery system (Brimo DDS Allergan®, Irvine, CA, USA) in geographic atrophy from age-related macular degeneration [26]. The administration of Brimo DDS® requires an applicator and therefore larger gauge needles, as well as re-implantation every 3 months. A potential sustained-release intravitreal injection-based therapy such as BRI/LAP IF could be effective and useful in these patients as it offers advantages such as injection with smaller micrometric needles, nanoscale formulation and longer therapeutic effects lasting up to 6 months [9].

Repeated intravitreal injections can increase intraocular pressure (IOP) and alter the structure of the optic nerve [27], which can hinder or skew diagnosis and follow-up based on OCT measurements, which are very important in assessing progression in glaucoma. Hence, the use of sustained release systems is necessary in order to reduce re-injection and risk to patients. In this regard, Laponite produced sustained release of drugs for at least 6 months [7–9] and improved the solubility of hydrophobic substances such as brimonidine, thereby facilitating their administration and diffusion within the vitreous.

For the formulation injected into the vitreous to reach the retinal cells (and exert its effect), it must pass through the posterior vitreous cortex (PVC) as well as the ILM, which has pores measuring 10–20 nm. OCT showed hyperreflective aggregates capable of traversing the PVC and ILM and reaching the intraretinal space, possibly by diffusion (Figure 2) due to the small size of the Laponite platelets (1 nm high, 30 nm diameter) [6] and the lipophilicity of brimonidine. In this regard, various authors also found internalisation of drug delivery systems in the retina. Koo et al. [28] described the passage of intravitreal nanoparticles through the retina by both diffusion and endocytosis by the Müller cells, and Xu et al. [29] found that cationic amphiphilic intravitreal polymers reached RPE cells. The space between the ILM and the PVC houses an interdigitate extracellular matrix [15]. In this space, the authors observed that the BRI/LAP IF arranged itself in a row with the aggregates ordered one after the other at different heights, concentrically (see Figure 2A,C and Figure 6). This arrangement is similar to that proposed in the formation of Laponite film, [30] exhibiting a side-by-side arrangement of the Laponite platelets and subsequent stacking of them in different layers. This arrangement is favoured by several film-forming methods, including the Langmuir–Blodgett method, in a liquid–solid interface similar to the vitreous–retina interface, and even more so in the case of hybrid films with organic molecules and macromolecules [31].

OCT was fundamental to demonstrate in vivo degradation of the amount of BRI/LAP IF injected (based on total aggregate area) and morphological and dynamic aggregation of the Laponite molecules (based on mean aggregate area). Acidosis [32] and inflammatory proteins [33] have been detected in the vitreous of glaucoma patients. In both situations, Laponite degradation increases. In our in vivo study (coinciding with the in vitro study), the highest rate of BRI/LAP IF degradation with brimonidine release occurred in the early stages (the largest decrease in total aggregate area occurred in the first 2–6 weeks (Figure 4A)). However, between the middle of the study and the end (at 24 weeks) degradation happened very slowly and the size of the aggregates remained stable. In our previous paper [9], we demonstrated that the BRI/LAP IF produced an early hypotensive effect until 6–8 weeks (peaking at 2 weeks) (see Table 1) that coincided with higher levels of brimonidine in the eye, with the greatest aggregates' area (Figure 4B) and relative intensities of VIT/RPE (Figure 5A), as well as a neuroprotective effect mainly occurring in the later stages (with sustainedly low levels of brimonidine), quantified in the form of reduced retinal RGC death. This reduced RGC death, which brimonidine achieves by blocking the excitotoxicity of the glutamate [34], is probably why the vitreous acidosis was maintained or did not increase and, consequently, why the BRI/LAP IF degradation rate was slower in the later stages. In addition, Laponite aggregates in situations in which pH is very low (acidosis) [35]. Greatest aggregation observed using OCT (measured as an increase in the area of the aggregate) was found in the early stages, coinciding with the onset of the damage induced by ocular hypertension and, therefore, increased acidosis. However, at later stages the aggregates were much smaller, suggesting less acidosis. Both OCT analyses of the aggregates (degradation based on total aggregate area, and aggregation based on mean aggregate area) support the idea of lower cell death due to neuroprotection in the later stages. This suggests a possible correlation/association between analysis of the vitreous using OCT with BRI/LAP IF and the results of structural analysis using OCT and retinal histology [9].

Table 1. Effect of BRI/LAP IF on intraocular pressure.

TIME	OHT (>20 mmHg) EYES (in %)		Intraocular Pressure (X ± sd)		
	Non-Treated	Treated	Non-Treated	Treated	*p*
BASELINE	0	0	9.12 ± 1.48	8.86 ± 1.69	0.476
2 w	88	4.8	23.34 ± 3.53	14.96 ± 4.16	<0.001
4 w (1 m)	91.7	28.1	25.26 ± 3.69	17.36 ± 4.10	<0.001
6 w	100	58.8	27.22 ± 3.15	20.64 ± 5.04	<0.001
8 w (2 m)	95	43.8	28.93 ± 7.11	19.85 ± 4.51	<0.001
12 w (3 m)	36.8	50	19.10 ± 3.07	19.70 ± 2.39	0.423
16 w (4 m)	58.3	80	20.05 ± 4.35	21.79 ± 1.42	0.364
20 w (5 m)	28.6	60	17.38 ± 2.87	21.19 ± 5.49	0.166
24 w (6 m)	71.4	60	23.66 ± 5.45	23.26 ± 4.82	0.684

Abbreviations: BRI/LAP IF. Brimonidine/laponite intravitreal formulation; OHT: ocular hypertension; w. week; m: month; $p < 0.05$: statistical significance; %: percentage; X ± sd: media ± standard deviation. Data from [9] (CC BY 4.0 license).

The OCT study of the vitreoretinal interface was also helpful in understanding a phenomenon that was unresponsive in our previous study [9]. We found that although BRI/LAP IF generally exerted a hypotensive effect on the eye treated, a peak in IOP was detected in week 3 compared to the non-treated LE. Laponite swells in aqueous media, so we hypothesised that an increase in the size of the aggregate was responsible for the IOP increase. In this study based on OCT monitoring of aggregates, as expected, an increase in size of the BRI/LAP IF was measured in the early stages (2–3 weeks), confirming our hypothesis.

Studying pharmacokinetics or tracing in relation to an IF in the visual pathway is not simple [14] as it requires invasive biopsies or tests that are either very expensive or only accessible to researchers [18]. OCT is a non-invasive technology capable of offering almost histological images depending on the light transmitted or reflected as light passes through different structures with differing densities. Those areas that light finds it harder to pass through have higher optical densities (e.g., lipid or calcium membranes), and different optical density ratios have been found according to pathology [36]. The increase in signal offered by BRI/LAP IF may be a consequence of the lipophilicity of the brimonidine and the silicon and magnesium components of the Laponite.

As OCT is a light-scattering imaging technique, higher VIT/RPE relative intensity would indicate greater light scattering, with risk of perception of floaters. In this regard, the size of the aggregates was in the order of microns (from 850 to 760 microns) (Figure 4B), much smaller than the commercially available Ozurdex® implant measuring 0.46 × 6 mm (22G needle) or Brimo DDS® (25G needle) [26]. Larger aggregates potentially perceivable as floaters (Figure 2D) were nevertheless observed occasionally. It was only in the largest and least frequently occurring sizes that a posterior shadow was detected. In most aggregates no shadow was detected, suggesting that potential floater perception would be minimal or non-existent. This was reinforced by the fact that the animals did not exhibit any abnormal behaviour.

Two previous studies involving intravitreal administration of Laponite and using indirect ophthalmoscopy [7,8] describe the IF as a single floccule/lump floating in the vitreous. However, in this study observations of large floccules were incidental/isolated. Laponite has thixotropic characteristics that facilitate IF injection fluidity by using smaller-gauge needles (such as the Hamilton µLSyringes® used in this study) [9]. Likewise, the injection force or speed and the needle gauge used have been shown to influence turbulence and mixing after injection of aqueous and viscous solutions into the vitreous gel [37]. This study suggests that BRI/LAP IF administration using smaller-gauge needles would, in addition to causing less patient discomfort, prevent the formation of large floccules.

In this paper, OCT analysis of the vitreous shows that VIT/RPE relative intensity is (1) significantly higher in eyes treated with IF than in non-treated eyes; (2) that intensity values decrease over time; (3) that scores can be calculated with a high degree of reproducibility; and (4) that the total aggregate area correlates with the amount of brimonidine at all stages of the study and shows a similar degradation curve. Therefore, VIT/RPE relative intensity would be an objective marker. The advantage of this OCT-guided analysis of IF persistence in the vitreous would be the possibility of acquiring simple measurements in repeatable explorations at any stage of disease development. This would help detect or predict a loss of treatment efficacy, avoiding detection of the absence of therapeutic effect only after retinal structural damage occurs, in other words as the disease progresses, as is currently the case with glaucoma. Moreover, it also makes it possible to evaluate the rate of IF degradation individually per patient, thereby making precision medicine more personalised [38]. In addition, guided OCT evaluation can reduce sample size as well as cost both in animal studies and in future clinical trials with patients.

VIT/RPE relative intensity has been used because in previous studies it proved, as a marker of inflammation, to be a repeatable measure with a high degree of reproducibility and sensitivity [16]. Furthermore, Sreekantam et al. [17] mentioned that the RPE signal may be slightly attenuated in the case of macular oedema, resulting in lower VIT/RPE relative intensity. However, glaucoma does not present with oedema, so presumably the utility would be maintained in this pathology, perhaps with even greater reliability.

Limitations of the Study

The depth of the vitreous analysed using OCT is partial and limited to a maximum of 1.9 mm. The authors consider that the analysis performed on the vitreoretinal interface using a follow-up protocol (which involves studying the exact same location in serial scans) presents a representative sample of the complete vitreous gel. This view is shared by other researchers who demonstrated the use of vitreoretinal interface analysis as a non-invasive measure correlated with eye inflammation in animal and human studies [21,39]. The high correlation shown in the results (OCT signal intensity vs. brimonidine concentration in the eye) demonstrates applicability in rats and, presented as a logarithmic scale, suggests that study of the whole vitreous body would not be necessary. However, these animals have a huge lens and therefore a very small vitreous volume compared to humans. In further studies full analysis of the vitreous body would be recommended to corroborate the applicability of this monitoring in animals with a similar organisational structure to humans, such as pigs or dogs. For that purpose, swept-source OCT would help to enhance visualisation of the vitreous cavity. Moreover, as noted above, the increased signal obtained with IF may be a consequence of lipolicity of brimonidine inserted between the silica and magnesium components of the Laponite. This technique seems to be suitable for hyperreflective IF, in contrast to previous therapies injected into the vitreous humour. In this study, blank Laponite was not used because it was previously shown to have an intraocular durability of up to 6 months [7–9]. We are now focusing on IF monitoring for therapeutic application of glaucoma over a long period of time. However, it would be desirable to conduct further studies with only Laponite evaluated with OCT. This study was conducted without enhanced vitreous imaging technology, which could have helped reveal more subtle diffusion characteristics that were not found with the technology used. This research was performed using a commercially available OCT device employed in animal study and a protocol customised specifically for OCT image analysis. Automated analysis of the type that already exists for the study of the neuroretina and that would allow for graduation of signal intensity loss or its rate at the time of acquisition would be beneficial and would facilitate real-time clinical decision-making.

Another limitation could be that some of the hyperreflective dots were due to latent inflammation [16] secondary to the induction of glaucoma and alteration or increase in signal intensity. Eye infection and severe vitritis were discarded in rat eyes injected with BRI/LAP IF in our previous study [9], (CC BY 4.0 license). In this regard, the vitreous cells, hyalocytes, can be exacerbated in inflamed eyes [40] and vitreous changes are early markers of retinal damage [41]. Several studies have demonstrated the capability of monitoring acute and obvious ocular inflammation in vitreous by OCT and correlated it with retinal disease progression [16,17,21,39,42]. However, this first study opens a window to the possibility of also evaluating subclinical inflammation by vitreous imaging. To our knowledge, this is the first OCT-based study to detect an alteration in the vitreous of eyes with glaucoma (higher signal intensity) when compared with healthy eyes. As both eyes were injected to induce OHT, the increased signal intensity found in the RE is considered a consequence of BRI/LAP IF.

Considering translation to clinical settings, one issue to take into consideration would be the vitreous opacities that are normally present in older humans, which are the primary target population for this formulation. However, in general, floaters are usually kept in a stable range, and the monitoring method presented in this study is conducted with a relative signal (VIT/RPE). Therefore, the change of signal in the successive re-scans (monitoring) would be the consequence of a change in the formulation. Furthermore, in the case of pathology, the metabolism of the drugs is altered. Recently, an increase in vitreous signal VIT/RPE has been described in pathologies such as diabetic retinopathy [39], meaning future studies would be necessary to shed light on these doubts. Nevertheless, this study presents a non-invasive, cost-efficient and customisable monitoring method that would facilitate precision medicine [38].

5. Conclusions

This longitudinal study describes for the first time a qualitative and quantitative method of using OCT to analyse the signal generated in the vitreous by the BRI/LAP IF for glaucoma treatment. It enables initial monitoring of a therapeutic intravitreal formulation based on objective measurement of changes in the vitreous using OCT and demonstrates an adequate correlation with brimonidine drug levels. These results are a preliminary step in the validation of this potential biomarker identified with OCT for use in therapeutic monitoring, IF monitoring or tracing and could also be useful for conducting more accurate clinical trials based on early critical points of loss of efficacy. They could also potentially be transferred to clinical settings employing new OCT devices that offer higher image resolution.

6. Patents

J.M.F., J.A.M., V.P. and E.G.M. are inventors on a pending European patent application (No. 20 382 021.2) related to this technology. The terms of this arrangement are being managed by the Aragon Health Research Institute (IIS Aragon) and Zaragoza University in accordance with its conflict of interest policies.

Author Contributions: Conceptualisation, M.J.R. and A.P.d.P.; formal analysis, A.P.d.P., A.M. and E.V.; investigation, J.C. and J.A.M.; methodology, M.J.R., A.P.d.P., A.M., S.M.-M., M.S., M.J.C., T.M.-R. and J.M.F.; resources, V.P.; software, A.M., M.S. and T.M.-R.; validation, M.J.R.; visualisation, A.M., J.M.F., J.A.M. and E.G.-M.; writing—original draft, M.J.R., A.P.d.P., A.M., S.M.-M., J.M.F. and E.G.-M.; writing—review and editing, M.J.R., A.P.d.P. and E.G.-M. All authors have read and agreed to the published version of the manuscript.

Funding: This study was supported by Carlos III Health Institute, (grants numbers: M17/00213, PI17/01726, PI17/01946), and by MINECO/AEI/ERDF, EU (grants numbers: MAT2017-83858-C2-2).

Institutional Review Board Statement: This study was approved beforehand by the Ethics Committee for Animal Research of Zaragoza University (PI34/17, 27 June 2017) and was carried out in strict accordance with the Association for Research in Vision and Ophthalmology's Statement for the Use of Animals.

Informed Consent Statement: Not applicable.

Data Availability Statement: The data presented in this study are available on request from the corresponding author.

Conflicts of Interest: J.M.F., J.A.M., V.P. and E.G.M., are inventors on a pending European patent application (No. 20 382 021.2) related to this technology. The terms of this arrangement are being managed by the Aragon Health Research Institute (IIS Aragon) and Zaragoza University in accordance with its conflict of interest policies. The funders had no role in the design of the study; in the collection, analyses, or interpretation of data; in the writing of the manuscript, or in the decision to publish the results.

References

1. Walters, T.R. Development and use of brimonidine in treating acute and chronic elevations of intraocular pressure: A review of safety, efficacy, dose response, and dosing studies. *Surv. Ophthalmol.* **1996**, *41*, S19–S26. [CrossRef]
2. Nizari, S.; Guo, L.; Davis, B.M.; Normando, E.M.; Galvao, J.; Turner, L.; Bizrah, M.; Dehabadi, M.; Tian, K.; Cordeiro, M.F. Non-amyloidogenic effects of $\alpha 2$ adrenergic agonists: Implications for brimonidine-mediated neuroprotection. *Cell Death Dis.* **2016**, *7*, e2514. [CrossRef]
3. Simó, R.; Hernández, C.; Porta, M.; Bandello, F.; Grauslund, J.; Harding, S.P.; Aldington, S.J.; Egan, C.; Frydkjaer-Olsen, U.; García-Arumí, J.; et al. Effects of Topically Administered Neuroprotective Drugs in Early Stages of Diabetic Retinopathy: Results of the EUROCONDOR Clinical Trial. *Diabetes* **2019**, *68*, 457–463. [CrossRef] [PubMed]
4. Kim, K.E.; Jang, I.; Moon, H.; Kim, Y.J.; Jeoung, J.W.; Park, K.H.; Kim, H. Neuroprotective Effects of Human Serum Albumin Nanoparticles Loaded With Brimonidine on Retinal Ganglion Cells in Optic Nerve Crush Model. *Investig. Opthalmol. Vis. Sci.* **2015**, *56*, 5641. [CrossRef]
5. Dossarps, D.; Bron, A.M.; Koehrer, P.; Aho-Glélé, L.S.; Creuzot-Garcher, C.; Berthon, L.; Maftouhi, Q.-E.; Bakhti, A.; Conrath, J.; Le Mer, Y.; et al. Endophthalmitis After Intravitreal Injections: Incidence, Presentation, Management, and Visual Outcome. *Am. J. Ophthalmol.* **2015**, *160*, 17–25.e1. [CrossRef]
6. Tomás, H.; Alves, C.S.; Rodrigues, J. Laponite®: A key nanoplatform for biomedical applications? *Nanomed. Nanotechnol. Biol. Med.* **2018**, *14*, 2407–2420. [CrossRef]
7. Prieto, E.; Vispe, E.; De Martino, A.; Idoipe, M.; Rodrigo, M.J.; Garcia-Martin, E.; Fraile, J.M.; Polo-Llorens, V.; Mayoral, J.A. Safety study of intravitreal and suprachoroidal Laponite clay in rabbit eyes. *Graefe's Arch. Clin. Exp. Ophthalmol.* **2018**, *256*, 535–546. [CrossRef]
8. Prieto, E.; Cardiel, M.J.; Vispe, E.; Idoipe, M.; Garcia-Martin, E.; Fraile, J.M.; Polo, V.; Mayoral, J.A.; Pablo, L.E.; Rodrigo, M.J. Dexamethasone delivery to the ocular posterior segment by sustained-release Laponite formulation. *Biomed. Mater.* **2020**, *15*, 065021. [CrossRef] [PubMed]

9. Rodrigo, M.J.; Cardiel, M.J.; Fraile, J.M.; Mendez-Martinez, S.; Martinez-Rincon, T.; Subías, M.; Polo, V.; Ruberte, J.; Ramirez, T.; Vispe, E.; et al. Brimonidine-LAPONITE® intravitreal formulation has an ocular hypotensive and neuroprotective effect throughout 6 months of follow-up in a glaucoma animal model. *Biomater. Sci.* **2020**, *8*, 6246–6260. [CrossRef] [PubMed]
10. Lapasin, R.; Abrami, M.; Grassi, G.; Šebenik, U. Rheology of Laponite-scleroglucan hydrogels. *Carbohydr. Polym.* **2017**, *168*, 290–300. [CrossRef] [PubMed]
11. Holekamp, N.M. The Vitreous Gel: More than Meets the Eye. *Am. J. Ophthalmol.* **2010**, *149*, 32–36. [CrossRef]
12. Margolis, R. Diagnostic vitrectomy for the diagnosis and management of posterior uveitis of unknown etiology. *Curr. Opin. Ophthalmol.* **2008**, *19*, 218–224. [CrossRef]
13. Bévalot, F.; Cartiser, N.; Bottinelli, C.; Fanton, L.; Guitton, J. Vitreous humor analysis for the detection of xenobiotics in forensic toxicology: A review. *Forensic Toxicol.* **2016**, *34*, 12–40. [CrossRef]
14. Del Amo, E.M.; Rimpelä, A.-K.; Heikkinen, E.; Kari, O.K.; Ramsay, E.; Lajunen, T.; Schmitt, M.; Pelkonen, L.; Bhattacharya, M.; Richardson, D.; et al. Pharmacokinetic aspects of retinal drug delivery. *Prog. Retin. Eye Res.* **2017**, *57*, 134–185. [CrossRef]
15. Uji, A.; Yoshimura, N. Microarchitecture of the Vitreous Body: A High-Resolution Optical Coherence Tomography Study. *Am. J. Ophthalmol.* **2016**, *168*, 24–30. [CrossRef] [PubMed]
16. Keane, P.A.; Karampelas, M.; Sim, D.A.; Sadda, S.R.; Tufail, A.; Sen, H.N.; Nussenblatt, R.B.; Dick, A.D.; Lee, R.W.; Murray, P.I.; et al. Objective Measurement of Vitreous Inflammation Using Optical Coherence Tomography. *Ophthalmology* **2014**, *121*, 1706–1714. [CrossRef] [PubMed]
17. Sreekantam, S.; Macdonald, T.; Keane, P.; Sim, D.; Murray, P.; Denniston, A.K. Quantitative analysis of vitreous inflammation using optical coherence tomography in patients receiving sub-Tenon's triamcinolone acetonide for uveitic cystoid macular oedema. *Br. J. Ophthalmol.* **2016**, *101*, 175–179. [CrossRef] [PubMed]
18. Fernández-Ferreiro, A.; Luaces-Rodríguez, A.; Aguiar, P.; Pardo-Montero, J.; González-Barcia, M.; García-Varela, L.; Herranz, M.; Silva-Rodríguez, J.; Gil-Martínez, M.; Bermudez, M.; et al. Preclinical PET Study of Intravitreal Injections. *Investig. Ophthalmol. Vis. Sci.* **2017**, *58*, 2843–2851.
19. Li, S.K.; Lizak, M.J.; Jeong, E.-K. MRI in ocular drug delivery. *NMR Biomed.* **2008**, *21*, 941–956. [CrossRef]
20. Morrison, J.C.; Cepurna, W.O.; Johnson, E.C. Modeling glaucoma in rats by sclerosing aqueous outflow pathways to elevate intraocular pressure. *Exp. Eye Res.* **2015**, *141*, 23–32. [CrossRef]
21. Chu, C.J.; Herrmann, P.; Carvalho, L.S.; Liyanage, S.E.; Bainbridge, J.W.B.; Ali, R.R.; Dick, A.D.; Luhmann, U.F. Assessment and In Vivo Scoring of Murine Experimental Autoimmune Uveoretinitis Using Optical Coherence Tomography. *PLoS ONE* **2013**, *8*, e63002. [CrossRef]
22. Liba, O.; Lew, M.D.; SoRelle, E.D.; Dutta, R.; Sen, D.; Moshfeghi, D.M.; Chu, S.; De La Zerda, A. Speckle-modulating optical coherence tomography in living mice and humans. *Nat. Commun.* **2017**, *8*, 15845. [CrossRef]
23. Fraile, J.M.; Garcia-Martin, E.; Gil, C.; Mayoral, J.A.; Pablo, L.; Polo-Llorens, V.; Prieto, E.; Vispe, E. Laponite as carrier for controlled in vitro delivery of dexamethasone in vitreous humor models. *Eur. J. Pharm. Biopharm.* **2016**, *108*, 83–90. [CrossRef]
24. Kalapesi, F.B.; Coroneo, M.T.; Hill, M.A. Human ganglion cells express the alpha-2 adrenergic receptor: Relevance to neuroprotection. *Br. J. Ophthalmol.* **2005**, *89*, 758–763. [CrossRef]
25. Lambert, W.S.; Carlson, B.J.; Van Der Ende, A.E.; Shih, G.; Dobish, J.N.; Calkins, D.J.; Harth, E. Nanosponge-Mediated Drug Delivery Lowers Intraocular Pressure. *Transl. Vis. Sci. Technol.* **2015**, *4*, 1. [CrossRef]
26. Kuppermann, B.D.; Patel, S.S.; Boyer, D.S.; Augustin, A.J.; Freeman, W.R.; Kerr, K.J.; Guo, Q.; Schneider, S.; López, F.J. Phase 2 Study of the Safety and Efficacy of Brimonidine Drug Delivery System (Brimo Dds) Generation 1 in Patients with Geographic Atrophy Secondary to Age-Related Macular Degeneration. *Retina* **2021**, *41*, 144–155. [CrossRef] [PubMed]
27. Gómez-Mariscal, M.; Puerto, B.; Muñoz-Negrete, F.J.; De Juan, V.; Rebolleda, G. Acute and chronic optic nerve head biomechanics and intraocular pressure changes in patients receiving multiple intravitreal injections of anti-VEGF. *Graefe's Arch. Clin. Exp. Ophthalmol.* **2019**, *257*, 2221–2231. [CrossRef] [PubMed]
28. Koo, H.; Moon, H.; Han, H.; Na, J.H.; Huh, M.S.; Park, J.H.; Woo, S.J.; Park, K.H.; Kwon, I.C.; Kim, K.; et al. The movement of self-assembled amphiphilic polymeric nanoparticles in the vitreous and retina after intravitreal injection. *Biomaterials* **2012**, *33*, 3485–3493. [CrossRef] [PubMed]
29. Xu, X.; Xu, Z.; Liu, J.; Zhang, Z.; Chen, H.; Li, X.; Shi, S. Visual tracing of diffusion and biodistribution for amphiphilic cationic nanoparticles using photoacoustic imaging after ex vivo intravitreal injections. *Int. J. Nanomed.* **2016**, *11*, 5079–5086. [CrossRef] [PubMed]
30. Le Luyer, C.; Lou, L.; Bovier, C.; Plenet, J.; Dumas, J.; Mugnier, J. A thick sol–gel inorganic layer for optical planar waveguide applications. *Opt. Mater.* **2001**, *18*, 211–217. [CrossRef]
31. Schoonheydt, R.A. Functional hybrid clay mineral films. *Appl. Clay Sci.* **2014**, *96*, 9–21. [CrossRef]
32. Gala, A. Observations on the Hydrogen Ion Concentration in the Vitreous Body of the Eye with Reference to Glaucoma. *Br. J. Ophthalmol.* **1925**, *9*, 516–519. [CrossRef]
33. Mirzaei, M.; Gupta, V.B.; Chick, J.M.; Greco, T.M.; Wu, Y.; Chitranshi, N.; Wall, R.V.; Hone, E.; Deng, L.; Dheer, Y.; et al. Age-related neurodegenerative disease associated pathways identified in retinal and vitreous proteome from human glaucoma eyes. *Sci. Rep.* **2017**, *7*, 1–16. [CrossRef]

34. Lee, D.; Kim, K.-Y.; Noh, Y.H.; Chai, S.; Lindsey, J.D.; Ellisman, M.H.; Weinreb, R.N.; Ju, W.-K. Brimonidine Blocks Glutamate Excitotoxicity-Induced Oxidative Stress and Preserves Mitochondrial Transcription Factor A in Ischemic Retinal Injury. *PLoS ONE* **2012**, *7*, e47098. [CrossRef]
35. Tawari, S.L.; Koch, D.L.; Cohen, C. Electrical Double-Layer Effects on the Brownian Diffusivity and Aggregation Rate of Laponite Clay Particles. *J. Colloid Interface Sci.* **2001**, *240*, 54–66. [CrossRef] [PubMed]
36. Fujimoto, J.G. Optical coherence tomography for ultrahigh resolution in vivo imaging. *Nat. Biotechnol.* **2003**, *21*, 1361–1367. [CrossRef] [PubMed]
37. Hartman, R.R.; Kompella, U.B. Intravitreal, Subretinal, and Suprachoroidal Injections: Evolution of Microneedles for Drug Delivery. *J. Ocul. Pharmacol. Ther.* **2018**, *34*, 141–153. [CrossRef] [PubMed]
38. Moroi, S.E.; Reed, D.M.; Sanders, D.S.; AlMazroa, A.; Kagemann, L.; Shah, N.; Shekhawat, N.; Richards, J.E. Precision medicine to prevent glaucoma-related blindness. *Curr. Opin. Ophthalmol.* **2019**, *30*, 187–198. [CrossRef] [PubMed]
39. Korot, E.; Comer, G.M.; Steffens, T.; Antonetti, D.A. Algorithm for the Measure of Vitreous Hyperreflective Foci in Optical Coherence Tomographic Scans of Patients with Diabetic Macular Edema. *JAMA Ophthalmol.* **2016**, *134*, 15–20. [CrossRef]
40. Sakamoto, T.; Ishibashi, T. Hyalocytes: Essential cells of the vitreous cavity in vitreoretinal pathophysiology? *Retina* **2011**, *31*, 222–228. [CrossRef]
41. Vagaja, N.N.; Chinnery, H.R.; Binz, N.; Kezic, J.M.; Rakoczy, E.P.; McMenamin, P.G. Changes in Murine Hyalocytes Are Valuable Early Indicators of Ocular Disease. *Investig. Ophthalmol. Vis. Sci.* **2012**, *53*, 1445–1451. [CrossRef] [PubMed]
42. Liu, X.; Hui, B.T.; Way, C.; Beese, S.; Adriano, A.; Keane, P.; Moore, D.J.; Denniston, A.K. Noninvasive Instrument-based Tests for Detecting and Measuring Vitreous Inflammation in Uveitis: A Systematic Review. *Ocul. Immunol. Inflamm.* **2020**, 1–12. [CrossRef] [PubMed]

Chapter 3

Conclusions and contributions

This chapter presents the main conclusions as a result of this thesis. In addition, the original contributions are listed and future lines of work are presented.

3.1 Conclusions

This thesis presented several computational methodologies for the monitoring, diagnosis, prediction and treatment of neurodegenerative diseases using OCT technology. Based on the application of the results, the main conclusions of this thesis have been grouped according to clinical application:

- RNFL evolution in MS patients
    - The different relative contributions of autoimmune inflammation and axonal degeneration would explain the complex dynamics of MS.
    - Axonal damage occurs cumulatively from the onset of MS and most of the RNFL thinning occurs before the patient becomes significantly disabled.
    - RNFL thickness, measured by OCT, could be a reliable biomarker of MS. OCT data from MS patients can be used to predict the progression of RNFL thinning and thus disease progression, improving the selection of patient-specific therapies.
- MS diagnosis and prognosis by OCT and AI

  - RNFL thickness measurements obtained with DRI OCT Triton, Cirrus HD-OCT or Spectralis OCT have an excellent ability to diagnose MS using machine learning techniques.
  - AI models, using clinical and OCT data, can help predict the long-term disability progression in MS patients.

- Glaucoma monitoring with vitreous imaging
  - Vitreous parainflammation of chronic glaucoma can be monitored by vitreous OCT imaging and could be a reliable biomarker of glaucoma onset and progression. Glaucomatous eyes showed a higher VIT/RPE relative intensity, as well as a higher number of vitreous opacities.
  - BRI/LAP IF as treatment for glaucoma can be monitored non-invasively using OCT images of the vitreoretinal interface. The vitreous hyperreflective aggregates were mixed in the vitreous and tended to deposit on the retinal surface. The relative intensity and size of the aggregates progressively decreased in the eyes of treated rats as the BRI/LAP IF degraded.

3.2 Contributions

This thesis is an important step in the use of OCT technology with computational methods to better understand and analyse different neurodegenerative diseases. The original contributions resulting from this thesis are set out below, grouped into the different clinical applications:

- RNFL evolution in MS patients
  - A mathematical model to predict RNFL thinning in MS patients, taking into account the biological processes that influence the dynamics of this disease.
- MS diagnosis and prognosis by OCT and AI
  - MS diagnosis model for three different DRI OCT Triton protocols using RNFL data from 80 MS patients and 180 healthy controls.

  - MS diagnosis model for Cirrus HD-OCT using RNFL data from 108 MS patients and 104 healthy controls.
  - MS diagnosis model for three different Spectralis OCT protocols using RNFL data from 72 MS patients and 30 healthy controls.
  - MS prognosis model with 3-year follow-up for Cirrus HD-OCT using RNFL data from 82 MS patients.
  - MS prognosis model with two and three years of follow-up for three different Spectralis OCT protocols using RNFL data from 72 MS patients.

- Glaucoma monitoring with vitreous imaging
  - Computational method to analyse vitreous parainflammation in animal models of glaucoma using vitreous OCT imaging, characterising hyperreflective opacities at the vitreoretinal interface and their dynamics through changes in number, size, intensity, eccentricity and orientation.
  - Non-invasive method to monitor drug levels in the vitreous using OCT and computational analysis.

3.2.1 Journal publications

1. A. Pérez del Palomar, J. Cegoñino, **A. Montolío**, E. Orduna, E. Vilades, B. Sebastián, L.E. Pablo, E. Garcia-Martin, Swept source optical coherence tomography to early detect multiple sclerosis disease. The use of machine learning techniques, PLoS One. 14 (2019) e0216410.
   https://doi.org/10.1371/journal.pone.0216410.

2. **A. Montolío**, J. Cegoñino, E. Orduna, B. Sebastian, E. Garcia-Martin, A. Pérez del Palomar, A mathematical model to predict the evolution of retinal nerve fiber layer thinning in multiple sclerosis patients, Comput. Biol. Med. 111 (2019) 103357.
   https://doi.org/10.1016/j.compbiomed.2019.103357.

3. B. Cordón, J. Pérez, M.J. Vicente, E. Viladés, E. Orduna, A. Pérez del Palomar, J. Cegoñino, **A. Montolio**, J.R. Ara, M.J. Rodrigo, M. Satué, E. Garcia-Martin, Evaluation with angiography by optical coherence tomography of patients with multiple sclerosis, Acta Ophthalmol. 97 (2019) j.1755-3768.2019.5172.
   https://doi.org/10.1111/j.1755-3768.2019.5172.

4. J. Pérez, M.J. Vicente, E. Viladés, E. Orduna, A. Pérez del Palomar, J. Cegoñino, **A. Montolío**, M. Satué, E. Garcia-Martin, B. Cordón, Physiological changes in retinal layers thicknesses measured with swept source optical coherence tomography, Acta Ophthalmol. 97 (2019) j.1755-3768.2019.5169.
https://doi.org/10.1111/j.1755-3768.2019.5169.

5. M.J. Rodrigo, A. Pérez del Palomar, **A. Montolío**, S. Mendez-Martinez, M. Subias, M.J. Cardiel, T. Martinez-Rincon, J. Cegoñino, J.M. Fraile, E. Vispe, J.A. Mayoral, V. Polo, E. Garcia-Martin, Monitoring New Long-Lasting Intravitreal Formulation for Glaucoma with Vitreous Images Using Optical Coherence Tomography, Pharmaceutics. 13 (2021) 217.
https://doi.org/10.3390/pharmaceutics13020217.

6. **A. Montolío**, A. Martín-Gallego, J. Cegoñino, E. Orduna, E. Vilades, E. Garcia-Martin, A.P. del Palomar, Machine learning in diagnosis and disability prediction of multiple sclerosis using optical coherence tomography, Comput. Biol. Med. 133 (2021) 104416.
https://doi.org/10.1016/j.compbiomed.2021.104416.

7. M.J. Rodrigo, M. Subías, **A. Montolío**, S. Méndez-Martínez, T. Martínez-Rincón, L. Arias, D. García-Herranz, I. Bravo-Osuna, J. Garcia-Feijoo, L. Pablo, J. Cegoñino, R. Herrero-Vanrell, A. Carretero, J. Ruberte, E. Garcia-Martin, A. Pérez del Palomar, Analysis of Parainflammation in Chronic Glaucoma Using Vitreous-OCT Imaging, Biomedicines. 9 (2021) 1792.
https://doi.org/10.3390/biomedicines9121792.

8. M. Subías, L. Arias, M.J. Vicente, A. Tello, L. Castro-Roger, E. Viladés, B. Cordón, A. Pérez del Palomar, J. Cegoñino, **A. Montolío**, E. Garcia-Martin, M.J. Rodrigo, Analysis of vitreous opacities in chronic glaucoma by vitreo-optical coherence tomography imaging, Acta Ophthalmol. 100 (2022) j.1755-3768.2022.097.
https://doi.org/10.1111/j.1755-3768.2022.097.

9. **A. Montolío**, J. Cegoñino, E. Garcia-Martin, A. Pérez del Palomar, Comparison of machine learning methods using Spectralis OCT for diagnosis and disability progression prognosis in multiple sclerosis, Ann. Biomed. Eng. (2022) s10439-022-02930-3.
https://doi.org/10.1007/s10439-022-02930-3.

3.2.2 Oral communications in conferences

1. **A. Montolío**, A. Martín-Gallego, J. Cegoñino, E. Garcia-Martin, A. Pérez del Palomar. How Ionic Imbalances Alter Axonal Conduction. A Computational Study.
   Virtual Physiological Human Conference, September 2018, Zaragoza (Spain).

2. A. Martín-Gallego, E. Garcia-Martin, **A. Montolío**, J. Cegoñino, A. Pérez del Palomar. The use of neural networks to help in pathologies diagnosis.
   Virtual Physiological Human Conference, September 2018, Zaragoza (Spain).

3. **A. Montolío**, J. Cegoñino, E. Garcia-Martin, A. Pérez del Palomar. Numerical model of the evolution of axonal degeneration.
   European Society of Biomechanics Conference, July 2019, Vienna (Austria).

4. **A. Montolío**, A. Martín-Gallego, J. Cegoñino, E. Garcia-Martin, A. Pérez del Palomar. The use of classifications algorithms to predict the disease evolution.
   European Society of Biomechanics Conference, July 2019, Vienna (Austria).

5. B. Cordón, J. Pérez, E. Viladés, E. Orduna, A. Pérez del Palomar, J. Cegoñino, **A. Montolío**, M.J. Rodrigo. Vascular changes in the retina of multiple sclerosis patients using optical coherence tomography angiography.
   95th Congress of the Spanish Ophthalmology Society, September 2019, Madrid (Spain).

6. B. Cordón, J. Pérez, M.J. Vicente, E. Viladés, E. Orduna, A. Pérez del Palomar, J. Cegoñino, **A. Montolio**, J.R. Ara, M.J. Rodrigo, M. Satué, E. Garcia-Martin. Evaluation with angiography by optical coherence tomography of patients with multiple sclerosis.
   2019 European Association for Vision and Eye Research Conference, October 2019, Nice (France).
   https://doi.org/10.1111/j.1755-3768.2019.5172.

7. J. Pérez, M.J. Vicente, E. Viladés, E. Orduna, A. Pérez del Palomar, J. Cegoñino, **A. Montolío**, M. Satué, E. Garcíia-Martin, B. Cordón. Physiological changes in retinal layers thicknesses measured with swept source optical coherence tomography.
   2019 European Association for Vision and Eye Research Conference, October 2019, Nice (France).
   https://doi.org/10.1111/j.1755-3768.2019.5169.

8. **A. Montolío**, J. Cegoñino, E. Garcia-Martin, A. Pérez del Palomar. LSTM recurrent neural network to predict the disability course.
   Virtual Physiological Human Conference, August 2020, Paris (France).

9. **A. Montolío**, J. Cegoñino, E. Garcia-Martin, A. Pérez del Palomar. How to predict the long-term course of neurodegenerative diseases?
   IX Meeting of Young Researchers of the I3A, December 2020, Zaragoza (Spain).
   https://doi.org/10.26754/jjii3a.4886.

10. **A. Montolío**, J. Cegoñino, E. Garcia-Martin, A. Pérez del Palomar. The retina as a biomarker of neurodegenerative diseases.
    I Annual Congress of Doctoral Students, February 2021, Elche (Spain).

11. **A. Montolío**, J. Cegoñino, E. Garcia-Martin, A. Pérez del Palomar. Retinal nerve fiber layer as a biomarker of disability progression in multiple sclerosis patients using machine learning techniques.
    17th International Symposium on Computer Methods in Biomechanics and Biomedical Engineering and 5th Conference on Imaging and Visualization, September 2021, Bonn (Germany).

12. M. Subías, L. Arias, M.J. Vicente, A. Tello, L. Castro-Roger, E. Viladés, B. Cordón, A. Pérez del Palomar, J. Cegoñino, **A. Montolío**, E. Garcia-Martin, M.J. Rodrigo. Analysis of vitreous opacities in chronic glaucoma by vitreo-optical coherence tomography imaging.
    2021 European Association for Vision and Eye Research Conference, October 2021, Nice (France).
    https://doi.org/10.1111/j.1755-3768.2022.097.

13. **A. Montolío**, J. Cegoñino, E. Garcia-Martin, A. Pérez del Palomar. Neural networks to diagnose multiple sclerosis with retinal ganglion cell layer thickness.
    II Annual Congress of Doctoral Students, February 2022, Elche (Spain).

14. **A. Montolío**, J. Cegoñino, E. Garcia-Martin, A. Pérez del Palomar. Can deep learning diagnose neurodegenerative diseases with retinal ganglion cell layer?
    8th European Congress on Computational Methods in Applied Science and Engineering, June 2022, Oslo (Norway).

3.2.3 Poster communications in conferences

1. **A. Montolío**, J. Cegoñino, E. Garcia-Martin, A. Pérez del Palomar. Retinal nerve fiber layer as a biomarker of axonal damage in multiple sclerosis patients using machine learning techniques.
   37th Congress of the European Committee for Treatment and Research in Multiple Sclerosis, October 2021, Vienna (Austria).

3.2.4 Symposiums

1. **A. Montolío**, J. Cegoñino, E. Garcia-Martin, A. Pérez del Palomar. A mathematical model to predict the evolution of axonal degeneration in multiple sclerosis patients.
   VI Doctoral Meeting of the PhD Program in Mechanical Engineering, June 2019, Zaragoza (Spain).

2. **A. Montolío**, J. Cegoñino, E. Garcia-Martin, A. Pérez del Palomar. The use of machine learning to diagnose and predict multiple sclerosis.
   VII Doctoral Meeting of the PhD Program in Mechanical Engineering, December 2020, Zaragoza (Spain).

3. **A. Montolío**, M. J. Rodrigo, J. Cegoñino, E. Garcia-Martin, A. Pérez del Palomar. The use of OCT in monitoring, diagnosis, prediction and treatment of neurodegenerative diseases.
   IX Doctoral Meeting and IV Dissemination Meeting of the Group 9 Universities (G-9), May 2022, Bilbao (Spain).

3.3 Future work

As discussed throughout this dissertation, a large number of studies have been performed in relation to the use of OCT technology in neurodegenerative diseases from both a clinical and computational point of view. However, there is still a long way to go to achieve the clinical application of these methodologies. In this thesis, different clinical applications of OCT have been analysed with the aim of increasing the knowledge about them. Nevertheless, this thesis raises new fields of experimental and computational study that can be addressed in future work:

- The study of biological processes underlying MS-induced CNS damage using larger amounts of data.
- Validation of our models in other populations to demonstrate their utility and confirm the validity of RNFL thickness as a reliable biomarker for both diagnosis and prognosis of MS.
- The incorporation of these mathematical models into OCT devices to directly obtain the diagnosis and prognosis of the disease, reducing waiting times.
- Validation of vitreous signal intensity, obtained from OCT images, as a biomarker for use in therapeutic monitoring and IF monitoring or tracing.

Chapter 4

Conclusiones y contribuciones[1]

En este capítulo se presentan las principales conclusiones como resultado de esta tesis. Además, se enumeran las contribuciones originales y se presentan las futuras líneas de trabajo.

4.1 Conclusiones

Esta tesis presentó varias metodologías computacionales para la monitorización, el diagnóstico, la predicción y el tratamiento de enfermedades neurodegenerativas mediante la tecnología OCT. En base a la aplicación de los resultados, las principales conclusiones de esta tesis se han agrupado según la aplicación clínica:

- Evolución de la capa de fibras nerviosas de la retina en pacientes con esclerosis múltiple
    - Las diferentes contribuciones relativas de la inflamación autoinmune y la degeneración axonal explicarían la compleja dinámica de la esclerosis múltiple.
    - El daño axonal se produce de forma acumulativa desde el inicio de la esclerosis múltiple y la mayor parte del adelgazamiento de la capa de

---

[1] De acuerdo con los requisitos para optar a la mención de “Doctor Internacional”, establecidos por el art. 18 del Reglamento sobre Tesis Doctorales de la Universidad de Zaragoza y el art. 12.2 del Procedimiento de depósito, autorización y defensa de tesis de la Universidad de Zaragoza, se incluyen las conclusiones en español.

  fibras nerviosas de la retina se produce antes de que el paciente presente una discapacidad significativa.

  - El espesor de la capa de fibras nerviosas de la retina, medido mediante OCT, podría ser un biomarcador fiable de la esclerosis múltiple. Los datos OCT de pacientes con esclerosis múltiple pueden utilizarse para predecir la progresión del adelgazamiento de la capa de fibras nerviosas de la retina y, por tanto, la progresión de la enfermedad, mejorando la selección de terapias específicas para los pacientes.

- Diagnóstico y pronóstico de la esclerosis múltiple mediante OCT e inteligencia artificial

  - Las mediciones del espesor de la capa de fibras nerviosas de la retina obtenidas con DRI OCT Triton, Cirrus HD-OCT o Spectralis OCT tienen una excelente capacidad para diagnosticar la esclerosis múltiple utilizando técnicas de aprendizaje automático.
  - Los modelos de inteligencia artificial, utilizando datos clínicos y de OCT, pueden ayudar a predecir la progresión de la discapacidad a largo plazo en pacientes con esclerosis múltiple.

- Monitorización del glaucoma con imágenes vítreas

  - La parainflamación vítrea del glaucoma crónico puede monitorizarse mediante imágenes OCT vítreas y podría ser un biomarcador fiable del inicio y la progresión del glaucoma. Los ojos glaucomatosos mostraron una mayor intensidad relativa entre el vítreo y el epitelio pigmentario de la retina, así como un mayor número de opacidades vítreas.
  - La formulación intravítrea BRI/LAP como tratamiento del glaucoma puede ser monitorizado de forma no invasiva mediante imágenes OCT de la interfaz vitreorretiniana. Los agregados hiperreflectantes vítreos se mezclaban en el vítreo y tendían a depositarse en la superficie retiniana. La intensidad relativa y el tamaño de los agregados disminuyeron progresivamente en los ojos de las ratas tratadas a medida que se degradaba la formulación intravítrea BRI/LAP.

4.2 Contribuciones

Esta tesis es un paso importante en el uso de la tecnología OCT con métodos computacionales para entender y analizar mejor diferentes enfermedades neurodegenerativas. A continuación se exponen las aportaciones originales resultantes de esta tesis, agrupadas en las diferentes aplicaciones clínicas:

- Evolución de la capa de fibras nerviosas de la retina en pacientes con esclerosis múltiple
    - Un modelo matemático para predecir el adelgazamiento de la capa de fibras nerviosas de la retina en pacientes con esclerosis múltiple, teniendo en cuenta los procesos biológicos que influyen en la dinámica de esta enfermedad.
- Diagnóstico y pronóstico de la esclerosis múltiple mediante OCT e inteligencia artificial
    - Modelo de diagnóstico de la esclerosis múltiple para tres protocolos diferentes de DRI OCT Triton utilizando datos de la capa de fibras nerviosas de la retina de 80 pacientes con esclerosis múltiple y 180 controles sanos.
    - Modelo de diagnóstico de la esclerosis múltiple para Cirrus HD-OCT utilizando datos de la capa de fibras nerviosas de la retina de 108 pacientes con esclerosis múltiple y 104 controles sanos.
    - Modelo de diagnóstico de la esclerosis múltiple para tres protocolos diferentes de Spectralis OCT utilizando datos de la capa de fibras nerviosas de la retina de 72 pacientes con esclerosis múltiple y 30 controles sanos.
    - Modelo de pronóstico de la esclerosis múltiple con seguimiento a tres años para Cirrus HD-OCT utilizando datos de la capa de fibras nerviosas de la retina de 82 pacientes con esclerosis múltiple.
    - Modelo de pronóstico de la esclerosis múltiple con dos y tres años de seguimiento para tres protocolos diferentes de Spectralis OCT utilizando datos de la capa de fibras nerviosas de la retina de 72 pacientes con esclerosis múltiple.
- Monitorización del glaucoma con imágenes vítreas

- Método computacional para analizar la parainflamación vítrea en modelos animales de glaucoma mediante imágenes OCT vítreas, caracterizando las opacidades hiperreflectivas en la interfaz vitreoretiniana y su dinámica a través de los cambios en número, tamaño, intensidad, excentricidad y orientación.
- Método no invasivo para monitorizar los niveles de fármacos en el vítreo mediante OCT y análisis computacional.

4.2.1 Publicaciones en revistas

1. A. Pérez del Palomar, J. Cegoñino, **A. Montolío**, E. Orduna, E. Vilades, B. Sebastián, L.E. Pablo, E. Garcia-Martin, Swept source optical coherence tomography to early detect multiple sclerosis disease. The use of machine learning techniques, PLoS One. 14 (2019) e0216410.
https://doi.org/10.1371/journal.pone.0216410.

2. **A. Montolío**, J. Cegoñino, E. Orduna, B. Sebastian, E. Garcia-Martin, A. Pérez del Palomar, A mathematical model to predict the evolution of retinal nerve fiber layer thinning in multiple sclerosis patients, Comput. Biol. Med. 111 (2019) 103357.
https://doi.org/10.1016/j.compbiomed.2019.103357.

3. B. Cordón, J. Pérez, M.J. Vicente, E. Viladés, E. Orduna, A. Pérez del Palomar, J. Cegoñino, **A. Montolio**, J.R. Ara, M.J. Rodrigo, M. Satué, E. Garcia-Martin, Evaluation with angiography by optical coherence tomography of patients with multiple sclerosis, Acta Ophthalmol. 97 (2019) j.1755-3768.2019.5172.
https://doi.org/10.1111/j.1755-3768.2019.5172.

4. J. Pérez, M.J. Vicente, E. Viladés, E. Orduna, A. Pérez del Palomar, J. Cegoñino, **A. Montolío**, M. Satué, E. Garcíia-Martin, B. Cordón, Physiological changes in retinal layers thicknesses measured with swept source optical coherence tomography, Acta Ophthalmol. 97 (2019) j.1755-3768.2019.5169.
https://doi.org/10.1111/j.1755-3768.2019.5169.

5. M.J. Rodrigo, A. Pérez del Palomar, **A. Montolío**, S. Mendez-Martinez, M. Subias, M.J. Cardiel, T. Martinez-Rincon, J. Cegoñino, J.M. Fraile, E. Vispe, J.A. Mayoral, V. Polo, E. Garcia-Martin, Monitoring New Long-Lasting Intravitreal Formulation for Glaucoma with Vitreous Images Using Optical Co-

herence Tomography, Pharmaceutics. 13 (2021) 217.
https://doi.org/10.3390/pharmaceutics13020217.

6. **A. Montolío**, A. Martín-Gallego, J. Cegoñino, E. Orduna, E. Vilades, E. Garcia-Martin, A.P. del Palomar, Machine learning in diagnosis and disability prediction of multiple sclerosis using optical coherence tomography, Comput. Biol. Med. 133 (2021) 104416.
https://doi.org/10.1016/j.compbiomed.2021.104416.

7. M.J. Rodrigo, M. Subías, **A. Montolío**, S. Méndez-Martínez, T. Martínez-Rincón, L. Arias, D. García-Herranz, I. Bravo-Osuna, J. Garcia-Feijoo, L. Pablo, J. Cegoñino, R. Herrero-Vanrell, A. Carretero, J. Ruberte, E. Garcia-Martin, A. Pérez del Palomar, Analysis of Parainflammation in Chronic Glaucoma Using Vitreous-OCT Imaging, Biomedicines. 9 (2021) 1792.
https://doi.org/10.3390/biomedicines9121792.

8. M. Subías, L. Arias, M.J. Vicente, A. Tello, L. Castro-Roger, E. Viladés, B. Cordón, A. Pérez del Palomar, J. Cegoñino, **A. Montolío**, E. Garcia-Martin, M.J. Rodrigo, Analysis of vitreous opacities in chronic glaucoma by vitreo-optical coherence tomography imaging, Acta Ophthalmol. 100 (2022) j.1755-3768.2022.097.
https://doi.org/10.1111/j.1755-3768.2022.097.

9. **A. Montolío**, J. Cegoñino, E. Garcia-Martin, A. Pérez del Palomar, Comparison of machine learning methods using Spectralis OCT for diagnosis and disability progression prognosis in multiple sclerosis, Ann. Biomed. Eng. (2022) s10439-022-02930-3.
https://doi.org/10.1007/s10439-022-02930-3.

4.2.2 Comunicaciones orales en congresos

1. **A. Montolío**, A. Martín-Gallego, J. Cegoñino, E. Garcia-Martin, A. Pérez del Palomar. How Ionic Imbalances Alter Axonal Conduction. A Computational Study.
Virtual Physiological Human Conference, Septiembre 2018, Zaragoza (España).

2. A. Martín-Gallego, E. Garcia-Martin, **A. Montolío**, J. Cegoñino, A. Pérez del Palomar. The use of neural networks to help in pathologies diagnosis.
Virtual Physiological Human Conference, Septiembre 2018, Zaragoza (España).

3. **A. Montolío**, J. Cegoñino, E. Garcia-Martin, A. Pérez del Palomar. Numerical model of the evolution of axonal degeneration.
   European Society of Biomechanics Conference, Julio 2019, Viena (Austria).

4. **A. Montolío**, A. Martín-Gallego, J. Cegoñino, E. Garcia-Martin, A. Pérez del Palomar. The use of classifications algorithms to predict the disease evolution.
   European Society of Biomechanics Conference, Julio 2019, Viena (Austria).

5. B. Cordón, J. Pérez, E. Viladés, E. Orduna, A. Pérez del Palomar, J. Cegoñino, **A. Montolío**, M.J. Rodrigo. Cambios vasculares en la retina de pacientes con esclerosis múltiple mediante angiografía por tomografía de coherencia óptica.
   95º Congreso Sociedad Española de Oftalmología, Septiembre 2019, Madrid (España).

6. B. Cordón, J. Pérez, M.J. Vicente, E. Viladés, E. Orduna, A. Pérez del Palomar, J. Cegoñino, **A. Montolio**, J.R. Ara, M.J. Rodrigo, M. Satué, E. Garcia-Martin. Evaluation with angiography by optical coherence tomography of patients with multiple sclerosis.
   2019 European Association for Vision and Eye Research Conference, Octubre 2019, Niza (Francia).
   https://doi.org/10.1111/j.1755-3768.2019.5172.

7. J. Pérez, M.J. Vicente, E. Viladés, E. Orduna, A. Pérez del Palomar, J. Cegoñino, **A. Montolío**, M. Satué, E. Garcíia-Martin, B. Cordón. Physiological changes in retinal layers thicknesses measured with swept source optical coherence tomography.
   2019 European Association for Vision and Eye Research Conference, Octubre 2019, Niza (Francia).
   https://doi.org/10.1111/j.1755-3768.2019.5169.

8. **A. Montolío**, J. Cegoñino, E. Garcia-Martin, A. Pérez del Palomar. LSTM recurrent neural network to predict the disability course.
   Virtual Physiological Human Conference, Agosto 2020, Paris (Francia).

9. **A. Montolío**, J. Cegoñino, E. Garcia-Martin, A. Pérez del Palomar. How to predict the long-term course of neurodegenerative diseases?
   IX Jornada de Jóvenes Investigadores del I3A, Diciembre 2020, Zaragoza (España).
   https://doi.org/10.26754/jjii3a.4886.

10. **A. Montolío**, J. Cegoñino, E. Garcia-Martin, A. Pérez del Palomar. The retina as a biomarker of neurodegenerative diseases.
    I Congreso Anual de Estudiantes de Doctorado , Febrero 2021, Elche (España).

11. **A. Montolío**, J. Cegoñino, E. Garcia-Martin, A. Pérez del Palomar. Retinal nerve fiber layer as a biomarker of disability progression in multiple sclerosis patients using machine learning techniques.
    17th International Symposium on Computer Methods in Biomechanics and Biomedical Engineering and 5th Conference on Imaging and Visualization, Septiembre 2021, Bonn (Alemania).

12. M. Subías, L. Arias, M.J. Vicente, A. Tello, L. Castro-Roger, E. Viladés, B. Cordón, A. Pérez del Palomar, J. Cegoñino, **A. Montolío**, E. Garcia-Martin, M.J. Rodrigo. Analysis of vitreous opacities in chronic glaucoma by vitreo-optical coherence tomography imaging.
    2021 European Association for Vision and Eye Research Conference, Octubre 2021, Niza (Francia).
    https://doi.org/10.1111/j.1755-3768.2022.097.

13. **A. Montolío**, J. Cegoñino, E. Garcia-Martin, A. Pérez del Palomar. Neural networks to diagnose multiple sclerosis with retinal ganglion cell layer thickness.
    II Congreso Anual de Estudiantes de Doctorado , Febrero 2022, Elche (España).

14. **A. Montolío**, J. Cegoñino, E. Garcia-Martin, A. Pérez del Palomar. Can deep learning diagnose neurodegenerative diseases with retinal ganglion cell layer?
    8th European Congress on Computational Methods in Applied Science and Engineering, Junio 2022, Oslo (Noruega).

4.2.3 Pósters en congresos

1. **A. Montolío**, J. Cegoñino, E. Garcia-Martin, A. Pérez del Palomar. Retinal nerve fiber layer as a biomarker of axonal damage in multiple sclerosis patients using machine learning techniques.
   37th Congress of the European Committee for Treatment and Research in Multiple Sclerosis, Octubre 2021, Viena (Austria).

4.2.4 Seminarios

1. **A. Montolío**, J. Cegoñino, E. Garcia-Martin, A. Pérez del Palomar. A mathematical model to predict the evolution of axonal degeneration in multiple sclerosis patients.
   VI Jornada doctorandos del Programa de Doctorado en Ingeniería Mecánica, Junio 2019, Zaragoza (España).
2. **A. Montolío**, J. Cegoñino, E. Garcia-Martin, A. Pérez del Palomar. The use of machine learning to diagnose and predict multiple sclerosis.
   VII Jornada doctorandos del Programa de Doctorado en Ingeniería Mecánica, Deciembre 2020, Zaragoza (España).

   item **A. Montolío**, M. J. Rodrigo, J. Cegoñino, E. Garcia-Martin, A. Pérez del Palomar. The use of OCT in monitoring, diagnosis, prediction and treatment of neurodegenerative diseases.
   IX Jornadas Doctorales y IV Jornadas de Divulgación del Grupo 9 de Universidades (G-9), Mayo 2022, Bilbao (Spain).

4.3 Trabajo futuro

Como se ha comentado a lo largo de esta disertación, se han realizado un gran número de estudios en relación con el uso de la tecnología OCT en las enfermedades neurodegenerativas, tanto desde el punto de vista clínico como computacional. Sin embargo, aún queda mucho camino por recorrer para lograr la aplicación clínica de estas metodologías. En esta tesis se han analizado diferentes aplicaciones clínicas de la OCT con el objetivo de aumentar el conocimiento sobre las mismas. No obstante, esta tesis plantea nuevos campos de estudio experimental y computacional que pueden ser abordados en futuros trabajos:

- El estudio de los procesos biológicos que subyacen al daño del sistema nervioso central inducido por la esclerosis múltiple utilizando mayores cantidades de datos.
- La validación de nuestros modelos en otras poblaciones para demostrar su utilidad y confirmar la validez del espesor de la capa de fibras nerviosas de la retina como biomarcador fiable tanto para el diagnóstico como para el pronóstico de la esclerosis múltiple.

- La incorporación de estos modelos matemáticos en dispositivos OCT para obtener directamente el diagnóstico y pronóstico de la enfermedad, reduciendo los tiempos de espera.
- La validación de la intensidad de la señal vítrea, obtenida a partir de imágenes OCT, como biomarcador para su uso en el seguimiento terapéutico y en la monitorización o rastreo de formulaciones intravítreas.

Bibliography

[1] B. Abadia, I. Suñen, P. Calvo, F. Bartol, G. Verdes, and A. Ferreras. Choroidal thickness measured using swept-source optical coherence tomography is reduced in patients with type 2 diabetes. *PLoS ONE*, 13(2):1–11, 2018.

[2] R. Alonso, D. Gonzalez-Moron, and O. Garcea. Optical coherence tomography as a biomarker of neurodegeneration in multiple sclerosis: A review. *Multiple Sclerosis and Related Disorders*, 22:77–82, may 2018.

[3] S. Aumann, S. Donner, J. Fischer, and F. Müller. Optical Coherence Tomography (OCT): Principle and Technical Realization. In *High Resolution Imaging in Microscopy and Ophthalmology*, pages 59–85. Springer International Publishing, Cham, 2019.

[4] R. L. Avery, D. J. Pieramici, M. D. Rabena, A. A. Castellarin, M. A. Nasir, and M. J. Giust. Intravitreal Bevacizumab (Avastin) for Neovascular Age-Related Macular Degeneration. *Ophthalmology*, 113(3):363–372, mar 2006.

[5] L. J. Balk, A. Cruz-Herranz, P. Albrecht, S. Arnow, J. M. Gelfand, P. Tewarie, J. Killestein, B. M. Uitdehaag, A. Petzold, and A. J. Green. Timing of retinal neuronal and axonal loss in MS: a longitudinal OCT study. *Journal of Neurology*, 263(7):1323–1331, 2016.

[6] F. Behar-Cohen, E. Gelizé, L. Jonet, and P. Lassiaz. Anatomie de la rétine. *médecine/sciences*, 36(6-7):594–599, jun 2020.

[7] B. Bengtsson, M. C. Leske, L. Hyman, and A. Heijl. Fluctuation of Intraocular Pressure and Glaucoma Progression in the Early Manifest Glaucoma Trial. *Ophthalmology*, 114(2):205–209, 2007.

[8] V. M. Beutgen, N. Perumal, N. Pfeiffer, and F. H. Grus. Autoantibody biomarker discovery in primary open angle glaucoma using serological proteome analysis (SERPA). *Frontiers in Immunology*, 10(MAR), 2019.

[9] C. M. Bishop, P. Bishop, G. Hinton, and O. U. Press. *Neural Networks for Pattern Recognition.* Advanced Texts in Econometrics. Clarendon Press, 1995.

[10] R. Bisht, A. Mandal, J. K. Jaiswal, and I. D. Rupenthal. Nanocarrier mediated retinal drug delivery: overcoming ocular barriers to treat posterior eye diseases. *Wiley Interdisciplinary Reviews: Nanomedicine and Nanobiotechnology*, 10(2):1–21, 2018.

[11] A. Bitsch and W. Brück. Differentiation of Multiple Sclerosis Subtypes. *CNS Drugs*, 16(6):405–418, 2002.

[12] A. Bosco, C. O. Romero, K. T. Breen, A. A. Chagovetz, M. R. Steele, B. K. Ambati, and M. L. Vetter. Neurodegeneration severity can be predicted from early microglia alterations monitored in vivo in a mouse model of chronic glaucoma. *DMM Disease Models and Mechanisms*, 8(5):443–455, 2015.

[13] C. Bowd, K. Chan, L. M. Zangwill, M. H. Goldbaum, T. W. Lee, T. J. Sejnowski, and R. N. Weinreb. Comparing neural networks and linear discriminant functions for glaucoma detection using confocal scanning laser ophthalmoscopy of the optic disc. *Investigative Ophthalmology and Visual Science*, 43(11):3444–3454, 2002.

[14] A. U. Brandt, E. H. Martinez-Lapiscina, R. Nolan, and S. Saidha. Monitoring the Course of MS With Optical Coherence Tomography. *Current Treatment Options in Neurology*, 19(4):15, apr 2017.

[15] G. Bsteh, K. Berek, H. Hegen, P. Altmann, S. Wurth, M. Auer, A. Zinganell, F. Di Pauli, P. Rommer, F. Leutmezer, F. Deisenhammer, and T. Berger. Macular ganglion cell–inner plexiform layer thinning as a biomarker of disability progression in relapsing multiple sclerosis. *Multiple Sclerosis Journal*, (July), 2020.

[16] G. Bsteh, H. Hegen, B. Teuchner, M. Amprosi, K. Berek, F. Ladstätter, S. Wurth, M. Auer, F. Di Pauli, F. Deisenhammer, and T. Berger. Peripapillary retinal nerve fibre layer as measured by optical coherence tomography is a prognostic biomarker not only for physical but also for cognitive disability progression in multiple sclerosis. *Multiple Sclerosis Journal*, 25(2):196–203, feb 2019.

[17] G. Bsteh, H. Hegen, B. Teuchner, K. Berek, S. Wurth, M. Auer, F. Di Pauli, F. Deisenhammer, and T. Berger. Peripapillary retinal nerve fibre layer

thinning rate as a biomarker discriminating stable and progressing relapsing–remitting multiple sclerosis. *European Journal of Neurology*, 26(6):865–871, 2019.

[18] C. Cavaliere, E. Vilades, M. Alonso-Rodríguez, M. Rodrigo, L. Pablo, J. Miguel, E. López-Guillén, E. Morla, L. Boquete, and E. Garcia-Martin. Computer-Aided Diagnosis of Multiple Sclerosis Using a Support Vector Machine and Optical Coherence Tomography Features. *Sensors*, 19(23):5323, dec 2019.

[19] E. W. E. Chan, X. Li, Y. C. Tham, J. Liao, T. Y. Wong, T. Aung, and C. Y. Cheng. Glaucoma in Asia: Regional prevalence variations and future projections. *British Journal of Ophthalmology*, 100(1):78–85, 2016.

[20] B. Chang, R. S. Smith, N. L. Hawes, M. G. Anderson, A. Zabaleta, O. Savinova, T. H. Roderick, J. R. Heckenlively, M. T. Davisson, and S. W. John. Interacting loci cause severe iris atrophy and glaucoma in DBA/2J mice. *Nature Genetics*, 21(4):405–409, 1999.

[21] P. C. Cheeseman, M. Self, J. Kelly, W. Taylor, D. Freeman, and J. C. Stutz. Bayesian Classification. In *Proceedings of the 7th National Conference on Artificial Intelligence, St. Paul, MN, USA, August 21-26, 1988.*, pages 607–611, 1988.

[22] H. Chen, K. S. Cho, T. H. Vu, C. H. Shen, M. Kaur, G. Chen, R. Mathew, M. L. McHam, A. Fazelat, K. Lashkari, N. P. B. Au, J. K. Y. Tse, Y. Li, H. Yu, L. Yang, J. Stein-Streilein, C. H. E. Ma, C. J. Woolf, M. T. Whary, M. J. Jager, J. G. Fox, J. Chen, and D. F. Chen. Commensal microflora-induced T cell responses mediate progressive neurodegeneration in glaucoma. *Nature Communications*, 9(1), 2018.

[23] X. Chen, L. Zhang, E. H. Sohn, K. Lee, M. Niemeijer, J. Chen, M. Sonka, and M. D. Abràmoff. Quantification of external limiting membrane disruption caused by diabetic macular edema from SD-OCT. *Investigative Ophthalmology and Visual Science*, 53(13):8042–8048, 2012.

[24] J. W. Cheng, S. W. Cheng, X. Y. Ma, J. P. Cai, Y. Li, and R. L. Wei. The prevalence of primary glaucoma in mainland China: A systematic review and meta-analysis. *Journal of Glaucoma*, 22(4):301–306, 2013.

[25] T. Chitnis, B. Glanz, S. Jaffin, and B. Healy. Demographics of pediatric-onset multiple sclerosis in an MS center population from the Northeastern United States. *Multiple Sclerosis*, 15(5):627–631, 2009.

[26] N. Choudhry, J. S. Duker, K. B. Freund, S. Kiss, G. Querques, R. Rosen, D. Sarraf, E. H. Souied, P. E. Stanga, G. Staurenghi, and S. V. R. Sadda. Classification and Guidelines for Widefield Imaging: Recommendations from the International Widefield Imaging Study Group. *Ophthalmology Retina*, 3(10):843–849, 2019.

[27] A. Choudhury and D. Gupta. *A Survey on Medical Diagnosis of Diabetes Using Machine Learning Techniques*, volume 740. Springer Singapore, 2019.

[28] F. Costello and J. Burton. Retinal imaging with optical coherence tomography: a biomarker in multiple sclerosis? *Eye and Brain*, Volume 10:47–63, jul 2018.

[29] M. Curcio and F. Bradke. Axon Regeneration in the Central Nervous System: Facing the Challenges from the Inside. *Annual Review of Cell and Developmental Biology*, 34(1):495–521, oct 2018.

[30] A. C. Day, G. Baio, G. Gazzard, C. Bunce, A. Azuara-Blanco, B. Munoz, D. S. Friedman, and P. J. Foster. The prevalence of primary angle closure glaucoma in European derived populations: A systematic review. *British Journal of Ophthalmology*, 96(9):1162–1167, 2012.

[31] E. De Brouwer, T. Becker, Y. Moreau, E. K. Havrdova, M. Trojano, S. Eichau, S. Ozakbas, M. Onofrj, P. Grammond, J. Kuhle, L. Kappos, P. Sola, E. Cartechini, J. Lechner-Scott, R. Alroughani, O. Gerlach, T. Kalincik, F. Granella, F. Grand'Maison, R. Bergamaschi, M. José Sá, B. Van Wijmeersch, A. Soysal, J. L. Sanchez-Menoyo, C. Solaro, C. Boz, G. Iuliano, K. Buzzard, E. Aguera-Morales, M. Terzi, T. C. Trivio, D. Spitaleri, V. Van Pesch, V. Shaygannejad, F. Moore, C. Oreja-Guevara, D. Maimone, R. Gouider, T. Csepany, C. Ramo-Tello, and L. Peeters. Longitudinal machine learning modeling of MS patient trajectories improves predictions of disability progression. *Computer Methods and Programs in Biomedicine*, 208:106180, 2021.

[32] A. Dey, A. L. Manthey, K. Chiu, and C. W. Do. Methods to Induce Chronic Ocular Hypertension: Reliable Rodent Models as a Platform for Cell Transplantation and Other Therapies. *Cell Transplantation*, 27(2):213–229, 2018.

[33] A. Eshaghi, A. L. Young, P. A. Wijeratne, F. Prados, D. L. Arnold, S. Narayanan, C. R. Guttmann, F. Barkhof, D. C. Alexander, A. J. Thompson, D. Chard, and O. Ciccarelli. Identifying multiple sclerosis subtypes using unsupervised machine learning and MRI data. *Nature Communications*, 12(1):1–12, 2021.

[34] F. Eslami, M. Ghiasian, E. Khanlarzade, and E. Moradi. Retinal nerve fiber layer thickness and total macular volume in multiple sclerosis subtypes and their relationship with severity of disease, a cross-sectional study. *Eye and Brain*, 12:15–23, 2020.

[35] C. Evans, S. G. Beland, S. Kulaga, C. Wolfson, E. Kingwell, J. Marriott, M. Koch, N. Makhani, S. Morrow, J. Fisk, J. Dykeman, N. Jetté, T. Pringsheim, and R. A. Marrie. Incidence and prevalence of multiple sclerosis in the americas: A systematic review. *Neuroepidemiology*, 40(3):195–210, 2013.

[36] L. Feiner and J. R. Piltz-Seymour. Collaborative initial Glaucoma Treatment Study: A summary of results to date. *Current Opinion in Ophthalmology*, 14(2):106–111, 2003.

[37] B. Ferguson, M. K. Matyszak, M. M. Esiri, and V. H. Perry. Axonal damage in acute multiple sclerosis lesions. *Brain : a journal of neurology*, 120(3):393–399, mar 1997.

[38] J. Fernandez de Canete, S. Gonzalez-Perez, and J. C. Ramos-Diaz. Artificial neural networks for closed loop control of in silico and ad hoc type 1 diabetes. *Computer Methods and Programs in Biomedicine*, 106(1):55–66, 2012.

[39] A. Fernández-Ferreiro, A. Luaces-Rodríguez, P. Aguiar, J. Pardo-Montero, M. González-Barcia, L. García-Varela, M. Herranz, J. Silva-Rodríguez, M. Gil-Martínez, M. A. Bermúdez, A. Vieites-Prado, J. Blanco-Méndez, M. J. Lamas, F. Gómez-Ulla, A. Ruibal, F. J. Otero-Espinar, and F. González. Preclinical PET study of intravitreal injections. *Investigative Ophthalmology and Visual Science*, 58(7):2843–2851, 2017.

[40] M. A. Fields, L. V. Del Priore, R. A. Adelman, and L. J. Rizzolo. Interactions of the choroid, Bruch's membrane, retinal pigment epithelium, and neurosensory retina collaborate to form the outer blood-retinal-barrier. *Progress in Retinal and Eye Research*, 76(March):100803, 2020.

[41] J. M. Frischer, S. D. Weigand, Y. Guo, N. Kale, J. E. Parisi, I. Pirko, J. Mandrekar, S. Bramow, I. Metz, W. Brück, H. Lassmann, and C. F. Lucchinetti.

Clinical and pathological insights into the dynamic nature of the white matter multiple sclerosis plaque. *Annals of Neurology*, 78(5):710–721, 2015.

[42] Y. Fu, T. M. Talavage, and J.-X. Cheng. New imaging techniques in the diagnosis of multiple sclerosis. *Expert opinion on medical diagnostics*, 2(9):1055–1065, sep 2008.

[43] R. L. Furlanetto, S. H. Teixeira, C. P. B. Gracitelli, C. L. Lottenberg, F. Emori, M. Michelan, E. Amaro, and A. Paranhos. Structural and functional analyses of the optic nerve and lateral geniculate nucleus in glaucoma. *PLOS ONE*, 13(3):e0194038, mar 2018.

[44] D. Garcia-Herranz, M. J. Rodrigo, M. Subias, T. Martinez-Rincon, S. Mendez-Martinez, I. Bravo-Osuna, A. Bonet, J. Ruberte, J. Garcia-Feijoo, L. Pablo, E. Garcia-Martin, and R. Herrero-Vanrell. Novel Use of PLGA Microspheres to Create an Animal Model of Glaucoma with Progressive Neuroretinal Degeneration. *Pharmaceutics*, 13(2):237, feb 2021.

[45] E. Garcia-Martin, J. R. Ara, J. Martin, C. Almarcegui, I. Dolz, E. Vilades, L. Gil-Arribas, F. J. Fernandez, V. Polo, J. M. Larrosa, L. E. Pablo, and M. Satue. Retinal and Optic Nerve Degeneration in Patients with Multiple Sclerosis Followed up for 5 Years. *Ophthalmology*, 124(5):688–696, 2017.

[46] E. Garcia-Martin, R. Herrero, M. P. Bambo, J. R. Ara, J. Martin, V. Polo, J. M. Larrosa, J. Garcia-Feijoo, and L. E. Pablo. Artificial neural network techniques to improve the ability of optical coherence tomography to detect optic neuritis. *Seminars in Ophthalmology*, 30(1):11–19, 2015.

[47] E. Garcia-Martin, M. Ortiz, L. Boquete, E. M. Sánchez-Morla, R. Barea, C. Cavaliere, E. Vilades, E. Orduna, and M. J. Rodrigo. Early diagnosis of multiple sclerosis by OCT analysis using Cohen's d method and a neural network as classifier. *Computers in Biology and Medicine*, 129(November 2020):104165, 2021.

[48] E. Garcia-Martin, L. E. Pablo, R. Herrero, J. R. Ara, J. Martin, J. M. Larrosa, V. Polo, J. Garcia-Feijoo, and J. Fernandez. Neural networks to identify multiple sclerosis with optical coherence tomography. *Acta Ophthalmologica*, 91(8):e628–e634, dec 2013.

[49] E. Garcia-Martin, V. Polo, J. M. Larrosa, M. L. Marques, R. Herrero, J. Martin, J. R. Ara, J. Fernandez, and L. E. Pablo. Retinal Layer Segmentation

in Patients with Multiple Sclerosis Using Spectral Domain Optical Coherence Tomography. *Ophthalmology*, 121(2):573–579, feb 2014.

[50] E. Garcia-Martin, D. Rodriguez-Mena, R. Herrero, C. Almarcegui, I. Dolz, J. Martin, J. R. Ara, J. M. Larrosa, V. Polo, J. Fernández, and L. E. Pablo. Neuro-ophthalmologic evaluation, quality of life, and functional disability in patients with MS. *Neurology*, 81(1):76–83, 2013.

[51] R. Gelman, W. Stevenson, C. Prospero Ponce, D. Agarwal, and J. B. Christoforidis. Retinal Damage Induced by Internal Limiting Membrane Removal. *Journal of Ophthalmology*, 2015:1–10, 2015.

[52] O. Geyer and Y. Levo. Glaucoma is an autoimmune disease. *Autoimmunity Reviews*, 19(6):102535, 2020.

[53] G. Giovannoni, G. Cutter, M. Pia-Sormani, S. Belachew, R. Hyde, H. Koendgen, V. Knappertz, D. Tomic, D. Leppert, R. Herndon, C. A. Wheeler-Kingshott, O. Ciccarelli, D. Selwood, E. V. di Cantogno, A. F. Ben-Amor, P. Matthews, D. Carassiti, D. Baker, and K. Schmierer. Is multiple sclerosis a length-dependent central axonopathy? The case for therapeutic lag and the asynchronous progressive MS hypotheses. *Multiple Sclerosis and Related Disorders*, 12(January):70–78, 2017.

[54] O. W. Gramlich, J. Teister, M. Neumann, X. Tao, S. Beck, H. D. von Pein, N. Pfeiffer, and F. H. Grus. Immune response after intermittent minimally invasive intraocular pressure elevations in an experimental animal model of glaucoma. *Journal of Neuroinflammation*, 13(1), 2016.

[55] S. Grover, R. K. Murthy, V. S. Brar, and K. V. Chalam. Normative Data for Macular Thickness by High-Definition Spectral-Domain Optical Coherence Tomography (Spectralis). *American Journal of Ophthalmology*, 148(2):266–271, 2009.

[56] J. D. Haines, M. Inglese, and P. Casaccia. Axonal Damage in Multiple Sclerosis. *Mount Sinai Journal of Medicine: A Journal of Translational and Personalized Medicine*, 78(2):231–243, mar 2011.

[57] T. Hastie, R. Tibshirani, and J. Friedman. *The Elements of Statistical Learning*. Springer Series in Statistics. Springer New York, New York, NY, 2009.

[58] M. J. Hogan. Histology of the human eye. *An atlas and textbook*, 1971.

[59] P. M. Hughes, O. Olejnik, J. E. Chang-Lin, and C. G. Wilson. Topical and systemic drug delivery to the posterior segments. *Advanced Drug Delivery Reviews*, 57(14 SPEC. ISS.):2010–2032, 2005.

[60] M. M. Islam, H. Iqbal, M. R. Haque, and M. K. Hasan. Prediction of breast cancer using support vector machine and K-Nearest neighbors. *5th IEEE Region 10 Humanitarian Technology Conference 2017, R10-HTC 2017*, 2018-Janua:226–229, 2018.

[61] I. Jankowska-Lech, J. Wasyluk, W. Palasik, B. Terelak-Borys, and I. Grabska-Liberek. Peripapillary retinal nerve fiber layer thickness measured by optical coherence tomography in different clinical subtypes of multiple sclerosis. *Multiple Sclerosis and Related Disorders*, 27(November 2018):260–268, 2019.

[62] J. B. Jonas, T. Aung, R. R. Bourne, A. M. Bron, R. Ritch, and S. Panda-Jonas. Glaucoma. *The Lancet*, 390(10108):2183–2193, 2017.

[63] J. B. Jonas and A. Dichtl. Evaluation of the retinal nerve fiber layer. *Survey of Ophthalmology*, 40(5):369–378, 1996.

[64] T. Kalincik, G. Cutter, T. Spelman, V. Jokubaitis, E. Havrdova, D. Horakova, M. Trojano, G. Izquierdo, M. Girard, P. Duquette, A. Prat, A. Lugaresi, F. Grand'Maison, P. Grammond, R. Hupperts, C. Oreja-Guevara, C. Boz, E. Pucci, R. Bergamaschi, J. Lechner-Scott, R. Alroughani, V. Van Pesch, G. Iuliano, R. Fernandez-Bolaños, C. Ramo, M. Terzi, M. Slee, D. Spitaleri, F. Verheul, E. Cristiano, J. L. Sánchez-Menoyo, M. Fiol, O. Gray, J. A. Cabrera-Gomez, M. Barnett, and H. Butzkueven. Defining reliable disability outcomes in multiple sclerosis. *Brain*, 138(11):3287–3298, 2015.

[65] V. V. Kapetanakis, M. P. Chan, P. J. Foster, D. G. Cook, C. G. Owen, and A. R. Rudnicka. Global variations and time trends in the prevalence of primary open angle glaucoma (POAG): A systematic review and meta-analysis. *British Journal of Ophthalmology*, 100(1):86–93, 2016.

[66] M. A. Kass. The Ocular Hypertension Treatment Study. *Archives of Ophthalmology*, 120(6):701, jun 2002.

[67] R. Kaur, Z. Chen, R. Motl, M. E. Hernandez, and R. Sowers. Predicting Multiple Sclerosis from Gait Dynamics Using an Instrumented Treadmill: A Machine Learning Approach. *IEEE Transactions on Biomedical Engineering*, 68(9):2666–2677, 2021.

[68] P. A. Keane, M. Karampelas, D. A. Sim, S. R. Sadda, A. Tufail, H. N. Sen, R. B. Nussenblatt, A. D. Dick, R. W. Lee, P. I. Murray, C. E. Pavesio, and A. K. Denniston. Objective Measurement of Vitreous Inflammation Using Optical Coherence Tomography. *Ophthalmology*, 121(9):1706–1714, sep 2014.

[69] D. F. Kiernan, W. F. Mieler, and S. M. Hariprasad. Spectral-Domain Optical Coherence Tomography: A Comparison of Modern High-Resolution Retinal Imaging Systems. *American Journal of Ophthalmology*, 149(1):18–31.e2, 2010.

[70] K. E. Kim, I. Jang, H. Moon, Y. J. Kim, J. W. Jeoung, K. H. Park, and H. Kim. Neuroprotective effects of human serum albumin nanoparticles loaded with brimonidine on retinal ganglion cells in optic nerve crush model. *Investigative Ophthalmology and Visual Science*, 56(9):5641–5649, 2015.

[71] S. Kishi. Impact of swept source optical coherence tomography on ophthalmology. *Taiwan Journal of Ophthalmology*, 6(2):58–68, 2016.

[72] H. Kolb. Organization of the outer plexiform layer of the primate retina: electron microscopy of Golgi-impregnated cells. *Philosophical transactions of the Royal Society of London. Series B, Biological sciences*, 258(823):261–283, may 1970.

[73] H. Kolb, K. A. Linberg, and S. K. Fisher. Neurons of the human retina: A Golgi study. *Journal of Comparative Neurology*, 318(2):147–187, 1992.

[74] E. Korot, G. Comer, T. Steffens, and D. A. Antonetti. Algorithm for the measure of vitreous hyperreflective foci in optical coherence tomographic scans of patients with diabetic macular edema. *JAMA Ophthalmology*, 134(1):15–20, 2016.

[75] E. Kotelnikova, N. A. Kiani, E. Abad, E. H. Martinez-Lapiscina, M. Andorra, I. Zubizarreta, I. Pulido-Valdeolivas, I. Pertsovskaya, L. G. Alexopoulos, T. Olsson, R. Martin, F. Paul, J. Tegnér, J. Garcia-Ojalvo, and P. Villoslada. Dynamics and heterogeneity of brain damage in multiple sclerosis. *PLOS Computational Biology*, 13(10):e1005757, 2017.

[76] C. Kozlowski and R. M. Weimer. An automated method to quantify microglia morphology and application to monitor activation state longitudinally in vivo. *PLoS ONE*, 7(2):1–9, 2012.

[77] M. Kuhn and K. Johnson. *Applied Predictive Modeling.* Springer New York, New York, NY, 2013.

[78] A. Kumar, S. V. Sehra, M. B. Thirumalesh, and V. Gogia. Secondary rhegmatogenous retinal detachment following intravitreal bevacizumab in patients with vitreous hemorrhage or tractional retinal detachment secondary to Eales' disease. *Graefe's Archive for Clinical and Experimental Ophthalmology*, 250(5):685–690, 2012.

[79] A. Kutzelnigg and H. Lassmann. Pathology of multiple sclerosis and related inflammatory demyelinating diseases. In *Handbook of Clinical Neurology*, volume 122, pages 15–58. Elsevier B.V., 1 edition, 2014.

[80] M. la Cour and B. Ehinger. The Retina. In J. Fischbarg, editor, *The Biology of the Eye*, volume 10 of *Advances in Organ Biology*, pages 195–252. Elsevier, 2005.

[81] J. Lambe, K. C. Fitzgerald, O. C. Murphy, A. G. Filippatou, E. S. Sotirchos, G. Kalaitzidis, E. Vasileiou, N. Pellegrini, E. Ogbuokiri, B. Toliver, N. J. Luciano, S. Davis, N. Fioravante, O. Kwakyi, H. Risher, C. M. Crainiceanu, J. L. Prince, S. D. Newsome, E. M. Mowry, S. Saidha, and P. A. Calabresi. Association of Spectral-Domain OCT With Long-term Disability Worsening in Multiple Sclerosis. *Neurology*, 96(16):e2058 LP – e2069, apr 2021.

[82] J. Lambe, O. C. Murphy, and S. Saidha. Can Optical Coherence Tomography Be Used to Guide Treatment Decisions in Adult or Pediatric Multiple Sclerosis? *Current Treatment Options in Neurology*, 20(4):9, apr 2018.

[83] W. S. Lambert, B. J. Carlson, A. E. Van der Ende, G. Shih, J. N. Dobish, D. J. Calkins, and E. Harth. Nanosponge-mediated drug delivery lowers intraocular pressure. *Translational Vision Science and Technology*, 4(1):1–16, 2015.

[84] S. J. Langenegger, J. Funk, and M. Töteberg-Harms. Reproducibility of retinal nerve fiber layer thickness measurements using the eye tracker and the retest function of spectralis SD-OCT in glaucomatous and healthy control eyes. *Investigative Ophthalmology and Visual Science*, 52(6):3338–3344, 2011.

[85] R. Lapasin, M. Abrami, M. Grassi, and U. Šebenik. Rheology of Laponite-scleroglucan hydrogels. *Carbohydrate Polymers*, 168:290–300, 2017.

[86] L. I. Lau, C. J. L. Liu, J. C. K. Chou, W. M. Hsu, and J. H. Liu. Patterns of visual field defects in chronic angle-closure glaucoma with different disease severity. *Ophthalmology*, 110(10):1890–1894, 2003.

[87] F. Lavinsky and D. Lavinsky. Novel perspectives on swept-source optical coherence tomography. *International Journal of Retina and Vitreous*, 2(1):1–11, 2016.

[88] M. T. Law, A. L. Traboulsee, D. K. Li, R. L. Carruthers, M. S. Freedman, S. H. Kolind, and R. Tam. Machine learning in secondary progressive multiple sclerosis: an improved predictive model for short-term disability progression. *Multiple Sclerosis Journal - Experimental, Translational and Clinical*, 5(4), 2019.

[89] M. Lawlor, H. Danesh-Meyer, L. A. Levin, I. Davagnanam, E. De Vita, and G. T. Plant. Glaucoma and the brain: Trans-synaptic degeneration, structural change, and implications for neuroprotection. *Survey of Ophthalmology*, 63(3):296–306, may 2018.

[90] J. Y. Lee, H. J. Jeong, J. H. Lee, Y. J. Kim, E. Y. Kim, Y. Y. Kim, T. Ryu, Z.-H. Cho, and Y.-B. Kim. An Investigation of Lateral Geniculate Nucleus Volume in Patients With Primary Open-Angle Glaucoma Using 7 Tesla Magnetic Resonance Imaging. *Investigative Opthalmology & Visual Science*, 55(6):3468, jun 2014.

[91] E. Leray, J. Yaouanq, E. Le Page, M. Coustans, D. Laplaud, J. Oger, and G. Edan. Evidence for a two-stage disability progression in multiple sclerosis. *Brain*, 133(7):1900–1913, jul 2010.

[92] C. K. Leung, S. Lam, R. N. Weinreb, S. Liu, C. Ye, L. Liu, J. He, G. W. Lai, T. Li, and D. S. Lam. Retinal nerve fiber layer imaging with spectral-domain optical coherence tomography: Analysis of the retinal nerve fiber layer map for glaucoma detection. *Ophthalmology*, 117(9):1684–1691, 2010.

[93] S. K. Li, M. J. Lizak, and E.-K. Jeong. MRI in ocular drug delivery. *NMR in Biomedicine*, 21(9):941–956, 2008.

[94] H. Liu and V. Prokosch. Energy metabolism in the inner retina in health and glaucoma. *International Journal of Molecular Sciences*, 22(7), 2021.

[95] C. Louapre and C. Lubetzki. Neurodegeneration in multiple sclerosis is a process separate from inflammation: Yes. *Multiple Sclerosis Journal*, 21(13):1626–1628, 2015.

[96] F. D. Lublin, S. C. Reingold, J. a. Cohen, G. R. Cutter, P. S. Sorensen, A. J. Thompson, J. S. Wolinsky, L. J. Balcer, B. Banwell, F. Barkhof, B. Bebo, P. A.

Calabresi, M. Clanet, G. Comi, R. J. Fox, M. S. Freedman, A. D. Goodman, M. Inglese, L. Kappos, B. C. Kieseier, J. A. Lincoln, C. Lubetzki, A. E. Miller, X. Montalban, P. W. O'Connor, J. Petkau, C. Pozzilli, R. A. Rudick, M. P. Sormani, O. Stuve, E. Waubant, and C. H. Polman. Defining the clinical course of multiple sclerosis: The 2013 revisions. *Neurology*, 83(3):278–286, jul 2014.

[97] R. Mancino, A. Martucci, M. Cesareo, C. Giannini, M. T. Corasaniti, G. Bagetta, and C. Nucci. Glaucoma and Alzheimer Disease: One Age-Related Neurodegenerative Disease of the Brain. *Current Neuropharmacology*, 16(7):971–977, jul 2018.

[98] R. E. Marc. Functional Neuroanatomy of the Retina. *City*, 28(2):979–522, 2009.

[99] R. A. Masri, F. Weltzien, S. Purushothuman, S. C. Lee, P. R. Martin, and U. Grünert. Composition of the inner nuclear layer in human retina. *Investigative Ophthalmology and Visual Science*, 62(9), 2021.

[100] A. Mathur and G. M. Foody. Multiclass and binary SVM classification: Implications for training and classification users. *IEEE Geoscience and Remote Sensing Letters*, 5(2):241–245, 2008.

[101] J. Matlach, S. Bender, J. König, H. Binder, N. Pfeiffer, and E. M. Hoffmann. Investigation of intraocular pressure fluctuation as a risk factor of glaucoma progression. *Clinical Ophthalmology*, 13:9–16, 2019.

[102] S. Meyer-Moock, Y.-S. Feng, M. Maeurer, F.-W. Dippel, and T. Kohlmann. Systematic literature review and validity evaluation of the Expanded Disability Status Scale (EDSS) and the Multiple Sclerosis Functional Composite (MSFC) in patients with multiple sclerosis. *BMC neurology*, 14(1):58, mar 2014.

[103] J. E. Morgan and J. R. Tribble. Microbead models in glaucoma. *Experimental Eye Research*, 141:9–14, 2015.

[104] J. C. MORRISON, C. G. MOORE, L. M. H. DEPPMEIER, B. G. GOLD, C. K. MESHUL, and E. C. JOHNSON. A Rat Model of Chronic Pressure-induced Optic Nerve Damage. *Experimental Eye Research*, 64(1):85–96, 1997.

[105] A. H. Neufeld. Nitric oxide: A potential mediator of retinal ganglion cell damage in glaucoma. *Survey of Ophthalmology*, 43(6 SUPPL.):129–135, 1999.

[106] S. Nizari, L. Guo, B. M. Davis, E. M. Normando, J. Galvao, L. A. Turner, M. Bizrah, M. Dehabadi, K. Tian, and M. F. Cordeiro. Non-amyloidogenic effects of $\alpha 2$ adrenergic agonists: Implications for brimonidine-mediated neuroprotection, 2016.

[107] R. B. Nussenblatt, B. Liu, L. Wei, and H. N. Sen. The immunological basis of degenerative diseases of the eye. *International Reviews of Immunology*, 32(1):97–112, 2013.

[108] K. T. Özbilen, T. Gündüz, S. N. Çukurova Kartal, A. C. Gedik, M. Eraksoy, and M. Kürtüncü. Bruch's membrane opening-minimum rim width: An alternative OCT biomarker study for multiple sclerosis. *European Journal of Ophthalmology*, 2021.

[109] V. Parisi, G. Manni, M. Spadaro, G. Colacino, R. Restuccia, S. Marchi, M. G. Bucci, and F. Pierelli. Correlation between morphological and functional retinal impairment in multiple sclerosis patients. *Investigative Ophthalmology and Visual Science*, 40(11):2520–2527, 1999.

[110] S. Pershing, S. J. Bakri, and D. M. Moshfeghi. Ocular hypertension and intraocular pressure asymmetry after intravitreal injection of anti-vascular endothelial growth factor agents. *Ophthalmic surgery, lasers & imaging retina*, 44(5):460–464, 2013.

[111] A. Petzold, L. J. Balcer, P. A. Calabresi, F. Costello, T. C. Frohman, E. M. Frohman, E. H. Martinez-Lapiscina, A. J. Green, R. Kardon, O. Outteryck, F. Paul, S. Schippling, P. Vermersch, P. Villoslada, L. J. Balk, and ERN-EYE IMSVISUAL. Retinal layer segmentation in multiple sclerosis: a systematic review and meta-analysis. *The Lancet. Neurology*, 16(10):797–812, 2017.

[112] A. Petzold, J. F. de Boer, S. Schippling, P. Vermersch, R. Kardon, A. Green, P. A. Calabresi, and C. Polman. Optical coherence tomography in multiple sclerosis: A systematic review and meta-analysis. *The Lancet Neurology*, 9(9):921–932, 2010.

[113] M. F. Pinto, H. Oliveira, S. Batista, L. Cruz, M. Pinto, I. Correia, P. Martins, and C. Teixeira. Prediction of disease progression and outcomes in multiple sclerosis with machine learning. *Scientific Reports*, 10(1):1–13, 2020.

[114] M. Pisa, S. Guerrieri, G. Di Maggio, S. Medaglini, L. Moiola, V. Martinelli, G. Comi, and L. Leocani. No evidence of disease activity is associated with

reduced rate of axonal retinal atrophy in MS. *Neurology*, 89(24):2469–2475, dec 2017.

[115] C. H. Polman, S. C. Reingold, B. Banwell, M. Clanet, J. A. Cohen, M. Filippi, K. Fujihara, E. Havrdova, M. Hutchinson, L. Kappos, F. D. Lublin, X. Montalban, P. O'Connor, M. Sandberg-Wollheim, A. J. Thompson, E. Waubant, B. Weinshenker, and J. S. Wolinsky. Diagnostic criteria for multiple sclerosis: 2010 Revisions to the McDonald criteria. *Annals of Neurology*, 69(2):292–302, 2011.

[116] C. H. Polman, S. C. Reingold, G. Edan, M. Filippi, H.-P. Hartung, L. Kappos, F. D. Lublin, L. M. Metz, H. F. McFarland, P. W. O'Connor, M. Sandberg-Wollheim, A. J. Thompson, B. G. Weinshenker, and J. S. Wolinsky. Diagnostic criteria for multiple sclerosis: 2005 revisions to the "McDonald Criteria". *Annals of Neurology*, 58(6):840–846, dec 2005.

[117] F. J. Povedano-Montero, R. N. Weinreb, I. Raga-Martínez, A. Romero, and F. López-Muñoz. Detection of neurological and ophthalmological pathologies with optical coherence tomography using retinal thickness measurements: A bibliometric study. *Applied Sciences (Switzerland)*, 10(16), 2020.

[118] E. Prieto, M. J. Cardiel, E. Vispe, M. Idoipe, E. Garcia-Martin, J. M. Fraile, V. Polo, J. A. Mayoral, L. E. Pablo, and M. J. Rodrigo. Dexamethasone delivery to the ocular posterior segment by sustained-release Laponite formulation. *Biomedical Materials (Bristol)*, 15(6), 2020.

[119] E. Prieto, E. Vispe, A. De Martino, M. Idoipe, M. J. Rodrigo, E. Garcia-Martin, J. M. Fraile, V. Polo-Llorens, and J. A. Mayoral. Safety study of intravitreal and suprachoroidal Laponite clay in rabbit eyes. *Graefe's Archive for Clinical and Experimental Ophthalmology*, 256(3):535–546, 2018.

[120] H. Quigley and A. T. Broman. The number of people with glaucoma worldwide in 2010 and 2020. *British Journal of Ophthalmology*, 90(3):262–267, 2006.

[121] J. M. Ramírez, A. Triviño, A. I. Ramírez, J. J. Salazar, and J. García-Sanchez. Structural specializations of human retinal glial cells. *Vision Research*, 36(14):2029–2036, 1996.

[122] J. N. Ratchford, S. Saidha, E. S. Sotirchos, J. A. Oh, M. A. Seigo, C. Eckstein, M. K. Durbin, J. D. Oakley, S. A. Meyer, A. Conger, T. C. Frohman, S. D. Newsome, L. J. Balcer, E. M. Frohman, and P. A. Calabresi. Active

MS is associated with accelerated retinal ganglion cell/inner plexiform layer thinning. *Neurology*, 80(1):47–54, 2013.

[123] A. S. Reis, N. O'Leary, H. Yang, G. P. Sharpe, M. T. Nicolela, C. F. Burgoyne, and B. C. Chauhan. Influence of clinically invisible, but optical coherence tomography detected, optic disc margin anatomy on neuroretinal rim evaluation. *Investigative ophthalmology & visual science*, 53(4):1852–1860, 2012.

[124] M. A. Rocca, N. Anzalone, L. Storelli, A. Del Poggio, L. Cacciaguerra, A. A. Manfredi, A. Meani, and M. Filippi. Deep Learning on Conventional Magnetic Resonance Imaging Improves the Diagnosis of Multiple Sclerosis Mimics. *Investigative Radiology*, 56(4), 2021.

[125] M. J. Rodrigo, M. J. Cardiel, J. M. Fraile, S. Mendez-Martinez, T. Martinez-Rincon, M. Subias, V. Polo, J. Ruberte, T. Ramirez, E. Vispe, C. Luna, J. A. Mayoral, and E. Garcia-Martin. Brimonidine-LAPONITE® intravitreal formulation has an ocular hypotensive and neuroprotective effect throughout 6 months of follow-up in a glaucoma animal model. *Biomaterials Science*, 2020.

[126] M. J. Rodrigo, T. Martinez-Rincon, M. Subias, S. Mendez-Martinez, L. E. Pablo, V. Polo, A. Aragon-Navas, D. Garcia-Herranz, J. G. Feijoo, I. B. Osuna, R. Herrero-Vanrell, and E. Garcia-Martin. Influence of Sex on Neuroretinal Degeneration: Six-Month Follow-Up in Rats With Chronic Glaucoma. *Investigative ophthalmology & visual science*, 62(13):9, 2021.

[127] A. Rothman, O. C. Murphy, K. C. Fitzgerald, J. Button, E. Gordon-Lipkin, J. N. Ratchford, S. D. Newsome, E. M. Mowry, E. S. Sotirchos, S. B. Syc-Mazurek, J. Nguyen, N. G. Caldito, L. J. Balcer, E. M. Frohman, T. C. Frohman, D. S. Reich, C. Crainiceanu, S. Saidha, and P. A. Calabresi. Retinal measurements predict 10-year disability in multiple sclerosis. *Annals of Clinical and Translational Neurology*, 6(2):222–232, feb 2019.

[128] V. Saccà, A. Sarica, F. Novellino, S. Barone, T. Tallarico, E. Filippelli, A. Granata, C. Chiriaco, R. Bruno Bossio, P. Valentino, and A. Quattrone. Evaluation of machine learning algorithms performance for the prediction of early multiple sclerosis from resting-state FMRI connectivity data. *Brain Imaging and Behavior*, 13(4):1103–1114, 2019.

[129] S. Saidha, O. Al-Louzi, J. N. Ratchford, P. Bhargava, J. Oh, S. D. Newsome, J. L. Prince, D. Pham, S. Roy, P. van Zijl, L. J. Balcer, E. M. Frohman, D. S. Reich, C. Crainiceanu, and P. A. Calabresi. Optical coherence tomography

reflects brain atrophy in multiple sclerosis: A four-year study. *Annals of Neurology*, 78(5):801–813, nov 2015.

[130] L. M. Sakata, J. DeLeon-Ortega, V. Sakata, and C. A. Girkin. Optical coherence tomography of the retina and optic nerve - A review. *Clinical and Experimental Ophthalmology*, 37(1):90–99, 2009.

[131] G. Savini, M. Carbonelli, and P. Barboni. Spectral-domain optical coherence tomography for the diagnosis and follow-up of glaucoma. *Current Opinion in Ophthalmology*, 22(2):115–123, 2011.

[132] C. L. Schlamp, Y. Li, J. A. Dietz, K. T. Janssen, and R. W. Nickells. Progressive ganglion cell loss and optic nerve degeneration in DBA/2J mice is variable and asymmetric. *BMC Neuroscience*, 7:1–14, 2006.

[133] M. A. Schmidt, M. Knott, R. Heidemann, G. Michelson, T. Kober, A. Dörfler, and T. Engelhorn. Investigation of lateral geniculate nucleus volume and diffusion tensor imaging in patients with normal tension glaucoma using 7 tesla magnetic resonance imaging. *PLOS ONE*, 13(6):e0198830, jun 2018.

[134] N. Schurz, L. Sariaslani, P. Altmann, F. Leutmezer, C. Mitsch, B. Pemp, P. Rommer, T. Zrzavy, T. Berger, and G. Bsteh. Evaluation of retinal layer thickness parameters as biomarkers in a real-world multiple sclerosis cohort. *Eye and Brain*, 13:59–69, 2021.

[135] R. Seccia, D. Gammelli, F. Dominici, S. Romano, A. C. Landi, M. Salvetti, A. Tacchella, A. Zaccaria, A. Crisanti, F. Grassi, and L. Palagi. Considering patient clinical history impacts performance of machine learning models in predicting course of multiple sclerosis. *PLoS ONE*, 15(3):1–18, 2020.

[136] R. Seccia, S. Romano, M. Salvetti, A. Crisanti, L. Palagi, and F. Grassi. Machine learning use for prognostic purposes in multiple sclerosis. *Life*, 11(2):1–18, 2021.

[137] J. Sepulcre, M. Murie-Fernandez, A. Salinas-Alaman, A. Garcia-Layana, B. Bejarano, and P. Villoslada. Diagnostic accuracy of retinal abnormalities in predicting disease activity in MS. *Neurology*, 68(18):1488–1494, may 2007.

[138] R. C. Sergott, E. Frohman, R. Glanzman, and A. AL-Sabbagh. The role of optical coherence tomography in multiple sclerosis: Expert panel consensus. *Journal of the Neurological Sciences*, 263(1-2):3–14, 2007.

[139] T. A. M. Siepman, M. W. Bettink-Remeijer, and R. Q. Hintzen. Retinal nerve fiber layer thickness in subgroups of multiple sclerosis, measured by optical coherence tomography and scanning laser polarimetry. *Journal of Neurology*, 257(10):1654–1660, 2010.

[140] R. Simó, C. Hernández, M. Porta, F. Bandello, J. Grauslund, S. P. Harding, S. J. Aldington, C. Egan, U. Frydkjaer-Olsen, J. García-Arumí, J. Gibson, G. E. Lang, R. Lattanzio, P. Massin, E. Midena, B. Ponsati, L. Ribeiro, P. Scanlon, C. Lobo, M. Â. Costa, and J. Cunha-Vaz. Effects of topically administered neuroprotective drugs in early stages of diabetic retinopathy: Results of the EUROCONDOR clinical trial. *Diabetes*, 68(2):457–463, 2019.

[141] N. Snaidero and M. Simons. Myelination at a glance. *Journal of Cell Science*, 127(14):2999–3004, 2014.

[142] S. Sreekantam, T. Macdonald, P. A. Keane, D. A. Sim, P. I. Murray, and A. K. Denniston. Quantitative analysis of vitreous inflammation using optical coherence tomography in patients receiving sub-Tenon's triamcinolone acetonide for uveitic cystoid macular oedema. *British Journal of Ophthalmology*, 101(2):175–179, 2017.

[143] M. C. Staniford, M. M. Lezhnina, M. Gruener, L. Stegemann, R. Kuczius, V. Bleicher, C. A. Strassert, and U. H. Kynast. Photophysical efficiency-boost of aqueous aluminium phthalocyanine by hybrid formation with nano-clays. *Chemical Communications*, 51(70):13534–13537, 2015.

[144] G. Staurenghi, S. Sadda, U. Chakravarthy, and R. F. Spaide. Proposed Lexicon for Anatomic Landmarks in Normal Posterior Segment Spectral-Domain Optical Coherence Tomography. *Ophthalmology*, 121(8):1572–1578, aug 2014.

[145] L. S. Talman, E. R. Bisker, D. J. Sackel, D. A. Long, K. M. Galetta, J. N. Ratchford, D. J. Lile, S. K. Farrell, M. J. Loguidice, G. Remington, A. Conger, T. C. Frohman, D. A. Jacobs, C. E. Markowitz, G. R. Cutter, G. S. Ying, Y. Dai, M. G. Maguire, S. L. Galetta, E. M. Frohman, P. A. Calabresi, and L. J. Balcer. Longitudinal study of vision and retinal nerve fiber layer thickness in multiple sclerosis. *Annals of Neurology*, 67(6):749–760, 2010.

[146] M. N. Thabit, M. M. Farouk, M. Awni, and A. A. B. Mohamed. Early disability in ambulatory patients with multiple sclerosis: optical coherence tomography versus visual evoked potentials, a comparative study. *Egyptian Journal of Neurology, Psychiatry and Neurosurgery*, 56(1), 2020.

[147] Y. C. Tham, X. Li, T. Y. Wong, H. A. Quigley, T. Aung, and C. Y. Cheng. Global prevalence of glaucoma and projections of glaucoma burden through 2040: A systematic review and meta-analysis. *Ophthalmology*, 121(11):2081–2090, 2014.

[148] A. J. Thompson, B. L. Banwell, F. Barkhof, W. M. Carroll, T. Coetzee, G. Comi, J. Correale, F. Fazekas, M. Filippi, M. S. Freedman, K. Fujihara, S. L. Galetta, H. P. Hartung, L. Kappos, F. D. Lublin, R. A. Marrie, A. E. Miller, D. H. Miller, X. Montalban, E. M. Mowry, P. S. Sorensen, M. Tintoré, A. L. Traboulsee, M. Trojano, B. M. Uitdehaag, S. Vukusic, E. Waubant, B. G. Weinshenker, S. C. Reingold, and J. A. Cohen. Diagnosis of multiple sclerosis: 2017 revisions of the McDonald criteria. *The Lancet Neurology*, 17(2):162–173, 2018.

[149] J. Toledo, J. Sepulcre, A. Salinas-Alaman, A. García-Layana, M. Murie-Fernandez, B. Bejarano, and P. Villoslada. Retinal nerve fiber layer atrophy is associated with physical and cognitive disability in multiple sclerosis. *Multiple Sclerosis*, 14(7):906–912, 2008.

[150] H. Tomás, C. S. Alves, and J. Rodrigues. Laponite®: A key nanoplatform for biomedical applications? *Nanomedicine: Nanotechnology, Biology, and Medicine*, 14(7):2407–2420, 2018.

[151] Y. Tong, Y. L. Zhou, Y. Zheng, M. Biswal, P. Q. Zhao, and Z. Y. Wang. Analyzing cytokines as biomarkers to evaluate severity of glaucoma. *International Journal of Ophthalmology*, 10(6):925–930, 2017.

[152] A. Tousignant, P. Lemaitre, D. Precup, D. L. Arnold, and T. Arbel. Prediction of Disease Progression in Multiple Sclerosis Patients using Deep Learning Analysis of MRI Data. *Proceedings of Machine Learning Research*, 102:483–492, 2019.

[153] B. D. Trapp, J. Peterson, R. M. Ransohoff, R. Rudick, S. Mörk, and L. Bö. Axonal Transection in the Lesions of Multiple Sclerosis. *New England Journal of Medicine*, 338(5):278–285, 1998.

[154] T. Tsai, S. Reinehr, A. M. Maliha, and S. C. Joachim. Immune Mediated Degeneration and Possible Protection in Glaucoma. *Frontiers in Neuroscience*, 13(September):1–13, 2019.

[155] S. H. Tsang and P. Gouras. Molecular physiology and pathology of the retina. *Duane's Clinical Ophthalmology*, 3, 1996.

[156] A. Uji and N. Yoshimura. Microarchitecture of the Vitreous Body: A High-Resolution Optical Coherence Tomography Study. *American Journal of Ophthalmology*, 168:24–30, 2016.

[157] W. M. Ursey and J. A. Henry. Visual Functions of the Thalamus. *Annual Review of Vision Science*, 344(6188):1173–1178, 2015.

[158] N. N. Vagaja, H. R. Chinnery, N. Binz, J. M. Kezic, E. P. Rakoczy, and P. G. McMenamin. Changes in murine hyalocytes are valuable early indicators of ocular disease. *Investigative Ophthalmology and Visual Science*, 53(3):1445–1451, 2012.

[159] M. T. Wallin, W. J. Culpepper, E. Nichols, Z. A. Bhutta, T. T. Gebrehiwot, S. I. Hay, I. A. Khalil, K. J. Krohn, X. Liang, M. Naghavi, A. H. Mokdad, M. R. Nixon, R. C. Reiner, B. Sartorius, M. Smith, R. Topor-Madry, A. Werdecker, T. Vos, V. L. Feigin, and C. J. Murray. Global, regional, and national burden of multiple sclerosis 1990–2016: a systematic analysis for the Global Burden of Disease Study 2016. *The Lancet Neurology*, 18(3):269–285, 2019.

[160] T. R. Walters. Development and use of brimonidine in treating acute and chronic elevations of intraocular pressure: A review of safety, efficacy, dose response, and dosing studies. *Survey of Ophthalmology*, 41(SUPPL. 1), 1996.

[161] J. Wang, G. Wang, Y. Sun, Y. Wang, Y. Yang, Y. Yuan, Y. Li, and C. Liu. In Situ formation of pH-/thermo-sensitive nanohybrids via friendly-assembly of poly(N -vinylpyrrolidone) onto LAPONITE®. *RSC Advances*, 6(38):31816–31823, 2016.

[162] X. Wei, K. S. Cho, E. F. Thee, M. J. Jager, and D. F. Chen. Neuroinflammation and microglia in glaucoma: time for a paradigm shift. *Journal of Neuroscience Research*, 97(1):70–76, 2019.

[163] H. Wu, J. F. de Boer, and T. C. Chen. Reproducibility of Retinal Nerve Fiber Layer Thickness Measurements Using Spectral Domain Optical Coherence Tomography. *Journal of Glaucoma*, 20(8):470–476, oct 2011.

[164] Z. Wu, D. S. Weng, R. Rajshekhar, A. Thenappan, R. Ritch, and D. C. Hood. Evaluation of a qualitative approach for detecting glaucomatous progression using wide-field optical coherence tomography scans. *Translational Vision Science and Technology*, 7(3), 2018.

[165] S. Xiao, R. Castro, D. Maciel, M. Gonçalves, X. Shi, J. Rodrigues, and H. Tomás. Fine tuning of the pH-sensitivity of laponite-doxorubicin nanohybrids by polyelectrolyte multilayer coating. *Materials Science and Engineering C*, 60:348–356, 2016.

[166] S. Yang, J. Zhou, and D. Li. Functions and Diseases of the Retinal Pigment Epithelium. *Frontiers in Pharmacology*, 12(July):1–7, 2021.

[167] X. Yang, H. Zou, G. Jung, G. Richard, S. J. Linke, M. Ader, and U. Bartsch. Nonneuronal control of the differential distribution of myelin along retinal ganglion cell axons in the mouse. *Investigative Ophthalmology and Visual Science*, 54(13):7819–7827, 2013.

[168] M. S. Yeung, S. Zdunek, O. Bergmann, S. Bernard, M. Salehpour, K. Alkass, S. Perl, J. Tisdale, G. Possnert, L. Brundin, H. Druid, and J. Frisén. Dynamics of oligodendrocyte generation and myelination in the human brain. *Cell*, 159(4):766–774, 2014.

[169] Y. Yoo, L. Y. W. Tang, D. K. B. Li, L. Metz, S. Kolind, A. L. Traboulsee, and R. C. Tam. Deep learning of brain lesion patterns and user-defined clinical and MRI features for predicting conversion to multiple sclerosis from clinically isolated syndrome. *Computer Methods in Biomechanics and Biomedical Engineering: Imaging & Visualization*, 7(3):250–259, may 2019.

[170] J. Yperman, T. Becker, D. Valkenborg, V. Popescu, N. Hellings, B. V. Wijmeersch, and L. M. Peeters. Machine learning analysis of motor evoked potential time series to predict disability progression in multiple sclerosis. *BMC Neurology*, 20(1):1–15, 2020.

[171] H. Zhang, E. Alberts, V. Pongratz, M. Mühlau, C. Zimmer, B. Wiestler, and P. Eichinger. Predicting conversion from clinically isolated syndrome to multiple sclerosis–An imaging-based machine learning approach. *NeuroImage: Clinical*, 21(November 2018):101593, 2019.

[172] N. Zhang, J. Wang, Y. Li, and B. Jiang. Prevalence of primary open angle glaucoma in the last 20 years: a meta-analysis and systematic review. *Scientific Reports*, 11(1):13762, dec 2021.

[173] Y. Zhao, B. C. Healy, D. Rotstein, C. R. G. Guttmann, R. Bakshi, H. L. Weiner, C. E. Brodley, and T. Chitnis. Exploration of machine learning techniques in predicting multiple sclerosis disease course. *PloS one*, 12(4):e0174866, apr 2017.

[174] M. Zurita, C. Montalba, T. Labbé, J. P. Cruz, J. Dalboni da Rocha, C. Tejos, E. Ciampi, C. Cárcamo, R. Sitaram, and S. Uribe. Characterization of relapsing-remitting multiple sclerosis patients using support vector machine classifications of functional and diffusion MRI data. *NeuroImage: Clinical*, 20(July):724–730, 2018.

Appendix

In accordance with the requirements established by art. 20 of the Doctoral Thesis Regulations, approved by agreement of 25/06/2020 of the Governing Council of the University of Zaragoza, an appendix is included with the data of the published works, the impact factor of the journals and the thematic areas corresponding to the publications included in this Doctoral Thesis by compendium of publications.

- **Manuscript 1:** A mathematical model to predict the evolution of retinal nerve fiber layer thinning in multiple sclerosis patients
  Authors: Alberto Montolío, José Cegoñino, Elvira Orduna, Berta Sebastian, Elena Garcia-Martin, Amaya Pérez del Palomar
  Status: Published, 2019. Computers in Biology and Medicine 111, 103357
  https://doi.org/10.1016/j.compbiomed.2019.103357
  Journal: Computers in Biology and Medicine
  Journal impact factor (JCR): 3.434, Q1 (2019)
  Thematic categories of Web of Sciences: Engineering, Biomedical; Computer Sciences, Interdisciplinary Applications; Mathematical & Computational Biology; Biology

- **Manuscript 2:** Swept source optical coherence tomography to early detect multiple sclerosis disease. The use of machine learning techniques
  Authors: Amaya Pérez del Palomar, José Cegoñino, Alberto Montolío, Elvira Orduna, Elisa Vilades, Berta Sebastian, Luis E. Pablo, Elena Garcia-Martin
  Status: Published, 2019. PLos ONE 14(5), e0216410
  https://doi.org/10.1371/journal.pone.0216410
  Journal: PLoS ONE
  Journal impact factor (JCR): 2.740, Q2 (2019)
  Thematic categories of Web of Sciences: Multidisciplinary Sciences

- **Manuscript 3:** Machine learning in diagnosis and disability prediction of

multiple sclerosis using optical coherence tomography
Authors: Alberto Montolío, Alejandro Martín-Gallego, José Cegoñino, Elvira Orduna, Elisa Vilades, Elena Garcia-Martin, Amaya Pérez del Palomar
Status: Published, 2021. Computers in Biology and Medicine 133, 104416
https://doi.org/10.1016/j.compbiomed.2021.104416
Journal: Computers in Biology and Medicine
Journal impact factor (JCR): 4.589, Q1 (2020)
Thematic categories of Web of Sciences: Engineering, Biomedical; Computer Sciences, Interdisciplinary Applications; Mathematical & Computational Biology; Biology

- **Manuscript 4:** Comparison of machine learning methods using Spectralis OCT for diagnosis and disability progression prognosis in multiple sclerosis
  Authors: Alberto Montolío, José Cegoñino, Elena Garcia-Martin, Amaya Pérez del Palomar
  Status: Published, 2022. Annals of Biomedical Engineering, s10439-022-02930-3
  https://doi.org/10.1007/s10439-022-02930-3
  Journal: Annals of Biomedical Engineering
  Journal impact factor (JCR): 3.934, Q2 (2020)
  Thematic categories of Web of Sciences: Engineering, Biomedical

Apéndice

De acuerdo con los requisitos establecidos por el art. 20 del Reglamento de la Tesis Doctorales, aprobado por acuerdo de 25/06/2020 del Consejo de Gobierno de la Universidad de Zaragoza, se incluye un apéndice con los datos de los trabajos publicados, el factor de impacto de las revistas y las áreas temáticas correspondientes a las publicaciones que se recogen en esta Tesis Doctoral por compendio de publicaciones.

- **Manuscrito 1:** A mathematical model to predict the evolution of retinal nerve fiber layer thinning in multiple sclerosis patients
  Autores: Alberto Montolío, José Cegoñino, Elvira Orduna, Berta Sebastian, Elena Garcia-Martin, Amaya Pérez del Palomar
  Estado: Publicado, 2019. Computers in Biology and Medicine 111, 103357
  https://doi.org/10.1016/j.compbiomed.2019.103357
  Revista: Computers in Biology and Medicine
  Factor de impacto de la revista (JCR): 3.434, Q1 (2019)
  Categorías temáticas de Web of Sciences: Engineering, Biomedical; Computer Sciences, Interdisciplinary Applications; Mathematical & Computational Biology; Biology

- **Manuscrito 2:** Swept source optical coherence tomography to early detect multiple sclerosis disease. The use of machine learning techniques
  Autores: Amaya Pérez del Palomar, José Cegoñino, Alberto Montolío, Elvira Orduna, Elisa Vilades, Berta Sebastian, Luis E. Pablo, Elena Garcia-Martin
  Estado: Publicado, 2019. PLos ONE 14(5), e0216410
  https://doi.org/10.1371/journal.pone.0216410
  Revista: PLoS ONE
  Factor de impacto de la revista (JCR): 2.740, Q2 (2019)
  Categorías temáticas de Web of Sciences: Multidisciplinary Sciences

- **Manuscrito 3:** Machine learning in diagnosis and disability prediction of

multiple sclerosis using optical coherence tomography
Autores: Alberto Montolío, Alejandro Martín-Gallego, José Cegoñino, Elvira Orduna, Elisa Vilades, Elena Garcia-Martin, Amaya Pérez del Palomar
Estado: Publicado, 2021. Computers in Biology and Medicine 133, 104416
https://doi.org/10.1016/j.compbiomed.2021.104416
Revista: Computers in Biology and Medicine
Factor de impacto de la revista (JCR): 4.589, Q1 (2020)
Categorías temáticas de Web of Sciences: Engineering, Biomedical; Computer Sciences, Interdisciplinary Applications; Mathematical & Computational Biology; Biology

- **Manuscrito 4:** Comparison of machine learning methods using Spectralis OCT for diagnosis and disability progression prognosis in multiple sclerosis
  Autores: Alberto Montolío, José Cegoñino, Elena Garcia-Martin, Amaya Pérez del Palomar
  Estado: Publicado, 2022. Annals of Biomedical Engineering, s10439-022-02930-3
  https://doi.org/10.1007/s10439-022-02930-3
  Revista: Annals of Biomedical Engineering
  Factor de impacto de la revista (JCR): 3.934, Q2 (2020)
  Categorías temáticas de Web of Sciences: Engineering, Biomedical

1542

Universidad
Zaragoza